



universität
wien

DISSERTATION

Titel der Dissertation

„Micromechanics of Mechanoreceptors in Arthropods”

„Mikromechanik von Mechanorezeptoren bei Arthropoden”

Verfasser

Mag. rer. nat. Clemens Florian Schaber

angestrebter akademischer Grad

Doktor der Naturwissenschaften (Dr. rer. nat.)

Wien, 2011

Studienkennzahl lt. Studienblatt:

A 091 439

Dissertationsgebiet lt. Studienblatt:

Dr.-Studium der Naturwissenschaften Zoologie

Betreuerin / Betreuer:

em. O. Univ.-Prof. Dr. Friedrich G. Barth

Contents / Inhaltsverzeichnis

| | Page / Seite |
|--|--------------|
| Abstract | 4 |
| Kurzzusammenfassung (Deutsch) | 5 |
| Summary..... | 6 |
| Zusammenfassung (Deutsch) | 10 |
| Acknowledgements / Danksagungen | 15 |
| | |
| Force transformation in spider strain sensors: white light interferometry | 17 |
| | |
| Spider joint hair sensilla: micromechanics and adaptation to proprioceptive stimulation..... | 39 |
| | |
| Viscoelastic nanoscale properties of cuticle contribute to the high-pass properties of spider vibration receptor (<i>Cupiennius salei</i> Keys.) | 63 |
| | |
| Surface force spectroscopic point load measurements and viscoelastic modelling of the micromechanical properties of air flow sensitive hairs of a spider (<i>Cupiennius salei</i>) | 74 |
| | |
| Addendum: Finite element modeling of arachnid slit sensilla: II. Actual lyriform organs and the face deformations of the individual slits | 91 |
| | |
| Addendum: In search of differences between the two types of sensory cells innervating spider slit sensilla (<i>Cupiennius salei</i> Keys.) | 106 |
| | |
| Addendum: Published Abstracts | 118 |
| | |
| Research Activities Clemens F. Schaber | 140 |
| Lebenslauf (Deutsch) | 145 |

Abstract

This dissertation comprises six manuscripts and publications dealing with the basal mechanical events leading to the stimulation of different mechanoreceptors of the spider *Cupiennius salei*. The main focus is the transformation of the mechanical stimuli on their way to the dendrites of the sensory cells, the cuticular structures involved, and their specific material properties.

The different types of mechanoreceptors are hair sensilla on the one hand, which are stimulated by the movement of their hair shaft, and slit sensilla on the other hand, which are stimulated by their compression as a consequence of strains in the exoskeleton. In both structural receptor types proprioceptors sensible for movements of leg segments during locomotion are compared with receptors for environmental stimuli like vibrations and air flow. Whereas for the proprioceptors the biological range of operation is limited by the biomechanics of the spider's leg, in the exteroceptors the stimulus amplitudes span a range of several powers of magnitude.

One manuscript directly compares a proprioceptive slit organ stimulated by lateral excursions of a leg segment with a highly sensitive exteroceptive vibration slit sensor. The range of operation of the proprioceptor is well covered by the linear transformation of the stimulus force to the sensory effective slit compression. In case of the vibration receptor the force transformation follows the stimulus amplitude exponentially, which is reasonable for the detection of different and widely unknown vibration amplitudes. Another manuscript deals with the material properties of a viscoelastic cuticular structure located on the way of the vibrations to the vibration receptor. By its viscoelastic material properties this cuticular structure represents an efficient mechanical filter for the biologically relevant vibration frequencies.

A further manuscript addresses proprioceptive hair sensilla sensitive for the velocity of flexion of a leg joint. Here the properties of the hair suspension are especially adapted to deal with the mechanical loads of hair deflection at every step of the spider walking. In contrast, the hair suspension of the highly sensitive air flow receptive hairs, the trichobothria, facilitates the sensory effective hair deflection by the minute forces of friction with the particles of moving air (manuscript 4). The mechanical properties of the hair suspension of the trichobothria are adapted to the oscillating nature of hair deflection due to the biologically relevant air movements.

The results show that apparently small changes of the mechanically relevant cuticular structures and their material properties result in the adaption of the different mechanoreceptor types to their particular range of operation. This fine-tuning to the properties of the biological stimuli becomes even more obvious when the sensory responses to adequate stimulation are taken into account.

Kurzzusammenfassung

Die vorliegende Dissertation umfasst sechs Manuskripte und Publikationen, die sich mit den grundlegenden mechanischen Ereignissen bei der Reizung, mit den cuticularen Strukturen, deren Materialeigenschaften, und im Speziellen mit der Umwandlung der mechanischen Reize auf dem Weg zu den Dendriten der Sinneszellen (Reiztransformation) unterschiedlicher Mechanorezeptoren der Spinne *Cupiennius salei* befassen.

Die behandelten Rezeptortypen sind einerseits Haarsensillen, die durch die Bewegung ihres Haarschafts gereizt werden, und andererseits Spaltsensillen, die auf ihre Kompression infolge von Spannungen im Exoskelett reagieren. Ein Schwerpunkt der Untersuchungen bei beiden Rezeptortypen ist der Vergleich von Propriozeptoren, die für Bewegungen des Spinnenbeins bei der Lokomotion sensibel sind, und deren biologischer Einsatzbereich durch die Biomechanik des Beins begrenzt ist, mit exterozeptiven Sensillen, die ein breites Spektrum unterschiedlicher Reizamplituden aus der Umwelt detektieren.

Das erste Manuskript widmet sich direkt dem Vergleich eines propriozeptiven Spaltsinnesorgans, das durch laterale Auslenkungen eines Beinglieds gereizt wird, mit einem exterozeptiven Vibrationsrezeptor. Der Einsatzbereich des propriozeptiven Organs wird durch die lineare Umwandlung der Reizkraft in die reizwirksame Spaltkompression gut abgedeckt. Beim Vibrationsrezeptor verläuft die Kraftumwandlung exponentiell, was zur Detektion unterschiedlicher und weitgehend unbekannter Vibrationsamplituden sinnvoll ist. Ein weiteres Manuskript behandelt die Materialeigenschaften einer viskoelastischen cuticularen Struktur, die diesem Vibrationsrezeptor auf dem Weg der Vibrationen vom Substrat vorgeschaltet ist, und die sich als effizienter mechanischer Filter für die biologisch relevanten Vibrationsfrequenzen erweist.

Ein Manuskript befasst sich mit propriozeptiven Haarsensillen, die für die Geschwindigkeit des Abbiegens eines Beingelenks sensibel sind. Bei diesem Sensillentypus sind die Eigenschaften der Haaraufhängung an die mechanischen Belastungen durch die Haarauslenkung infolge von Berührungen bei jedem Schritt der Spinne angepasst. Im Gegensatz dazu ermöglicht die Haaraufhängung der hochempfindlichen Luftbewegungsdetektoren, der Trichobothrien, die reizwirksame Bewegung des Haares durch die winzigen Kräfte, die durch Reibung mit den Partikeln der Luft entstehen (Manuskript 4). Die mechanischen Eigenschaften der Haaraufhängung der Trichobothrien stellen eine Anpassung an den oszillierenden Charakter der biologisch relevanten Luftbewegungen dar.

Die Ergebnisse zeigen, dass bei den unterschiedlichen Mechanorezeptoren durch scheinbar geringe Unterschiede der mechanischen Strukturen und des beteiligten Materials (Cuticula) eine hochgradige Anpassung an den jeweiligen biologischen Aufgabenbereich erreicht wird. Diese Feinabstimmung an die relevanten Reize zeigt sich auch deutlich an den sensorischen Antworteigenschaften bei adäquater Reizung.

Summary

Force transformation in spider strain sensors: white light interferometry. (Manuscript in preparation for publication)

Scanning white light interferometry and micro-force measurements were applied on biological strain sensor structures to explain the mechanical stimulus transformation in the exoskeleton of the spider *Cupiennius salei* on the way to the sensory cells of two different compound slit sense organs (lyriform organs).

The transformation of the stimulus force leads to strains in the cuticle and, as a result of that, to the compression of the individual slits of the lyriform organs, which are located at articulations of the legs of the spider. The compression of the slits to reach the sensory threshold is not more than 30 nm. The two lyriform organs examined are the highly sensitive vibration receptor HS-10 and the proprioceptive organ HS-8.

For the proprioceptor the loading curve is linear, which is very reasonable for the sensor's biological range of operation in resolving the lateral angular deflection of the metatarsus relative to the tibia. In HS-8 the mechanical sensitivity of the individual slits gradually decreases with decreasing slit length and compression values from 106 nm/mN down to 13 nm/mN.

The force to compress the slits of the vibration receptor HS-10 rises highly exponentially making this exteroceptive organ well suited to detect a wide range of stimulus amplitudes. In HS-10 the two slits examined differ roughly 3-fold in the mechanical differential sensitivity with compression values of 522 nm/mN and 195 nm/mN in the biologically most relevant range. Therefore, the gradual stimulus amplitude detection by the individual slits of the organ HS-10 is very likely.

Spider joint hair sensilla: micromechanics and adaptation to proprioceptive stimulation. (Manuscript in preparation for publication)

The present work deals with proprioceptive hair sensilla of the wandering spider *Cupiennius salei*, which are deflected by joint flexion during locomotion. The hairs are located at the articulation of tibia and metatarsus on all walking legs.

On the tibia 20 such sensory hairs form a distinct row. They face about 75 sensilla on the metatarsus. When two opposing hairs get into contact during flexion of the joint, they deflect each other, reversibly interlocked by microtrichs on their hair shafts.

The torques resisting hair deflections are much lower into the direction of natural stimulation than into the other directions, indicating a pronounced mechanical directionality of the hair suspension. Whereas in the preferred direction the torsional restoring constant S of the hair suspension is in the range of 10^{-10} Nm rad⁻¹ up to a deflection angle of about 30° (mean of natural deflections), it is larger by one to two powers of ten in other directions.

Within the spider's natural step frequency between 0.3 and 3 Hz the sensory response (action potentials) of the joint hair sensilla follows the velocity of hair deflection. Action potentials are set off at every step of the walking spider, when the hairs are deflected from their resting position. At hair deflections with constant angular velocities but different final deflection angles the maximum frequency of the action potentials remains constant. These results indicate that the joint hair sensilla are sensitive to the step frequency and the velocity of joint flexion.

All findings point to the morphological, mechanical and physiological adaptation of the joint hair sensilla to their natural stimulation during locomotion.

Viscoelastic nanoscale properties of cuticle contribute to the high-pass properties of spider vibration receptor (*Cupiennius salei* Keys). (Published in: Journal of the Royal Society Interface 4, 1135-1143, 2007)

Atomic force microscopy (AFM) and surface force spectroscopy were applied in live spiders to their joint pad material located distal of the metatarsal lyriform organs, which are highly sensitive vibration sensors.

The surface topography of the material is sufficiently smooth to probe the local nanomechanical properties with nanometre elastic deflections. Nanoscale loads were applied in the proximad direction on the distal joint region simulating the natural stimulus situation.

The force curves obtained indicate the presence of a soft, liquid-like epicuticular layer (20 – 40 nm thick) above the pad material, which has much higher stiffness. The Young's modulus of the pad material is close to 15 MPa at low frequencies, but increases rapidly with increasing frequencies approximately above 30 Hz to approximately 70 MPa at 112 Hz. The adhesive forces drop sharply by about 40 % in the same frequency range.

The strong frequency dependence of the elastic modulus indicates the viscoelastic nature of the pad material, its glass transition temperature being close to room temperature ($25^{\circ} \pm 2^{\circ} \text{C}$) and, therefore, to its maximized energy absorption from low-frequency mechanical stimuli. These viscoelastic properties of the cuticular pad are suggested to be at least partly responsible for the high-pass characteristics of the vibration sensor's physiological properties demonstrated earlier.

Surface force spectroscopic point load measurements and viscoelastic modelling of the micromechanical properties of air flow sensitive hairs of a spider (*Cupiennius salei*). (Published in: Journal of the Royal Society Interface 6, 681-694, 2009)

The micromechanical properties of spider air flow hair sensilla (trichobothria) were characterized with nanometre resolution using surface force spectroscopy (SFS) under conditions of different constant deflection angular velocities $\dot{\theta}$ (rad s^{-1}) for hairs 900 – 950 μm long prior to shortening for measurement purposes.

In the range of angular velocities examined ($4 \times 10^{-4} - 2.6 \times 10^{-1} \text{ rad s}^{-1}$), the torque T (Nm) resisting hair motion and its time rate of change \dot{T} (Nm s^{-1}) were found to vary with deflection velocity according to power functions. In this range of angular velocities, the motion of the hair is most accurately captured by a three-parameter solid model, which numerically describes the properties of the hair suspension. A fit of the three-parameter model (3p) to the experimental data yielded the two torsional restoring parameters, $S_{3p} = 2.91 \times 10^{-11} \text{ Nm rad}^{-1}$ and $S'_{3p} = 2.77 \times 10^{-11} \text{ Nm rad}^{-1}$ and the damping parameter $R_{3p} = 1.46 \times 10^{-12} \text{ Nm s rad}^{-1}$.

For angular velocities larger than 0.05 rad s^{-1} , which are common under natural conditions, a more accurate angular momentum equation was found to be given by a two-parameter Kelvin solid model. For this case, the multiple regression fit yielded $S_{2p} = 4.89 \times 10^{-11} \text{ Nm rad}^{-1}$ and $R_{2p} = 2.83 \times 10^{-14} \text{ Nm s rad}^{-1}$ for the model parameters.

While the two-parameter model has been used extensively in earlier work primarily at high hair angular velocities, to correctly capture the motion of the hair at both low and high angular velocities it is necessary to employ the three-parameter model. It is suggested that the viscoelastic mechanical properties of the hair suspension work to promote the phasic response behaviour of the sensilla.

Addendum: Finite element modeling of arachnid slit sensilla: II. Actual lyriform organs and the face deformations of the individual slits. (First author: Bernhard Höbl. Published in: *Journal of Comparative Physiology A* 195, 881-894, 2009)

Arachnid slit sensilla respond to minute strains in the exoskeleton. After having applied Finite Element (FE) analysis to simplified arrays of five straight slits (Höbl et al. *J Comp Physiol A* 193:445–459, 2007) we now present a computational study of the effects of more subtle natural variations in geometry, number and arrangement of slits on the slit face deformations.

Our simulations show that even minor variations in these parameters can substantially influence a slit's directional response. Using white-light interferometric measurements of the surface deformations of a lyriform organ, it is shown that planar FE models are capable of predicting the principal characteristics of the mechanical responses. The magnitudes of the measured and calculated slit face deformations are in good agreement. At threshold, they measure between 1.7 and 43 nm.

In a lyriform organ and a closely positioned loose group of slits, the detectable range of loads increases to approximately 3.5 times the range of the lyriform organ alone.

Stress concentration factors (up to ca. 29) found in the vicinity of the slits were evaluated from the models. They are mitigated due to local thickening of the exocuticle and the arrangement of the chitinous microfibrils that prevents the formation of cracks under physiological loading conditions.

Addendum: In search of differences between the two types of sensory cells innervating spider slit sensilla (*Cupiennius salei* Keys.). (First author: Jorge Molina.

Published in: Journal of Comparative Physiology A 195, 1031-1041, 2009)

The metatarsal lyriform organ of the spider *Cupiennius salei* is a vibration detector consisting of 21 cuticular slits supplied by two sensory cells each, one ending in the outer and the other at the inner slit membrane.

In search of functional differences between the two cell types due to differences in stimulus transmission, we analyzed (1) the adaptation of responses to electrical stimulation, (2) the thresholds for mechanical stimulation and (3) the representation of male courtship vibrations using intracellular recording and staining techniques.

Single- and multi-spiking receptor neurons were found among both cell types, which showed high-pass filter characteristics. Below 100-Hz threshold, tarsal deflections were between 1° and 10°. At higher frequencies, they decreased down to values as small as 0.05°, corresponding to 4.5 nm tarsal deflections, in the most sensitive cases. Different slits in the organ and receptor cells with slow or fast adaptation did not differ in this regard.

When stimulated with male courtship vibrations, both types of receptor cells again did not differ significantly regarding number of action potentials, latency and synchronization coefficients. Surprisingly, the differences in dendrite coupling were not reflected by the physiological responses of the two cell types innervating the slits.

Zusammenfassung

Krafttransformation bei der Detektion von Spannungen im Exoskelett von Spinnen durch Spaltsinnesorgane: Weißlichtinterferometrie. (Manuskript in Vorbereitung für die Veröffentlichung)

Für ein tieferes Verständnis der Umwandlung mechanischer Belastungen des Exoskeletts zur reizwirksamen Kompression der Rezeptoren für Spannungen in der Cuticula (lyraförmige Spaltsinnesorgane) wurden dreidimensionale Weißlichtinterferometrie und Mikrokraftmessungen an zwei Beingelenken der Spinne *Cupiennius salei* durchgeführt.

Zum Vergleich der Reiztransformation bei zwei lyraförmigen Organen mit unterschiedlichen Funktionen wurden der hochempfindliche exterozeptive Vibrationsrezeptor, das lyraförmige Organ HS-10 am Metatarsus, und das propriozeptive lyraförmige Organ HS-8 auf der Tibia ausgewählt.

Die bei der Auslenkung von Beingliedern auftretenden Kräfte führen durch Belastungen der Cuticula im Gelenkbereich zu Verformungen an der Stelle der Spannungsrezeptoren und zur Kompression der einzelnen, circa 2 μm breiten, Spalte dieser lyraförmigen Organe. Zum Erreichen des sensorischen Schwellenwerts, bei dem ein Aktionspotential der Sinneszellen durch die Verformung der, mit der spaltbedeckenden Membran gekoppelten, Dendritenspitze ausgelöst wird, sind Spaltkompressionen von nicht mehr als 30 nm ausreichend.

Die Belastungskurve für das propriozeptive Organ HS-8 verläuft linear. Durch die abgestufte Kompression der sieben bis acht unterschiedlich langen Spalte wird der Winkel der Auslenkung des Metatarsus zur Tibia aufgelöst. Die mechanische Empfindlichkeit der einzelnen Spalte sinkt schrittweise mit abnehmender Spaltlänge. Die Kompressionswerte an der Kopplungsstelle des sensorischen Dendrits mit der Spaltmembran liegen zwischen 106 nm/mN beim längsten und 13 nm/mN beim kürzesten Spalt. Die Linearität der Reiztransformation ist im Fall des propriozeptiven Organs äußerst sinnvoll, da der biologische Einsatzbereich des Rezeptors bekannt ist und dieser mittels linearer Kraftumwandlung gut aufgelöst werden kann.

Die Belastungskurve für den exterozeptiven Vibrationsrezeptor HS-10 ist hochgradig exponentiell. Dies ist hier insofern sinnvoll, da die Amplitude der zu detektierenden Vibrationen weitgehend unbekannt ist und dadurch ein breiter Einsatzbereich abgedeckt wird. Auch beim lyraförmigen Organ HS-10 zeigt sich eine abgestufte mechanische Empfindlichkeit der einzelnen cuticulären Spalte. Die differenzielle Empfindlichkeit der zwei für diese Studie ausgewählten Spalte unterscheidet sich mit Kompressionswerten von 522 nm/mN und 195 nm/mN im biologisch relevanten Bereich zwischen 0,5 mN und 3 mN grob um das Dreifache. Das deutet darauf hin, dass auch beim

Vibrationsrezeptor HS-10 die Reizamplitude mechanisch durch die einzelnen Spalte des Organs aufgelöst wird.

Gelenkhaarsensillen der Spinne *Cupiennius salei*: Mikromechanik und Adaptation an propriozeptive Reizung. (Manuskript in Vorbereitung für die Veröffentlichung)

Diese Studie beschäftigt sich mit propriozeptiven Haarsensillen der Spinne *Cupiennius salei*, die beim Abbiegen des Tibia-Metatarsus-Gelenks während der Lokomotion ausgelenkt und damit gereizt werden. Diese Haare befinden sich ventral an allen vier Laufbeinpaaren am Gelenk zwischen Tibia und Metatarsus.

Am distalen Ende der Tibia bilden ungefähr 20 dieser Sinneshaare eine von der „üblichen Behaarung“ des Beins abgesetzte Reihe. Auf der gegenüberliegenden Seite des Gelenks, dem proximalen Ende des Metatarsus, stehen circa 75 Gelenkhaare in annähernd rechtem Winkel von der Cuticulaoberfläche ab. Beim Abbiegen des Gelenks in der Dorsoventralebene treffen diese Haare aufeinander und lenken sich in der Folge gegenseitig aus. Dabei sind sie durch Mikrotrichen auf ihren Haarschäften reversibel gekoppelt und gleiten nicht aneinander vorbei.

Die Drehmomente, die der Haarauslenkung entgegenwirken, weisen auf eine deutliche Richtungscharakteristik der Haaraufhängung hin. Die Federkonstanten S sind in die Richtung der natürlichen propriozeptiven Reizung mit Werten im Bereich von 10^{-10} Nm rad⁻¹ um das Zehn- bis Hundertfache geringer als in die anderen Richtungen. Diese, für taktile Haare äußerst geringe, Werte gelten bis zu einem Auslenkungswinkel von 30 Grad aus der Ruhelage. Ein Auslenkungswinkel von 30 Grad ist gleichzeitig der Mittelwert der Auslenkungen während der Lokomotion und weist auf eine strukturelle Anpassung der Haaraufhängung an die natürlichen Reize hin.

Die Simulation der Auslenkungen, die bei normaler, geradeausgerichteter Lokomotion der Spinne auftreten, im elektrophysiologischen Experiment zeigt, dass die Auslenkung der Gelenkhaarsensillen aus der Ruhelage bei jedem Schritt der Spinne zu einer Salve von Aktionspotentialen führt. Dadurch wird die Schrittfrequenz detektiert. Weiters kann durch die sensorische Antwort die Geschwindigkeit des Abbiegens des Gelenks im Bereich der natürlichen Schrittfrequenzen (0.3 bis 3 Schritte pro Sekunde) von den Gelenkhaarsensillen aufgelöst werden.

Alle Ergebnisse weisen auf die Adaptation der Gelenkhaarsensillen an die Parameter der natürlichen Reizung während der Lokomotion von *Cupiennius salei* auf struktureller, morphologischer, mechanischer und physiologischer Ebene hin.

Viskoelastische Eigenschaften der Cuticula im Nanometerbereich tragen zur Hochpass-Charakteristik des Vibrationsrezeptors der Spinne *Cupiennius salei* bei. (Veröffentlicht in: Journal of the Royal Society Interface 4, 1135-1143, 2007)

Die Materialeigenschaften einer weichen cuticuläre Struktur, des so genannten metatarsalen Gelenkpolsters, wurden mit Atomkraft-Mikroskopie (AFM) und Oberflächen-Kraftspektroskopie (SFS) untersucht. Dabei wurde mit dem Cantilever des Atomkraft-Mikroskops mit unterschiedlichen Wiederholffrequenzen in das Material gedrückt und dessen mechanischer Widerstand im Nanonewtonbereich gemessen.

Das untersuchte metatarsale Gelenkpolster ist dem lyraförmigen Organ HS-10, einem hochempfindlichen Vibrationssensor der Spinne *Cupiennius salei*, auf dem Weg der Vibrationen vom Substrat vorgeschaltet. Die Richtung der mechanischen Belastungen in der vorliegenden Untersuchung entsprach der von natürlichen Reizen.

Die Ergebnisse zeigen eine 20 bis 40 nm dicke, weiche, und flüssigkeitsähnliche Schicht oberhalb des härteren cuticulären Polstermaterials. Die Materialeigenschaften des cuticulären Polstermaterials selbst ändern sich mit zunehmender Prüfgeschwindigkeit erheblich. Während das E-Modul bei niedrigen Wiederholffrequenzen bis zu 30 Hz etwa 15 MPa beträgt, steigt es bis zur höchsten Wiederholffrequenz von 112 Hz auf circa 70 MPa an. Im gleichen Messbereich sinken die Adhäsionskräfte um circa 40 %.

Die starke Frequenzabhängigkeit der Materialeigenschaften des cuticulären Polsters zeigen, dass diese Cuticulastruktur hoch viskoelastisch ist. Die aus den Daten berechnete Glas-Gummi-Übergangstemperatur des Materials liegt mit $25^{\circ} \text{C} \pm 2^{\circ} \text{C}$ nahe der Raumtemperatur. Dadurch wird die Energie niedrigfrequenter mechanischer Reize maximal absorbiert.

Für die physiologischen Eigenschaften des Vibrationsrezeptors bedeutet dies, dass die viskoelastischen Eigenschaften des cuticulären Polstermaterials höchstwahrscheinlich für die schon früher gemessene Hochpass-Charakteristik des Vibrationssensors verantwortlich sind. Biologisch unrelevante, niedrigfrequente Reize werden ausgefiltert, während hochfrequente Vibrationen, die von Räubern oder Beute der Spinne erzeugt werden, effizient zu den Vibrationsdetektoren weitergeleitet werden.

Oberflächen-kraftspektroskopische Punktbelastungsmessungen und viskoelastische Modellierung der mikromechanischen Eigenschaften luftströmungsempfindlicher Haarsensillen der Spinne *Cupiennius salei*. (Veröffentlicht in: Journal of the Royal Society Interface 6, 681-694, 2009)

Die mikromechanischen Eigenschaften luftströmungsempfindlicher Haarsensillen (Trichobothrien) von Spinnen wurden mittels Oberflächen-Kraft-Spektroskopie (Surface Force Spectroscopy, SFS) im Nanometerbereich charakterisiert. Dazu wurden 900 μm bis 950 μm lange Haarsensillen, die zu Messzwecken gekürzt wurden, mit unterschiedlichen Winkelgeschwindigkeiten linear ausgelenkt.

Im Messbereich, bei Winkelgeschwindigkeiten zwischen $4 \times 10^{-4} \text{ rad s}^{-1}$ und $2,6 \times 10^{-1} \text{ rad s}^{-1}$, nehmen das Drehmoment, das der Haarauslenkung entgegenwirkt, und dessen zeitliche Änderungsrate mit ansteigender Auslenkungsgeschwindigkeit zu und folgen dabei Potenzfunktionen. Am besten können diese viskoelastischen mechanischen Eigenschaften der Haaraufhängung mathematisch mit dem dreiparametrischen Zener-Modell beschrieben werden, das aus zwei Hooke'schen Federelementen (S , S') und einem Dämpfungselement (R) besteht. Die Anpassung dieses Modells an die experimentellen Daten ergibt für die beiden parallelen Federelemente die Federkonstanten $S = 2,91 \times 10^{-11} \text{ Nm rad}^{-1}$ und $S' = 2,77 \times 10^{-11} \text{ Nm rad}^{-1}$, sowie die Dämpfungskonstante $R = 1,46 \times 10^{-12} \text{ Nm s rad}^{-1}$.

Die Daten bei größeren Winkelgeschwindigkeiten als $0,05 \text{ rad s}^{-1}$ können auch mit einem zweiparametrischen Voigt-Kelvin-Modell beschrieben werden, in dem ein Federelement (S) und ein Dämpfungselement (R) parallel angeordnet sind. Die Anpassung dieses Modells an die experimentellen Daten durch Mehrfachregression ergibt Werte für $S = 4,89 \times 10^{-11} \text{ Nm rad}^{-1}$ für das Federelement und $R = 2,83 \times 10^{-14} \text{ Nm s rad}^{-1}$ für das Dämpfungselement.

Für die sensorische Funktion der Trichobothrien bedeutet dies, dass die Viskoelastizität der Haaraufhängung den Beginn einer Haarauslenkung aus der Ruheposition erleichtert, was eine Anpassung an den oszillierenden Charakter biologisch relevanter Reize darstellt. In der Diskussion des Kapitels wird der Beitrag dieser mechanischen Eigenschaften zum phasischen physiologischen Antwortverhalten der Trichobothrien erörtert.

Anhang: Finite-Elemente-Modellierung der Spaltsensillen von Arachniden: lyraförmige Organe und die Verformung der einzelnen Spalte. (Erstautor: Bernhard Höbl. Veröffentlicht in: *Journal of Comparative Physiology A* 195, 881-894, 2009)

Die Spaltsensillen von Arachniden antworten auf winzige Spannungen im Exoskelett. Nach der vorangegangenen Finite-Elemente- (FE) Analyse vereinfachter Anordnungsmuster von fünf geraden Spalten (Höbl et al., *J Comp Physiol A* 193, 445-459, 2007) wurden in der vorliegenden Studie die Auswirkungen der, wie sich zeigte raffinierten, natürlichen Variationen der Geometrie, der Anzahl und der Anordnungsmuster der Spalte auf deren Verformung bei Belastung berechnet. Die FE-Computersimulationen zeigen, dass selbst geringfügige Änderungen dieser Parameter die Richtungscharakteristik der Spaltverformung substantiell beeinflussen können.

Weißlichtinterferometrische Messungen der Oberflächendeformation an einem lyraförmigen Organ (einem Spaltsinnesorgan, das aus mehreren benachbart und weitgehend parallel angeordneten Einzelspaltsensillen besteht) einer lebenden Spinne zeigen, dass ebene FE-Modelle die wesentlichen Charakteristiken der mechanischen Antworten der einzelnen Spalte vorhersagen können. Die Ausmaße der gemessenen und

der berechneten Spaltverformungen stimmen gut überein. Am sensorischen Schwellenwert betragen die reizwirksamen Spaltkompressionen zwischen 1,7 und 43 nm.

Im Fall eines lyraförmigen Organs, das mit einer in der Nähe positionierten losen Spaltgruppe kombiniert wurde, steigt der detektierbare Belastungsbereich auf das ungefähr 3,5-fache im Vergleich zum Detektionsbereich des lyraförmigen Organs allein. Stresskonzentrationsfaktoren (bis zu etwa 29) in der Umgebung der Spalte wurden an den Modellen abgelesen. Unter physiologischen Belastungsbedingungen werden diese Stresskonzentrationen durch lokale Verdickungen der Exocuticula und die Anordnung der Chitin-Mikrofasern abgeschwächt, damit Rissbildungen verhindert werden.

Anhang: Auf der Suche nach Unterschieden bei den zwei Typen von Sinneszellen, die die Spaltsensillen der Spinne *Cupiennius salei* innervieren. (Erstautor: Jorge Molina. Veröffentlicht in: Journal of Comparative Physiology A 195, 1031-1041, 2009)

Das metatarsale lyraförmige Organ der Spinne *Cupiennius salei* ist ein Vibrationsdetektor. Es besteht aus 21 cuticulären Spalten, die jeweils mit zwei Sinneszellen ausgestattet sind. Der sensorische Dendrit der einen Sinneszelle endet in der äußeren und der der anderen an der inneren Spaltmembran.

Auf der Suche nach funktionellen Unterschieden zwischen den zwei Zelltypen durch Unterschiede in der Reizübertragung analysierten wir (1) die Adaptation der Antworten an elektrische Reizung, (2) die Schwellenwerte bei mechanischer Reizung, und (3) die Abbildung männlicher Balzvibrationen mit intrazellulären Ableitungs- und Färbetechniken.

Rezeptorneurone, die entweder mit einem einzelnen (single-spiking) oder mit mehreren (multi-spiking) Aktionspotentialen antworteten, wurden bei beiden Zelltypen gefunden. Ebenso zeigten beide Zelltypen eine Hochpass-Filtercharakteristik. Unter 100 Hz Vibrationsfrequenz betrug der Auslenkungswinkel des Tarsus zum Erreichen des sensorischen Schwellenwerts zwischen 1° und 10°. Bei höheren Frequenzen sanken die Schwellenwerte bis zu den Minimalwerten von 0,05° entsprechend 4,5 nm tarsaler Auslenkung in den empfindlichsten Fällen.

Die unterschiedlichen Spalte des Organs und die Rezeptorzellen mit schneller oder langsamer Adaptation wiesen in diesem Hinblick keine Unterschiede auf. Auch bei der Reizung mit männlichen Balzvibrationen unterschieden sich die Anzahl der Aktionspotentiale, die Latenz, und die Synchronisationskoeffizient der beiden Rezeptorzelltypen nicht signifikant. Erstaunlicherweise schlugen sich die Unterschiede in der Kopplung der Dendriten an die Spalte nicht im physiologischen Antwortverhalten der beiden Zelltypen nieder.

Acknowledgements / Danksagungen

Ich danke meinem Dissertations-Betreuer Friedrich G. Barth für seine fachkompetente Beratung, die Unterstützung der Auslandsaufenthalte, die Anstellung im Projekt BioSenSE und seinen unermüdlichen Einsatz beim Verbessern der Publikationen.

Großer Dank gilt meinen Eltern Peter Schaber und Renate Schaber für die großzügige Unterstützung auf allen Ebenen. Danke! Danke an meine Großeltern Maria Schaber und Christian Schaber†. Danke an die vielen lieben Verwandten, die mich immer unterstützt und motiviert haben. Ganz herzlichen Dank an meine Schwester Judith Schaber.

Für Auflockerungen und Diskussionen außerhalb der universitären Mauern danke ich herzlich Martina Schorkopf, Philipp Haydn-Oguz, Didem Haydn-Oguz, Verena Leitner, René Illetschek, Kristian Juric, Pablo Einar Eslava Duch, Hadrien Bosetti, Hossein Rezai, Antonella Brizioli, Hannes Enthofer und Florina Apostoiu. Ein Dankeschön an Aril Yahyabeik, dem ich von Herzen das Allerbeste in seiner neuen Umgebung wünsche.

Der schwierigste Teil der Danksagungen betrifft nun die Kollegen und Ex-Kollegen, die Mitarbeiter des Departments und der Universität, wo innerhalb der „wissenschaftlichen Familie“ die Grenzen von dienstlich und privat oft aufgelöst scheinen. Ein Danke an Rainer Müllan und Christian Klopsch für die Zusammenarbeit im „Always 200% - Projekt“. Herzlichen Dank an Jorge Alberto Molina Escobar, unter anderem für Kollegialität ohne Grenzen. Danke Dir. Dirk Louis P. Schorkopf gebührt außerordentlicher Dank für die außerordentliche Kollegialität und die erfrischenden Stunden unterwegs. Danke. Danke an Michael Hrcir, Veronika Schmidt, Lisa Fenk, Janine Johara Jaegers und Stefan Jarau. Danke an Bernhard Höbl. Danke an Elisabeth Vogel. Ein herzliches Dankeschön an Maria Wieser. Danke Miroslav Dragasev, gäbe es diese Dissertation ohne Dich und die Spinnen? Danke an Elisabeth Fritz, Margit Kainerstorfer, Walter Witek und Thomas Hoinkes. Vielen Dank an Axel Schmid und Harald Tichy. Es hat Spaß gemacht. Lieben Dank an Maria Burgstaller und Lydia Zopf. Danke Andreas Szpetkowski und Ewald Gingl. Und ein liebes Dankeschön an Melanie Pilat, Simon Tragust und Tamara Theil.

Vielen Dank an alle, die ich während meiner wissenschaftlichen Reisen kennenlernen durfte. Aus der guten Zeit in Stuttgart sind hier besonders zu erwähnen Stanislav N. Gorb, Elena V. Gorb, Dagmar Voigt, Gerrit Huber, Eduard Arzt, Pablo J. Perez Goodwyn†, Jan M. Schuppert, Naoe Hosoda, Patric A. Gruber, Emerson J. de Souza,

Susanne Enders, Ralph Spolenak, Ulrike G. K. Wegst, Gerhard Dehm, Holger Pfaff, Andrei Peressadko, Adam P. Summers, W. Jon P. Barnes, Victoria Kastner, Cornelia Miksch und Jutta Hess. For the good times in Ames, IA, my thanks go to Vladimir V. Tsukruk, Michael D. Julian, Michael E. McConney, Maryna Ornatska and Sergiy Peleshanko. Vielen Dank für die Betreuung während meiner Zeit in Konstanz an C. Giovanni Galizia, Ana Silbering, Anneke Meyer und Paul Szyszka.

Special thanks to Joseph A. C. Humphrey† for the many hours of fruitful discussions, the insights into fluid dynamics, mathematical modeling, and the excellent collaboration, which resulted in a really astonishing publication.

The guest colleagues Fernando Antonio Soley Guardia, Tetsutaro Hiraguchi, W. Craig Eberhardt, Yoshihiro Toh, Anne Wignall and Taina Conrad brought new facets into university life and diverting hours outside the university walls. Thank you so much.

Ein Danke auch an alle Studentinnen und Studenten der Spezial- und Projektpraktika Neurobiologie und der Tierphysiologischen Übungen für den Spaß, den mir das Unterrichten bereitet hat.

Bei allen, die ich jetzt in der „Hitze des Fertigschreibens“ vergessen habe, möchte ich mich vielmals entschuldigen. Das bedeutet sicher nicht, dass ich nie an Euch denke.

Schaber et al. (in preparation for publication in: Journal of the Royal Society Interface)

Force transformation in spider strain sensors: white light interferometry

Clemens F. Schaber^{1,*}, Stanislav N. Gorb², Friedrich G. Barth¹

¹ Department of Neurobiology, Center for Organismal Systems Biology (COSB), Faculty of Life Sciences, University of Vienna, Althanstraße 14, 1090 Wien, Austria

² Zoologisches Institut der Christian-Albrechts-Universität zu Kiel, Am Botanischen Garten 1-9, 24118 Kiel, Germany

* Author for correspondence (clemens.schaber@univie.ac.at)

Author contributions

CFS, SNG and FGB designed the experiments, CFS performed the measurements, analyzed the data, wrote the paper in its present form, and FGB improved the paper by critical comments on earlier versions of the manuscript.

The following pages contain the manuscript in preparation for publication in the state as of January 8th, 2011.

Citation:

(in preparation for publication in: Journal of the Royal Society Interface)

SUMMARY

Scanning white light interferometry and micro-force measurements were applied on biological strain sensor structures to explain the mechanical stimulus transformation in the exoskeleton of the spider *Cupiennius salei* on the way to the sensory cells of two different compound slit sense organs (lyriform organs). The transformation of the stimulus force leads to strains in the cuticle and, as a result of that, to the compression of the individual slits of the lyriform organs, which are located at articulations of the legs of the spider. The compression of the slits to reach the sensory threshold is not more than 30 nm. The two lyriform organs examined are the highly sensitive vibration receptor HS-10 and the proprioceptive organ HS-8. For the proprioceptor the loading curve is linear, which is very reasonable for the sensor's biological range of

operation in resolving the lateral angular deflection of the metatarsus relative to the tibia. In HS-8 the mechanical sensitivity of the individual slits gradually decreases with decreasing slit length and compression values from 106 nm/mN down to 13 nm/mN. The force to compress the slits of the vibration receptor HS-10 rises highly exponentially making this exteroceptive organ well suited to detect a wide range of stimulus amplitudes. In HS-10 the two slits examined differ roughly 3-fold in the mechanical differential sensitivity with compression values of 522 nm/mN and 195 nm/mN in the biologically most relevant range. Therefore, the gradual stimulus amplitude detection by the individual slits of the organ HS-10 as well is very likely.

Keywords: spiders, slit sensilla, white light interferometry, stimulus transformation, mechanoreception

1. INTRODUCTION

Among the arthropods spiders have the most elaborate system of strain detectors embedded in their exoskeleton. Their lyriform organs form arrays of up to 30 fine slits in the cuticle closely arranged in parallel in widely differing patterns and locations (Barth & Libera 1970). The majority of the lyriform organs of the spider *Cupiennius salei* is located in the vicinity of the leg joints. Here they sense deflections of adjacent leg limbs responding to movement-related forces in the cuticle. The stimulus transmitting and transforming structures of the individual slits of an organ are (i) the slit in the cuticle, approximately 2 μm wide and up to 200 μm long, (ii) the cuticular membrane covering the slit, and (iii) the so-called coupling cylinder of the covering membrane where a dendrite ends (Barth 1971, 1972). Compression of the individual slits perpendicular to their long axis is the adequate and most effective stimulus (Barth 1972).

According to recent finite element analyses (Höbl *et al.* 2007, 2009) even minor variations of the geometry, number, and arrangement of the slits substantially affect their deformation and thus stimulation. These simulations are thought to be used as models for synthetic strain sensors for technical applications. In the present study we use white light interferometry and micro force measurements to quantitatively characterize the relation between stimulus load and slit compression with high resolution.

To compare different natural stimulation modes generating adequate cuticular strains two lyriform organs were selected (figure 1), which had been studied before for other purposes. Lyriform organ HS-8 distally on the tibia is a proprioceptor effectively stimulated by posteriad deflections of the metatarsus and the subsequent

deformation of the cross-section of the tibia. This organ is involved in kinaesthetic orientation and elicits muscle reflexes when stimulated (Barth & Seyfarth 1971; Seyfarth & Barth 1972; Seyfarth 1978; Seyfarth & Pflüger 1984). Direct measurements of strains in the cuticle of freely moving spiders using miniaturized technical strain gauges showed that the organ is compressed and stimulated during the stance phase of a step and hence acts as a cuticular load sensor (Blickhan & Barth 1985; Barth 2002). By contrast, the exteroceptive lyriform metatarsal organ HS-10 is effectively stimulated when the tarsus moves upwards and presses against the metatarsus where the organ is located. Organ HS-10 is a highly sensitive vibration sensor which the spider uses to detect vibrations generated by prey, mates, or predators (Barth & Geethabali 1982; Hergenröder & Barth 1983; Gingl *et al.* 2006; Molina *et al.* 2009). As recently shown by atomic force microscopy and surface force spectroscopy the viscoelastic properties of a cuticular pad in front of the organ largely explain its physiological high pass properties (McConney *et al.* 2007).

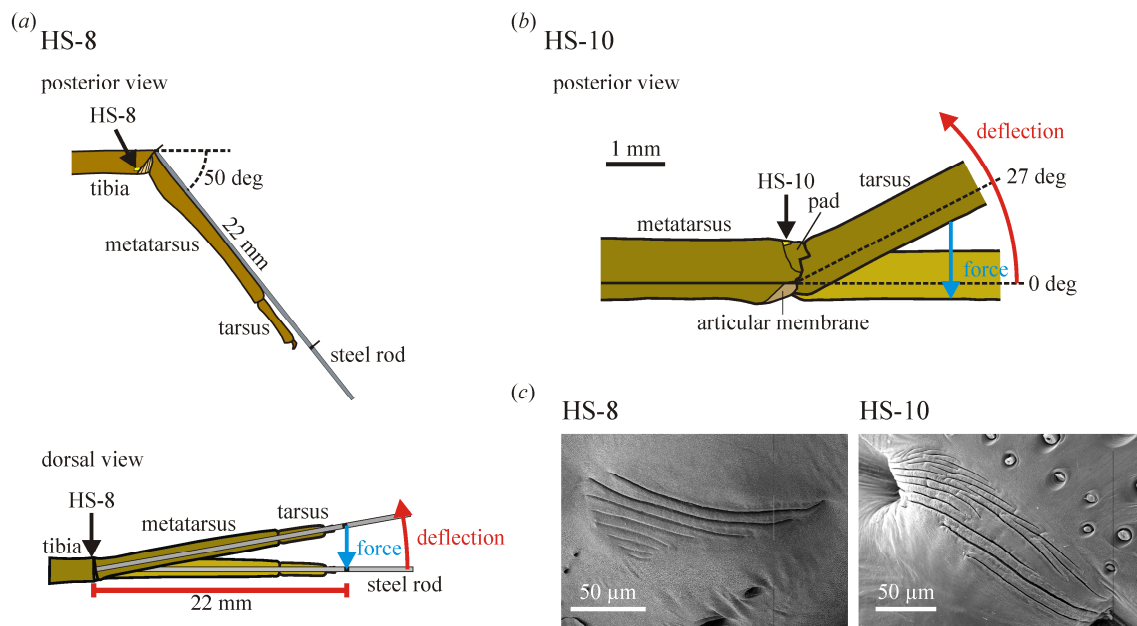


Figure 1. (a) Arrangement of the tibia metatarsus joint for the adequate stimulation of the lyriform organ HS-8. Top: The metatarsus was kept at an angle of 50 deg to the fixed tibia. Below: For stimulation under the white light interferometer the metatarsus was deflected backward (red arrow) and the forces resisting this deflection (blue arrow) measured at a distance of 22 mm from the pivot point. (b) Arrangement of the metatarsus tarsus joint for adequate stimulation of the lyriform organ HS-10. The tarsus was deflected upward (red arrow) and contacted the metatarsal pad at the mechanical threshold angle of 27 deg. At larger angles the slits of organ HS-10 were compressed. The force resisting this deflection (blue arrow) was measured directly at the tarsus with the strap of the force transducer. (c) left: SEM micrograph of the lyriform organ HS-8; right: SEM micrograph (by courtesy of R. Müllan) of the metatarsal lyriform organ HS-10.

2. MATERIALS AND METHODS

2.1. *Animals*

Adult females of the large Central American wandering spider *Cupiennius salei* Keyserling (Ctenidae) taken from our breeding stock in Vienna were used for all the experiments. This spider has already served for many studies in arthropod mechanoreception (Barth 2002; Fratzl & Barth 2009). For white light interferometry the hairs covering the lyriform organs were removed by gently wiping the surface with a small pad of cotton after brief anesthetization of the spider with CO₂ and immobilizing it by attaching it onto an aluminium plate with adhesive tape. Legs of the first or second leg pairs were used for all experiments.

2.2. *Force application*

The arrangement of the leg joints and their controlled movements used to measure the forces of adequate stimulation were similar to those used in previous electrophysiological studies of the same organs (Barth & Bohnenberger 1978; Bohnenberger 1981; Barth & Geethali 1982; figure 1).

2.2.1. *Lyriform organ HS-8*

For the study of the lyriform organ HS-8 the tibia was embedded in a mixture of beeswax and colophony except for its distal part starting 3 mm away from the joint with the metatarsus. Organ HS-8 was facing up and the spider could still actively move the joint. An insect pin waxed onto the metatarsus dorsally was coupled to a force transducer (FORT 10, World Precision Instruments) using a small wire loop. A distance of 22 mm from the dorsal edge of the tibia-metatarsus joint was marked on the pin as the point of initial force application (figure 1). The force transducer was mounted horizontally on a motorized micromanipulator and calibrated with pieces of tin-solder of known mass. The metatarsus was kept at an angle of 50 deg from the stretched position in the dorsoventral plane relative to the tibia in agreement with the previous electrophysiological studies of the organ (figure 1a; Barth & Bohnenberger 1978; Bohnenberger 1981). The forces were applied using the force transducer by controlled stepwise deflections of the metatarsus towards its posterior aspect and perpendicular to the insect pin. The forces resisting deflection were recorded continuously and stored on the hard disk of a computer with a sampling rate of 500 Hz (Biopac MP100 analogue/digital converter; UM 100A interface module; TCI 102 adapter; Software ACQ 3.7). The vertical deflection of the metatarsus from the initial position was read

from the scale of the micromanipulator and the corresponding angle calculated with the tangent function.

2.2.2. Metatarsal organ HS-10

In case of the metatarsal lyriform organ HS-10 the force was introduced by deflecting the tarsus upwards directly with the strap of the force transducer. Similar to organ HS-8 the metatarsus was embedded up to 3 mm away from HS-10 and the lyriform organ was pointing upwards (figure 1b).

At the start of a measurement series the tarsus was carefully aligned with the metatarsus and in parallel to the strap of the force transducer. The distance of the point of force application (outer edge of the force transducer) from the pivot point of the joint was measured using macro-photographs taken from the lateral side of the leg. Then the tarsus was deflected upwards in a stepwise manner. The vertical displacement of the tarsus was read from the scale of the micromanipulator and the angle of deflection calculated with the tangent function. The tarsus was found to make contact with the metatarsus at a dorsad deflection angle (relative to the horizontal plane) by 27 deg, which was defined as the mechanical threshold deflection angle (figure 1b) and is in good agreement with previous findings (Barth & Geethabali 1983; Molina *et al.* 2009).

2.3. White light interferometry

The cuticular surface of the organs and their immediate surroundings were scanned after each stepwise force increase using a scanning white light interferometer (zygo NewView 5010; software MetroPro 7.9.0). The entire setup was placed on a vibration isolation table (TMC micro g). The scans were started one minute after the deflection of the leg segments, when the interference fringes had stabilized and the measured forces had reached a nearly constant level (figure 2). The scans lasted from 10 seconds up to 6 minutes depending on the selected vertical scan height, which in turn depended on the selected optical magnification.

2.4. Data analysis

2.4.1. Force and deflection

The forces corresponding to the interferograms were measured at the start of the interference scans as the mean of the values recorded during the following 10 seconds (5000 points; standard deviation s.d. <1%; software ACQ) (figure 2). The values of

vertical deflection read from the micromanipulator were corrected taking the displacement of the force transducer ($2.4 \mu\text{m}/\text{mN}$) into account.

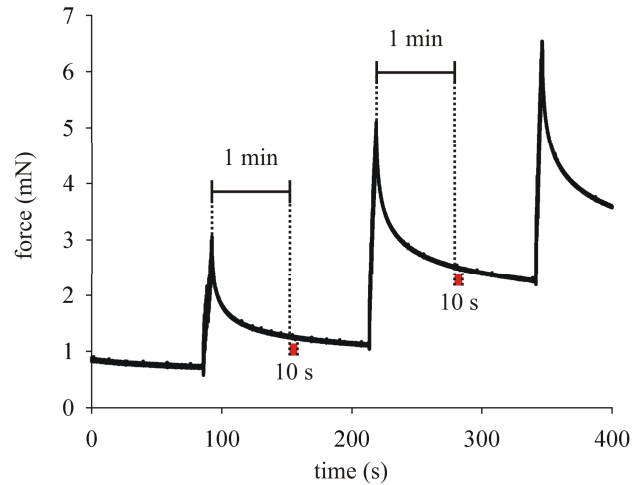


Figure 2. Measurement of the forces applied to the metatarsus stimulating the tibial lyriform organ HS-8. The white light interference scans were taken one minute after the loading and the corresponding force values read out at the times marked by red squares. The three deflection steps shown here deflected the metatarsus by $300 \mu\text{m}$ (0.78 deg), $600 \mu\text{m}$ (1.56 deg), and $900 \mu\text{m}$ (2.34 deg) from the zero position.

2.4.2. Three-dimensional interferometry maps

The three-dimensional deformation of the cuticle was measured using image metrology software (SPIP 4.1.1). Two-dimensional profiles of the cuticle surface were extracted manually using the same landmarks consistently.

2.5. Limitations of the technique

Due to the time needed for the interference scans it was not possible to visualize changes in the exoskeleton close to the initial force peak following a loading step. Therefore the results of this study deal with the forces and cuticular deformations at quasistatic loading conditions. Because all measurements were performed on live animals small-scale deformation of the cuticle due to hemolymph pressure and muscle activity could not be excluded. However, only data from experiments with no such interferences and no visible signs of movements were analysed.

For the delicate measurements of the width and depth of the individual slits of the lyriform organs the following sources of measurement errors exist. At the maximum optical magnification (100×) of the white light interferometer used in these measurements light reflected from the specimen's surface exceeding an angle of 35 degree to the horizontal plane is not sent back into the objective lens, and is therefore not available for the sensor of the instrument. Such data points occurred especially at the rounded edges of the slits, were automatically set to invalid by the software of the interferometer, and marked as black dots in the interferogram. To reach maximum accuracy the valid data points closest to the slit edges were used to measure the slit width. An additional factor of uncertainty is the manual superposition of the corresponding lines of the two-dimensional profiles. The manual placement was necessary due to the horizontal and angular shifts of the slits when the organs were loaded and done with greatest possible care. Errors up to roughly 4 pixels (0.4 μm) in the horizontal plane in a single measurement cannot be excluded and only measurement series exhibiting a significant trend were further analysed.

3. RESULTS

3.1. Forces

3.1.1. Lyriform organ HS-8

The forces resisting lateral deflections of the metatarsus and stimulating the lyriform organ HS-8 on the tibia increase linearly with displacement of the metatarsus towards its posterior aspect (figure 3a). The forces rise steadily from zero degree when the joint socket of the metatarsus just contacts the posterior joint ball at the dorsal aspect of the tibia. The forces follow those of the deflections in a highly linear way with values from 0.93–1.90 mN/deg and the mean for six individual preparations of 1.35 ± 0.36 mN/deg (mean \pm s.d., N=6, n=18). The corresponding correlation coefficients R^2 of the linear regression line vary between 0.986 and 0.999 (0.994 ± 0.005 , mean \pm s.d., N=6, n=18). The dependence of the metatarsal deflection angle from the force resisting deflection amounts to 0.77 ± 0.19 deg/mN (N=6, n=18), taken from linear regression lines ($R^2 = 0.995 \pm 0.003$; N=6) derived from the mean values shown in figure 3a.

3.1.2. Lyriform organ HS-10

In contrast to the linearity found for organ HS-8 the forces needed for dorsad deflections of the tarsus leading to the compression and stimulation of the slits of the vibration

sensitive lyriform organ HS-10 rise exponentially (figure 3b). They increase slowly with increasing angles below 27 deg and quickly beyond that value, which marks the contact between the proximal dorsal rim of the tarsus and the joint pad located in front of the organ (figure 1b). The force-deflection data can be well described using the function $y = y_0 e^{rx}$. The corresponding correlation coefficients R^2 are between 0.990 and 0.999 (0.995 ± 0.004 , mean \pm s.d., $N=6$). The values of the constant growth factor r determined from these fittings vary between 0.142 and 0.187. Therefore the relative increase rates of the force are 14.2 – 18.7 %/deg (16.2 ± 1.9 %/deg, mean \pm s.d., $N=6$). y_0 indicates the force holding the metatarsus horizontally (0 deg). It varies only slightly (0.003–0.021 mN; 0.014 ± 0.011 mN, mean \pm s.d., $N=6$) again indicating the precision of the fitting analysis.

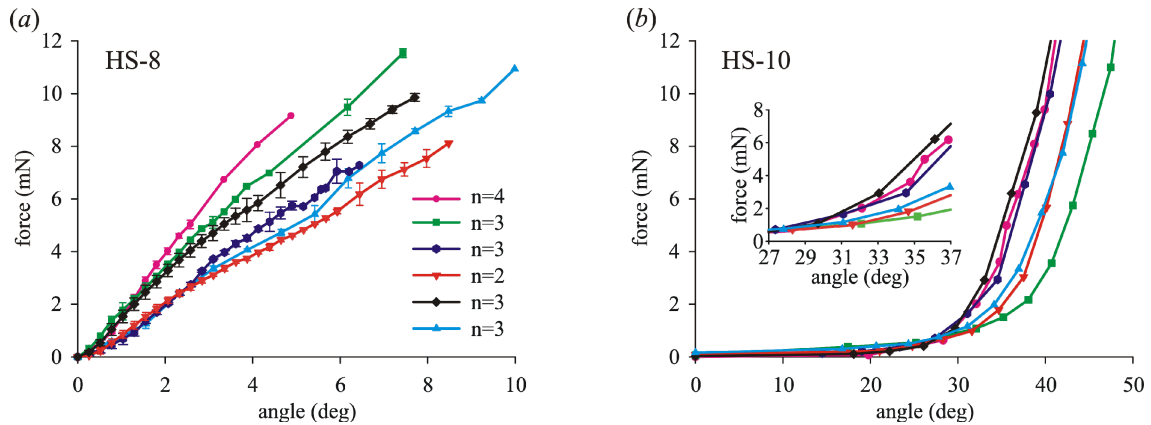


Figure 3. Loading of the exoskeleton of *Cupiennius salei* to stimulate two different lyriform organs, HS-8 on the tibia and HS-10 on the metatarsus. (a) For the proprioceptive stimulation of organ HS-8 by backward deflection of the metatarsus the forces increase highly linearly ($N=6$; $n=18$). (b) When stimulating the vibration sensitive metatarsal organ HS-10 by the upward deflection of the tarsus the forces increase exponentially. Inset: x-axis scaled as in (a); note the exponential increase of force from the tarsal deflection angle of 27 deg (mechanical threshold) onward ($N=6$; $n=6$).

3.2. Arrangement and deformation of lyriform organ HS-8

As seen in the surface profile perpendicular to the long axis of the tibia and roughly to the slits of lyriform organ HS-8, the organ is surrounded by relatively flat cuticle dorsally and curved cuticle ventrally (figure 4a,b). Close to the middle of the posterior tibia surface there is a point, where no deformation of the cuticle was found. Organ HS-8 is located ventrally of it. This particular location at the transition between flat and curved cuticle indicates a mechanically sensitive region of the profile, where

deformations of the cuticle under load are large and pressure stresses in the cuticle run roughly perpendicular to the long axis of the slits of organ HS-8 (Barth & Pickelmann 1975).

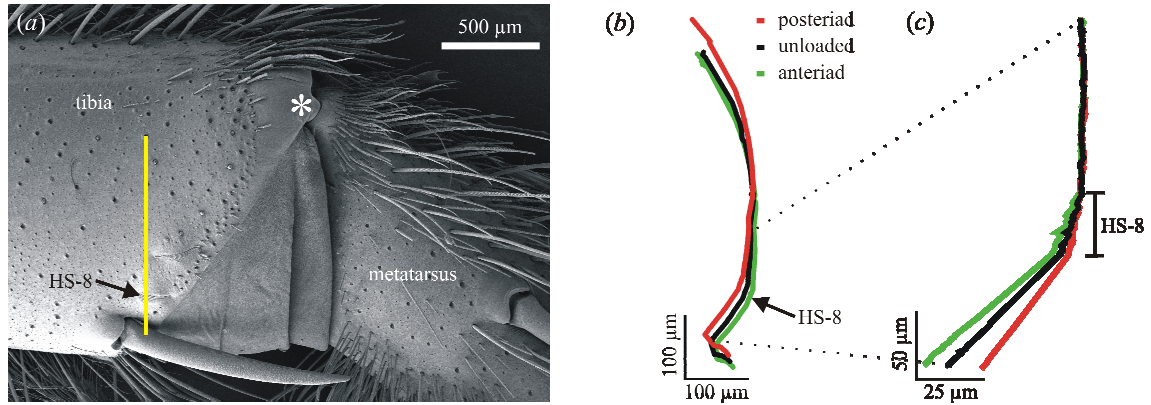


Figure 4. (a) SEM micrograph of the posterior aspect of the tibia-metatarsus joint. The yellow line marks the line of the surface profiles shown in (b) and (c). The asterisk indicates the pivot point of the joint where the joint ball of the tibia contacts the joint pan on the metatarsus. (b) Profiles of the tibia surface in the resting position (black), and at antieriad (green) and posteriad (red) deflections of the metatarsus by 10.2 deg. (c) Flattening and bulging of the cuticle at the lyriform organ HS-8 perpendicular to the long axes of the slits. The profiles are superimposed and aligned at the upper right (posterior aspect of the tibia dorsally of the organ).

When the metatarsus is deflected towards its posterior aspect during stimulation the curvature of the cuticle around organ HS-8 flattens and as a consequence the slits are compressed. In contrast the slits of organ HS-8 are dilated when the metatarsus is deflected towards its anterior side and the curvature is enhanced. Figure 4c illustrates the interferometrically determined profile of the tibial cuticular cylinder in the resting position, and following backward and forward deflections of the metatarsus.

In the white light interferograms, the inward movement (towards the centre of the tibia) of the whole organ as a consequence of the deformation of the tibia's cross-section due to loading of the metatarsus is obvious (figures 4b and 5a,b; ESM figure 1 (at the end of this manuscript)). This vertical displacement follows the applied force and the displacement of the metatarsus linearly with $1.72 \pm 0.55 \mu\text{m}/\text{deg}$ ($R^2 = 0.995 \pm 0.003$; $N=6$), and $1.26 \pm 0.54 \mu\text{m}/\text{mN}$ ($R^2 = 0.996 \pm 0.003$; $N=6$), respectively. The vertical displacement of $2.40 \mu\text{m}/\text{deg}$ ($N=1$) of the anterior aspect of the tibia, where the lyriform organ VS-4 is located, is only slightly larger (ESM figure 1 (at the end of this manuscript)).

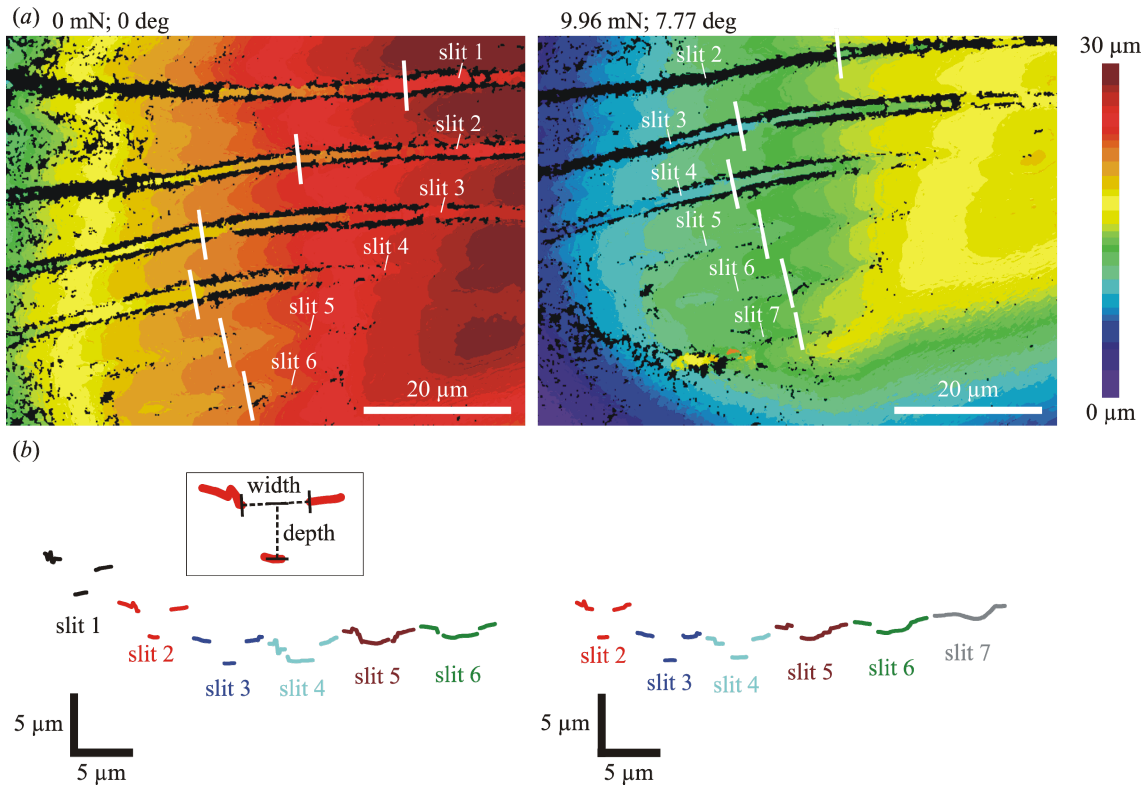


Figure 5. White light interferograms and profiles of the slits of the lyriform organ HS-8. (a) Left: six slits of the unloaded organ. The white lines are drawn at a right angle to the long axes of the slits and next to the coupling cylinder with the dendrite tip. They mark the positions of the profiles shown in (b). Right: downward shifted flattened cuticle surface and compressed slits when loading the metatarsus by 9.96 mN (deflection angle 7.77 deg). The z-axis is represented by the colour coding. (b) Surface profiles of the slits used for the measurements of slit width and depth corresponding to the interferograms in (a). The inset shows an example (slit 2) of the data points used for the measurement of slit width and depth.

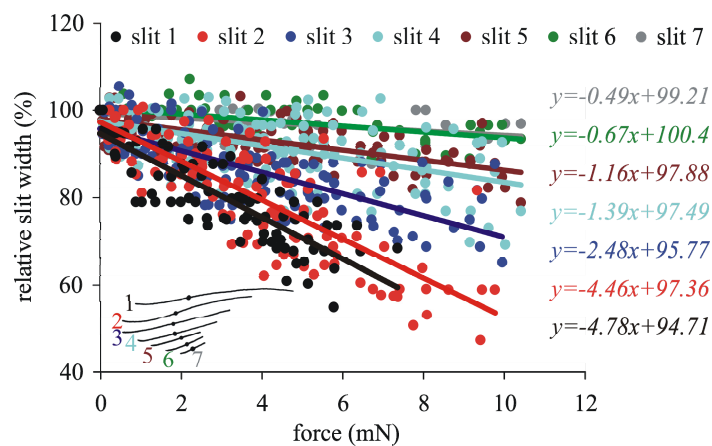


Figure 6. Slit widths determined interferometrically in the lyriform organ HS-8 at the position indicated in the inset (dendrite coupling cylinder) relative to the unloaded state (N=6, n=6). The mechanical sensitivity goes down sequentially from 4.78 %/mN in slit 1 to 0.49 %/mN in slit 7 as indicated by the linear regressions.

3.3. Change of slit width and depth in lyriform organ HS-8

In the absence of a stimulus the slit widths measured as indicated in figure 5 amount to $2.23 \pm 0.32 \mu\text{m}$ for slit 1, $2.29 \pm 0.32 \mu\text{m}$ for slit 2, $2.66 \pm 0.38 \mu\text{m}$ for slit 3, $3.08 \pm 0.30 \mu\text{m}$ for slit 4, $3.27 \pm 0.33 \mu\text{m}$ for slit 5, $3.17 \pm 0.26 \mu\text{m}$ for slit 6, and $2.74 \pm 0.59 \mu\text{m}$ for slit 7 (N=5). When loading the tibia by the backward deflection of the metatarsus the compression of the slits of organ HS-8 follows force linearly and the mechanical sensitivity decreases gradually from the longest slit 1 to the shortest slit 7. Close to the dendrite coupling cylinder slit 1 is compressed by 4.78 %/mN, slit 2 by 4.46 %/mN, slit 3 by 2.48 %/mN, slit 4 by 1.39 %/mN, slit 5 by 1.16 %/mN, slit 6 by 0.67 %/mN, and slit 7 by 0.49 %/mN (figure 6).

With increased compression the depth of the trough-shaped outer covering membrane of the selected slits 2, 3 and 4 of the lyriform organ HS-8 increases as well. When loading the organ the deepest point of the covering membrane of slit 2 (initial depth $2.42 \pm 0.06 \mu\text{m}$; N=4) moved downward by 24 nm/mN relative to the slit edges at the dendrite attachment point, followed by slit 3 (initial depth $1.85 \pm 0.04 \mu\text{m}$; N=4) with 12 nm/mN, and slit 4 (initial depth $1.42 \pm 0.26 \mu\text{m}$; N=4) with 7 nm/mN (figure 7a).

A correlation of slit compression and slit depth increase during stimulation is suggested by the similarity of the ratios between the individual slits of both parameters, when the steepness of the regression lines is compared. The compression of slit 3 and the depth increase of its covering membrane compared to that of slit 2 yields ratios of 0.56, and 0.50, respectively. Therefore, the mechanical deformability of slit 3 in both parameters is only about half of that of slit 2. The ratios of slit compression and depth increase of the covering membrane of slit 4 versus slit 3 is in the same range with 0.56, and 0.57, respectively. When both parameters are compared in slit 4 versus slit 2 the ratios are lower, with 0.31 in slit compression, and 0.28 in depth increase. Likely the physiological sensitivity differences described earlier (Barth & Bohnenberger 1978; Bohnenberger 1981) result from these deformation differences, which explains itself when considering the geometry of the slit's covering membrane (Barth 1972; see also Discussion).

For simple geometrical reasons Barth (1972) predicted that the bending of the covering membrane of the unloaded slits correlates with the membrane's deformability at slit compression. The more the slit membrane is bent inwards in the initial unloaded state, the more the membrane is further bent downwards during compression of the slit. If it is assumed that in slits with a deeper covering membrane the slit membrane is more bent initially, the data of the white light interferometric measurements well confirm this prediction, although the value of the increased deformability is as small as 12.5 pm/mN per nm initial depth (figure 7b).

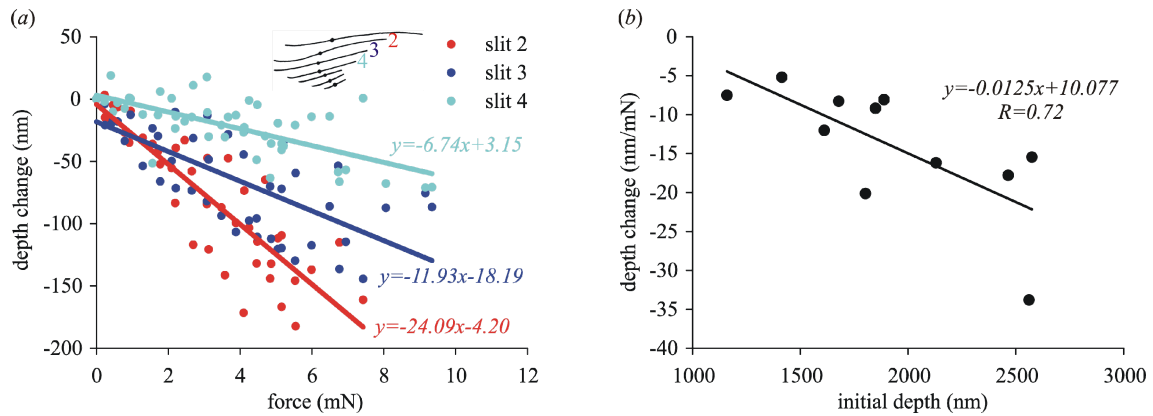


Figure 7. (a) Gradual increase of the depth of three selected slits of the lyriform organ HS-8 (N=4, n=4). Negative values represent an increase of slit depth. (b) Correlation between depth change following stimulation and initial depth of 11 slits (N=4).

3.4. Arrangement and deformation of lyriform organ HS-10

The slits of the metatarsal lyriform organ HS-10 bridge a pronounced furrow separating the soft cuticular pad (McConney *et al.* 2007) from the well sclerotised cuticle at the distal end of the metatarsus (figure 8a). When the tarsus is loaded and deflected upward it pushes against the cuticular pad, which transmits the forces to the slits of the lyriform organ and compresses them perpendicular to their long axis.

In profiles of the cuticular surface it can well be seen that the furrow in the metatarsal cuticle is roughly 100 μm deep, whereas the cuticular bridge formed by lyriform organ HS-10 continues seamlessly from the “normal” metatarsal cuticle to the cuticular pad (figure 8b).

The width of the entire organ HS-10 perpendicular to the long axes of the slits changes linearly with tarsal deflection angle (figure 8c). In the range from 27 deg (mechanical threshold) to approximately 35 deg tarsal upward deflection no significant compression of the pad can be measured under quasistatic loading conditions (figure 8c).

3.5. Change of slit width in organ HS-10

The 21 slits of the metatarsal organ HS-10 differ in length and are organized in characteristic groups as described earlier (figure 1c; Barth 2002; Molina *et al.* 2009). The width of the slits in the unloaded organ varies from approximately 2 to 4 μm when measured as indicated for organ HS-8 in figure 5b.

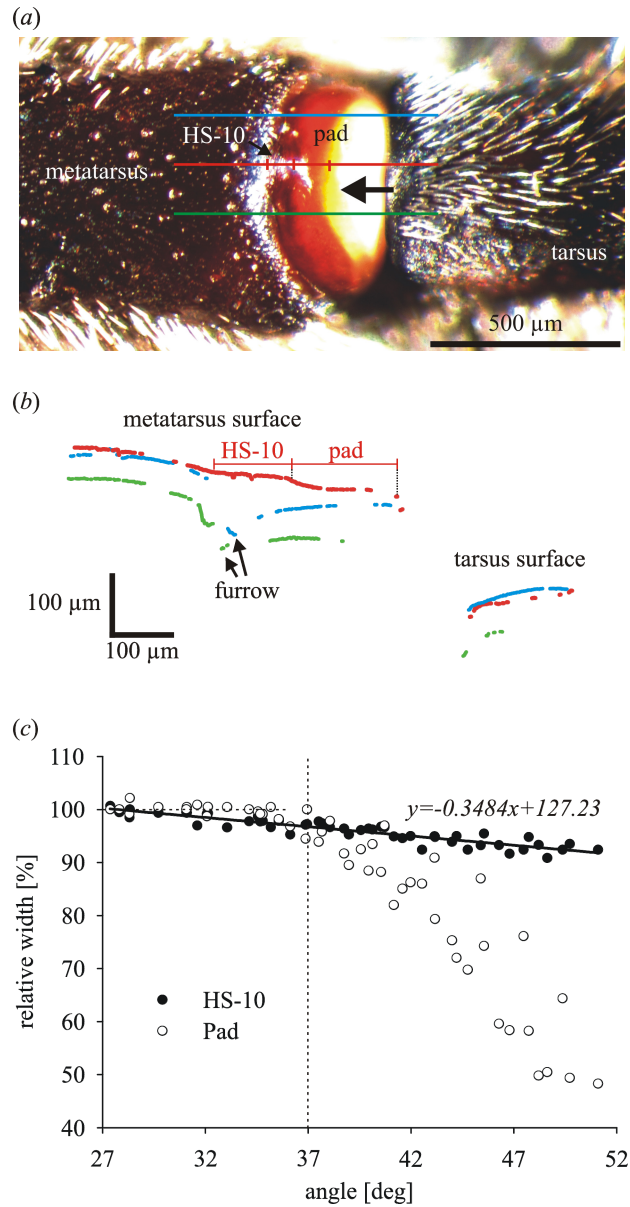


Figure 8. (a) Dorsal view of the metatarsus-tarsus leg joint including the metatarsal lyriform organ HS-10. At stimulation the tarsus pushes against the pad on the metatarsus (black arrow) compressing the slits of organ HS-10 perpendicular to their long axis. The colour lines indicate the surface profiles shown in (b). (b) White light interferometric surface profiles along the leg's long axis as indicated in (a). The lines of the profiles are broken because of many invalid data points at low magnification. The red profile is taken at an angle of 90 deg to the slits of the metatarsal lyriform organ HS-10. The thin straight red line indicates the length of organ HS-10 and of the cuticular pad in the profiles used for the measurements in (c). The blue and green line show the surface profiles anteriorly and posteriorly of the lyriform organ clearly representing the furrow between the soft pad and the well sclerotised cuticle of the metatarsus. (c) Relative width of organ HS-10 and the pad under loading compared to the mechanical threshold at contact of the metatarsus at 27 deg dorsad deflection. The lyriform organ is compressed linearly as indicated by the regression line and more than the pad up to an angle of approximately 37 deg (vertical dotted line).

The slits of organ HS-10 are compressed when the tarsus is deflected dorsally by more than approximately 27 degrees. The initially widest and longest slits are compressed first, whereas the smaller slits follow successively (figure 9). For the measurement of slit width at the site of the dendrite coupling to the covering membrane the long and prominent slits 2 and 6 were selected. They were most easily accessible and the dendrite attachment site could be identified in interferograms taken from the dorsal aspect.

Slit 2 spans over the entire curvature of the cuticular bridge structure and its dendrite attachment site is located towards the anterior aspect of the leg. Its initial width measured $3.46 \pm 0.55 \mu\text{m}$ (N=5) and the length measured on SEM images in a plane was $152 \mu\text{m}$ (figures 1c and 9). Slit 6 is located more proximally within the organ and its dendrite attachment site found close to the middle of the cuticular bridge. The unloaded width amounted to $3.68 \pm 0.91 \mu\text{m}$ (N=5) and slit length was approximately $116 \mu\text{m}$ (figures 1c and 9).

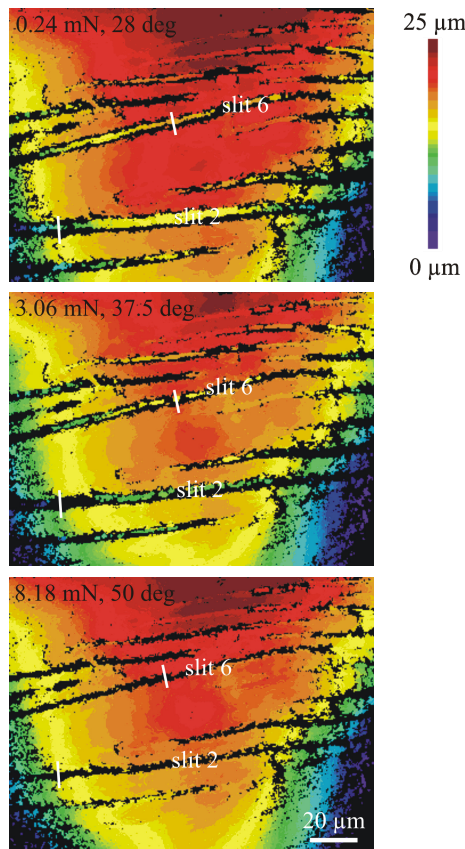


Figure 9. From top to bottom: White light interferograms of the central region of the metatarsal vibration receptor HS-10 of a first left leg under increasing load. The uppermost interferogram was taken close to the mechanical threshold deflection of the tarsus (27 deg). Note the increasing compression of the slits. The z-axis is represented by the colour code. The white lines are drawn next to the dendrite attachment site and indicate the positions for the measurement of the widths of slit 2 and slit 6.

The biologically most relevant sensitivity range of organ HS-10 is between the threshold at a tarsal-metatarsal angle (approximately 27 deg) and 10 degrees beyond (approximately 37 deg) (Molina *et al.* 2009). It corresponds to forces pushing the tarsus upward between 0.5 and 3 mN. Within this range a differential sensitivity difference of slit 2 and slit 6 can be read from the the slopes of the curves shown in figure 10. The compression of slit 2 relative to the resting position follows the stimulus linearly and amounts to 15.1 %/mN. In the same range the compression of slit 6 shows a linear behaviour as well and measures 5.3 %/mN. Consequently, slit 2 is threefold mechanically more sensitive than slit 6.

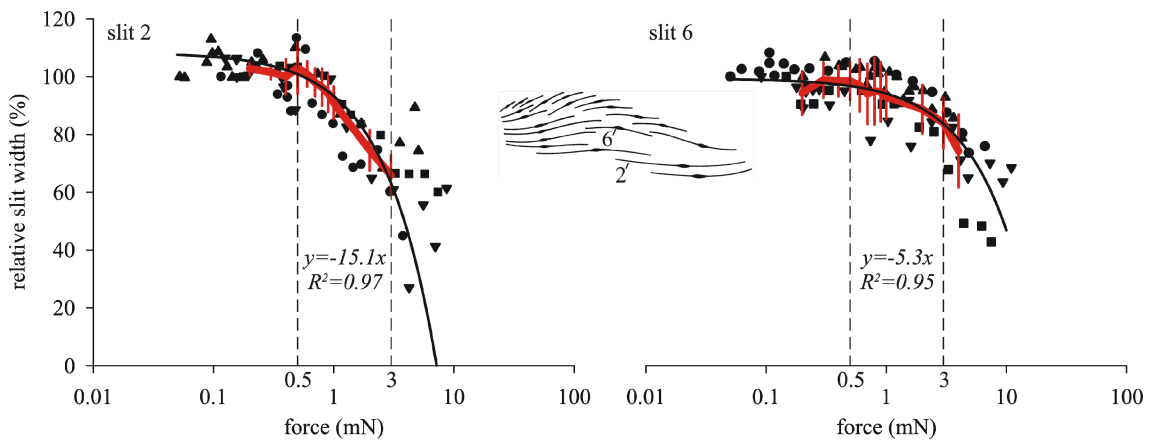


Figure 10. Width of slit 2 (left) and slit 6 (right) of the metatarsal organ (see inset) under loading relative to the resting position. The red lines connect the mean values (\pm s.d.) of five measurements in five preparations each. The solid black lines indicate linear regression lines calculated from the values within the biologically most important range between the dashed vertical lines. The steepness of the lines (i.e. relative slit compression per mN) and the regression coefficients R^2 are given between the dashed lines.

4. DISCUSSION

4.1. White light interferometry applied to functional morphology

As mentioned in § 2.5 there are several sources for possible errors in measurements with sub-micrometre precision on life animals. However, the measurements were done with greatest care and only data showing a trend clearly were further evaluated. The sources of the relatively large spreading of the data in figures 6, 7, and 10 are the curvature of the slit edges, which leads to interferences not detectable by the white light interferometer and the optical resolution of the instrument (0.11 μm).

When the widths of the slits in the lyriform organs HS-8 and HS-10 measured with the white light interferometer according to the method described in § 2.5 and figure 5b are compared with scanning electron micrographs (SEM; figure 1c) and transmission electron microscopic (TEM) images (Müllan 2005) they are in the same range, if the curvature of the slit edges beyond 35 deg to the surface (not detectable by the white light interferometer) is taken into account.

4.2. Viscoelasticity of the leg joints

4.2.1. Tibia-metatarsus joint (organ HS-8)

The shape of the loading curves in figure 2 showing the quick relaxation of the material after the initial loading step indicates that the tibia metatarsus joint of *Cupiennius* is a highly viscoelastic system. This was already shown by Blickhan (1986), who measured hysteresis loops typical of viscoelastic materials at constant deflection and restoring rates of the metatarsus.

In our experiments the loading of the exoskeleton was quasistatic with the metatarsus kept in a certain deflected position for the long time necessary for the white light interference scans. The shape of the force curve with the large initial peak indicates that the elastic restoring force of the joint is dominant at and shortly after the loading step (peaks of the curve) while the viscosity increases with the duration of the static deflection of the metatarsus. In case of the example shown in figure 2 the half-value-period from the initial peak is 30 and 60 seconds, dependent on the deflection angle.

The main source of the joint's viscoelasticity is the joint pan of the tibia that consists of a clearly softer material than the sclerotised exocuticle (own observations). When loading, the joint head of the metatarsus, made of hard sclerotized cuticle, pushes into the soft joint pan material of the tibia. Very likely the joint pan material resists to the deflection of the metatarsus much more at the loading step and subsequently absorbs the force exerted on it by the metatarsal joint head, similar to the joint pad at the distal end of the metatarsus, which was shown to be highly viscoelastic (McConney *et al.* 2007). The force curves recorded when stimulating organ HS-10 by pushing the tarsus dorsally against the joint pad of the metatarsus are very similar to those deflecting the metatarsus stimulating organ HS-8 (figure 2).

The joint pad located at the distal end of the metatarsus serves as a mechanical high-pass filter for vibration stimuli on the way to the lyriform organ HS-10. The elasticity and the Young's modulus of the joint pad material increase with increasing frequency and velocity of dynamic stimuli (McConney *et al.* 2007). We suggest a similar function of the joint pan material of the tibia, thereby having an influence on the

strains in the cuticle stimulating organ HS-8. As well the soft joint pan material leads to the proper coupling between the metatarsus and the tibia and makes organ HS-8 most sensitive to changes of the metatarsal deflection angle.

The force decrease after a stepwise loading of the metatarsus is similar to the decrease of the rate of action potentials recorded from single slits of organ HS-8 following a power law function after a step deflection of the metatarsus (Barth & Bohnenberger 1978; Bohnenberger 1978; Bohnenberger 1981), which at least to a large extent now explains itself as a consequence of the material properties of the tibia-metatarsus joint.

The linear course of the force increase at increasing deflection angles of the metatarsus (figure 3a) is very reasonable for the function of a proprioceptor like organ HS-8, where the limits of the operating conditions are known and given by the biomechanics of the joint. Thereby the single slits of the lyriform organ gradually detect the deflection angle of the metatarsus with their different mechanical and physiological sensitivities. The proper coupling between the tibia and the metatarsus is essential for a proprioceptive organ like HS-8.

4.2.2. *Metatarsus-tarsus joint (organ HS-10)*

The exponential force transformation for the stimulation of organ HS-10 (figure 3b) implies an adaptation to a wide range of stimulus amplitudes. This makes sense for exteroceptive vibration detectors like organ HS-10, where the amplitudes of the stimuli transmitted from the substrate to the sensor vary within large limits.

Interestingly in the biologically important range up to a tarsal deflection angle by roughly 37 deg (up to 10 deg above the threshold; Molina *et al.* 2009) the organ and its slits get more compressed than the joint pad located in front of it (figure 8c). At tarsal deflection angles exceeding 37 deg the pad absorbs most of the force acting on the metatarsus by being compressed by up to 50 % at angles larger than 47 deg (20 deg above threshold). Thus, in addition to being a high-pass filter, the joint pad protects the metatarsal organ from overloading and strains which might be harmful to the sensory structures.

At dynamic stimulation like the biologically most relevant small amplitude vibrations caused by prey and predators the viscoelastic behaviour of the pad plays an important role for signal filtering. Thereby the compression of the pad and the compression of the slits together are important for the stimulus transformation.

4.3. Comparison with electrophysiological data

4.3.1. Lyriform organ HS-8

4.3.1.1. Range fractionation

Previous electrophysiological studies of the lyriform organ HS-8 show that it is suited to measure the angle of metatarsal deflection and a range fractionation of stimulus amplitudes by the individual slits (Barth & Bohnenberger 1978; Bohnenberger 1978; Bohnenberger 1981). Barth & Bohnenberger (1978) give threshold values of metatarsal deflection needed to elicit two to three action potentials using ramp and hold stimuli. The longest slit 1 was shown to be the most sensitive responding to displacements of the metatarsus by less than 0.01 degree only. The physiological sensitivity of the slits within organ HS-8 decreases gradually with decreasing slit length.

If 1.35 mN/deg, the mean ratio of angle vs. force from all the six preparations of the present study (figure 3a), is used to calculate the force to reach the physiological threshold angles we get threshold forces for the individual slits of 0.01 mN for slit 2, 0.15 mN for slit 3, 0.57 mN for slit 4, 0.88 mN for slit 5, and 1.24 mN for slit 6. Threshold values for slit 1 and slit 7 are not included in Barth & Bohnenberger (1978) due to technical limitations.

The relative threshold compression of the slits inferred from the regression lines of the white light interferometric measurements (figure 6) is not more than roughly 1 % of the width of the unloaded slit with values of 0.06 % for slit 2, 0.37 % for slit 3, 0.79 % for slit 4, 1.02 % for slit 5, and 0.83 % for slit 6. Taking into account the mean absolute values of initial slit width, the threshold compression of the slits at the site of the coupling cylinder is not more than roughly 30 nm with values of 1.4 nm for slit 2, 9.8 nm for slit 3, 24.3 nm for slit 4, 33.3 nm for slit 5, and 26.4 nm at slit 6. The depth increase of the covering membrane at the physiological threshold amounts to 0.3 nm in slit 2, 1.8 nm in slit 3, and 3.8 nm in slit 4.

The difference in absolute threshold slit compression at the site of the dendrite attachment from slit 2 to 6 varies 24-fold compared to the 92-fold difference in the physiological threshold values given by Barth & Bohnenberger (1978). The shape of the loading curves in figure 2 strongly reminds of the sensory step response properties with high action potential frequencies immediately at and after the metatarsal deflection followed by an exponential decay (Bohnenberger 1978; Bohnenberger 1981). Although the stimulus transformation mechanisms directly at the dendrite coupling cylinder could not be analyzed using the current methodologies, the white light interferometric data imply that the source of the differing sensitivity cannot be found at the mechanical deformation of the slit only. A possible additional source may be differences of

dynamic viscoelastic stimulus transformation among the different slits, as Bohnenberger (1981) found at least a 10-fold physiological sensitivity increase of slit 4 in a frequency range of sinusoidal deflections of the metatarsus between 1 Hz and 100 Hz.

4.3.2. Lyriform organ HS-10

The placement of the metatarsal lyriform organ HS-10 on the mechanically weak bridge structure makes it additionally sensitive for vibrations of the substrate. The slits are not more than approximately 7 μm deep, much shallower than the 100 μm deep trench separating the sclerotised cuticular cylinder of the metatarsus from the soft joint pad structure, and therefore superficially embedded in the cuticle. This arrangement makes the site of organ HS-10 very sensitive for movements of the pad against the metatarsal leg cylinder, and the slits are located at the place where the strains in the cuticle are the largest. During quasistatistical loading of the lyriform organ the slits are visibly compressed before the pad is, being the mechanically weakest structures in the system. This does not exclude the filtering function of the pad described earlier by McConney *et al.* (2007), which is more active at high frequencies and not at low frequencies, like the quasistatistical loading described in this paper.

For the metatarsal lyriform organ HS-10 the relation between relative slit width and tarsal deflection force in the biologically most relevant range between 0.5 mN and 3 mN (corresponding to tarsal deflection angles between the mechanical threshold at 27 deg and 37 deg; figure 3*b*) is linear in slit 2 as well as in slit 6 (figure 10). Within this range slit 2 is compressed more than slit 6 by a factor of 3, likely indicating a stimulus amplitude fractionation by the individual slits of organ HS-10.

According to electrophysiological studies all the individual slits of the metatarsal organ behave like high-pass filters for vibration frequencies above approximately 30 Hz (Barth & Geethabali 1982; Molina *et al.* 2009). The main source for this tuning of the vibration receptor are the viscoelastic material properties of the joint pad (McConney *et al.* 2007; Fratzl & Barth 2009). At contact between tarsus and metatarsus (mechanical threshold) a deflection of the tarsus by approximately 10 deg down to 1 deg suffices at sinusoidal deflection frequencies from 5 Hz to 100 Hz to elicit suprathreshold action potentials (Molina *et al.* 2009). This range corresponds to a force change on the tarsus in the range from about 4.5 mN at 10 deg down to 195 μN at 1 deg (calculated with the mean values of the fitted exponential functions). At higher frequencies the physiological threshold angle decreases dramatically by 3 to 4 orders of magnitude down to 0.005 deg and a tarsal movement by 4.5 nm at 1000 Hz (Barth & Geethabali 1982; Molina *et al.* 2009) corresponding to a load change on the metatarsus by 0.9 μN only. These values are useful for a rough estimation of the range of forces stimulating organ HS-10, although they are calculated from the quasistatistical phase of the force measurements

(figure 2). At dynamical stimulation certainly larger force values are expected due to the significant increase of the Young's modulus of the metatarsal pad at vibration frequencies above 30 Hz (McConney et al. 2007; Fratzi & Barth 2009).

4.4. Comparison with finite elements modelling

Finite element models of various patterns of slit arrangements showed that the positioning of the slits within a lyriform organ and the direction of load strongly affect the compression of the individual slits and consequently their response to various stimulus parameters (Höbbl *et al.* 2007; 2009).

For organ HS-8 the slit compression at the dendrite position under load was simulated in a model with the exact arrangement and shape of the slits projected in a plane (Höbbl *et al.* 2009). When the values calculated from the linear regression lines of slit compression (figure 6), the mean values of initial slit widths, and the mean correlation of force and metatarsal angular deflection (1.35 mN/deg) of the actual white light interferometry data are compared with the values from the finite element model they show reasonably good agreement within a factor of about 2.

At a metatarsal deflection angle of 0.75 deg, at which the slit width in the finite element (FE) model was evaluated, the compression of the present white light interferometry study amounted to 107 nm for slit 1 (FE 206 nm), 102 nm for slit 2 (FE 145 nm), 66 nm for slit 3 (FE 67 nm), 43 nm for slit 4 (FE 48 nm), 38 nm for slit 5 (FE 20 nm), 21 nm for slit 6 (FE 9 nm), and 13 nm for slit 7 (no FE data). The small deviations of the model from the data collected using white light interferometry potentially arise from the modelling in a perfectly even plane and the influence of even small deviations of slit width, orientation towards the loading force, and the shape of the slits in finite element modelling.

Substantially both methods show the same trend of the gradual compression of the slits with the longest one being the most sensitive and decreasing sensitivity of slits 2 to 7 according to their decreasing length, which supports the results of the fractionated stimulus amplitude resolution by the individual slits of organ HS-8 found in the earlier electrophysiological studies (Barth & Bohnenberger 1978).

We thank Eduard Arzt for his kind hospitality at the Max-Planck-Institute of Metals Research in Stuttgart, Germany, Jan Schuppert for help with the scanning electron microscope, and Jorge Molina for many valuable discussions. The present work was supported by a travel grant of the University of Vienna to C.F.S. and project P16348 of the Austrian Science Foundation (FWF) to F.G.B..

REFERENCES

- Barth, F. G. 1971 Der sensorische Apparat der Spaltsinnesorgane (*Cupiennius salei* Keys., Araneae). *Z. Zellforsch.* **112**, 212–246.
- Barth, F. G. 1972 Die Physiologie der Spaltsinnesorgane II. Funktionelle Morphologie eines Mechanorezeptors. *J. Comp. Physiol.* **81**, 315–186.
- Barth, F. G. 2002 *A spider's world: senses and behavior*. Berlin, Heidelberg, Germany; New York, NY: Springer.
- Barth, F. G. & Bohnenberger, J. 1978 Lyriform slit sense organ: thresholds and stimulus amplitude ranges in a multi-unit mechanoreceptor. *J. Comp. Physiol. A* **125**, 37–43.
- Barth, F. G. & Geethabali 1983 Spider vibration receptors: threshold curves of individual slits in the metatarsal lyriform organ. *J. Comp. Physiol. A* **148**, 175–185.
- Barth, F. G. & Libera, W. 1970 Ein Atlas der Spaltsinnesorgane von *Cupiennius salei* Keys. Chelicerata (Araneae). *Z. Morph. Tiere* **68**, 343–368.
- Barth, F. G. & Pickelmann, P. 1975 Lyriform slit sense organs: modelling an arthropod mechanoreceptor. *J. Comp. Physiol.* **103**, 39–54.
- Barth, F.G. & Seyfarth, E.-A. 1971 Slit sense organs and kinesthetic orientation. *Z. vergl. Physiol.* **74**, 326–328.
- Blickhan, R. 1986 Stiffness of an arthropod leg joint. *J. Biomechanics* **19**, 375–384.
- Blickhan, R. & Barth, F. G. 1985 Strains in the exoskeleton of spiders. *J. Comp. Physiol. A* **157**, 115–147.
- Bohnenberger, J. 1978 The transfer characteristics of a lyriform slit sense organ. *Symp. Zool. Soc. Lond.* **42**, 449–455.
- Bohnenberger, J. 1981 Matched transfer characteristics of single units in a compound slit sense organ. *J. Comp. Physiol. A* **142**, 391–402.
- Fratzl, P. & Barth, F. G. 2009 Biomaterial systems for mechanosensing and actuation. *Nature* **462**, 442–448.
- Gingl, E., Burger, A.-M. & Barth, F. G. 2006 Intracellular recording from a spider vibration receptor. *J. Comp. Physiol. A* **192**, 551–558.
- Hergenröder, R. & Barth, F. G. 1983 The release of attack and escape behavior by vibratory stimuli in a wandering spider (*Cupiennius salei* Keys.). *J. Comp. Physiol. A* **152**, 347–358.
- Höbl, B., Böhm, H. J., Rammerstorfer, F. G. & Barth, F. G. 2007 Finite element modeling of arachnid slit sensilla–I. The mechanical significance of different slit arrays. *J. Comp. Physiol. A* **193**, 445–459.
- Höbl, B., Böhm, H. J., Schaber, C. F., Rammerstorfer, F. G., Barth, F. G. 2009 Finite element modeling of arachnid slit sensilla: II. Actual lyriform organs and the face deformations of the individual slits. *J. Comp. Physiol. A* **195**, 881–894.
- McConney, M. E., Schaber, C. F., Julian, M. D., Barth, F. G. & Tsukruk, V. V. (2007)

- Viscoelastic nanoscale properties of cuticle contribute to the high-pass properties of spider vibration receptor (*Cupiennius salei* Keys). *J. R. Soc. Interface* **4**, 1135-1143.
- Molina, J., Schaber, C. F. & Barth, F. G. 2009 In search of differences between the two types of sensory cells innervating spider slit sensilla (*Cupiennius salei* Keys.) *J. Comp. Physiol. A* **195**, 1031–1041.
- Müllan, R. 2005 Feinbau und Rekonstruktion der Cuticulastrukturen lyraförmiger Sinnesorgane der Spinne *Cupiennius salei*. Diploma thesis, University of Vienna.
- Seyfarth, E.-A. & Barth, F. G. 1972 Compound slit sense organs on the spider leg: mechanoreceptors involved in kinesthetic orientation. *J. Comp. Physiol.* **78**, 176–191.
- Seyfarth, E.-A. 1978 Lyriiform slit sense organs and muscle reflexes in the spider leg. *J. Comp. Physiol. A* **125**, 45–57.
- Seyfarth, E.-A. & Pflüger, H. J. 1984 Proprioceptor distribution and control of a muscle reflex in the tibia of spider legs. *J. Neurobiol.* **15**, 365–374.

ELECTRONIC SUPPLEMENTAL MATERIAL

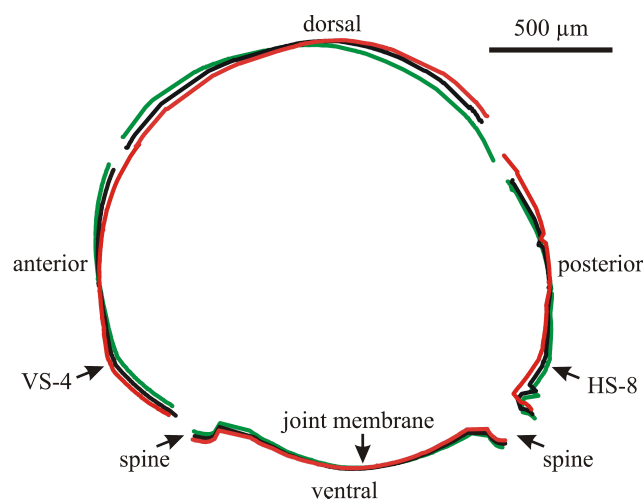


Figure 1. Change of the cross-section of the tibia (cuticle surface) at the location of the lyriiform organ HS-8 due to deflections of the metatarsus. Black: unloaded; red: backward deflection of the metatarsus by 10.2 deg which effectively stimulates HS-8; green: forward deflection of the metatarsus by 10.2 deg which stimulates VS-4 on the anterior aspect of the tibia.

Spider joint hair sensilla: micromechanics and adaptation to proprioceptive stimulation

Clemens F. Schaber*, Friedrich G. Barth

Department of Neurobiology, University of Vienna, Althanstraße 14, 1090 Wien, Austria

* Author for correspondence (clemens.schaber@univie.ac.at)

Author contributions

CFS designed the experiments, performed the measurements, analyzed the data, wrote the paper, and FGB helped writing the paper by comments on several earlier versions of the manuscript.

The following pages contain the manuscript in preparation for publication in the state as of January 14th, 2011.

Citation:

(in preparation for publication in: The Journal of Experimental Biology)

Summary

The present work deals with proprioceptive hair sensilla of the wandering spider *Cupiennius salei*, which are deflected by joint flexion during locomotion. The hairs are located at the articulation of tibia and metatarsus on all walking legs. On the tibia 20 such sensory hairs form a distinct row. They face about 75 sensilla on the metatarsus. When two opposing hairs get into contact during flexion of the joint, they deflect each other, reversibly interlocked by microtrichs on their hair shafts. The torques resisting hair deflections are much lower into the direction of natural stimulation than into the other directions, indicating a pronounced mechanical directionality of the hair suspension. Whereas in the preferred direction the torsional restoring constant S of the hair suspension is in the range of 10^{-10} Nm rad⁻¹ up to a deflection angle of about 30 deg (mean of natural deflections), it is larger by one to two powers of ten in other directions. Within the spider's natural step frequency between 0.3 and 3 Hz the sensory response (action potentials) of the joint hair sensilla follows the velocity of hair deflection.

Action potentials are set off at every step of the walking spider, when the hairs are deflected from their resting position. At hair deflections with constant angular velocities but different final deflection angles the maximum frequency of the action potentials remains constant. These results indicate that the joint hair sensilla are sensitive to the step frequency and the velocity of joint flexion. All findings point to the morphological, mechanical and physiological adaptation of the joint hair sensilla to their natural stimulation during locomotion.

Keywords Mechanosensors · Hair sensilla · Proprioception · Locomotion · Mechanical directional characteristics

Introduction

The precise coordination of the eight walking legs of a spider requires sensory feedback about the degree of flexion of their joints and the velocities of movement. In the present study the likely adaptation of hair sensilla at the tibia-metatarsus joint of the hunting spider *Cupiennius salei* to a proprioceptive function is examined.

On a walking leg of an adult *Cupiennius salei* spider there are about 150.000 hair sensilla (estimation from hair density and leg surface area) covering a large spectrum of functional types. The most sensitive among them are the trichobothria or filiform hairs. They respond to the frictional forces due to the slightest movements of air (Barth and Höller, 1999; Barth, 2002; Barth, 2004; Humphrey and Barth, 2008; McConney et al., 2009). By far the majority of hair sensilla on the spider's leg respond to tactile stimulation. Long exteroceptive hair sensilla located dorsally on the tarsus and metatarsus were identified as "event detectors" mainly responding to the onset of tactile stimuli (Albert et al., 2001). A single row of proprioceptive bristles proximally on the leg was found to be adapted to measure the distance between the coxae of neighbouring legs (Eckweiler et al., 1989). Groupings of particularly short sensilla forming hair plates at the joint between coxa and prosoma are proposed to inform the spider about its position in three-dimensional space (Seyfarth et al., 1990). Furthermore, hair sensilla bridging the metatarsus-tarsus joint respond to vibrations and are stimulated by dorsoventral displacement of the tarsus (Speck-Hergenröder and Barth, 1988). Finally, tactile stimulation of hairs on the sternum elicits reflexes adjusting the distance of the body to the ground of a spider walking over obstacles (Eckweiler and Seyfarth, 1988). Seyfarth (1985) postulated a proprioceptive function of the several hundred hair sensilla bridging the leg joints of *Cupiennius*.

Here we examine yet another type of mechanosensitive hair sensilla found at the tibia-metatarsus joint and suggest its proprioceptive function. The joint is of the hinge

type with its main plane of movement in the dorso-ventral direction and the axis of rotation on the dorsal side (Fig. 1A). To examine whether the sensory hairs at this leg articulation are adapted to monitoring joint deflection the following aspects were examined. (i) The joint angles and hair deflections during locomotion, (ii) the arrangement of the sensory hairs, (iii) the hair surface structures leading to reversible adhesion to hairs on the opposing leg segments during joint flexion, (iv) the mechanical directional characteristics of the suspension of selected hairs, and (v) the potential tuning to the natural deflection frequencies during locomotion as seen from its nervous discharges (action potentials).

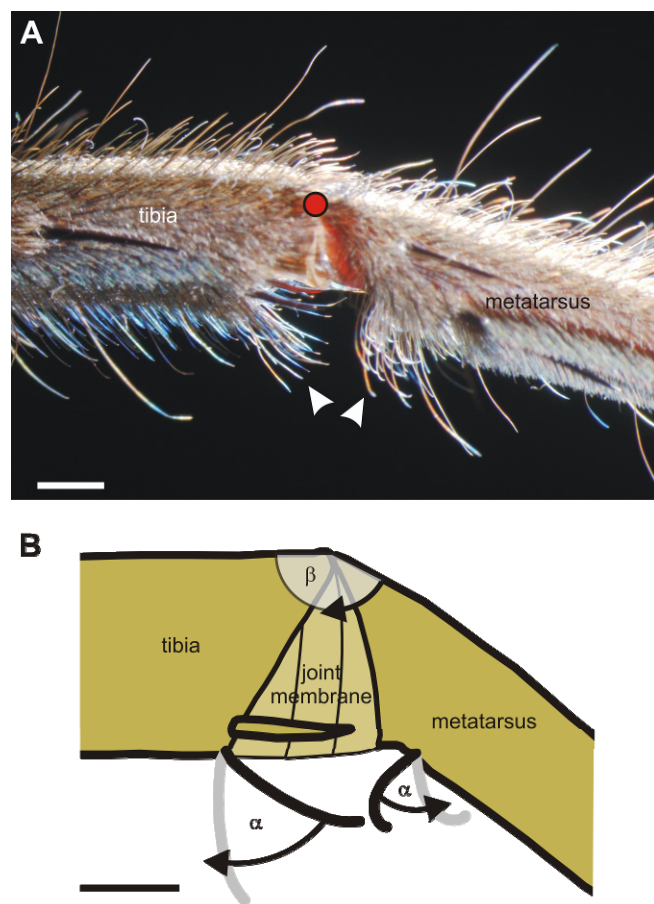


Fig. 1. (A) Photomicrograph of the tibia-metatarsus joint of a second walking leg; front view. The dot marks the centre of rotation of the joint. The arrowheads point to the ventral joint hairs examined in detail in this study. (B) When the joint angle β decreases during joint flexion, the ventral joint hairs of tibia and metatarsus deflect each other from contact onward by the angle α in the direction indicated by the arrows. The resting positions of exemplary hairs are drawn as thick black lines and the maximum deflections indicated in gray. The thickness of the hairs is not to scale. Scale bars 1 mm

Materials and methods

Animals

The experiments were carried out on adult females of the Central American wandering spider *Cupiennius salei* (Keyserling, 1877) bred in the Department of Neurobiology of the University of Vienna. For the measurements of the hair angle during the deflection of the joint, for force measurements, and electrophysiological experiments the animals were briefly anesthetized with CO₂ and tethered onto a holder with adhesive tape. The legs were fixed with drops of a mixture of colophony and beeswax.

Video analysis

Spiders were filmed in profile (at a right angle to their long axis) during straight runs with a digital video camera (Canon XL 1; Canon Inc., Tokyo, Japan) at 25 frames per second. By the chosen perspective angular distortions were negligible, because *Cupiennius salei* moves the tibia-metatarsus joint of its first pair of legs in parallel to the longitudinal axis of the body. Furthermore, the field of view was no more than 15 cm wide so that lens distortions were negligible. In 54 control experiments with five spiders filmed from above the translational movement of the tibia-metatarsus joint was in parallel to the longitudinal axis of the body in more than 99% of the steps.

The animals walked in a Perspex gangway (length 60 cm, height 3.5 cm, width 10.5 cm) illuminated by daylight fluorescent tubes. The openings of the gangway at its end were closed with black cardboard, because *Cupiennius salei* orients towards dark objects under light conditions (Schmid, 1998). The room temperature during the experiments was 30°C. The exposure time per frame was set to 1/1000 s to 1/2000 s. The recordings were transferred to a PC (Studio DV plus; Pinnacle Systems, Mountain View, CA, USA) and the joint angle measured frame by frame by marking the dorsal edges of the tibia and metatarsus and the centre of the joint's rotational axis (on-screen measurement error 0.38%, n=10; Software: Videopoint 2.5; Lenox Softworks, Lenox, MA, USA). The mean running speed was determined from the time and the spider's horizontal translational movement between the first and last frame of a recording.

Mapping and identification of proprioceptive hairs

The hairs deflected by joint movements were observed in live spiders or freshly autotomized legs and documented using a stereomicroscope and a digital camera (Nikon Coolpix 990; Nikon Corporation, Tokyo, Japan). For mapping the topography of the proprioceptive hair sensilla under the microscope the joint was dissected. A

longitudinal cut ventrally in the leg followed by immersion of the preparation into 5% KOH solution for ca. 1 hour allowed to spread out and flatten the tube shaped leg segment. The specimens were dehydrated through a graded concentration series of ethanol and Xylene and embedded in DPX (distyrene, a plasticizer, and xylene) mounting medium (Agar Scientific Ltd., Stansted, UK) on microscope slides. To keep the cuticle flat during hardening of the mounting medium the cover slips were loaded with metal cubes. The outlines of the sockets of the proprioceptive hairs were drawn using a camera lucida. In order to correlate the shape of their shafts with their position at the joint individual hairs were plucked out and photographed using a digital laboratory imaging system (Lucia M/Comet 3.52a, Laboratory Imaging s.r.o., Prague, Czech Republic; Camera Sony Power HAD 3CCD, Sony Corporation, Tokyo, Japan on a Laborlux D microscope, Ernst Leitz Wetzlar GmbH, Wetzlar, Germany).

Controlled joint flexion

For the measurement of the angles of the proprioceptive hair deflections live spiders were mounted on a metal platform. Hairs not normally deflected by joint movements were removed. The deflection plane of the hairs of interest was adjusted to the plane of focus of the stereomicroscope with the camera of the digital imaging system. The tibia was fixed with beeswax while the metatarsus was free to be moved using a wire loop. Pictures of the hairs were taken at increasing flexion of the joint. At a joint angle of $\beta = 180$ deg the joint was stretched with the mid-dorsal aspect of tibia and metatarsus forming a straight line. At $\beta < 180$ deg the metatarsus was flexed towards the ventral aspect. The deflection angles α of the hair shaft were measured relative to its resting position (Fig. 1B). The measurement was very reproducible, with a maximum measurement error (SE) found to be 1.83% at 8 repetitions of the experiment in the same preparation.

Scanning electron microscopy

Tibia-metatarsus joints of freshly autotomized legs and kept at an angle β of approximately 135 deg with small insect pins were fixed in buffered glutar-di-aldehyde (0.2 M in sodiumcacodylate buffer, 4% sucrose, pH 7.8) followed by staining with osmium tetroxide (1%), dehydrated with dimethoxypropane (DMP), pure ethanol and pure acetone, and dried by hexamethyldisilazane (HMDS) evaporation (all chemicals supplied by Sigma-Aldrich Handels GmbH, Wien, Austria) Specimens were sputter coated with gold for 100 seconds (Model 108; Agar Scientific Ltd., Stansted, UK) and

examined in a scanning electron microscope (Philips XL 20; FEI, Eindhoven, The Netherlands) at acceleration voltages of 15 – 20 kV.

Restoring torques

For the measurement of the restoring moments opposing hair deflection originating in the hair suspension the method developed by H.-E. Dechant (2001) and described in detail in Albert et al. (2001) and Barth et al. (2004) was used. In short, the force opposing hair deflection was measured by the deflection of an individually calibrated glass fibre. The amount of fibre deflection, the lever arm and the degree of hair deflection from the unloaded position were quantified in serial digital photographs.

Glass fibres were made from borosilicate glass capillaries (Vitrex; outer diameter 1 mm, inner diameter 0.58 mm, length 100 mm, with filament; Modulohm A/S, Herlev, Denmark) using a laser micropipette puller (Sutter P-2000; settings: heat 600, fil 4, vel 50, del 150, pul 100; Sutter Instrument, Novato, CA, USA). The glass fibres were calibrated at a marked point along their length by bending them in defined steps against a razor blade mounted on a micro balance (Mettler BE 22; Balance Control BA25; Mettler Instrumente AG, Greifensee, Switzerland). Deflection amplitudes were up to 1 mm. The calibration procedures were controlled optically and carried out on a vibration isolation table (TMC micro g; Technical Manufacturing Corporation, Peabody, MA, USA) in a closed room. The deflection of the glass fibre correlated highly linearly and reproducibly (R^2 0.994; $n=15$) with the applied force by $0.044 \mu\text{N}$ per μm .

Single joint hairs were adjusted at right angle to the vertically mounted glass fibre at the calibration mark. The hair was then pushed stepwise against the glass fibre and image sequences were recorded and analyzed for hair angle and glass fibre deflection with the image analysis system. The correct position of the calibration mark was controlled optically during the experiments. The torque was calculated as the product of fibre displacement in the image plane and the calibration factor of the glass fibre (force) and the distance of the point where the load was applied on the hair shaft to the hair socket (lever arm).

Electrophysiology

Action potentials were recorded extracellularly from single joint hairs with electrolytically sharpened tungsten electrodes. The different electrode was inserted a few micrometers deep into the cuticle proximally of the sensillum socket using a nanostepper (Scientific Precision Instruments GmbH, Oppenheim, Germany) mounted on a micromanipulator. The grounded indifferent electrode was a silver wire inserted

into the opisthosoma. For mechanical stimulation a fork made of tungsten wire and mounted on an electrodynamic shaker (Model V101, Ling Dynamic Systems Ltd., Royston, UK) with custom made feedback control was used (Bohnenberger et al. 1983). The shaker was attached to a micromanipulator on a turntable for the precise adjustment of the deflection stimulus in the proprioceptive plane. The stimulator was driven by an externally triggered function generator (Model 20, Wavetek, San Diego, CA, USA) and the stimulus magnitude adjusted by an attenuator.

Stimuli were either ongoing or single sinusoidal movements at a temporal distance of 30 s to simulate a natural stimulus. At zero point of the sine wave the stimulator just slightly touched the joint hair, without deflecting it from its resting position. The half sine wave above zero deflected and returned the hair to its initial position in the direction of its normal proprioceptive stimulation. During the half wave below zero there was no contact between stimulator and hair shaft. The hair deflection amplitude was adjusted optically with an angular grid in the ocular lens of a dissection microscope (Wild M5A, magnification 100x, Wild Leitz Ltd., Heerbrugg, Switzerland).

The recording trace was band pass filtered between 100 and 3000 Hz and monitored using a loudspeaker and an oscilloscope. Data were recorded together with the displacement signal of the stimulator via an analogue-digital-interface (CED 1401, Cambridge Electronic Design Ltd., Cambridge, UK) onto the hard disk of a PC (resolution 10000 samples per second). The setup was arranged within a Faraday cage and on a vibration isolation table (TMC micro-g, Technical Manufacturing Corporation, Peabody, MA, USA).

Results

Movement of the joint during locomotion

In freely running animals the joint angle β reaches a maximum of $174.2 \text{ deg} \pm 7.6 \text{ deg}$ (mean \pm s.d., $N=7$, $n=41$) when the leg touches down on the ground at the end of the swing phase. Maximum joint flexion and thus the smallest angle β of $119.4 \text{ deg} \pm 8.6 \text{ deg}$ ($N=7$, $n=42$) occur before the leg is lifted from the substrate at the end of the power stroke. Figure 2A shows a representative example of the time-course of the joint angle β at a moderate walking speed of 2 cm s^{-1} of the spider. The mean amount of joint flexion, defined as the difference between the maximum and the following minimum during a step cycle ($\Delta\beta$), is $54.6 \text{ deg} \pm 8.9 \text{ deg}$ ($N=7$, $n=46$). The joint is never flexed to angles of

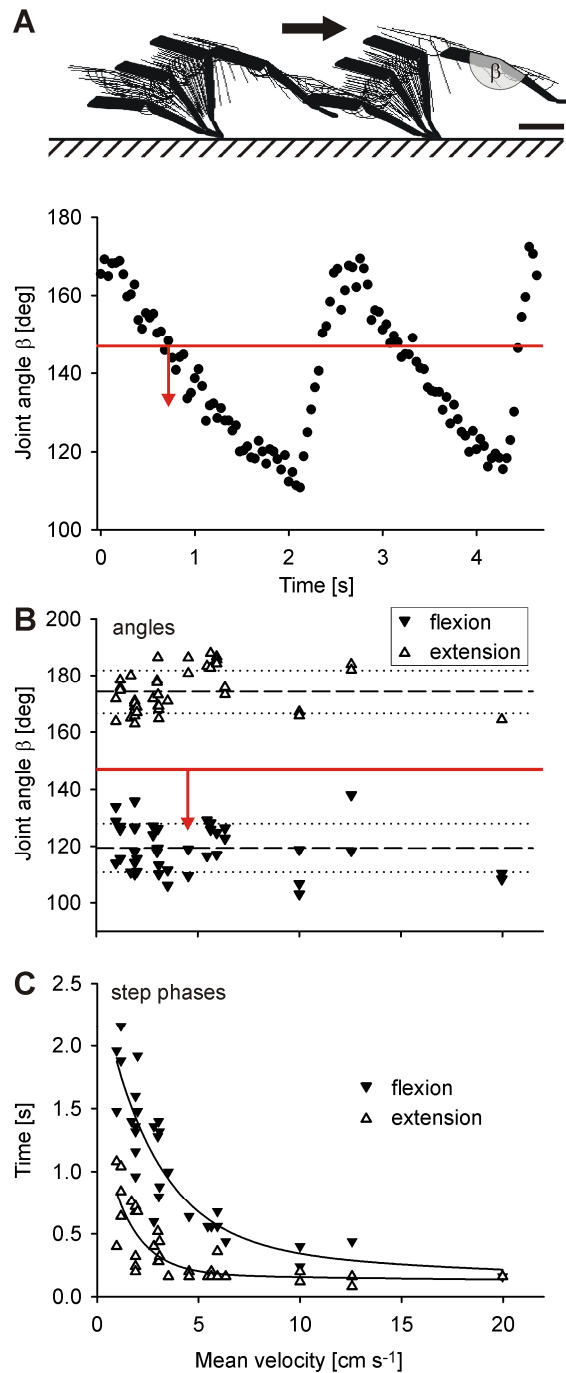


Fig. 2. Movements of the tibia-metatarsus joint during straight forward locomotion. (A) Two steps at a mean walking velocity of 2 cm s^{-1} . The upper trace shows the positions of tibia, metatarsus, and tarsus from frame-to-frame video analysis, the diagram below the corresponding values of joint angle β . The red line indicates the mean threshold angle for the deflection of the ventral joint hair sensilla during joint flexion. Scale bar 1 cm. (B) Maximum (extension) and minimum (flexion) angles of the joint at different running speeds. The dashed lines mark the level of the mean extension and the mean flexion angles, the dotted lines the corresponding standard deviations ($N=7$, $n=24$). The red line indicates the mean threshold angle for the deflection of the ventral joint hair sensilla during joint flexion. (C) Duration of the joint's flexion and extension phases at different running speeds ($N=7$, $n=23$).

$\beta < 100$ deg, but frequently extended up to an angle β of approximately 190 deg (Fig. 2B).

The step duration, which is the time needed for a power stroke (joint flexion) and the following swing phase (joint extension without contacting the substrate), decreases from about 3 s at a running speed of 1 cm s⁻¹ to about 0.8 s at 6 cm s⁻¹. From 6 cm s⁻¹ to 20 cm s⁻¹ the step duration decreases more slowly down to 0.32 s. Up to a running speed of 3.5 cm s⁻¹ the flexion and extension phases of the steps decrease simultaneously, whereas at larger velocities the time for joint extension (swing phase) remains fairly constant and only the duration of the power stroke decreases (Fig. 2C). Consequently, the stepping frequency of the first leg pair of *Cupiennius salei* during straight forward locomotion under light conditions is 0.3 Hz to 3 Hz at running speeds between 1 and 20 cm s⁻¹.

Distribution and proprioceptive deflection of all hair sensilla at the tibia-metatarsus joint

The shape of the joint hair sensilla at the tibia-metatarsus joint and the pattern of their distribution are the same for all the eight legs of the spider. Distally on the tibia there are about 310 and on the metatarsus about 400 hair sensilla, which are deflected by movements of the joint. The large majority of them are deflected by contact with hairs on the other segment of the leg. Only the most distal dorsal hairs dorsally on the tibia are deflected of the tibia by contact with the metatarsal cuticle.

The approximately 480 hairs arranged dorsally on the tibia and the metatarsus are deflected only slightly from their resting position and only when the leg is stretched, the angle β being close to 180 deg. The approximately 230 hair sensilla on the lateral and ventral aspects of the joint are longer than the dorsal ones. They are deflected by angles up to 60 degree when the joint is flexed during the power stroke.

Six types of proprioceptive hair sensilla can be distinguished by their shape and arrangement pattern and the kind of their proprioceptive deflection as follows (Fig. 3A,B).

(Ti 1) Tibia, dorsally: The hair shafts cover the hairless cuticle which is found directly at and around the joint pans (condyli). Their sockets are arranged in multiple rows so that several layers of hair shafts bridge the gap to the metatarsus. About 200 such hairs arranged in multiple rows are found on the entire dorsal aspect. They are deflected away from the skeletal cuticle by the metatarsal dorsal sensilla when the joint is stretched.

(Me 1) Metatarsus, dorsally: About 280 sensilla are arranged in multiple rows. The hair tips point distally and the hair shafts form a small angle with the cuticle surface. The angle and the length of these hairs increase with distance from the joint. When the joint is stretched they are pushed down slightly by the dorsal sensilla of the tibia.

(Ti 2) Tibia, anterior and posterior: The multiple rows of short hairs dorsally merge to a single row of long hairs ventrally. Anterior-ventrally there are about 40 hairs between the dorsal edge and the ventral cuticular spine. Their length varies from about 800 μ m (most dorsal hairs) to 1600 μ m (most ventral ones). Posterior-ventrally are about 50 proprioceptive hairs arranged similarly like on the anterior-ventral aspect and lengths ranging from 700 μ m to 1500 μ m.

(Me 2 and 3) Metatarsus, ventrally: About 120 proprioceptively deflected sensilla are arranged on the ventral aspect starting below the joint sockets of the, in cross-section half-lentil-shaped metatarsal joint region. Here the basal hair shafts form roughly a right angle (88 deg \pm 12 deg; N=6,

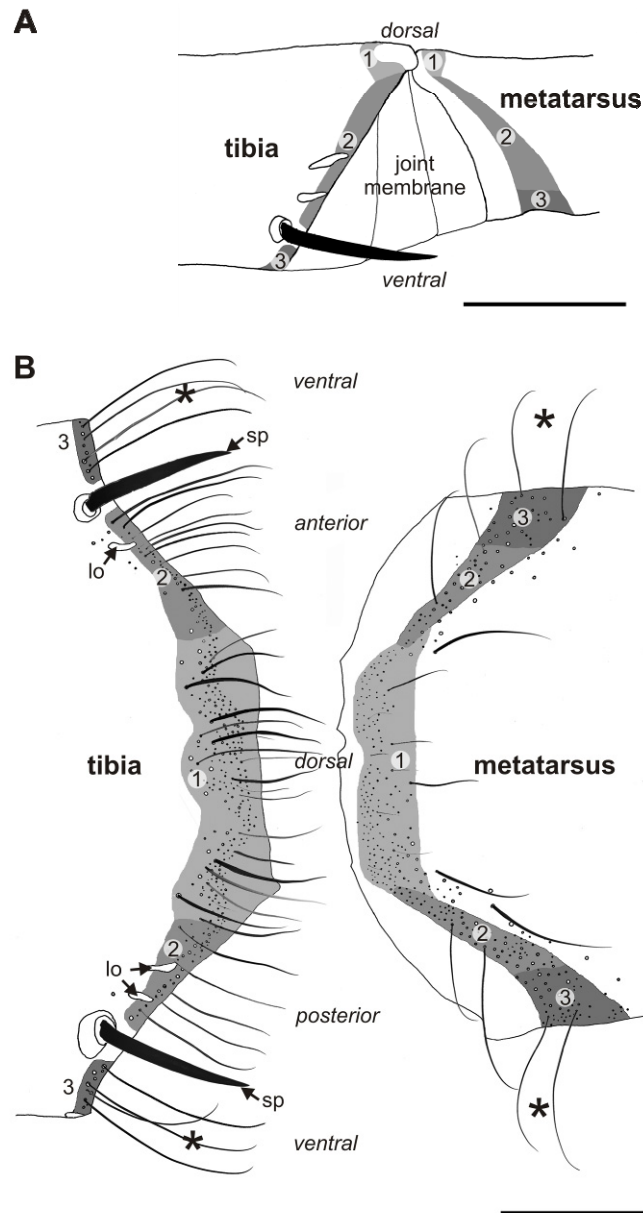


Fig. 3. (A) Posterior view of the joint between tibia and metatarsus. The different areas of joint hairs are indicated by different shadings of grey and numbers referring to the text. (B) Examples of the typical hair shapes in the areas 1 to 3 (compare with (A)) are drawn in reference to their sockets in a flattened cuticle preparation. Asterisks mark joint hairs representing those examined in detail in the present study. The cuticular spines (sp) and lyriform organs (lo) on the tibia are drawn as landmarks. Scale bars 1 mm

n=18) with the exoskeletal surface and the hair tips are bent point distally. During joint flexion they are deflected by the Ti 2 and Ti 3 hairs opposing them on the anterior, posterior and ventral aspect of the tibia.

(Ti 3) Tibia, ventrally: Ventrally between the two large cuticular spines are 20 ± 4 ($N=20$) joint hair sensilla that form a row at the edge of the sclerotized cuticle to the joint membrane. The sockets of these hairs are about $50 \mu\text{m}$ away from the “normal” hair coat of the tibia. Their shafts are 1400 ± 200

μm ($N=8$, $n=32$) long and deflected away from the joint membrane by type *Me 3* hairs of the metatarsus (Figs 1B, 3B).

The two hydraulically erectile spines on the tibia have to be counted as cuticular sensilla with a lever arm as well (Harris and Mill, 1977; Foelix, 1996). They are shorter (about $1200 \mu\text{m}$) than the hairs surrounding them and deflected only by direct contact with the cuticle of the metatarsus at large angles of joint flexion β from 125 deg to 135 deg onward.

Mechanical threshold and proprioceptive deflection of the ventral joint hairs

The mechanical threshold of hair deflection is indicated by the onset of hair shaft movement due to flexion of the joint. Of the ventral hair sensilla of the tibia (*Ti 3*) the deflection threshold is at a joint angle β of $147 \text{ deg} \pm 10 \text{ deg}$ ($N=8$, $n=32$). A similar value is found for the neighbouring *Ti 2* sensilla at $148 \text{ deg} \pm 19 \text{ deg}$ ($N=4$, $n=25$) anteriorly and $147 \text{ deg} \pm 7 \text{ deg}$ ($N=4$, $n=16$) posteriorly. Together they form a functional entity of approximately 110 hair sensilla, which are simultaneously deflected during flexions of the joint at joint angles of $\beta < 147 \text{ deg}$ onward, which is reached in every step of the walking spider (Fig. 2B), by the approximately 120 opposing *Me 2* and *Me 3* sensilla of the metatarsus.

Interestingly, within the biological range of joint flexions up to joint angles of β by 100 deg the mean deflection curves of the ventral tibia (*Ti 3*) and metatarsal (*Me 3*) joint hairs, which are examined in more detail in the present study, are very similar with maximum hair deflection angles α of approximately 60 deg . Within the biologically most relevant mean range of joint flexions up to joint angles β of approximately 120 deg (Fig. 2B), both the ventral joint hairs of the tibia and those of the metatarsus deflect each other up to hair deflection angles α of approximately 30 deg (Fig. 4).

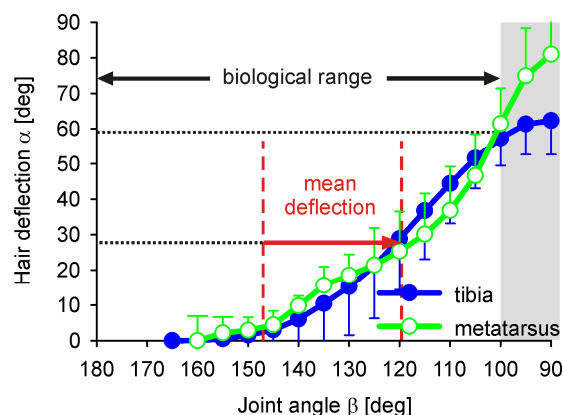


Fig. 4. Mean deflection α (\pm s.d.) of ventral tibia ($N=8$, $n=32$) and metatarsus ($N=6$, $n=18$, each measured 6 times) joint hairs as a function of joint angle β (bin width 5 deg). Joint angles β within the shaded area ($< 100 \text{ deg}$) are not reached during active locomotion of the spider.

Functional morphology of the hair shafts and sockets

The shafts of the ventral joint hairs of both the tibia and the metatarsus are covered with tens of thousands of cuticular protuberances (microtrichs). Their absolute number on a single hair strongly depends on the length and diameter of the hair shaft. The microtrichs emerge from ripples parallel to the long axis of the hair shaft starting from 25 μm above the suspension of the hair in the cuticle up to the hair tip. The microtrichs form regular rows with a distance of 1 μm between them. Dependent on the hair shaft's cross section there are from 15 microtrichs per μm of hair length in the tip region up to 25 microtrichs per μm in the basal region of the hair shaft. They are cone shaped, 5 μm long, and about 1 μm thick at their base. Their tips are 150 nm wide and form a small hook. When the joint hairs of the metatarsus and the tibia are in contact during flexion of the leg joint the contact area is limited to the tip region of the microtrichs (Fig. 5). Thereby, during joint flexion the two joint hairs deflect one another loosely and reversibly coupled.

Viewed from above the sockets of the tibia hairs are nearly circular. In the undeflected state the membrane of the hair suspension bulges outward between the basal hair shaft and the socket wall at the side of proprioceptive deflection. Here the distance between the hair shaft and the socket wall is much larger than into the other possible directions of hair deflection (Figs 6A,B). The socket of the metatarsus hairs viewed from above is slightly elliptic with its longer diameter in the plane of proprioceptive movement. At the side of proprioceptive deflections the wall of the hair socket is lower compared to the other sides (Fig. 6C). These arrangements of the hair shafts inside their

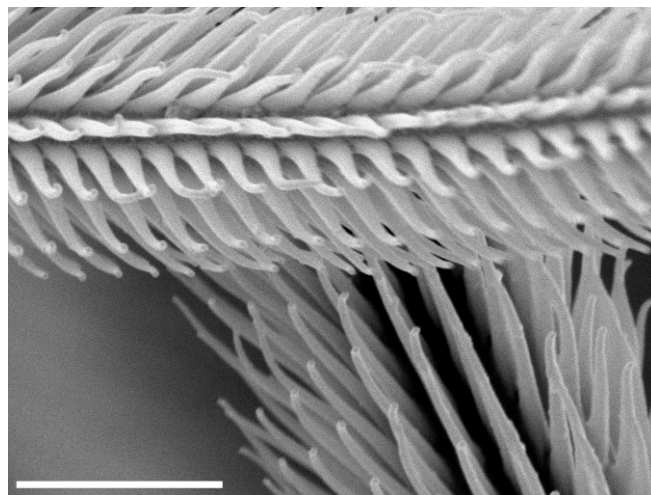


Fig. 5 Microtrichs on the hair shaft of a tibia (top) and a metatarsus hair (below) in contact at a joint angle β of 135 deg. Microtrichs interlock slightly. Scale bar 5 μm

hair sockets and the structures of the socket walls facilitate large angle deflections into the proprioceptive directions before the hair shafts are bent. These structures of the hair suspensions appear to be adaptations to proprioceptively directed large angle deflections.

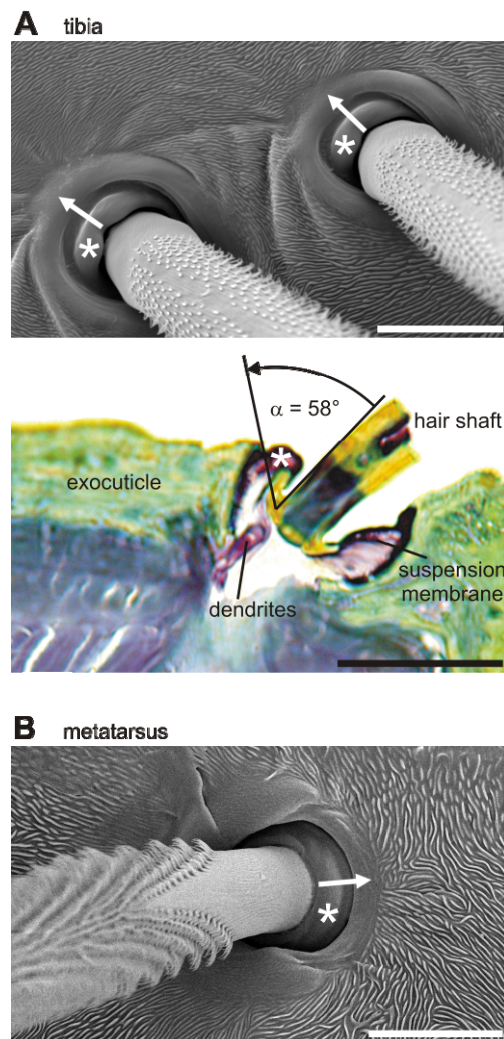


Fig. 6. Hair sockets of the ventral joint hairs. The proprioceptive deflection directions are indicated by the arrows. (A) SEM micrograph of two sockets of tibia hairs. Below a photomicrograph of a semi-thin section of a hair socket. Toluidine blue stained (slice by courtesy of R. Müllan). Asterisks indicate the bulging joint membrane. (B) Socket of a metatarsus hair. Scale bars 20 μm

Mechanical directional characteristics

The restoring torques of the tibia sensilla were measured at the hairs ventrally of the posterior cuticular spine. On the metatarsus the restoring torques were obtained from sensilla opposing those of the tibia (Fig. 3B). Each preparation was examined by six consecutive deflections of the hair shaft in four directions (proximad, distad, anteriad, posteriad) and the torques needed for the deflection plotted as a function of the hair deflection angle α (Fig. 7A).

At deflections up to a hair angle of $\alpha \leq 50$ deg in the proprioceptive direction the torques rise slowly from zero to about 1 nNm in both the tibia and the metatarsus sensilla. At angles of $\alpha > 50$ deg the torques needed to deflect the hairs further increase

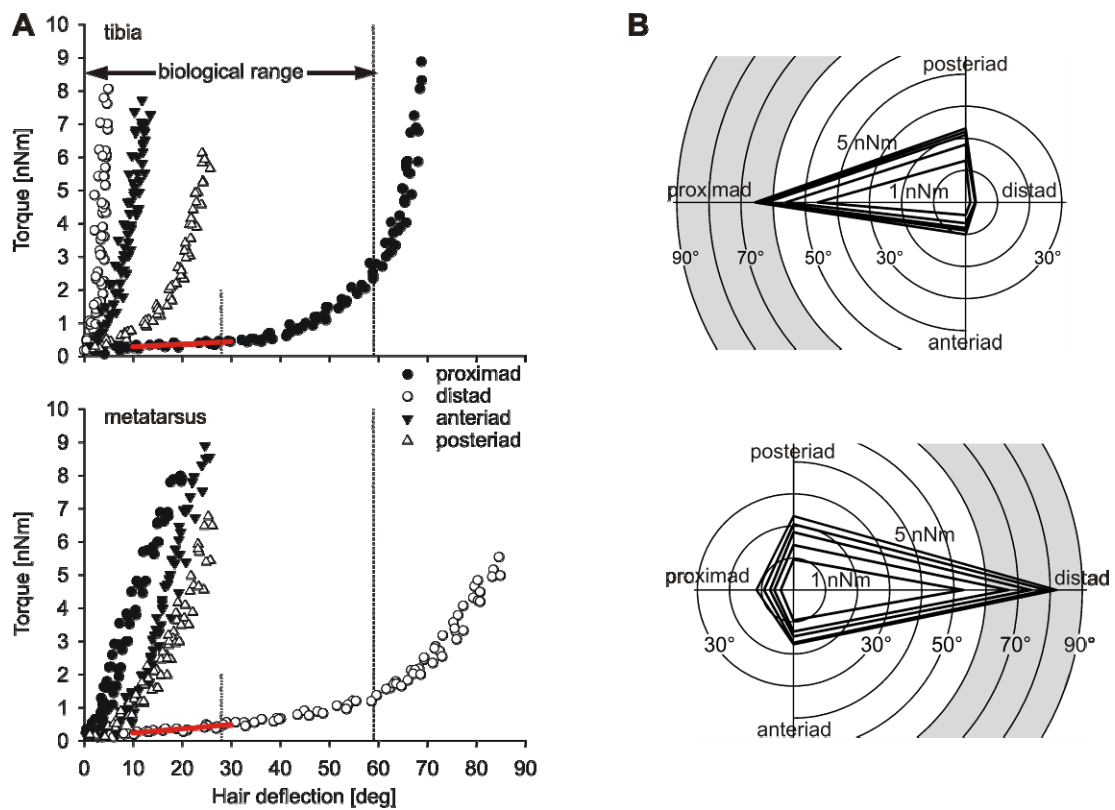


Fig. 7. Mechanical directional characteristics of the joint hairs. (A) Torques at deflections of a tibia hair in four different directions relative to the leg's long axis (proximad-distad). The vertical line at 59 degrees marks the maximum hair deflection by joint flexion during locomotion, the line at 28 degrees the mean value of hair deflection during locomotion (compare Fig. 4). The regression line (red) was used to determine the torsional restoring constant S . Below is the corresponding graph for a metatarsus joint hair. (B) Polar plots of the torques. The iso-torque lines connect the mean angles of deflection ($n=6$) required to reach torques from 1 nNm (innermost line) to 5 nNm (outermost line). In the proprioceptive direction angles within the shaded area are not reached during locomotion.

significantly, indicating the contact of the basal hair shafts with the socket walls and therefore the bending of the hair shafts (Fig. 6A). When the hair shafts are deflected into the other directions (i.e. opposite to the proprioceptive direction, anteriad, and posteriad) the torque values increase much faster with deflection angle, the greatest resistance being in the direction opposite to the proprioceptive one (Fig. 7A). The iso-torque plots shown in Fig. 7B clearly demonstrate the directional characteristics of the hair suspensions.

The torque (T) increase with deflection angle α [deg] in each direction can be well described mathematically ($R^2 > 0.85$) by the exponential function $T = T_0 + ae^{b\alpha}$, where T_0 , a and b are constants (table 1).

Table 1. Parameters (mean values) and correlation coefficients R^2 of the exponential function $T = T_0 + ae^{b\alpha}$ [$\text{Nm} \times 10^{-9}$] fitted to the measured torque values T (six preparations and hairs each). T_0 is the extrapolated value of T at a hair deflection angle of 0 deg. a and b are constants, and R^2 is the correlation coefficient of the fitted curve with the experimental data.

| | T_0 | a | B | R^2 |
|------------------|-------------------|------------------|-----------------|-----------------|
| Tibia hairs | | | | |
| Proximad* | 0.37 ± 0.08 | 0.00 ± 0.00 | 1.17 ± 0.02 | 0.96 ± 0.02 |
| Distad | -3.55 ± 4.43 | 3.59 ± 4.45 | 0.22 ± 0.22 | 0.86 ± 0.08 |
| Anteriad | -4.60 ± 4.42 | 4.15 ± 4.21 | 0.09 ± 0.04 | 0.92 ± 0.05 |
| Posteriad | -0.50 ± 0.86 | 0.63 ± 0.72 | 0.12 ± 0.05 | 0.96 ± 0.02 |
| Metatarsus hairs | | | | |
| Proximad | -6.63 ± 10.46 | 6.38 ± 10.49 | 0.08 ± 0.06 | 0.91 ± 0.05 |
| Distad* | 0.12 ± 0.18 | 0.07 ± 0.08 | 0.06 ± 0.03 | 0.98 ± 0.01 |
| Anteriad | -3.42 ± 3.06 | 3.19 ± 2.85 | 0.06 ± 0.04 | 0.96 ± 0.02 |
| Posteriad | -3.38 ± 4.01 | 3.25 ± 3.88 | 0.05 ± 0.04 | 0.96 ± 0.02 |

* proprioceptive

Torsional restoring constants S

In the proprioceptive direction the torsional restoring constant S of the hair suspension can be evaluated from the linear region of the torque curve between the angles of hair deflection of $\alpha = 10$ deg and $\alpha = 30$ deg (Fig. 7A). The values of S of the tibia joint hairs are in the range from 5.0×10^{-12} to 2.3×10^{-11} Nm deg^{-1} , and 2.9×10^{-10} to 1.3×10^{-9} Nm rad^{-1} , respectively ($N=6$). The torsional restoring constants of the metatarsus joint

hairs are similar, between 5.4×10^{-12} to 1.7×10^{-11} Nm deg⁻¹, and 3.1×10^{-10} to 1.6×10^{-9} Nm rad⁻¹, respectively (N=6) (table 2). Within this linear range the restoring torques can be related to the extension of a linear spring element within the hair suspension. Consequently, because of the similarity of the S values of the tibia and metatarsus hair suspensions, both hairs are deflected by roughly the same amount when the joint is flexed during locomotion.

Into other than the proprioceptive direction the stiffness of the hair suspension is larger. For these not proprioceptively directed deflections the values of S listed in table 2 were derived from the quasi-linear rise of the torque curves at deflection angles below 5 deg. Compared to deflections in the proprioceptive (proximad) direction the stiffness of the suspension of the tibia hairs is 62-times larger in the distad direction of deflection, 37-times in the anteriad, and 12-times in the posteriad direction. For the metatarsal joint hairs the mechanical directional characteristics are slightly less pronounced with a 19-fold larger stiffness towards the proximal and anterior direction, and 8-fold stiffness posteriadly, when compared to the proprioceptive distad deflections.

Table 2. Linear torsional restoring values S of the ventral tibia and metatarsus joint hairs in four deflection directions (six preparations and hairs each)

| | Mean [Nm rad ⁻¹] | s.d. [Nm rad ⁻¹] | Minimum [Nm rad ⁻¹] | Maximum [Nm rad ⁻¹] |
|------------------|------------------------------|------------------------------|---------------------------------|---------------------------------|
| Tibia hairs | | | | |
| Proximad* | 5.92×10^{-10} | 3.85×10^{-10} | 2.86×10^{-10} | 1.33×10^{-9} |
| Distad | 3.69×10^{-8} | 2.64×10^{-8} | 5.40×10^{-9} | 8.02×10^{-8} |
| Anteriad | 2.17×10^{-8} | 1.34×10^{-8} | 8.10×10^{-9} | 3.93×10^{-8} |
| Posteriad | 6.90×10^{-9} | 2.69×10^{-9} | 4.22×10^{-9} | 1.10×10^{-8} |
| Metatarsus hairs | | | | |
| Proximad | 1.51×10^{-8} | 1.05×10^{-8} | 3.59×10^{-9} | 2.86×10^{-8} |
| Distad* | 8.03×10^{-10} | 4.54×10^{-10} | 3.09×10^{-10} | 1.60×10^{-9} |
| Anteriad | 1.50×10^{-8} | 9.29×10^{-9} | 4.85×10^{-9} | 2.74×10^{-8} |
| Posteriad | 6.19×10^{-9} | 3.70×10^{-9} | 2.04×10^{-9} | 1.21×10^{-8} |

* proprioceptive

Electrophysiological response properties

To approximate the natural stimulus pattern sinusoidal half wave deflections by angles of $\alpha = 30$ deg were applied to single joint hair sensilla into the proprioceptive

direction at different frequencies. This quasi-natural stimulus pattern roughly corresponds to the flexion of the joint by joint angles from $\beta = 150$ deg to $\beta = 120$ deg, which is the mean range of joint flexion during locomotion.

Bursts of up to 50 action potentials follow in response to deflection of the hairs away from their resting position at the slowest stimulus (0.1 Hz). No action potentials are generated during the return of the hairs to their resting position. The number of action potentials decreases quickly with increasing stimulus frequency down to 5 at 5 Hz (Figs 8A,B).

To test whether the frequency of the action potentials during one burst correlates with the stimulus frequency and therefore the velocity of the hair deflection the shortest inter-spike interval and the resulting maximum impulse frequency during one burst were compared at different stimulus frequencies.

The velocity of joint flexion is represented by the frequency of the action potentials during one burst especially at low stimulus frequencies well within the biological range. From 0.1 Hz to 1 Hz the mean maximum frequency (N=6, n=36) more than doubles from about 40 to 100 Hz. At stimulus frequencies from 1 Hz to the upper limit of the biological range at 3 Hz the maximum frequency of the action potentials increases further from about 100 Hz to 140 Hz. At deflection frequencies beyond the biological range (> 3 Hz) the impulse rate does not increase further and the velocity of joint flexion cannot be resolved by the frequency of the action potentials any more (Figs 8A,B).

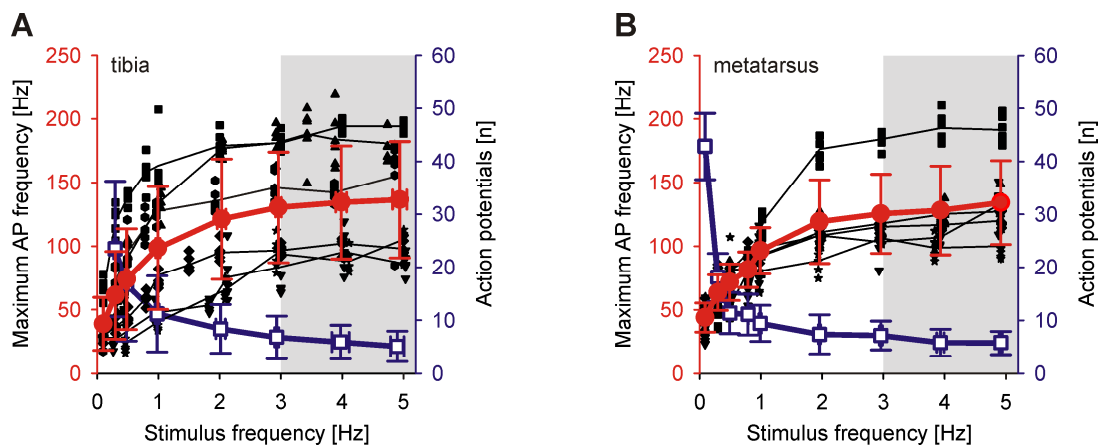


Fig. 8. Sensory response (action potentials) of the ventral joint hair sensilla to proprioceptive deflections by $\alpha = 30$ deg by sinusoidal half waves. (A) Tibia hairs. The thick red and blue lines connect the means of six joint hairs (\pm s.d.; N=6, n=36). Maximum frequency of action potentials per stimulus (full red circles), number of action potentials per stimulus (open blue squares), original data (small symbols). The thin black lines connect the mean values of each preparation (N=1, n=6). Stimulus frequencies within the shaded area are not reached during locomotion of the spider. (B) Metatarsus hairs (N=5, n=30). Details same as in (A).

Therefore, the velocity of joint movement may be monitored by the frequency of the action potentials during one burst, whereas the stepping frequency of the spider during locomotion is detected by the synchrony of the bursts with the beginning of the deflection of the hairs from their resting positions. These electrophysiological data are even more manifest, if the synchronous deflection of the about 100 ventral, anterior- and posterior-ventral joint hairs of the tibia together with about 100 joint hairs at the ventral aspect of the metatarsus at flexion of the joint is taken into account.

The mean threshold hair deflection α necessary to elicit one action potential with quasi-natural sinusoidal stimulation is 8 deg at all frequencies tested up to 10 Hz (N=4, n=4). The angular threshold may be as large as $\alpha = 20$ deg at 0.1 Hz and as low as $\alpha = 3$ deg at 1 Hz in single preparations.

At linear ramp-and-hold deflections with a constant hair deflection velocity of 40 deg s^{-1} towards final angles between $\alpha = 6$ deg (threshold angle of the preparation) and $\alpha = 30$ deg the maximum action potential frequency of the sensory response remains the same. In the same angular range the number of action potentials increases from 100 to about 250, which is thought to be mainly due to the longer duration of the dynamic stimulus phase of the hair movement (Fig. 9). The latter response properties again indicate that the joint hair sensilla are dynamical receptors for the velocity of flexion of the tibia-metatarsus joint during locomotion of the spider.

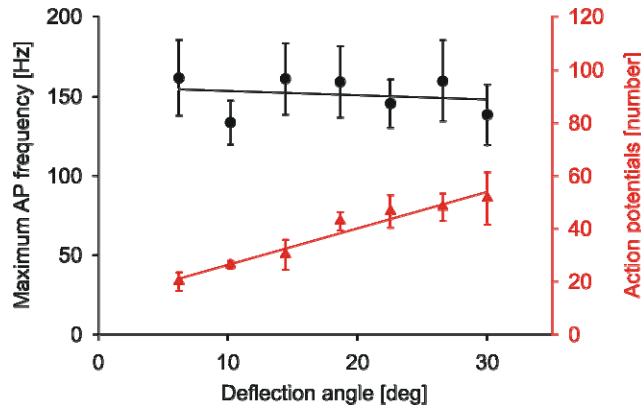


Fig. 9. Sensory response of a ventral tibia joint hair to ramp-and-hold deflections into the proprioceptive direction by different final angles at a constant angular velocity of 40 deg s^{-1} (mean \pm s.d.; N=1, n=6)

Discussion

Pattern of hair arrangement

During locomotion a multitude of hair sensilla at the tibia-metatarsus joint of *Cupiennius salei* is stimulated due to their pattern of arrangement and shape. The tips of the sensilla in the areas *Ti 2* and *Ti 3* on the tibia roughly form a straight line in their resting positions (Fig. 3). These sensilla represent a kind of sensory collar consisting of approximately 110 hairs, which are initially stimulated when their tips get in contact with the approximately 120 ventral joint hairs in the areas *Me 2* and *Me 3* of the metatarsus at a joint flexion by an angle β of about 150 deg. At lower angles of joint flexion β these about 230 joint hair sensilla deflect each other loosely and reversibly coupled by the microtrichs on their hair shafts (Fig. 5) and are stimulated following the spider's stepping pattern. The dorsal sensilla of the *Ti 1* of the tibia and *Me 1* of the metatarsus (Fig. 3) may be stimulated when the leg is stretched to angles around 180 deg, but no physiological data are available yet for this situation.

Locomotion and micromechanics of hair deflection

Flexion of the tibia-metatarsus joint during locomotion typically leads to a deflection of the joint hairs of both the tibia and of the metatarsus by angles of $\alpha = 30$ deg (Fig. 4). The microtrichs on the hair shafts (Fig. 5) enhance the friction between two interacting hairs of the two leg segments and ensure fixation during hair deflection by their slight interlocking, which is reversed when the joint is extended again.

The torque needed to deflect a joint hair in its mechanically preferred (proprioceptive) direction is well below 1 nNm for angles of $\alpha \leq 30$ deg. From $30 \text{ deg} \leq \alpha \leq 60 \text{ deg}$ the resistance to deflection increases non-linearly. At $\alpha > 60 \text{ deg}$ the torque values rise steeply and reach values of 9 nNm at $\alpha = 70 \text{ deg}$ (Fig. 7). This steep rise is due to the structure of the hair socket. At $\alpha = 60 \text{ deg}$ the hair shaft is already in contact with the socket wall and further deflection leads to its bending, whereas at smaller angles the hair shaft behaves like a stiff rod and rotates around the pivot point inside the hair suspension (Fig. 6A).

Interestingly, the hair deflection angle of $\alpha = 60 \text{ deg}$ coincides with the joint angle of $\beta = 100 \text{ deg}$, which is the upper limit of the biological range of joint flexion during locomotion. The hair socket structures seem to be well adapted to deal with the deflections of the hair shaft actually arising during locomotion.

The slightly softer suspension of the metatarsal hairs compared to the tibia hairs into the proprioceptive direction likely is a result of the lack of the elevated socket

wall at the proprioceptive side (Fig. 6). Therefore, the shafts of the metatarsal hairs get in contact with their socket walls at larger deflection angles than the tibia hairs, which is indicated by the lower values of torque (Fig. 7).

A similar structural arrangement may explain the stiffer hair suspension in the not proprioceptive directions of both the tibia and the metatarsus hairs. In their resting position the hair shafts are closer to the socket walls in the not proprioceptive directions, which leads to contact between these structures at smaller deflection angles, and results in the larger deflection torques and the earlier rise of the curves shown in figure 7.

Although the exponential dependence of the torque T on the hair deflection angle α has not been deeply analyzed, one might argue that the increasing resistance of the suspension and the bending of the hair shaft together are the main parameters determining this mechanical behaviour.

Proprioceptors for the flexion velocity of the joint

The proprioceptive neural response of the joint hair sensilla is limited to the deflections into the proprioceptive direction. No action potentials are generated when the hair returns to its resting position. Therefore, the ventral joint hair sensilla monitor the flexion of the tibia-metatarsus joint during forward locomotion when the joint angles β fall below approximately 150 deg, which is the case in every step of the spider (Fig. 2B). The joint hair sensilla are movement detectors and do not respond to stationary hair deflection. Whereas the velocity of the hair deflection at stepping frequencies as they occur naturally are well resolved by the maximum frequencies of the action potentials during one step, the response saturates at deflection frequencies exceeding 3 Hz (Fig. 8). Nevertheless, the stepping frequency is resolved as well by the bursts of action potentials, which are elicited at the start of the hair deflection every time the joint angle β passes approximately 150 degree during flexion.

The eight walking legs of *Cupiennius* are also used in behavioural contexts other than locomotion. Flexion of the tibia-metatarsus joints also occurs when the spider is manipulating prey, copulating or spinning a cocoon. Most of these movements are slow and well below flexion frequencies of 1 Hz, where the velocity is well resolved by the sensory response. An exception is the quick grabbing of prey where the velocity is in the saturation range.

Comparison with other hair-shaped sensilla of *Cupiennius salei*

Up to date among the many mechanoreceptive hair sensilla of *Cupiennius* the mechanical and physiological properties are known in more detail only for the air flow sensing trichobothria and of the long tactile hair sensilla on the tarsi and metatarsi. In both cases the properties of the hair suspensions are well adapted to their specific sensory functions causing strikingly different movabilities of the hair shaft (Barth, 2004).

The tactile hair sensilla are stimulated by direct contact with solid substrate (Albert et al., 2001). Their mechanical directional characteristics are nearly isotropic. Compared with the joint hair sensilla their socket wall is higher and lacks an “opening” leading to a mechanically preferred direction of hair deflection. The torque of the tactile sensilla resisting their deflection rises exponentially to 1 nNm at a deflection angle of $\alpha \approx 7$ deg to 5 nNm at $\alpha \approx 15$ deg. These torque values are similar to those of the joint hair sensilla when they are deflected into other than their proprioceptive directions. When deflected the hair shaft of the tactile hairs is not only bent when it touches the socket rim of its cuticular socket, but bends inside the socket at even smaller deflections protecting it from breakage (Barth et al. 2004). In the joint hair sensilla bending of the hair shaft during proprioceptive large angle deflections is thought to be minimized by the distance of the hair shaft from the hair socket (Fig. 6).

The restoring constant S of the tactile hairs amounts to 3×10^{-8} Nm rad⁻¹ (Albert et al. 2001). This value is again well in the range of those found for the joint hair sensilla at deflections to other than into the proprioceptive direction (2.04×10^{-9} to 8.02×10^{-8} Nm rad⁻¹). However, it is larger by one to two orders of magnitude than S of the joint hair sensilla when they are deflected in their proprioceptive direction (2.86×10^{-10} to 1.60×10^{-9} Nm rad⁻¹). Compared to the suspension stiffness of the air flow sensing trichobothria, where the S values are as small as 4.30×10^{-12} to 6.2×10^{-11} Nm rad⁻¹ (Barth et al., 1993; McConney et al., 2009), the resistance of the joint hair sensilla even to deflections in the proprioceptive direction is larger by two orders of magnitude.

The mechanical and structural adaptations of the joint hair sensilla facilitate the large angle deflections at every step of the spider during locomotion and minimize mechanical stresses on the sensory structures.

In the trichobothria the physiological deflection threshold angle generating one action potential is in the range of 0.01 deg to 0.1 deg making them excellent sensors for slightest movements of the air. With a threshold angle of 1 deg the tactile hairs are well suited as detectors for rapid touch events. In the joint hair sensilla the threshold angle of about 8 deg is pretty large. It may help to filter out stimuli by movements of the

substrate irrelevant for the sensing of the joint's flexion velocity during the stance phase of the spider walking.

Parallel processing of sensory information from different joint receptors

Besides hair sensilla like those described in the present study there are multiterminal neurons sensing angular position of spider leg joints with dendrites ending beneath the articular membranes (Foelix and Choms, 1979). Among these the receptors at the femur-patella joint of the theraphosid *Eurypelma hentzi* exhibit many tonic units, which respond to changes of the joint angle by altering their stationary impulse frequency (Rathmayer, 1967). Similar findings are reported for the internal proprioceptors at the tibia-metatarsus joint of the meshweb weaver *Amaurobius* (= *Ciniflo*; Mill and Harris, 1977).

In addition to the hair sensilla examined in the present study the tibia-metatarsus joint of *Cupiennius salei* is equipped with four lyriform organs on the tibia responding to articular strains generated during locomotion (Blickhan and Barth, 1985) and two dorsolateral groups of internal joint receptors (Seyfarth and Pflüger, 1984). The axons of their sensory cells go together with those of the joint hair sensilla (Seyfarth and Pflüger, 1984), which makes a parallel processing of the information from the three different proprioceptor types by the central nervous system of the spider very likely.

ACKNOWLEDGEMENTS

CFS gratefully acknowledges the generous support of his family during all the years of his study.

REFERENCES

- Albert, J. T., Friedrich, O. C., Dechant, H.-E. and Barth, F. G. (2001). Arthropod touch reception: spider hair sensilla as rapid touch detectors. *J. Comp. Physiol. A* 187, 303-312.
- Barth, F. G. (2002). A spider's world: senses and behavior. Berlin, Heidelberg, New York: Springer.
- Barth, F. G. (2004). Spider mechanoreceptors. *Curr. Opinion Neurobiol.* 14, 415-422.
- Barth, F. G., Höller, A. (1999). Dynamics of arthropod filiform hairs. V. The response of spider trichobothria to natural stimuli. *Phil. Trans. R. Soc. Lond. B* 354, 183-192.
- Barth, F. G., Wastl, U., Humphrey, J. A. C., Devarakonda, R. (1993). Dynamics of

- arthropod filiform hairs. II. Mechanical properties of spider trichobothria (*Cupiennius salei* Keys.). *Phil. Trans. R. Soc. Lond. B* 340, 445-461.
- Barth, F. G., Németh, S. S., Friedrich, O. C. (2004). Arthropod touch reception: structure and mechanics of the basal part of a tactile hair. *J. Comp. Physiol. A* 190, 523-530.
- Blickhan, R., Barth, F. G. (1985) Strains in the exoskeleton of spiders. *J. Comp. Physiol. A* 157, 115-147.
- Bohnenberger, J., Seyfarth, E.-A., Barth, F. G. (1983) A versatile feedback controller for electro-mechanical stimulation devices. *J. Neurosci. Methods* 9, 335-341.
- Dechant, H.-E. (2001). Mechanical properties and finite element simulation of spider tactile hairs. Dissertation, Vienna University of Technology.
- Eckweiler, W., Hammer, K., Seyfarth, E.-A. (1989). Long, smooth hair sensilla on the spider leg coxa: Sensory physiology, central projection pattern, and proprioceptive function (Arachnida, Araneida). *Zoomorphology* 109, 97-102.
- Eckweiler, W., Seyfarth, E.-A. (1988). Tactile hairs and the adjustment of body height in wandering spiders: behavior, leg reflexes, and afferent projections in the leg ganglia. *J. Comp. Physiol. A* 162, 611-621.
- Foelix, R. F. (1996). *Biology of Spiders*. Oxford, NY: Oxford University Press.
- Foelix, R. F., Choms, A. (1979). Fine structure of a spider joint receptor and associated synapses. *Eur. J. Cell Biol.* 19, 149-159.
- Harris, D. J., Mill, P. J. (1977). Observations on the leg receptors of *Ciniflo* (Araneida: Dictynidae) I. External mechanoreceptors. *J. Comp. Phys.* 119, 37-54.
- Humphrey, J. A. C., Barth, F. G. (2008). Medium flow-sensing hairs: biomechanics and models. In *Insect mechanics and control. Advances in insect physiology* 34 (ed. J. Casas and S. Simpson), pp. 1-80. Amsterdam: Elsevier.
- Keyserling, E. (1877). Über amerikanische Spinnenarten der Unterordnung Citigradae. *Verh. Zool.-Bot. Ges. Wien* 26, 609-708.
- McConney, M. E., Schaber, C. F., Julian, M. D., Humphrey, J. A. C., Barth, F. G., Tsukruk, V. V. (2009). Surface force spectroscopic point load measurements and viscoelastic modelling of the micromechanical properties of air flow sensitive hairs of a spider (*Cupiennius salei*). *J. R. Soc. Interface* 4, 681-694
- Mill, P. J., Harris, D. J. (1977). Observations on the leg receptors of *Ciniflo* (Araneida: Dictynidae) III. Proprioceptors. *J. Comp. Physiol.* 119, 63-72.
- Rathmayer, W. (1967). Elektrophysiologische Untersuchungen an Proprioceptoren im Bein einer Vogelspinne (*Eurypelma hentzi* Chamb.). *Z. vergl. Physiol.* 54, 438-454.
- Schmid, A. (1998). Different functions of different eye types in the spider *Cupiennius salei*. *J. Exp. Biol.* 201, 221-225.
- Seyfarth, E.-A. (1985). Spider proprioception: receptors, reflexes and control of locomotion. In *Neurobiology of arachnids* (ed. F. G. Barth). pp. 230-248. New York:

Springer.

Seyfarth, E.-A., Pflüger, H. J. (1984). Proprioceptor distribution and control of a muscle reflex in the tibia of spider legs. *J. Neurobiol.* 15, 365-374.

Seyfarth, E.-A., Gnatzy, W., Hammer, K. (1990). Coxal hair plates in spiders: physiology, fine structure, and specific central projections. *J Comp Physiol A* 166, 633–642.

Speck-Hergenröder, J., Barth, F. G. (1988). Vibration sensitive hairs on the spider leg. *Experientia (Basel)* 44, 13-14.

Viscoelastic nanoscale properties of cuticle contribute to the high-pass properties of spider vibration receptor (*Cupiennius salei* Keys.)

Michael E. McConney^{1,*}, Clemens F. Schaber^{2,*}, Michael D. Julian³,
Friedrich G. Barth^{2,**}, Vladimir V. Tsukruk^{1,**}

¹ School of Materials Science & Engineering, Georgia Institute of Technology, Atlanta, GA 30332, USA

² Department of Neurobiology and Cognition Research, University of Vienna, Althanstraße 14, 1090
Wien, Austria

³ Department of Materials Science and Engineering, Iowa State University, Ames, IA 50011, USA

* These authors contributed equally to this work.

** Authors for correspondence (friedrich.g.barth@univie.ac.at;
vladimir@mse.gatech.edu).

Author contributions

CFS and MDJ designed the experiments, CFS made the biological preparations, MDJ and CFS performed the measurements, MDJ, MEM, and CFS analyzed the data, CFS, MDJ, MEM, FGB, and VVT wrote the paper, and CFS managed the contributions of all authors to the manuscript.

The following pages contain the final version published online April 3, 2007 and in print December 22, 2007.

Citation:

Journal of the Royal Society Interface 4:1135–1143

doi:10.1098/rsif.2007.1000

JOURNAL
— OF —
THE ROYAL
SOCIETY
Interface

ISSN 1742-5689

volume 4

number 17

pages 999–1183



Cross-disciplinary Sciences



Royal Society **Publishing**
Informing the science
of the future

22 December 2007

Cover image: An adult female spider from Costa Rica. Its leg span measures approximately 10 cm and its scientific name is *Cupiennius getazi* (Ctenidae). Spiders of this genus have become valuable and important animals in various fields of biological research such as sensory biology, neuroethology, toxicology, genetics and development, and others. (Photographer: Friedrich G. Barth)

Viscoelastic nanoscale properties of cuticle contribute to the high-pass properties of spider vibration receptor (*Cupiennius salei* Keys)

Michael E. McConney^{1,†}, Clemens F. Schaber^{2,†}, Michael D. Julian³,
Friedrich G. Barth^{2,*} and Vladimir V. Tsukruk^{1,*}

¹*School of Materials Science and Engineering, Georgia Institute of Technology, Atlanta, GA 30332, USA*

²*Department of Neurobiology and Cognition Research, University of Vienna, Althanstraße 14, 1090 Wien, Austria*

³*Department of Materials Science and Engineering, Iowa State University, Ames, IA 50011, USA*

Atomic force microscopy (AFM) and surface force spectroscopy were applied in live spiders to their joint pad material located distal of the metatarsal lyriform organs, which are highly sensitive vibration sensors. The surface topography of the material is sufficiently smooth to probe the local nanomechanical properties with nanometre elastic deflections. Nanoscale loads were applied in the proximad direction on the distal joint region simulating the natural stimulus situation. The force curves obtained indicate the presence of a soft, liquid-like epicuticular layer (20–40 nm thick) above the pad material, which has much higher stiffness. The Young modulus of the pad material is close to 15 MPa at low frequencies, but increases rapidly with increasing frequencies approximately above 30 Hz to approximately 70 MPa at 112 Hz. The adhesive forces drop sharply by about 40% in the same frequency range. The strong frequency dependence of the elastic modulus indicates the viscoelastic nature of the pad material, its glass transition temperature being close to room temperature (25 ± 2 °C) and, therefore, to its maximized energy absorption from low-frequency mechanical stimuli. These viscoelastic properties of the cuticular pad are suggested to be at least partly responsible for the high-pass characteristics of the vibration sensor's physiological properties demonstrated earlier.

Keywords: spider; vibration sensor; metatarsal lyriform organ; force spectroscopy; viscoelastic materials; high-pass characteristics

1. INTRODUCTION

Vibrations play an important role in the lives of spiders, which use them for prey detection, communication during courtship and other behaviours (Rovner & Barth 1981; Barth 1985). The key vibration receptor organ of spiders is the metatarsal organ. It represents a compound or lyriform slit sense organ and belongs to a class of sensory receptors, which are embedded in the spider's exoskeleton and measure the minute strains occurring in it due to muscle activity, haemolymph pressure, vibrations and other types of mechanical stimuli (Barth 2002). The threshold vibrations necessary to elicit a nervous response of the sensory cells supplying individual slits in this organ are known to exhibit pronounced high-pass characteristics, with low

sensitivity for frequencies approximately below 30 Hz and steeply increasing threshold sensitivity at higher frequencies (Barth & Geethabali 1982). Other than this change in sensitivity, the organs are not tuned to specific frequencies within the biologically relevant range. The dramatic change in sensitivity was found to be physiologically important for the spider, because it provides filtering of biologically irrelevant background noise, and at the same time preserves much higher sensitivity to biologically relevant vibrations like vibratory courtship signals and vibrations produced by prey motion (Barth 2002).

Located at the distal end of the metatarsus, just distal to the metatarsal lyriform organ, is a pad cushioning the joint between the tarsus and metatarsus (figure 1*a–d*). This pad is crescent shaped and its cuticle is approximately 100 µm thick. It is believed that this pad might be a mechanical source of the physiological high-pass filtering. Substrate vibrations naturally received and transmitted by the tarsus are detected

*Authors for correspondence (friedrich.g.barth@univie.ac.at; vladimir@mse.gatech.edu).

[†]These authors contributed equally to this work.

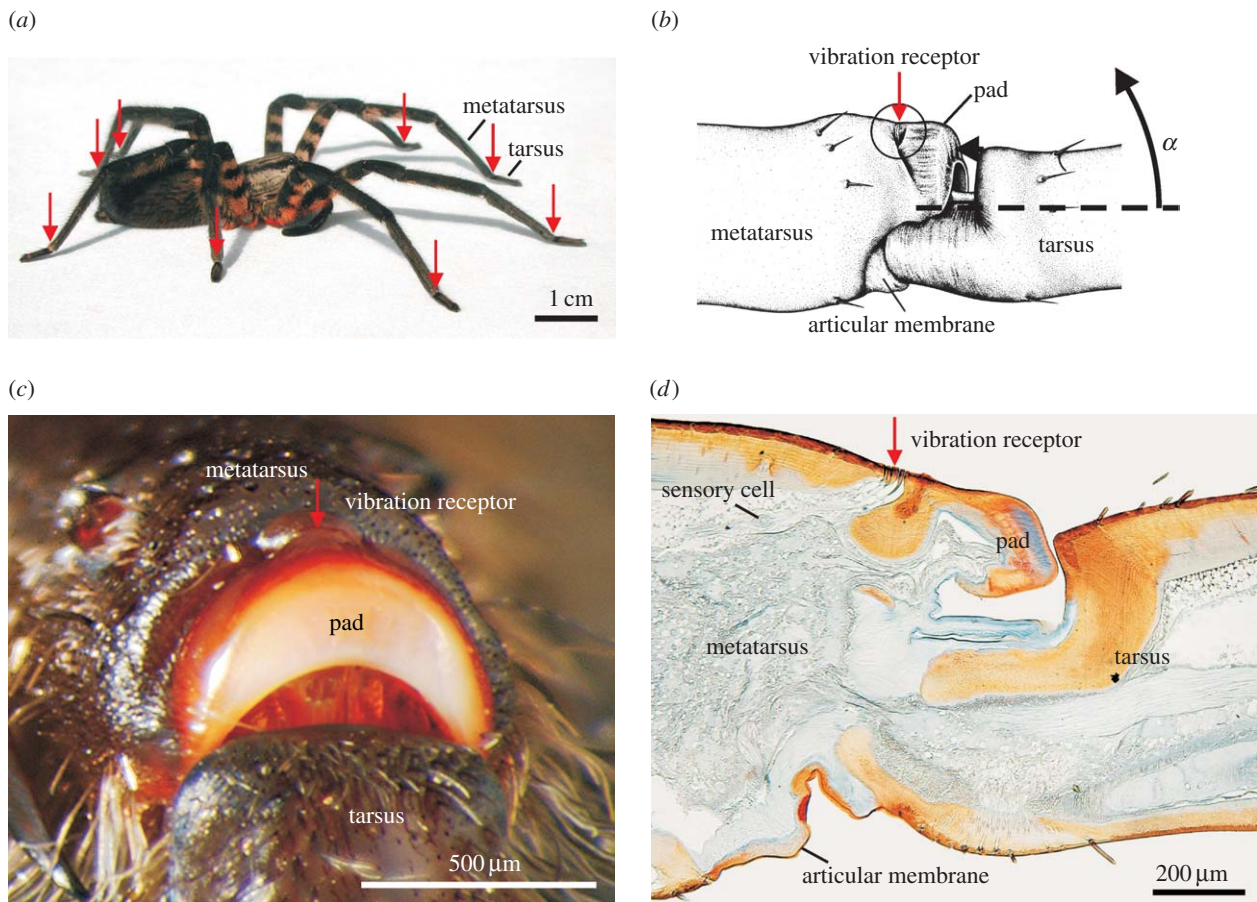


Figure 1. (a) Adult female wandering spider, *Cupiennius salei*. The damping pad examined and the vibration receptor organs are located on the metatarsus at the joint with the tarsus (red arrows). (b) Deflection of tarsus by an angle α exceeding 25° leads to pressure on the pad in front of the vibration receptor. (c) Vibration receptive lyriform organ located between the pad and the stiff cuticle of the metatarsus. (d) Sagittal section of the joint, Mallory stained. The pad consists of layers of different types of cuticle; the blue colour indicates soft, moderately sclerotized cuticle. Slits of the vibration receptor are innervated by bipolar sensory cells.

by the slits of the metatarsal lyriform organ when the proximal end of the tarsus pushes against the distal end of the metatarsus, which in turn compresses the slits (figure 1b). Therefore, this pad seems ideally placed to mechanically filter the stimuli to the lyriform organ through frequency-dependent damping of the mechanical vibrations. The present study is undertaken to support or reject this hypothesis.

The low forces applied in atomic force microscopy (AFM) and surface force spectroscopy (SFS) allow very soft materials to be probed with nanoscale resolution, while avoiding plastic deformation of the material (Chen & Vlassak 2001; Kovalev *et al.* 2004). There have been several previous studies investigating viscoelastic properties of polymeric and biological materials using AFM (Tsui *et al.* 2000; Bliznyuk *et al.* 2002; Kaliappan & Capella 2005, Chaudhuri *et al.* 2007). There are several nanoindentation studies of the mechanics of insect cuticle on the micrometre scale with forces in the millinewton range (Enders *et al.* 2004; Barbakadze *et al.* 2006). With AFM, the indentation depths are of the order of tens of nanometres under nanonewton forces unlike in conventional microindentation with micrometre indentation depths under micronewton forces. This allows limiting

the indentation to the selected surface areas of the material of interest without contributions from surrounding structures or materials. In addition, the small size of the AFM probes (nanometres for regular tips and micrometres for colloidal probes) defines small contact areas (diameters of the order of a fraction of a nanometre or a micrometre) and allows high spatial resolution when probing the material properties across the pad.

2. MATERIALS AND METHODS

Live adult females of *Cupiennius salei* (Ctenidae), which is a large (leg span approx. 10 cm) Central American wandering spider (Barth 2002), were immobilized on a solid substrate and fixed to the stage below the scanning probe. The tarsus of an individual leg was then deflected away from the metatarsus in order to expose the joint pad for the measurements. AFM topographical data and force–distance curves (including SFS) were obtained with a Dimension 3000 microscope (Digital Instruments, Inc.). The AFM images were obtained using established procedures of light-tapping mode scans in air with scan rates below 2 Hz and an overall resolution of 512×512 pixels for

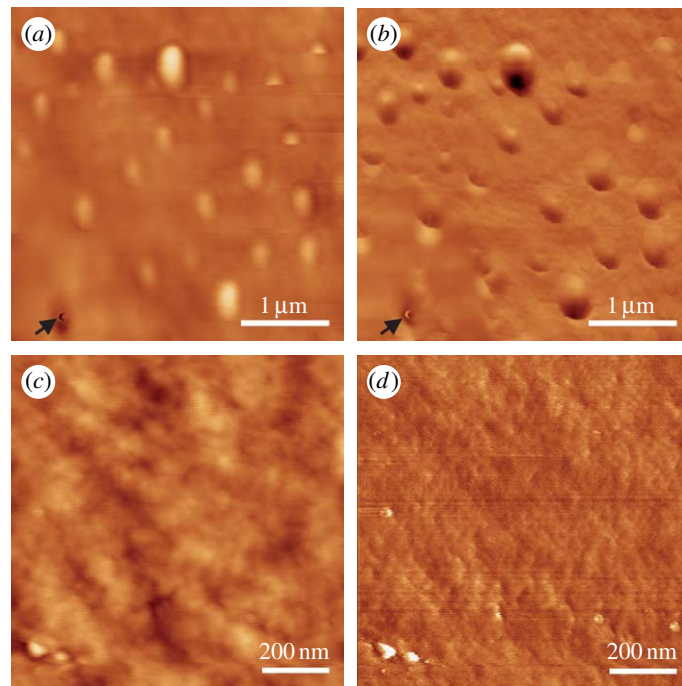


Figure 2. (a) AFM height image of the pad surface with 100 nm height range. (b) Phase image of the same surface area with 60° phase range. The dome-shaped structures are droplets of epicuticular substances, which are secreted through openings of pore canals. The arrows point to an individual pore canal opening. (c) Height image of the pad material at high magnification, 10 nm height range and (d) phase image of the same surface area with 30° phase range.

scans ranging from 1×1 to $30 \times 30 \mu\text{m}$ (Tsukruk & Reneker 1995; Tsukruk 1997). For these scans, standard silicon tips (MikroMasch, NSC11) were used.

The viscoelastic properties of the pad material were probed by acquiring both force–distance curves and force–volume maps using $5 \mu\text{m}$ spherical borosilicate microsphere probes (Novascan) to reduce local pressure in the contact area. All loads were applied in the proximad direction (similar to natural stimulation) to the distal joint region with the AFM tips approaching and retracting from the pad surface at different velocities. Spring constants were chosen between 1 and 3.6 N m^{-1} (Tsukruk *et al.* 2001). The cantilevers were calibrated applying the accepted spring on spring technique and using a manufacturer calibrated reference tip (MikroMasch) with a spring constant of 4.5 N m^{-1} (Gibson *et al.* 1996; Torii *et al.* 1996).

Force–distance data were collected in air at ambient temperature and humidity in force–volume mode, which included consecutive probing of selected surface areas (16×16 points, number of force–distance curves = 256). In this way, multiple force–distance curves were obtained at each surface location and different deflection thresholds studied in order to monitor any changes in the material properties due to plastic deformation by the following AFM scans of the surface area probed. No irreversible changes in the force curve shape were observed during the scans and no indentation marks have been observed after these probedings, thus confirming the non-damaging character of our measurements. Force–distance curves were then taken at three to five locations on each joint pad and the data averaged over these locations and thus for several hundred indentations. The frequencies chosen for

probing elastic responses (0.1–112 Hz) were limited by the sampling rates of the AFM scanner and its resonant frequencies. However, they cover a significant part of the biologically relevant range, including that of the courtship vibrations (see §3.4; Barth 2002). The pad penetration amplitudes were limited to 30 nm, which should not lead to any plastic deformation when considering the large contact area and the nominal spring constants used in this study. We checked for the presence of indentation marks as indicators of plastic deformation after AFM probing and found none. The temperature during experiments varied between 22 and 24°C only. It was accounted for in the data analysis (uncertainties in the calculated glass transition temperature).

Force–volume analysis was employed according to the established procedures and the measurements analysed with the MMANALYSIS software developed by Tsukruk & Gorbunov (2001, 2002). The photodiode sensitivity was measured by pressing the AFM tip against a silicon wafer. The positive deflection of the cantilever seen in the force–distance curves was then converted to indentation depth (penetration) versus loading force (loading curves) using previously described approaches, which consider piezo-element displacement versus tip deflection (Chizhik *et al.* 1998; Tsukruk *et al.* 1998). The data were then analysed for surface stiffness by linear fitting of the slopes. The elastic modulus was calculated from this data by fitting the loading curves according to the Hertzian contact mechanic model, which describes the interactions between the tip and the sample under the assumption of elastic deformation, small contact areas and negligible adhesive forces (Sviridenok *et al.* 1990).

Alternatively, the model of Johnson, Kendall and Roberts (JKR model; Johnson *et al.* 1971), which considers adhesive properties, and Sneddon's model (Sneddon 1965), which considers different tip shapes and the contact areas, were applied to derive the elastic modulus values. However, the results obtained with different models were close to each other and for simplicity we used the results obtained with the Hertzian model. The adhesive forces were determined from force–distance curves at the pull-off point.

Inherently, our force–distance measurements reflect the properties of the topmost layers of the pad structure examined. It is these layers to which we attribute the mechanical filtering described in the present paper. It should be noted that during natural stimulation the forces are introduced basically in the same way.

3. RESULTS AND DISCUSSION

3.1. Surface topography

AFM topographical images confirmed that the surface of the studied pad was consistently smooth with small bumps that are generally uniform and have a diameter of 200–400 nm and a height of 10–30 nm. There are several larger surface bumps as well (figure 2*a,b*). The phase image shows the same contrast level for both the surface and the surface bumps, implying that the bumps have similar composition (Leclere *et al.* 2000). The bumps are located above the openings of the pore canals, through which the topmost lipid layers of the epicuticle are secreted. Their distribution matches with that of the pore canals shown in previous transmission electron microscopy studies of the cuticle of *C. salei* (Barth 1969). The mechanical tests were performed so that the tip contact area would include these surface features, because they are included (or the substances smeared in the contact area) as well when the spider's tarsus contacts the pad under natural conditions.

The concurrent high-resolution phase image clearly shows a fine texture of globular aggregates with lateral dimensions below 100 nm (figure 2*c,d*). The root mean square (r.m.s.) micro roughness within a $1 \times 1 \mu\text{m}$ surface area was calculated to be very low at 0.8 nm. This value is on a par with molecularly smooth surfaces with local variations not exceeding two diameters of molecular backbones and very common for soft, amorphous polymeric materials with uniform chemical composition (Tsukruk 1997).

3.2. Force–distance curves

Figure 3 shows typical force–distance curves obtained for the pad material and the same tip probe on a silicon substrate used as a reference surface. The force–distance curve taken for the silicon surface was used to calibrate the sensitivity of the AFM measurements. This curve shows a very linear shape in the region of direct contact between the tip and the surface. A relatively high adhesion (high pull-off forces) is caused by strong capillary interactions between the hydrophilic AFM tip and the hydrophilic substrate under conditions of ambient humidity.

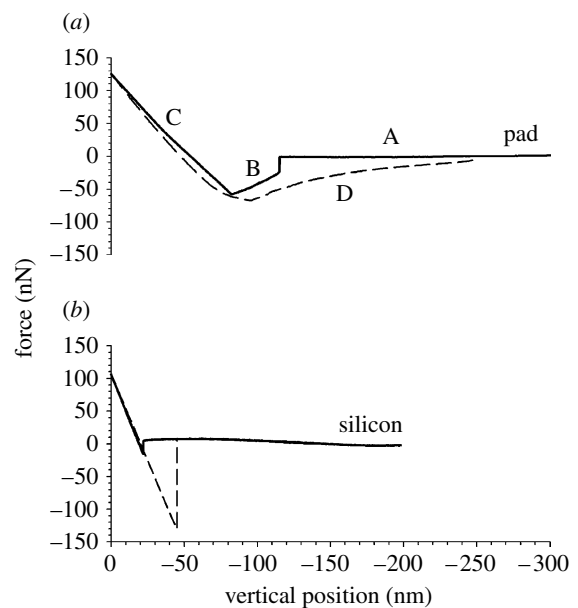


Figure 3. Characteristic force–distance curves obtained for (a) the pad material and (b) the silicon used for sensitivity calibrations. The solid lines represent data acquired while the tip was approaching the surface and have to be read from right to left according to convention. The dashed lines represent data acquired while the tip was retracting from the surface and have to be read from left to right, again according to convention. Therefore, the start (and end) region is at the right end of the curve, whereas its left end marks the point where the probe tip changes direction. Region A, approaching the sample; region B, contact with the sample; region C, increasing force applied to the sample; region D, adhesive forces between the pad and the tip.

Unlike in the case of the substrate force–distance data for the stiff and hydrophilic silicon, a sharp jump-in event with an extended area of negative tip deflection was consistently observed for the compliant pad surface (region B; figure 3). Direct mechanical contact was followed by a positive deflection (region C) and a broad pull-off region with lower forces (region D). At region A of the curve, the probe is approaching the surface and any attractive forces between the surface and the tip are negligible when compared with the cantilever stiffness thus generating a zero-deflection response. In region B, we see the expected quick jump into contact, followed by a less expected shallow deflection of the cantilever towards the surface, an unusual phenomenon for clean elastic surfaces. This behaviour is indicative of the tip passing through an extremely compliant viscous material that is not slowing its deflection towards the surface, but also generates attractive forces caused by the wetting of the glass probe with the topmost viscous layer (capillary phenomenon). Moreover, its presence is shown on the curve for probe retraction, where instead of a sharp pull-off event, a gradual decrease of adhesive forces is observed, which corresponds to the typical capillary behaviour (region D).

As the AFM probe is withdrawn from the surface, the attractive forces between the probe and the indented surface are overcome by the stiffness of the cantilever and the probe begins to return to its zero-deflection resting point with a gentle deflection finally

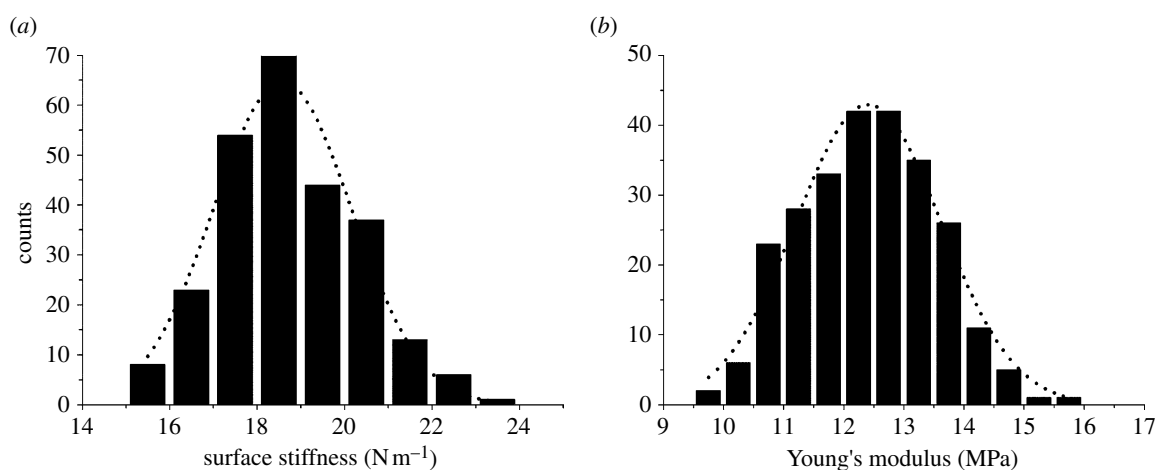


Figure 4. Typical distribution of values for surface stiffness (a) and Young's modulus (b) for the same pad at 13.9 Hz loading frequency derived from force–volume data taken in a 16×16 array of $1 \mu\text{m} \times 1 \mu\text{m}$ ($N=1$, $n=256$).

followed by a small sharp ‘snap from’ region (figure 3). Again, this indicates that the tip is passing through a viscous material and the long-range capillary forces are involved causing gradual thinning of the viscous meniscus before final rupture. The thickness of this surface viscous layer can be estimated from the tip deflection to be within 20–40 nm for different locations and probe frequencies. The appearance of such a viscous surface layer can be directly related to the presence of the oriented lipid layers, which lie above the cuticulin layer and the dense layer of the epicuticle of *C. salei* (Barth 1969). Our data suggest that this topmost viscous layer seen in the force curves is directly related to the bumps seen in figure 1a, which could be related to lipid droplets. The bump height is approximately the same as the thickness of the layer indicated by the force curves. Furthermore, there is nothing in region C of the force–distance curves which would indicate that the change in the contact area of the tip with its penetration into the pad is abnormal. In other words, the loading region of the force–distance curves indicates a smooth and flat surface thus pointing to the squeezing of bumps from the contact area during compression. The unexpected behaviour in region B of the force–distance curve, on the other hand, can be fully explained by the presence of the surface bumps.

At the positive slope of the force–distance curves (region C of figure 3, which has to be read from right to left), the tip has made contact with a stiffer elastic material with a measurable resistance to compression. The tip is deflected upwards as the probe pushes into the surface. This is the deformation region of the force curve, which reflects both tip deflection and surface deformation and can be used to analyse the elastic behaviour of the material probed.

3.3. Young's modulus

As mentioned earlier, the force curves indicated that there was significant wetting and adhesion between the tip and pad surface. In such a situation, the Hertzian approximation would tend to underestimate the contact radius, thereby leading to a slightly higher elastic modulus than is the case (usually between 5 and 10%

for elastic materials with modest adhesion; Chizhik *et al.* 1998). Generally, a better choice to calculate the elastic modulus of such a material would be the JKR model, which assumes high adhesion (Johnson 1985). As will be discussed later, the adhesion decreased significantly with increased frequencies. This means that when using the JKR model, the change in increase in modulus due to material properties would be slightly exaggerated, whereas using the Hertzian model will slightly underestimate the change in modulus with frequency. Although there was significant adhesion with several of the lower frequency measurements, using the JKR method leads to a more conservative estimation of the material's mechanical filtering abilities. Our estimation showed that for larger elastic deformations, the results obtained from both models (as well as from Sneddon's model) converge, the difference being insignificant for the purpose of this study. Thus, for the sake of clarity and consistency, we applied the Hertzian model to analyse all our data. To this end, we analysed the shapes of the loading curves and fitted them correspondingly for penetrations not usually exceeding 20–30 nm for loading forces below 200 nN. Thirty nanometres of displacement of the pad's dorsal edge corresponds to a change of the angle between metatarsus and tarsus of the spider leg by 0.007° and a displacement of the tarsus tip by about $0.4 \mu\text{m}$ (Gingl *et al.* 2006). This value represents the sensory threshold of individual slits of the metatarsal organ for substrate vibrations at 70 Hz (slit 6) up to 170 Hz (slit 7; Barth & Geethabali 1982).

Figure 4a shows a representative histogram of the surface stiffness data obtained at 13.9 Hz and calculated as the overall slope of the force–distance curve in the direct physical contact regime in linear approximation. The surface stiffness of the pad material at moderate probing frequencies of 13.9 Hz was about 18 N m^{-1} with a distribution in between the range of rubbery and glassy macromolecules (LeMieux *et al.* 2005). The distribution of values of the elastic modulus received for $16 \times 16 = 256$ overlapping locations of a $1 \mu\text{m}^2$ area for each spider was very uniform (figure 4b). The loading curves (penetration versus loading force) used for fitting analysis were smooth for all surface

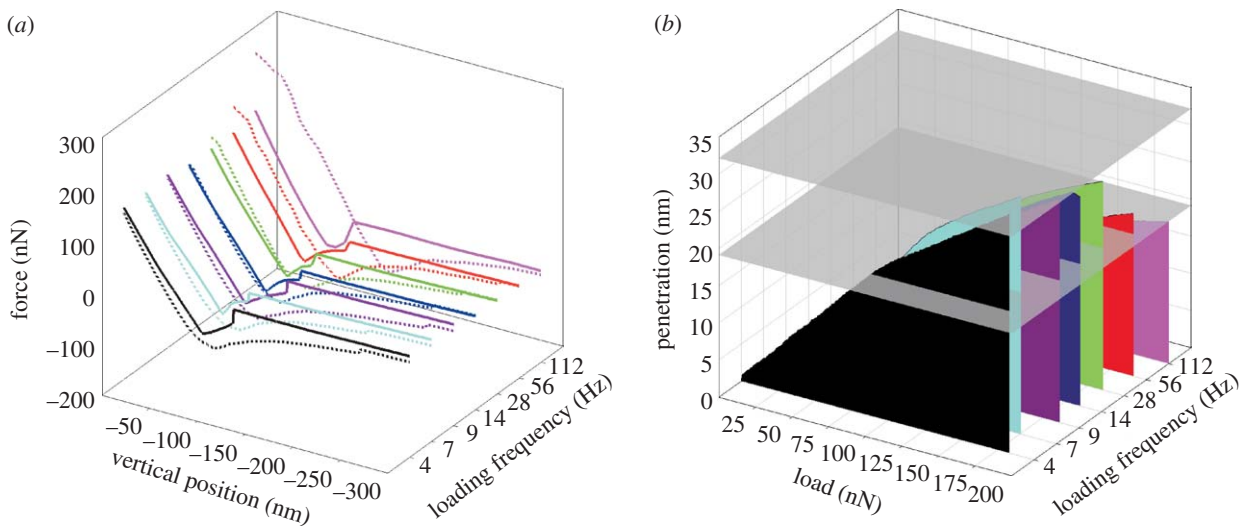


Figure 5. (a) Force–distance curves at different probing frequencies; solid lines, approach data; dotted lines, data for the retraction of the probe; the hystereses seen are discussed in the text. (b) Loading curves obtained at different frequencies for the pad surface at the same location. The horizontally oriented grey planes are drawn at the maximum penetration at 4 Hz loading frequency and the maximum penetration at 112 Hz loading frequency, respectively.

locations with indentation depths of up to 30–35 nm for loading forces below 200 nN. The value of the elastic modulus for these indentation depths is within a range common for compliant elastic macromolecular materials with low cross-linking density and above the glass transition temperature.¹ The relatively narrow distribution of the surface stiffness (s.d. within $\pm 5\%$ in most cases) indicated a very uniform elastic response of the pad materials under the probed conditions and with the contact area between the probe and the surface below $0.2 \mu\text{m}^2$.

3.4. Frequency dependence

Finally, we analysed the mechanical response of the pad surface at different probing frequencies ranging from 0.1 to 112 Hz (the frequency being limited by thermal drifts and piezo-element resonances), corresponding to a tip velocity from very slow (50 nm s^{-1}) to modest ($25 \mu\text{m s}^{-1}$). Figure 5a shows the characteristic force–distance curves obtained at different frequencies and their corresponding loading curves (figure 5b). At frequencies below 30 Hz, the force curves obtained have the characteristic shape discussed above with little variance. However, at higher frequencies, this shape changes significantly due to the change of the overall slope. The hysteresis between the approach and retraction curves observed at relatively high probing frequencies is a common AFM artefact. However, it does not significantly affect the measured values derived from the slope of the curve received during intimate contact. Examination of this hysteresis on silicon samples showed that the slope of the force–distance curves changed by less than 5% for this

frequency range. This is insignificant when compared with the change of the slope for the pad material itself we observed here. Therefore, the frequency-dependent elastic behaviour is a feature typical of the biological material examined.

Force–distance curves measured at frequencies lower than 10 Hz consistently resulted in values of Young's modulus between 10 and 20 MPa for the pad surfaces of five spiders probed at various locations (figure 6a). There was some variance in this value between different specimens; however, the modulus at each spot on the pad varied insignificantly between 0.1 and 10 Hz and all values calculated fell within $15 \pm 5 \text{ MPa}$ for all varieties of conditions tested. However, above 10 Hz, the value for Young's modulus gradually increased up to 70 MPa for the highest frequencies with a dramatic increase occurring at approximately 30 Hz and higher. Interestingly, the adhesive forces which were very high at low frequency, dropped significantly by approximately 40% in the same frequency range. This confirms the trend towards a more apparently resistant surface, which effectively decreases the contribution of the tip wetting for short contact times (figure 6c).

The frequency dependence observed here is attributed to the viscoelastic behaviour of the pad material caused by the time-dependent relaxation of the macromolecular materials in the vicinity of the glass transition (Sperling 1997). In fact, very similar frequency dependencies have been observed for elastomeric materials and were related to the lowered glass transition temperature of the surface caused by the presence of the swollen topmost surface layer (Tsukruk *et al.* 2000). Applying a similar approach allows one to use the time–temperature superposition principle by applying the Williams–Landel–Ferry (WLF) equation (after Sperling 2006) for the evaluation of the glass transition temperature of the pad material. The modulus data at various frequencies were fit using the universal WLF constants C_1 and C_2 as 17.44 and 51.6 as is common for amorphous macromolecular materials

¹Viscoelastic materials simultaneously exhibit a combination of elastic and viscous behaviour. In polymers the transition that separates the glassy state from the viscous state is known as the glass–rubber transition. In the range of this glass transition the stiffness of a polymer typically drops by a factor of about 1000 with a rise of temperature of 20 to 30°C (Sperling 2006).

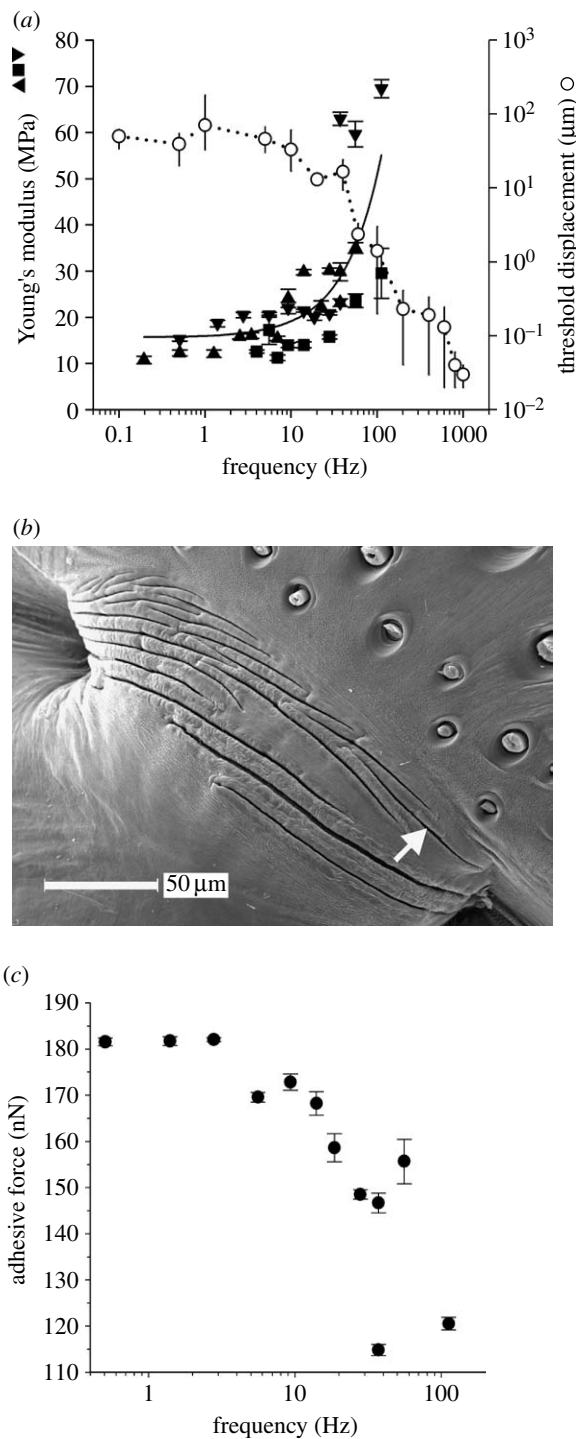


Figure 6. (a) Frequency dependence of Young's modulus (filled symbols) and of sensory thresholds of slit 7 of the metatarsal lyriform organ (open circles). The different datasets of Young's modulus are from three locations on joint pads of two spiders. Each data point represents 10–15 force–distance curves. Sensory threshold curve adapted from Barth & Geethabali (1982; $n=16$). (b) SEM micrograph of the metatarsal organ of *C. salei* (picture by R. Müllan). The arrow points to slit 7. (c) Adhesive forces measured at different loading frequencies at one location of a joint pad.

and applied here to the cuticular matrix. By using this approach, we estimated the glass transition temperature of the joint pad material to be $25 \pm 2^\circ\text{C}$, which is very close to the room temperature prevailing during our experiments ($22\text{--}24^\circ\text{C}$).

Thus, the change of the elastic modulus with shorter contact times follows common trends well known for viscoelastic macromolecular materials in the vicinity of the glass transition temperature (Sperling 1997). Upon elastic deformation of any material, some of the energy is stored and some of it is lost in the form of heat, or essentially absorbed. The storage modulus is a measure of the amount of energy stored upon deformation, whereas the loss modulus is a measure of the amount of energy released as heat upon deformation. The ratio of energy absorbed to energy stored reaches a maximum right in the vicinity of the glass transition region, which constitutes a viscoelastic damping phenomenon. When the temperature of a material goes below the glass transition temperature or the deformation rate becomes faster than the polymer's relaxation time, the elastic modulus dramatically increases. Therefore, materials with a glass transition temperature near the intended operating conditions, such as the spider's pad in the vicinity of room temperature, make very good energy absorbing materials with maximum energy dissipation at low frequencies (Sperling 1997).

Importantly, the frequency dependence of the elastic response observed here for the pad material is opposite to the frequency dependence of the sensory threshold reported previously for the metatarsal lyriform organ (Barth & Geethabali 1982; figure 6*a,b*). The deflection of the tarsus needed to elicit a nervous response (action potential) measured approximately between 100 and 10 μm at vibration frequencies up to 40 Hz and dropped steeply to values as low as 0.01–0.001 μm at 1 kHz (Barth 1998). The frequencies of wind-induced vibrations of the leaves of the dwelling plants of *C. salei* are significantly lower than 30 Hz. On banana plants and bromeliads, they do not exceed 7 Hz (Barth et al. 1988*a*). However, for higher frequencies of mechanical perturbations, such as prey-generated substrate vibrations or the vibratory signals of a sexual partner, the viscoelastic pad material partially loses its viscous nature effectively becoming stiffer, and thus transmitting external mechanical stimuli with higher efficiency (low dissipation). Vibrations of the dwelling plants of *C. salei* induced by prey, like a crawling cockroach, have a broad frequency spectrum containing frequencies higher than 200 Hz. Male abdominal courtship vibrations peak at approximately 75 Hz, whereas male drumming and scratching on the leaf results in vibrations of 250 Hz and higher. The dominant frequency of the female courtship vibration answering male signals is about 30 Hz (Barth 1998, 2002).

The average daily temperatures in the habitats of *C. salei* in Central America are around 20°C , with frequent daily maxima above 30°C all the year round (Barth et al. 1988*b*). During the day, when the ambient temperature is high, the spiders rest hidden in their retreats on the dwelling plants. Their hunting activity starts after sunset when the temperature is moderate, but well in the region of the glass transition temperature of the metatarsal pad. Owing to the lowered temperature at night the pad should be stiffer, and the metatarsal vibration receptive organ more sensitive to vibrations than during the rest period of the spider.

The mechanical filter properties described in this study will be useful by keeping the low frequencies (typical of biologically irrelevant stimuli) out of the nervous system, thereby enhancing the signal-to-noise ratio as was already argued in regard to the electrophysiologically determined threshold curves (review in Barth 2002). The mechanical filter does not exclude additional physiological filters whose presence follows from the transfer functions determined for the cells of other slit sense organs (Bohnenberger 1981; French *et al.* 2001).

4. CONCLUSIONS

Spiders strongly rely on substrate vibrations for the guidance of prey capture, predator avoidance and mating behaviour. These signals must be separated from the environmental noise. The most important vibration receptor organ in spiders is the metatarsal lyriform organ, which is relatively insensitive at frequencies below 30 Hz, but increasingly sensitive at higher frequencies. When deflected by vibrations, the tarsus first transmits the stimulus to a soft material pad, which in turn passes it on to the metatarsal vibration sensor immediately behind it. The pad material was found to be highly viscoelastic with its highest compliance and high energy dissipation at frequencies below 30 Hz. At frequencies above 30 Hz, the pad material quickly becomes stiffer, which allows better transmission of vibrations to the metatarsal lyriform organ. The temperature of the pad material was found to be near glass transition, where the energy absorption is maximized. However, if the deformation time is relatively short, the vibration frequency is relatively high, or the temperature is well below the glass transition temperature, the pad material becomes stiffer. Under these conditions, the effective Young's modulus will increase and mechanical losses will go down tremendously. These properties of the pad material make it an ideal high-pass filter, which filters out environmental noise and makes the frequency range of vibrations relevant for the spider most effective.

This work was supported by a grant from the US Defense Advanced Research Projects Agency (DARPA) project BioSenSE FA9550-05-1-0459 to F.G.B. and V.V.T., and by project P16348 of the Austrian Science Foundation (FWF) to F.G.B.

REFERENCES

- Barbakadze, N., Enders, S., Gorb, S. & Arzt, E. 2006 Local mechanical properties of the head articulation cuticle in the beetle *Pachnoda marginata* (Coleoptera, Scarabaeidae). *J. Exp. Biol.* **209**, 722–730. (doi:10.1242/jeb.02065)
- Barth, F. G. 1969 Die Feinstruktur des Spinneninteguments I. Die Cuticula des Laufbeins adulter häutungsferner Tiere (*Cupiennius salei* Keys). *Z. Zellforsch.* **97**, 137–159. (doi:10.1007/BF00331877)
- Barth, F. G. 1985 Neuroethology of the spider vibration sense. In *Neurobiology of arachnids* (ed. F. G. Barth), pp. 203–229. Berlin, Germany; New York, NY; Tokyo, Japan: Springer.
- Barth, F. G. 1998 The vibrational sense of spiders. In *Comparative hearing: insects* (eds R. R. Hoy, A. N. Popper & R. R. Fay), pp. 228–278. New York, NY: Springer.
- Barth, F. G. 2002 *A Spider's world: senses and behavior*. Berlin, Germany; New York, NY: Springer.
- Barth, F. G. & Geethabali 1982 Spider vibration receptors: threshold curves of individual slits in the metatarsal lyriform organ. *J. Comp. Physiol. A* **148**, 175–185. (doi:10.1007/BF00619124)
- Barth, F. G., Bleckmann, H., Bohnenberger, J. & Seyfarth, E.-A. 1988a Spiders of the genus *Cupiennius* Simon 1891 (Araneae, Ctenidae) II. On the vibratory environment of a wandering spider. *Oecologia* **77**, 194–201. (doi:10.1007/BF00379186)
- Barth, F. G., Seyfarth, E.-A., Bleckmann, H. & Schüch, W. 1988b Spiders of the genus *Cupiennius* Simon 1891 (Araneae, Ctenidae) I. Range distribution, dwelling plants, and climatic characteristics of the habitats. *Oecologia* **77**, 187–193. (doi:10.1007/BF00379185)
- Bliznyuk, V. N., Assender, H. E. & Briggs, G. A. D. 2002 Surface glass transition temperature of amorphous polymers: a new insight with SFM. *Macromolecules* **35**, 6613–6622. (doi:10.1021/ma011326a)
- Bohnenberger, J. 1981 Matched transfer characteristics of single units in a compound slit sense organ. *J. Comp. Physiol. A* **142**, 391–402. (doi:10.1007/BF00605451)
- Chaudhuri, O., Parekh, S. H. & Fletcher, D. A. 2007 Reversible stress softening of actin networks. *Nature* **445**, 295–298. (doi:10.1038/nature05459)
- Chen, X. & Vlassak, J. J. 2001 Numerical study on the measurement of thin film mechanical properties by means of nanoindentation. *J. Mater. Res.* **16**, 2974–2982.
- Chizhik, S. A., Huang, Z., Gorbunov, V. V., Myshkin, N. K. & Tsukruk, V. V. 1998 Micromechanical properties of elastic polymeric materials as probed by scanning force microscopy. *Langmuir* **14**, 2606–2609. (doi:10.1021/la980042p)
- Enders, S., Barbakadze, N., Gorb, S. N. & Arzt, E. 2004 Exploring biological surfaces by nanoindentation. *J. Mater. Res.* **19**, 880–887. (doi:10.1557/jmr.2004.0114)
- French, A. S., Höger, U., Sekizawa, S. & Torkkeli, P. H. 2001 Frequency response functions and information capacities of paired spider mechanoreceptor neurons. *Biol. Cybern.* **85**, 293–300. (doi:10.1007/s004220100260)
- Gibson, C. T., Watson, G. S. & Myhra, S. 1996 Determination of the spring constants of probes for force microscopy/spectroscopy. *Nanotechnology* **7**, 259–262. (doi:10.1088/0957-4484/7/3/014)
- Gingl, E., Burger, A.-M. & Barth, F. G. 2006 Intracellular recording from a spider vibration receptor. *J. Comp. Physiol. A* **192**, 551–558. (doi:10.1007/s00359-005-0092-3)
- Johnson, K. L. 1985 *Contact mechanics*. Cambridge, UK: Cambridge University Press.
- Johnson, K. L., Kendall, K. & Roberts, A. D. 1971 Surface energy and the contact of elastic solids. *Proc. R. Soc. A* **324**, 301–313. (doi:10.1098/rspa.1971.0141)
- Kaliappan, S. N. & Capella, B. 2005 Temperature dependent elastic-plastic behavior of polystyrene studied using AFM force-distance curves. *Polymer* **46**, 11 416–11 423. (doi:10.1016/j.polymer.2005.09.066)
- Kovalev, A., Shulha, H., LeMieux, M., Myshkin, N. & Tsukruk, V. V. 2004 Nanomechanical probing of layered nanoscale polymer films with atomic force microscopy. *J. Mater. Res.* **19**, 716–728. (doi:10.1557/jmr.2004.0092)
- Leclere, P., Bredas, J. L., Moineau, G., Minet, M., Dubois, P., Jerome, R. & Lazzaroni, R. 2000 Microphase separation and morphological transitions at the surface of block co-polymers. In *Microstructure and microtribology of*

- polymer surfaces* (eds V. V. Tsukruk & K. J. Wahl), pp. 356–368. Washington, DC: American Chemical Society.
- LeMieux, M. C., Lin, Y. H., Cuong, P. D., Ahn, H. S., Zubarev, E. R. & Tsukruk, V. V. 2005 Microtribological and nanomechanical properties of switchable y-shaped amphiphilic polymer brushes. *Adv. Funct. Mater.* **15**, 1529–1540. (doi:10.1002/adfm.200500088)
- Rovner, J. S. & Barth, F. G. 1981 Vibratory communication through living plants by a tropical wandering spider. *Science* **214**, 464–466. (doi:10.1126/science.214.4519.464)
- Sneddon, I. N. 1965 The relation between load and penetration in the axisymmetric boussinesq problem for a punch of arbitrary profile. *Int. J. Eng. Sci.* **3**, 47–57. (doi:10.1016/0020-7225(65)90019-4)
- Sperling, L. H. 1997 *Polymeric multicomponent materials: an introduction*. New York, NY: Wiley.
- Sperling, L. H. 2006 *Introduction to physical polymer science*, 4th edn. Hoboken, NJ: Wiley.
- Sviridenok, A. I., Chizhik, S. A. & Petrokovets, M. I. 1990 *Mechanics of a discrete friction contact*. Minsk, Russia: Nauki I Tekhnika.
- Torii, A., Sasaki, M., Hane, K. & Okuma, S. 1996 A method for determining the spring constant of cantilevers for atomic force microscopy. *Meas. Sci. Technol.* **7**, 179–184. (doi:10.1088/0957-0233/7/2/010)
- Tsui, O. K. C., Wang, X. P., Ho, J. Y. L., Ng, T. K. & Xiao, X. 2000 Studying surface glass-to-rubber transition using atomic force microscopic adhesion measurements. *Macromolecules* **33**, 4198–4204. (doi:10.1021/ma991473x)
- Tsukruk, V. V. 1997 Scanning probe microscopy of polymer surfaces. *Rubber Chem. Technol.* **70**, 430–467.
- Tsukruk, V. V. & Gorbunov, V. V. 2001 Nanomechanical probing with scanning force microscopy. *Microsc. Today* **9**, 8–14.
- Tsukruk, V. V. & Gorbunov, V. V. 2002 Nanomechanical analysis of polymer surfaces. *Probe Microsc.* **2**, 241–247. (doi:10.1080/13551850214942)
- Tsukruk, V. V. & Reneker, D. H. 1995 Scanning probe microscopy of organic and polymeric films: from self-assembled monolayers to composite multilayers. *Polymer* **36**, 1791–1808. (doi:10.1016/0032-3861(95)90925-R)
- Tsukruk, V. V., Huang, Z., Chizhik, S. A. & Gorbunov, V. V. 1998 Probing of micromechanical properties of compliant polymeric materials. *J. Mater. Sci.* **33**, 4905–4909. (doi:10.1023/A:1004457532183)
- Tsukruk, V. V., Gorbunov, V. V., Huang, Z. & Chizhik, S. 2000 Dynamic microprobing of viscoelastic polymer properties. *Polym. Int.* **49**, 441–444. (doi:10.1002/(SICI)1097-0126(200005)49:5<441::AID-PI240>3.0.CO;2-U)
- Tsukruk, V. V., Sidorenko, A., Gorbunov, V. V. & Chizhik, S. A. 2001 Surface nanomechanical properties of polymer nanocomposite layers. *Langmuir* **17**, 6715–6719. (doi:10.1021/la010761v)

Surface force spectroscopic point load measurements and viscoelastic modelling of the micromechanical properties of air flow sensitive hairs of a spider (*Cupiennius salei*)

Michael E. McConney^{1,*}, Clemens F. Schaber^{2,*}, Michael D. Julian³, William C. Eberhardt⁴, Joseph A. C. Humphrey⁴, Friedrich G. Barth^{2,**}, Vladimir V. Tsukruk^{1,**}

¹ *School of Materials Science and Engineering and School of Polymer, Fiber, and Textile Engineering, Georgia Institute of Technology, Atlanta, GA 30332, USA*

² *Department of Neurobiology and Cognition Research, Faculty of Life Sciences, University of Vienna, Althanstraße 14, 1090 Wien, Austria*

³ *Department of Chemistry, California State University Stanislaus, Turlock, CA 95382, USA*

⁴ *Department of Mechanical and Aerospace Engineering and Department of Biology, University of Virginia, Charlottesville, VA 22904, USA*

* These authors contributed equally to this work.

** Authors for correspondence (friedrich.g.barth@univie.ac.at; vladimir@mse.gatch.edu).

Author contributions

CFS, MEM, and MDJ designed the experiments, CFS made the biological preparations, MEM performed the measurements, MEM and CFS analyzed the data, JACH, CFS, and WCE established the model, CFS, MEM, JACH, FGB, and VVT wrote the paper, and CFS managed the contributions of all authors to the manuscript.

The following pages contain the final version published online December 16, 2008 and in print August 6, 2009.

Citation:

Journal of the Royal Society Interface 6: 681–694

doi:10.1098/rsif.2008.0463

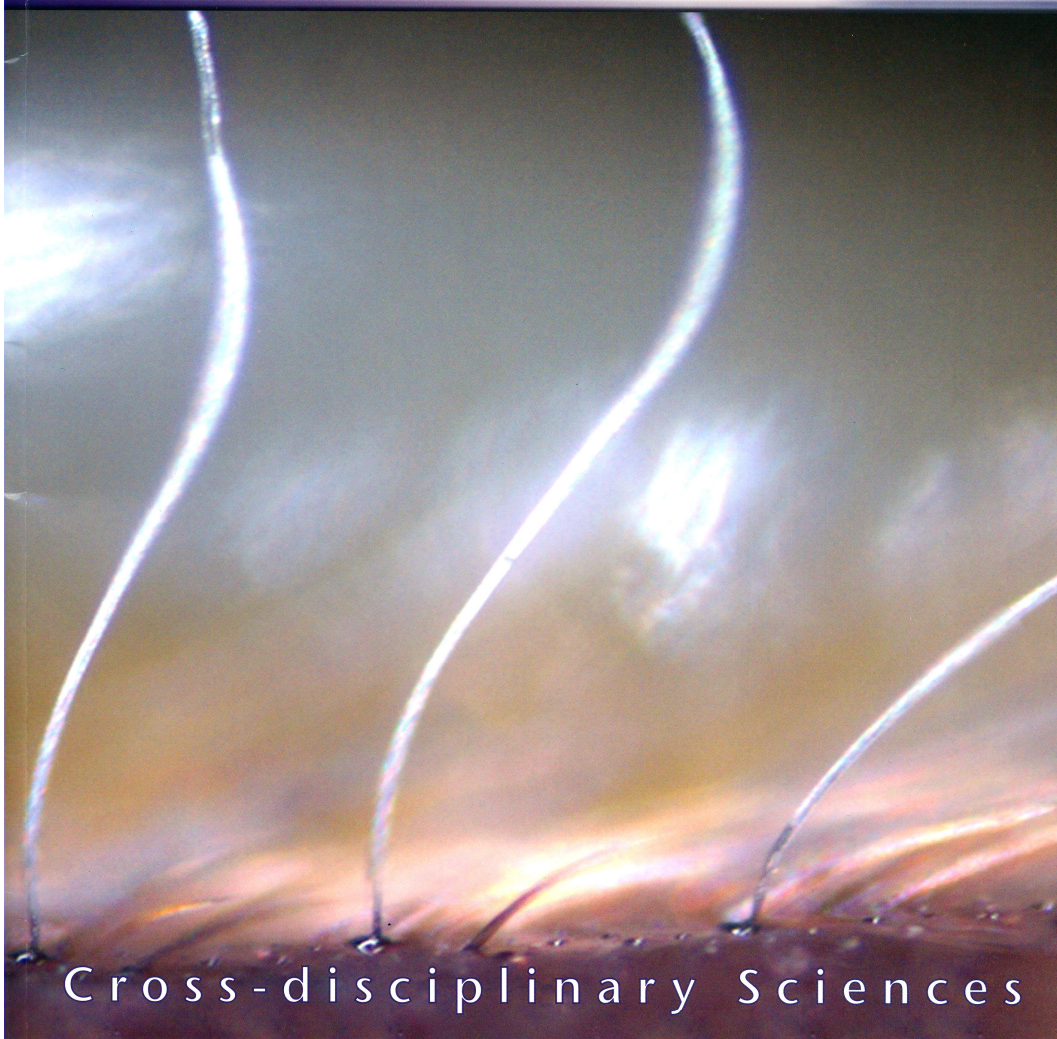
JOURNAL
— OF —
THE ROYAL
SOCIETY
Interface

ISSN 1742-5689

volume 6

number 37

pages 655–733



 Royal Society **Publishing**
*Informing the science
of the future*

6 August 2009

Cover image: So-called trichobothria of the wandering spider *Cupiennius salei*. These are hair-like micro air flow sensors of extreme sensitivity and impressive functional refinement. (image photographed by Clemens F. Schaber)

Surface force spectroscopic point load measurements and viscoelastic modelling of the micromechanical properties of air flow sensitive hairs of a spider (*Cupiennius salei*)

Michael E. McConney^{1,†}, Clemens F. Schaber^{2,†}, Michael D. Julian³, William C. Eberhardt^{4,5}, Joseph A. C. Humphrey^{4,5}, Friedrich G. Barth^{2,*} and Vladimir V. Tsukruk^{1,*}

¹School of Materials Science and Engineering and School of Polymer, Fiber, and Textile Engineering, Georgia Institute of Technology, Atlanta, GA 30332, USA ²Department of Neurobiology and Cognition Research, Faculty of Life Sciences, University of Vienna, Althanstraße 14, 1090 Wien, Austria ³Department of Chemistry, California State University Stanislaus, Turlock, CA 95382, USA ⁴Department of Mechanical and Aerospace Engineering, and ⁵Department of Biology, University of Virginia, Charlottesville, VA 22904, USA

The micromechanical properties of spider air flow hair sensilla (trichobothria) were characterized with nanometre resolution using surface force spectroscopy (SFS) under conditions of different constant deflection angular velocities $\dot{\theta}$ (rad s⁻¹) for hairs 900–950 μm long prior to shortening for measurement purposes. In the range of angular velocities examined (4×10^{-4} – 2.6×10^{-1} rad s⁻¹), the torque T (Nm) resisting hair motion and its time rate of change \dot{T} (Nm s⁻¹) were found to vary with deflection velocity according to power functions. In this range of angular velocities, the motion of the hair is most accurately captured by a three-parameter solid model, which numerically describes the properties of the hair suspension. A fit of the three-parameter model (3p) to the experimental data yielded the two torsional restoring parameters, $S_{3p} = 2.91 \times 10^{-11}$ Nm rad⁻¹ and $S'_{3p} = 2.77 \times 10^{-11}$ Nm rad⁻¹ and the damping parameter $R_{3p} = 1.46 \times 10^{-12}$ Nm s rad⁻¹. For angular velocities larger than 0.05 rad s⁻¹, which are common under natural conditions, a more accurate angular momentum equation was found to be given by a two-parameter Kelvin solid model. For this case, the multiple regression fit yielded $S_{2p} = 4.89 \times 10^{-11}$ Nm rad⁻¹ and $R_{2p} = 2.83 \times 10^{-14}$ Nm s rad⁻¹ for the model parameters. While the two-parameter model has been used extensively in earlier work primarily at high hair angular velocities, to correctly capture the motion of the hair at both low and high angular velocities it is necessary to employ the three-parameter model. It is suggested that the viscoelastic mechanical properties of the hair suspension work to promote the phasic response behaviour of the sensilla.

Keywords: trichobothria; spider; arthropod medium flow sensilla; atomic force microscope; force spectroscopy

1. INTRODUCTION

Trichobothria are wind-sensing hair-like sensilla on the legs and pedipalps of spiders capable of absorbing the energy of air flowing around them with outstanding efficiency (for reviews see Barth 2000; Barth 2002; Humphrey & Barth 2008). They serve the spider to detect and localize prey and predators. The measurements reported to date on spider trichobothria have been used in physical–mathematical models describing mechanical hair behaviour for oscillating air flows in the

biologically relevant frequency range between 10 and 950 Hz. In earlier studies, the frequency dependence of hair deflection was explained considering factors, such as the relationship of hair morphology with boundary-layer thickness and inertial effects. Both the hair suspension torsional restoring constant S and the damping constant R were calculated to be extremely small, being $S = 5.77 \times 10^{-12}$ Nm rad⁻¹, and $R = 2.20 \times 10^{-15}$ Nm s rad⁻¹ for a 750 μm long hair, and $S = 0.62 \times 10^{-12}$ Nm rad⁻¹ and $R = 0.27 \times 10^{-15}$ Nm s rad⁻¹ for a 250 μm long hair (Barth *et al.* 1993).

To date, trichobothria have been modelled using the data acquired by conventional optical microscopy, scanning electron microscopy and laser Doppler

*Authors for correspondence (friedrich.g.barth@univie.ac.at, vladimir@mse.gatech.edu).

[†]These authors contributed equally to this work.

anemometry (Barth *et al.* 1993; Bathellier *et al.* 2005). The mechanical hair behaviour was modelled using fluid mechanics to predict the amount of mechanical energy transferred from the air flow to the hair (Barth *et al.* 1993; Humphrey *et al.* 1993, 1998, 2001, 2003; Devarakonda *et al.* 1996; Humphrey & Barth 2008). These considerations quantitatively described the air–hair phase relationship, which allows the torsional restoring force of the hair suspension to be calculated under various assumptions related to the air–hair interactions. From the minimum deflection (measured with the optical microscope) that elicits an action potential combined with the estimates of the torsional restoring constant S , the minimum mechanical energy that effectively elicits a nervous response was estimated to be between 1.5×10^{-19} and 2.5×10^{-20} J (Humphrey *et al.* 2003). These are extremely small values indicating that trichobothria are among the most sensitive biological receptors.

In the present study, the mechanical properties of the trichobothrium suspension and of the hair shaft proper are measured directly. Mechanical stimuli were applied in different spatial and temporal regimes for both the small nanoscale deflections and the larger microscale deflections, and for a wide range of angular deflection velocities ranging from 0.0004 to 0.26 rad s⁻¹ at triangular wave frequencies ranging from 0.07 to 102 Hz (calculated as the reciprocal value of the duration of the triangular displacement). Moreover, this study is conducted with particularly high experimental precision (fraction of nanometre) by using surface force spectroscopy (SFS) and the application of directly calibrated forces in the range of nano-Newtons. SFS provides a force spectrum with pico-Newton precision, nano-Newton applied forces and nanoscale deflections (Tsukruk *et al.* 2000). SFS has already been proven to be an invaluable tool for studying biological receptors and the structures associated with them (Fuchigami *et al.* 2001; Gorbunov *et al.* 2002; McConney *et al.* 2007; Peleshanko *et al.* 2007). Here, we report on a methodology that combines representing the suspension of a trichobothrium as a linear viscoelastic material with direct measurements to determine the values of the three-parameter and two-parameter viscoelastic models explored. These are the torsional restoring constants, S_{3p} and S'_{3p} , and the damping constant R_{3p} , and the torsional restoring constant S_{2p} and the damping constant R_{2p} , inherent to the trichobothrium suspension represented by the spring and the dashpot elements of the models. The angles and velocities of the trichobothrium deflections measured are within the range relevant for the spider to distinguish air flow stimuli originating from prey, mates and predators from its noisy environment.

2. MATERIALS AND METHODS

2.1. Sample preparation

Live adult female *Cupiennius salei* (Ctenidae; figure 1*a*) spiders from the Vienna laboratory stock were anaesthetized with a CO₂/air mixture for 5 min and then attached to a Perspex substrate using adhesive tape

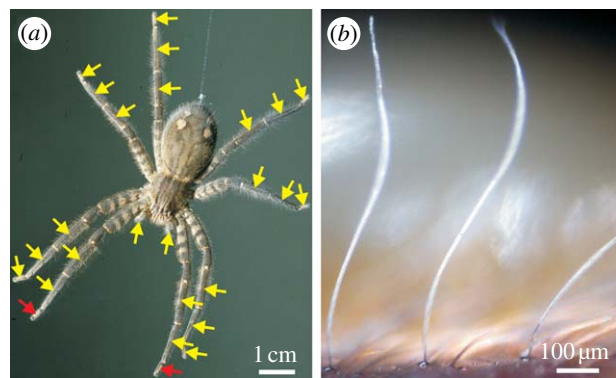


Figure 1. The spider and its trichobothria. (a) An adult female *Cupiennius salei*. The yellow arrows point to the leg segments carrying trichobothria. The red arrows point to the tarsi of the first walking legs whose trichobothria were examined in this study. (b) Three trichobothria in a row on the dorsal side of the first walking leg tarsus.

(3M Micropore), such that the metatarsus and tarsus of one of their first legs protruded beyond the substrate. Trichobothria on the tarsus of the first walking leg were identified optically (TaD group; for details of trichobothria topography see Barth *et al.* 1993) and other hairs in their vicinity removed (figure 1*b*). Particularly, two to four of the most distal trichobothria in the most frontal row on the tarsus were prepared in this way. For technical reasons the tarsus was secured on a metal sample mounting disc, so that the long axes of the trichobothria were oriented horizontally. To avoid mechanical interference with the atomic force microscope's (AFM) cantilever and to minimize air drag forces, the trichobothria were cut to lengths of approximately 100 μm and less using microscissors. The lengths of the trichobothria were measured using an optical microscope (Leica DM4000M) before and after the cutting procedure. A piece of silicon wafer cleaned with 'piranha solution' (1 : 2 hydrogen peroxide : sulphuric acid) was mounted beside the spider's tarsus on the metal disc. This was done to calibrate the sensitivity of the photodetector that measures the cantilever deflection used in SFS experiments. This is explained in detail in §2.2. Following the SFS measurements, the tarsus together with the trichobothrium tested was examined in a scanning electron microscope (JEOL JSM-6060V) for changes in the hair's surface structure owing to the interaction with the AFM cantilever probe.

2.2. SFS: hair deflection measurements

All AFM and SFS measurements were performed using a Multimode IIIa microscope with a Picoforce module and a Dimension 3000, Nanoscope IIIa microscope in accordance with well-established procedures (Cappella & Dietler 1999; LeMieux *et al.* 2003; Kovalev *et al.* 2004).

The AFM was warmed up by actuating the piezo elements for at least 30 min before the measurements began in order to prevent piezo thermal drift. The quadrant photodiode, which measured the deflection of the AFM cantilever, was calibrated by relating the distance of the cantilever tip deflection and the change

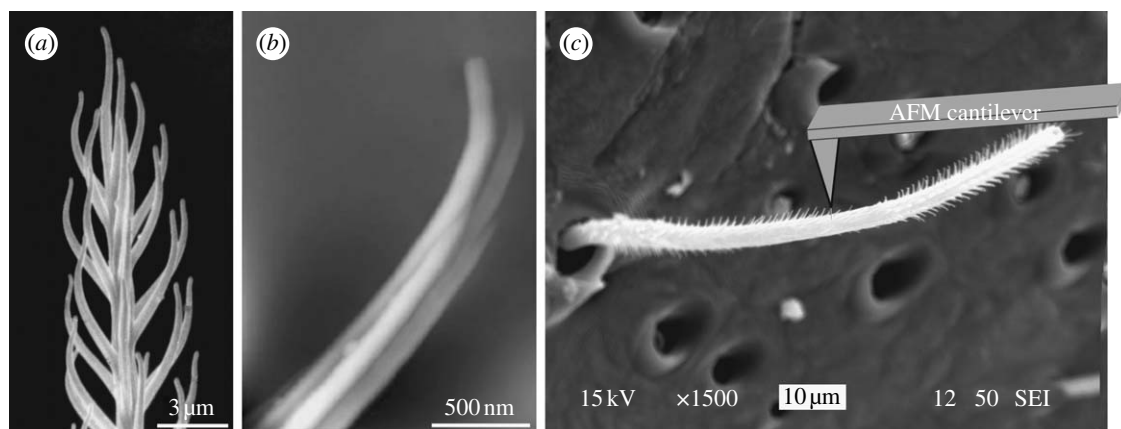


Figure 2. Hair shaft morphology. (a) SEM micrograph of the tip of a trichobothrium; note the hairs-on-hair morphology (microtrichs). (b) High-resolution AFM image of a single microtrich (z -range, 100 nm). Note that several striations make up a single microtrich. (c) SEM micrograph of a trichobothrium with partially removed microtrichs in the area close to the cantilever tip. Note the bald spot where the microtrichs were rubbed off by the cantilever tip (nanoshaving).

in position of the laser light shone on the photodiode. To calibrate the sensitivity of the photodiode, force curves were determined on a clean piece of silicon. A simple equation was used, $P + D = PM$, which relates the sum of the cantilever tip penetration into the substrate P and its deflection D to the movement of the piezo element PM . The freshly cleaned silicon was considered as an infinitely hard surface. Thus, the cantilever tip penetrated into the silicon by a negligible amount ($P = 0$), and the piezo movement equalled the deflection of the cantilever tip ($PM = D$). The voltage change in the photodiode was due to the same amount of deflection of the cantilever as the movement of the piezo element. Therefore, the photodiode was calibrated by setting the slope of the force–distance curve on silicon to 1. The photodiode was calibrated every time a new cantilever was used.

For the measurements, silicon cantilevers back-side coated with aluminium and with silicon nitride tips (nanometre-scale radius of cantilever tip end curvature) were used. Initially, microsphere-tipped probes seemed the most appropriate to prevent penetration into the hair surface, but owing to the large surface contact area adhesion of the hair to the microsphere persisted between two measurement cycles. The loss of contact between the two measurements provided a reference point when quantifying the total deflection of the hair during a measurement. The spring constants of the AFM cantilevers were calibrated using the standard ‘tip-on-tip’ method, as well as the thermal tuning method for softer cantilevers (Hutter & Bechhoefer 1993*a,b*; Gibson *et al.* 1996; Hazel & Tsukruk 1998, 1999).

For all measurements, the trichobothria were loaded by deflecting them in a triangular way at a constant angular velocity, with a predetermined repeat frequency and perpendicular to the long axis of the hair shaft. The hair shaft was deflected towards the posterior aspect of the tarsus. In oscillating air, the mechanical directional characteristics of hair deflection are nearly isotropic for the hairs examined here, with only a slight preference for the anterior–posterior plane (large to medium-sized hairs; Barth *et al.* 1993).

The trichobothria and the AFM cantilever were positioned under optical control (fibre optics, magnification by objective lens ($\times 50$) with large working distance, observation on video monitor). The metal disc, with the sample and the silicon, was placed onto the magnetic sample holder so that the long axis of the hair and the cantilever were in parallel. The micro-positioning stage of the AFM was used to position the cantilever with respect to the hair. Then, the tip position was fine adjusted to land in the centre of the hair. This was achieved by adjusting the offset of the horizontal plane piezo elements of the AFM to minimize the torsional deflection of the cantilever (monitored with the quadrant photodiode). The torsional motion was caused by a twisting motion of the cantilever when it contacted the hair not on its centre.

All hairs (of 910, 923, 950 μm length before cutting) were initially loaded using soft AFM cantilevers (spring constants between 0.018 and 0.045 N m^{-1}) to limit the forces applied to several nano-Newtons and to keep deflections below 100 nm. However, after the initial engagement, the force–distance curves showed significant instabilities caused by interactions between the AFM cantilever tip and the microtrichs on the main hair shaft (figure 2*a,b*). Repetition of the loading with the AFM cantilever tip at 1 Hz effectively micro-shaved the hair shaft owing to the cantilever’s slight horizontal displacements relative to the hair shaft, making the selected surface areas smooth and acceptable for stable engagement of the AFM cantilever tip (figure 2*c*). Because this horizontal displacement of the AFM cantilever (which can change the effective distance to the pivotal point and thus the resistance forces measured) was very small, it did not affect the calculations. Indeed, for hair deflection angles below 0.1° for high-resolution measurements, and below 12° for large deflection measurements, the corresponding correction factor was estimated to fall within 1–10 per cent. All critical experimental conditions are summarized in table 1. The cantilever force–distance curves were converted to hair loading curves (hair deflection versus normal load) by taking into account the preceding cantilever calibration. The contact point

Table 1. Experimental conditions for SFS measurements.

| testing variables | length, L^a (μm) | AFM cantilever stiffness (N m^{-1}) | ramp size ^b (nm) | velocity ($\mu\text{m s}^{-1}$) | trigger ^c (nm) |
|----------------------------|---------------------------------|--|-----------------------------|-----------------------------------|---------------------------|
| small forces (< 10 nN) | 20–50 | 0.018–0.045 | 3000–5000 | 0.05–41.9 | 10–150 |
| large forces (> 500 nN) | 21–62 | 8.9 | 5000–20 000 | 5–20 | 60–none |

^a The position of the cantilever on the hair is essential for the calculation of the torque.

^b Ramp size is the maximum distance that the sample can travel vertically when a single force–distance curve is measured. Ramp sizes had to be very large to ensure that the cantilever loses contact with the hair between measurements.

^c The trigger defines the maximum deflection of the cantilever when recording a force–distance curve.

was defined in accordance with an adaptation of the well-established approach given in Tsukruk *et al.* (1998). Specifically, we used the minimum deflection point of the approach curve, where the cantilever ‘snaps into’ the surface of the hair.

After performing the high-resolution SFS measurements within the limited range of deflections and forces, the soft AFM cantilever (spring constant less than or equal to 0.045 N m^{-1}) was replaced with a stiffer cantilever that had a spring constant of 8.9 N m^{-1} . The stiff cantilever allowed for loading forces exceeding $0.5 \mu\text{N}$ and led to hair deflections from 1 nm to $10 \mu\text{m}$. The measurements done with large hair deflections and the shaft-bending measurements were performed with and without a deflection trigger point (which is the maximum cantilever deflection before the displacement of the piezo element changes direction) to achieve the widest possible ranges of deflections and bending, respectively (figure 3; table 1).

For the theoretical considerations in the following paragraph, it is important to state that each force measurement curve was obtained at a constant angular velocity ($\dot{\theta}$), and thus zero angular acceleration ($\ddot{\theta}$).

2.3. Theoretical basis for the determination of the viscoelastic model parameters

In this section, we obtain two equations for the angular momentum of a trichobothrium. One, based on a three-parameter solid model for the viscoelastic hair suspension, will be shown to apply over the entire range of angular velocities explored ($4 \times 10^{-4} < \dot{\theta} < 2.6 \times 10^{-1} \text{ rad s}^{-1}$). The other, based on a two-parameter Kelvin solid model, will be shown to predict the motion of a hair with much better accuracy for angular velocities $\dot{\theta} > 0.05 \text{ rad s}^{-1}$, which is in the most biologically relevant range. For ease of presentation, we describe the two-parameter model first.

2.3.1. Two-parameter Kelvin solid model. In this approach, the suspension supporting the hair is approximated as a two-parameter Kelvin solid model consisting of a spring and a dashpot element connected in parallel (figure 4a). The hair is assumed to behave as a simple forced damped harmonic oscillator for which the conservation of angular momentum is given by

$$I\ddot{\theta} + R_{2p}\dot{\theta} + S_{2p}\theta = T, \quad (2.1)$$

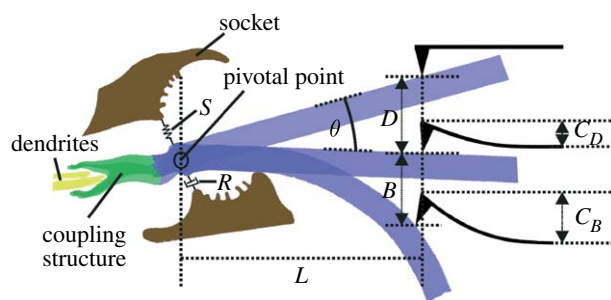


Figure 3. Hair parameters used for the calculations. The diagram defines the geometrical variables for the two regimes investigated: hair pivoting (deflection only) D and bending B , and the corresponding cantilever deflections C_D and C_B . L denotes the distance of the AFM cantilever tip from the pivotal point and θ , the deflection angle. The torsional restoring element S is represented by a spring, and the damping element R by a dashpot.

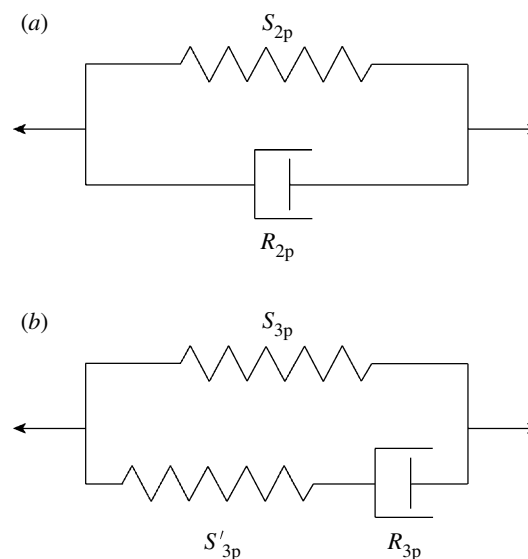


Figure 4. ‘Spring’ and ‘dashpot’ representations of (a) the two-parameter (2p) and (b) the three-parameter (3p) viscoelastic models representing the trichobothrium suspension material. In (a) the spring constant S_{2p} and the dashpot constant R_{2p} refer to the two-parameter model constants. In (b) the two spring constants S_{3p} and S'_{3p} , and the dashpot constant R_{3p} refer to the three-parameter model constants.

where I ($\text{Nm s}^2 \text{ rad}^{-1}$) is the hair’s moment of inertia; R_{2p} (Nm s rad^{-1}) is the hair’s damping constant; S_{2p} (Nm rad^{-1}) is the hair’s torsional restoring constant;

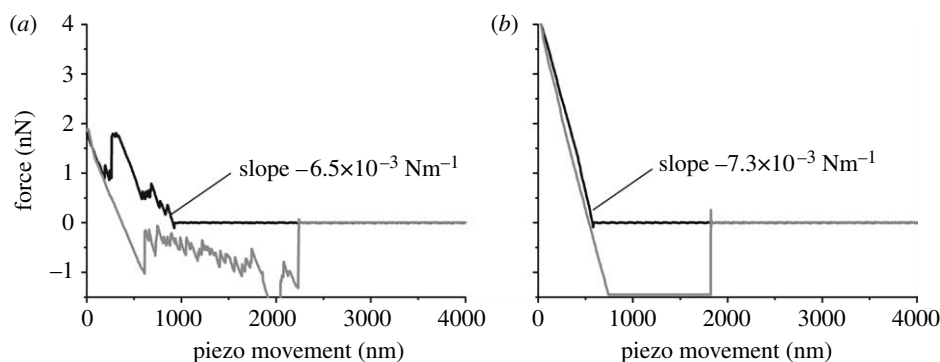


Figure 5. Hair shaving. (a) A force–distance curve obtained before the hair was shaved. (b) A force–distance curve obtained after removal of the microtrichs. The velocity of the piezo movement was $5.58 \mu\text{m s}^{-1}$. Note the significant improvement in the data quality compared to that in (a). The approach curves (black) in (a,b) should be read from right to left, and the retraction curves (grey) from left to right.

T (Nm) is the torque applied to the hair; and θ (rad), $\dot{\theta}$ (rad s^{-1}) and $\ddot{\theta}$ (rad s^{-2}) are the hair's deflection angle, angular velocity and angular acceleration, respectively. The subscript notation '2p' denotes 'two-parameter' model. Using this model, we show in appendix A that the torque terms associated with air friction and air added mass are negligible relative to the torque T_{SFS} imposed by the mechanical probe. The smallness of these effects is further confirmed by the fact that the loading curves showed no nonlinearities that could be due to these two medium-related forces.

Each experiment was conducted at a predetermined constant angular velocity $\dot{\theta}$, and as a consequence, equation (2.1) simplifies to

$$R_{2p}\dot{\theta} + S_{2p}\theta = T_{\text{SFS}}. \quad (2.2)$$

Using the experimentally determined data for $\dot{\theta}$ and T_{SFS} at a fixed angle θ , a multiple linear regression was performed using equation (2.2) to determine the model parameters.

2.3.2. Three-parameter solid model. The inability of the two-parameter model to correctly capture the variation of the hair's torque over the full range of angular velocities prompted us to explore a three-parameter solid model consisting of a spring element in parallel with a spring and a dashpot element in series (figure 4b). This type of linear viscoelastic model is documented in Flügge (1967), Fung (1993) and Fuchigami *et al.* (2001) for example, and the corresponding angular momentum equation for a trichobothrium is given by

$$I\ddot{\theta} + R_{3p}\left(1 + \frac{S_{3p}}{S'_{3p}}\right)\dot{\theta} + S_{3p}\theta = T + \frac{R_{3p}}{S'_{3p}}\dot{T}. \quad (2.3)$$

In this case, the model parameters are the damping constant R_{3p} (Nm s rad^{-1}) and two torsional restoring constants, S_{3p} (Nm rad^{-1}) and S'_{3p} (Nm rad^{-1}). Here, the subscript notation '3p' stands for 'three-parameter', and was chosen to distinguish from the 2p of the two-parameter model. The quantity $\dot{T} = (dT/dt)$ is the time rate of change of the torque. This is estimated from the relation $\dot{T} \cong (T_{\text{tot}}\dot{\theta}/\theta_{\text{tot}})$, where $\dot{\theta}$ and θ_{tot} are,

respectively, the angular velocity and the total angular deflection of a hair during a measurement; $T_{\text{tot}} (= T_{\text{SFS}})$ being the corresponding experimentally determined torque for these conditions. As mentioned above, for the conditions of this study, $\dot{\theta}$ is fixed to different but constant values and equation (2.3) simplifies to

$$R_{3p}\left(1 + \frac{S_{3p}}{S'_{3p}}\right)\dot{\theta} + S_{3p}\theta = T_{\text{SFS}} + \frac{R_{3p}}{S'_{3p}}\dot{T}_{\text{SFS}}. \quad (2.4)$$

Again, as in the two-parameter model, a multiple linear regression analysis was performed on the experimental data using equation (2.4) to determine the model parameters.

2.4. Testing methodology: nanoshaving

All SFS measurements were done with live animals. The micro-hairy surface (microtrichs) on the shaft of the trichobothrium added a significant challenge (figure 2). As mentioned above, the hairs-on-hair morphology initially prevented the acquisition of stable force–distance curves appropriate for further analysis. After taking many force–distance curves, their quality improved significantly as a result of nanoshaving. The linear region of the extension curves after engagement of the cantilever tip had identical slopes before and after this routine indicating that the fundamental hair resistance did not change (figure 5a,b).

For the experimental conditions of most of the SFS measurements on shaved hairs, we recorded very steady hair deflection, completely controlled by linear displacement of the piezoelectric crystal with random deviations smaller than 0.2 nm. No detectable thermal vibrations were recorded in the range of forces and distances examined, indicating significant viscous damping of the thermal vibrations and any other random deflections associated with environmental noise present in the laboratory. Moreover, no indications of large-scale displacements, associated with macroscopic movements, were recorded, indicating firm immobilization of the leg of the live spider.

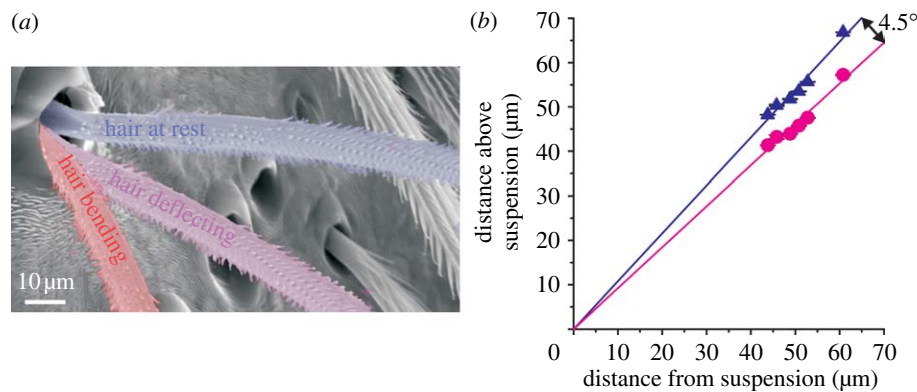


Figure 6. (a) SEM micrograph depicting the three regimes that characterize the large-scale load curves shown in figure 7a. (b) Positions of the trichobothrium in its zero (resting) position (triangles) and positions of first contact of the hair shaft with the socket rim (circles) with lines fit to the data. The origin of the curve represents the position of the hair suspension ($N=1$, $n=30$) (N , number of trichobothria; n , number of measurements).

2.5. Testing methodology: location of the axis of rotation

In order to measure the torque to deflect the trichobothrium, the distance L , from its pivoting axis O , to the region where the AFM cantilever tip contacted the hair shaft was required (figure 3). Precise values were obtained by making force–distance measurements at varying points along the hair shaft. From the zero position, the hair was deflected until its shaft contacted the socket at the limiting angle θ , and finally was bent slightly (figures 3 and 6a). The angle between the hair in its zero position and when touching the socket was used to identify the axis of rotation O . When the cantilever tip was moved towards or away from the hair suspension, the triangle described by the motion of the pivoting lever arm of length L changed area, but not angles. By changing the distance of the measurement location from the pivoting axis, the two lines representing the surface of the hair shaft at rest and at fully deflected states, respectively, were mapped out (figure 6b). The intersection of the two lines represents the location of the pivoting axis. The error regarding the distance from the AFM cantilever tip to the hair pivoting axis was estimated by taking the error of optical microscopy to be less than $\pm 1 \mu\text{m}$ for most of the SFS measurements conducted here.

Once the location of the pivoting axis was obtained, calculating the torque T , resisting hair deflection became unambiguous. The length of the hair shaft between the outer edge of the socket and the pivoting axis located at the suspension membrane was $12 \pm 1 \mu\text{m}$. These data are in good agreement with previous results, where the length of the hair shaft inside the socket was determined morphologically to be 10–15 μm for large trichobothria (Barth *et al.* 1993).

2.6. Testing methodology: deflection of a rigid hair

The force necessary to deflect the hair by a unit amount was measured by positioning the AFM cantilever tip at varying points along the length of the hair shaft and acquiring force–distance curves as discussed above. The results of the hair deflection measurements at

small forces (less than 500 nN) were based on two key assumptions: (i) the hair shaft does not bend in this regime and (ii) the AFM cantilever tip does not penetrate into the cuticle of the hair shaft.

Both assumptions were verified prior to the SFS measurements. The absence of hair bending under the nano-Newton forces used for high-resolution studies was confirmed by measurements of hair deflection using the same value of force applied at various distances L from the pivoting point along the hair shaft. The increase of hair deflection with increasing force applied at any particular point showed no nonlinearities that could have been due to contacting the socket edge or bending of the hair shaft. However, the same value of force applied at increasing distances L from the pivotal axis led to a quadratic increase ($R^2 > 0.99$) in hair displacement clearly indicating that the hair behaves as a rigid beam. The absence of local hair indentation was validated by performing independent SFS measurements on a hair that had been plucked and immobilized on a rigid substrate (silicon), considered to be infinitely hard. Under the modest normal loads used here, the indentation depth, if any, was close to the experimental uncertainty. It did not exceed 1 nm at the largest load and therefore only slightly penetrated into the topmost layer of the epicuticle leading to the adhesion seen in the retraction curves of the force–distance measurements (figure 5b). The thickness of the epicuticle on the leg of *Cupiennius* is 200 nm, with a thickness of the lipid layers of 10–40 nm (Barth 1969; McConney *et al.* 2007). By its smallness, the penetration into the epicuticle did not contribute to the deflection measurements. The hair was deflected as a rigid rod with its large stiffness relying mainly on the stiffness of the exocuticle, which has an elastic modulus of approximately 18 GPa in *C. salei* (Blickhan & Barth 1985; Barth 2002).

3. RESULTS

3.1. Measuring the torques resisting hair motion

The micromechanical behaviour of a hair under maximum forces normal to the long axis of the hair shaft and reaching 500 nN is presented in figure 7a. The complex and nonlinear loading curve reflects the

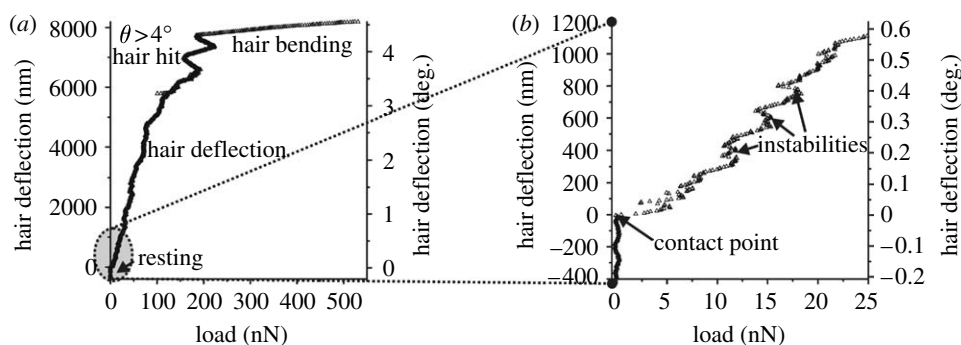


Figure 7. Hair shaft bending measurements. (a) A load–hair deflection curve, using relatively large forces. After significant deflection, the hair made contact with the socket and then the hair shaft was bent as seen from the small slope of the curve. (b) The same load curve as in (a), with the initial part of the curve enlarged to show the region where the AFM cantilever tip contacts the hair shaft.

contribution of several different mechanical regimes. First, the deflection of the hair just before making contact with the AFM cantilever tip is zero (figure 7*b*). Then, immediately after the engagement of the AFM cantilever tip at the contact point, the hair starts its nanoscale deflection, which is noisy but essentially linear up to loads close to 100 nN. The irregular deflections observed are caused by the interaction of the AFM cantilever tip with the microstructure of the hair shaft surface (see §2; figure 2*a*).

At larger normal loads hair deflection becomes erratic, especially between 7000 and 8000 nm, and finally alters dramatically (figure 7*a*). The erratic behaviour at approximately 7000 nm deflection is probably due to several different surface patches of the hair contacting the inner parts of the socket. For deflections larger than 7500 nm, the force required to deflect the hair further increases steeply indicating a change in the hair's mechanical behaviour. Figure 7*a* and *b* reflect the overall hair behaviour observed in our large deflection experiments: steady, close to linear deflection as a rigid body for deflections of less than approximately 7500 nm, followed by a steep increase in mechanical resistance when the hair contacts the socket rim and starts bending. The bending stiffness of the hair shaft of the 950 μm long trichobothrium, selected as a representative example, was measured to be $0.18 (\pm 0.03) \text{ N m}^{-1}$ ($n=15$), the AFM cantilever tip being 43.8 μm from the hair suspension membrane. The overall quadratic relation for the bending stiffness k of the hair shaft, as a function of distance from the pivoting point, L in μm , was $k=3.38 \times 10^{-4} L^2 - 4.35 \times 10^{-2} L + 1.44 (\text{N m}^{-1})$.

Considering the significant instabilities observed in the micromechanical behaviour measured under large deflection conditions, we conducted high-resolution experiments with more flexible cantilevers after nanoshaving the microtrichs to obtain the deflection characteristics in the range of very small forces (less than 2 nN). Under these conditions, the hair deflected fairly linearly with the force changing from 12.5 pN to 1.5 nN (figure 8*a,b*). Note that the first point in figure 7*b* is beyond the 0.5 nm uncertainty of the SFS measurement technique, and therefore well measurable. The loading curve is directly related to the torque resisting hair deflections by multiplying the force with the length of the lever arm. The trichobothrium could be

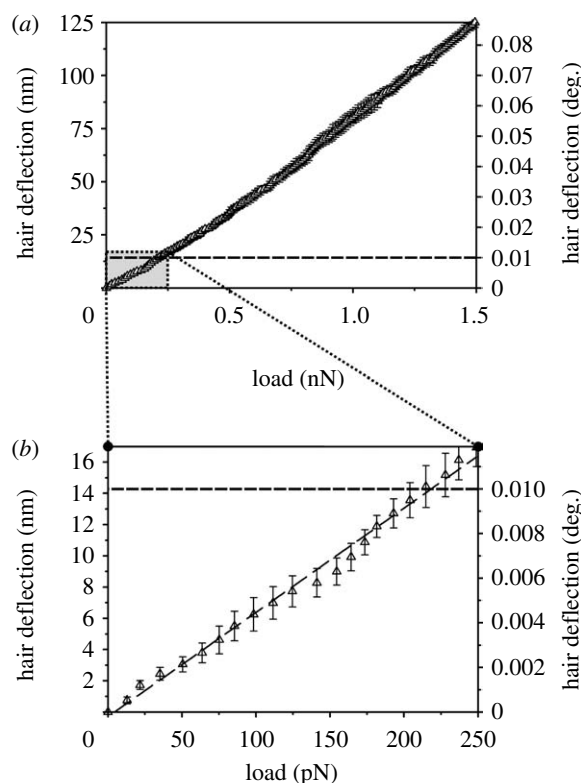


Figure 8. High-resolution hair shaft deflection measurements for a hair shortened to 114.5 μm . (a) High-resolution load–deflection curve; example of the load curves used to determine the two- and three-parameter model constants. Average of five measurements (\pm s.d.) obtained at an angular velocity of $0.029 \pm 0.004 \text{ rad s}^{-1}$. The dashed line represents the minimum angle of deflection necessary to elicit a nervous response as measured electrophysiologically (Barth & Höller 1999). (b) Enlarged initial region of the load–deflection curve displayed in (a).

reproducibly deflected by 0.001° (17.5 μrad). This is an extremely small value, well below the sensory threshold deflection angle down to 0.01° (Barth & Höller 1999). Hair deflection at small forces changed linearly by 0.85 nm increments per each 12.5 pN increase in load (figure 8*b*). The mechanical response of the hairs was linear at the specific angular velocities, even well below the sensory threshold deflection. Moreover, even under very small pico-Newton forces the hair response was smooth, with a mean deviation from linearity of the order of $\pm 0.2 \text{ nm}$ (figure 8*b*).

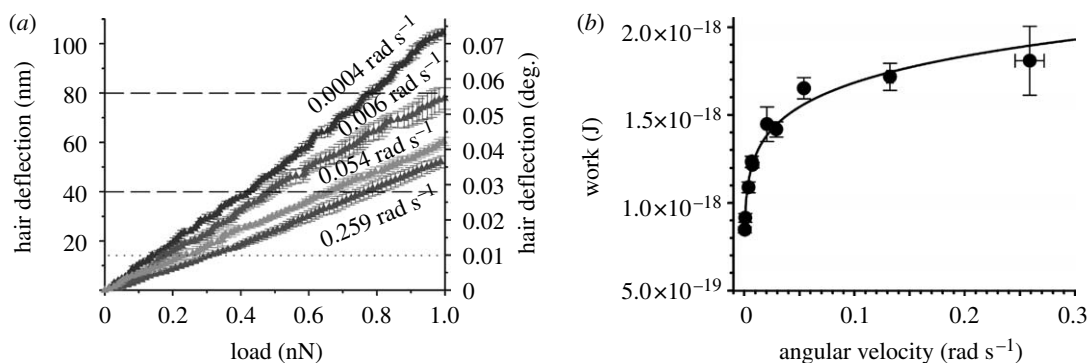


Figure 9. (a) High-resolution load–deflection curves. At lower angular velocity, the hair pivots much more with force. The curves shown are average curves \pm s.d. ($N=1$, $n=12$). (b) Work to reach the physiological threshold deflection of 0.01° (Barth & Höller 1999); see dotted line in (a). The line fitted to the data points (circles) follows the power-law function of work $W=2.24 \times 10^{-18} \times \dot{\theta}^{0.124}$ with an average overall uncertainty of 2.6%.

3.2. Viscoelastic model parameters

Preliminary values of the torsional restoring constant S , in which the contribution of the torque associated with damping was neglected, were obtained by relating the slope of the loading curves to a unit hair deflection of 1 rad. Previous data (Humphrey *et al.* 1993, 1998) and current findings suggest that values of the torsional restoring constant S obtained this way are close to the true values, although slightly overestimated. In investigations of hairs 910 and 923 μm long, the preliminary torsional restoring constants were measured to be 7.3×10^{-12} ($\pm 0.6 \times 10^{-12}$) Nm rad^{-1} and 4.3×10^{-12} ($\pm 0.1 \times 10^{-12}$) Nm rad^{-1} , respectively.

Given the potential importance of a trichobothrium's mechanical properties for its physiological response, we studied its torsional behaviour at angular velocities between 0.0004 and 0.26 rad s^{-1} by collecting force–distance data in the high-resolution mode (figure 9a). Surprisingly, the mechanical resistance of a hair to deflection forces, and consequently the work to deflect it to the physiological threshold angle, dropped sharply for angular velocities smaller than 0.05 rad s^{-1} (figures 9b and 10a). To the authors' knowledge, no previous work has reported such a trend in arthropod air flow-sensing hair receptors.

Table 2 provides mean and root mean square (r.m.s.) values of the experimental angular velocity, the torque and the time rate of change of torque from which the viscoelastic model parameters were determined. The torque values at a fixed hair deflection angle of 1.23×10^{-3} rad (0.07°) (which was the maximum angle that could be achieved at all deflection velocities with the same trigger deflection of the AFM's cantilever) are empirically related to the angular velocity by the expression $T=8.50 \times 10^{-14}-1.48 \times 10^{-14} \dot{\theta}^{-0.174}$ (Nm) (figure 10a). The empirical fit predicts the torque with an absolute difference smaller than 6 per cent over the entire range of angular velocities explored. The time rate of change of torque is empirically given by $\dot{T}=6.30 \times 10^{-11} \dot{\theta}^{1.11}$ (Nm s^{-1}) (figure 10b), with an absolute difference smaller than 4 per cent. We note that the torque T tends towards an asymptotic value of 8.50×10^{-14} Nm for very large angular velocities. This is to be expected since the viscoelastic dashpot element resists deformation induced by motions at high

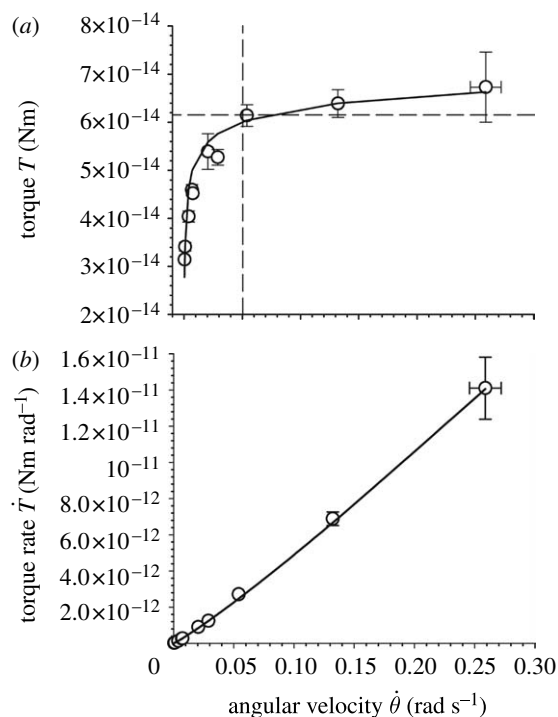


Figure 10. Comparison between measurements (circles; mean \pm s.d.) and empirical fits (lines; equations are given in the text) of (a) the torque and (b) its time rate of change as a function of the hair's angular velocity.

angular velocities and, as a consequence, deformation can only occur owing to the spring elements. The latter, however, deform in proportion to the torque irrespective of the rate of change and are responsible for the asymptotic behaviour observed.

Using the physical–mathematical procedure described in §2.3.1 for the two-parameter Kelvin model applied to all the measured data points, the model parameters were found to be $S_{2p}=3.57 \times 10^{-11}$ ($\pm 8.08 \times 10^{-12}$) Nm rad^{-1} and $R_{2p}=1.15 \times 10^{-13}$ ($\pm 1.05 \times 10^{-13}$) Nm s rad^{-1} . To check the goodness of this model, the torque T_{SF5} was calculated using equation (2.2) for the values of θ in table 2 and the values obtained for S_{2p} and R_{2p} . The difference between the measurements and the calculations averaged over the entire range of angular velocities is 14 per cent, reaching values as high as 39

Table 2. Angular velocity $\dot{\theta}$, torque T , and torque rate of change \dot{T} (mean \pm r.m.s. values) for a shortened trichobothrium originally 950 μm long at a deflection angle fixed to $\theta_{\text{tot}} = 1.226 \times 10^{-3}$ rad ($N=1$, $n=81$). (The rate of change of the torque is determined as explained in the text and its r.m.s. from the expression $\sigma_{\dot{T}} = T_{\text{SFS}}((\sigma_{T_{\text{SFS}}}^2/T_{\text{SFS}}^2) + (\sigma_{\dot{\theta}}^2/\dot{\theta}^2) + (\sigma_{\theta_{\text{tot}}}^2/\theta_{\text{tot}}^2))^{1/2}$ where σ denotes r.m.s. value. In this formula, the r.m.s. values for T_{SFS} and $\dot{\theta}$ are taken from the table entries, and that for θ_{tot} is estimated to be 2.45×10^{-9} rad from the experimental uncertainties of lever arm length and instrumental inaccuracies of the AFM.)

| data point | angular velocity mean (rad s ⁻¹) | angular velocity r.m.s. (rad s ⁻¹) | torque mean (Nm) | torque r.m.s. (Nm) | torque rate mean (Nm s ⁻¹) | torque rate r.m.s. (Nm s ⁻¹) |
|------------|--|--|------------------------|------------------------|--|--|
| 1 | 4.20×10^{-4} | 2.25×10^{-6} | 3.14×10^{-14} | 6.09×10^{-16} | 1.08×10^{-14} | 3.06×10^{-16} |
| 2 | 8.17×10^{-4} | 7.43×10^{-6} | 3.41×10^{-14} | 9.22×10^{-16} | 2.27×10^{-14} | 7.91×10^{-16} |
| 3 | 3.84×10^{-3} | 4.04×10^{-5} | 4.04×10^{-14} | 1.15×10^{-15} | 1.27×10^{-13} | 4.61×10^{-15} |
| 4 | 6.81×10^{-3} | 6.65×10^{-5} | 4.59×10^{-14} | 1.12×10^{-15} | 2.55×10^{-13} | 8.41×10^{-15} |
| 5 | 7.37×10^{-3} | 3.78×10^{-5} | 4.52×10^{-14} | 5.78×10^{-16} | 2.72×10^{-13} | 6.60×10^{-15} |
| 6 | 2.05×10^{-2} | 6.07×10^{-4} | 5.39×10^{-14} | 3.70×10^{-15} | 8.97×10^{-13} | 6.94×10^{-14} |
| 7 | 2.89×10^{-2} | 3.99×10^{-4} | 5.27×10^{-14} | 1.64×10^{-15} | 1.24×10^{-12} | 4.90×10^{-14} |
| 8 | 5.39×10^{-2} | 9.40×10^{-4} | 6.14×10^{-14} | 2.25×10^{-15} | 2.70×10^{-12} | 1.22×10^{-13} |
| 9 | 1.32×10^{-1} | 2.84×10^{-3} | 6.39×10^{-14} | 2.90×10^{-15} | 6.88×10^{-12} | 3.72×10^{-13} |
| 10 | 2.59×10^{-1} | 1.32×10^{-2} | 6.73×10^{-14} | 7.30×10^{-15} | 1.41×10^{-11} | 1.71×10^{-12} |

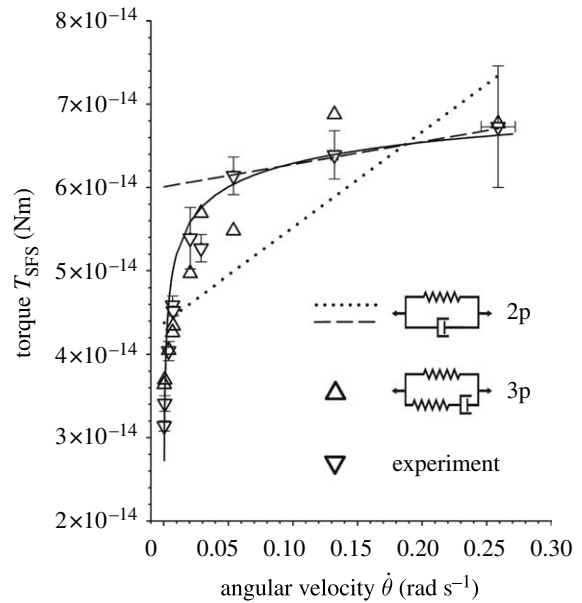


Figure 11. Comparison between measurements and calculations of the torque acting on a spider trichobothrium using the two-parameter (2p) and the three-parameter (3p) models described in the text: the measured data (down triangles, with error bars), the empirical fit (black solid curve), values calculated using the two-parameter model fitted to all the measured data points (dotted line), values calculated using the two-parameter model fitted to the three points at angular velocities larger than 0.05 rad s^{-1} (dashed line), and values calculated using the three-parameter model fitted to all the measured data points (up triangles).

per cent at the smallest angular velocity. Owing to the poor agreement, especially at low angular velocities, a second regression was performed using only the data corresponding to $\dot{\theta} > 0.05 \text{ rad s}^{-1}$. From this, it was found that $S_{2p} = 4.89 \times 10^{-11} (\pm 2.88 \times 10^{-13}) \text{ Nm rad}^{-1}$ and $R_{2p} = 2.83 \times 10^{-14} (\pm 2.07 \times 10^{-15}) \text{ Nm s rad}^{-1}$, which yielded calculated values of T_{SFS} differing from those measured by less than 0.5 per cent (figure 11).

For the three-parameter solid model described in §2.3.2, the multiple linear regression of the measured data in table 2 using equation (2.4) yielded $S_{3p} = 2.91 \times 10^{-11} (\pm 6.55 \times 10^{-12}) \text{ Nm rad}^{-1}$, $S'_{3p} = 2.77 \times 10^{-11} (\pm 9.84 \times 10^{-12})$ and $R_{3p} = 1.46 \times 10^{-12} (\pm 9.26 \times 10^{-13}) \text{ Nm s rad}^{-1}$. The results of the three-parameter model using the experimentally determined data of angular velocity $\dot{\theta}$ and torque rate \dot{T} are plotted in figure 11. The three-parameter model correctly captures the physical behaviour of the hair over the entire range of angular velocities including the drop of torque T for the small velocities, with an average absolute difference of 7 per cent, the largest difference being 16 per cent at the smallest angular velocity.

4. DISCUSSION

4.1. Comparison with fluid mechanic modelling studies

The preliminary statically determined values of S , as well as the two-parameter model values of S_{2p} and R_{2p} for the biologically most relevant angular velocities $\dot{\theta}$ larger

than 0.05 rad s^{-1} found in the present study, agree within one order of magnitude with the values obtained in earlier studies using a physical–mathematical flow modelling approach (Humphrey *et al.* 1993, 1998; Humphrey & Barth 2008). Similarly, the three-parameter model values of the two spring elements S_{3p} and S'_{3p} are quite comparable to previously determined values but, by contrast, the value of the damping element R_{3p} is approximately 100 times larger than R_{2p} . Because the three-parameter model correctly captures the qualitative variation of hair motion over the range of angular velocities and torque rates explored, it is deemed to be more fundamental of the two hair suspension viscoelastic models. Notwithstanding, for angular velocities larger than 0.05 rad s^{-1} , typical of many biologically relevant investigations, the two-parameter model yields very good predictions of hair behaviour (Humphrey *et al.* 1993, 1998; Shimozawa *et al.* 1998, 2003; Humphrey & Barth 2008).

Applying the two-parameter model, Barth *et al.* (1993) obtained constant values for S (corresponding to S_{2p}) and R (corresponding to R_{2p}) for a $750 \mu\text{m}$ long trichobothrium on the metatarsus (MeD1) of *Cupiennius salei* and found these to be $5.77 \times 10^{-12} \text{ Nm rad}^{-1}$ and $2.20 \times 10^{-15} \text{ Nm s rad}^{-1}$, respectively, in the case of a sinusoidally oscillating flow with a velocity amplitude of 50 mm s^{-1} driving the hair. The experimental fits for *Cupiennius* hairs provided in Humphrey *et al.* (2003) yield the constant values $S = 1.32 \times 10^{-11} \text{ Nm rad}^{-1}$ and $R = 3.34 \times 10^{-15} \text{ Nm s rad}^{-1}$ for a $950 \mu\text{m}$ long hair on the tibia (TiDA1). Our present results are also in good agreement with the constant S values of approximately $10^{-11} \text{ Nm rad}^{-1}$ found by Shimozawa & Kanou (1984a) for 1 mm long cricket filiform hairs for the case of quasistatic loading experiments. The filiform hairs on the cerci of crickets are similar to the spider trichobothria with regard to diameter and length, and they are sensitive to similar air flow velocities (Shimozawa & Kanou 1984b; Shimozawa *et al.* 1998; Casas *et al.* 2008). It should be noted that the flow conditions corresponding to the deflection of the above-mentioned MeD1 and TiDA1 spider trichobothria are associated with maximum angular velocities significantly larger than 1 rad s^{-1} . In this regard, the results of Humphrey & Barth (2008, fig. 18b) show that the angular velocities of MeD1 hairs $250\text{--}1000 \mu\text{m}$ long greatly exceed 1 rad s^{-1} in oscillating air flows with frequencies larger than 10 Hz and constant velocity amplitude of 10 mm s^{-1} . The same is true for MeD1 hairs $500 \mu\text{m}$ long in oscillating air flows with frequencies larger than 50 Hz and constant velocity amplitude of 2 mm s^{-1} (Humphrey & Barth 2008, fig. 23). Angular deflection velocities of trichobothria exposed to natural air flows eliciting prey capture behaviour of the spider as in the wake of a buzzing fly are frequently larger than 1 rad s^{-1} (figure 12; Barth 2002).

4.2. Modelling of the viscoelastic hair suspension

All models for linear viscoelastic materials are composed of linear springs and linear viscous dashpots to describe the stress–strain–time relations of such materials (Flügge 1967; Findley *et al.* 1976;

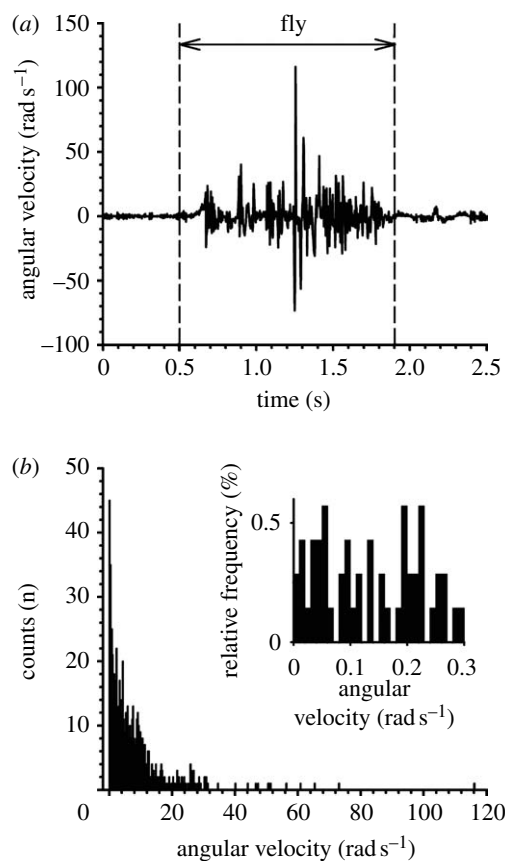


Figure 12. Angular velocity of a trichobothrium hit by the wake cone of a fly buzzing stationarily at a distance of 4 cm from the trichobothrium and at an angle of 45° to the long axis of the spider leg. (a) Time course of the angular velocity measured from high-speed video recordings (sampling rate, 500 frames per second). (b) Distribution of the angular velocity values from (a) between 0.5 and 1.9 s, bin size 0.25 rad s^{-1} and $n = 700$. Negative velocity values from (a) were accounted for as positive. Inset: relative frequencies of angular velocity values in the range from 0 to 0.3 rad s^{-1} ; bin size 0.01 rad s^{-1} .

Fung 1993). The form of equation (2.1), describing filiform hairs as forced damped harmonic oscillators, tacitly assumes that the viscoelastic behaviour of the hair suspension material can be approximated as a Kelvin solid, i.e. according to a linear viscoelastic model consisting of a spring element (S_{2p}) and a dashpot element (R_{2p}) in parallel. Thus, in equation (2.1) the torque T_m , characterizing the material's inherent resistance to motion is given by

$$T_m = R_{2p} \dot{\theta} + S_{2p} \theta, \quad (4.1)$$

where R_{2p} and S_{2p} are constants (Flügge 1967; Findley *et al.* 1976; Fung 1993). The response of this model to a suddenly imposed external torque is for the torque to be initially carried entirely by the viscous element R_{2p} , thus preventing any immediate deflection of the hair. However, as the viscous element elongates, it transfers an increasing portion of the applied torque to the elastic element S_{2p} , so that, finally, the entire torque is carried by the elastic element S_{2p} . Such behaviour is referred to as delayed elasticity (Findley *et al.* 1976).

By resorting to a three-parameter viscoelastic solid as described by equation (2.3), deformation can occur for any rate of applied torque. Whereas the two-parameter model would resist a deformation for a suddenly applied torque, the three-parameter model results in an initial deformation of the hair suspension by the two spring elements, S_{3p} and S'_{3p} , acting in parallel. Therefore, to achieve a particular angular deformation as the rate of deformation increases, the torque required to reach that angular deformation should asymptotically approach a constant value as observed in the experimental data. The two-parameter model achieves a similar effect by incorporating a numerical value for the dashpot that is three orders of magnitude smaller than the numerical value for the spring. The similar magnitudes of the three-parameter model constants allow the model to capture the deformation at low angular velocities.

These findings suggest that the viscoelastic nature of the hair suspension material and structure is complex at low angular velocities, with reversible elastic deformation and irreversible dissipation of mechanical energy strongly depending on both the deformation and the rate of deformation of the material. The mechanical behaviour of the hair can be associated with the time-dependent shearing properties of materials consisting of physical networks of molecules (Sperling 2006; Wineman & Shaw 2006), similar to the protein matrix in arthropod cuticle.

Not surprisingly, the work required to deflect the hairs to their physiological threshold angle of 0.01° (Barth & Höller 1999) at constant velocities essentially follows the changes of the torque T (figures 9*b* and 10*a*). The asymptotic, large angular velocity value for this work is approximately 2×10^{-18} J, close to the value of the area under the hair deflection versus load curve in figure 8*b* for 0.259 rad s^{-1} . When allowance is made for the fact that this load curve corresponds to the first half of a sawtooth wave, it is possible to compare with the work generated by a sinusoidally oscillating hair of similar characteristics (Humphrey *et al.* 2003). For such a wave, the absolute value of work generated during each quarter of the sinusoidal oscillation is a number ranging between 4×10^{-18} and 1×10^{-17} J, approximately. The correspondence between these values and the asymptotic one of the present study is acceptable, especially when allowance is made for the fact that neither the angular velocity nor the acceleration is constant for sinusoidally oscillating hairs. Note that, if instead of integrating a quarter of a sinusoidal cycle the integration is carried out for a full cycle, the net work obtained is smaller (10^{-20} to 10^{-19} J; Humphrey *et al.* 2003), because of the energy returned by the oscillating hair.

4.3. Sources of hair suspension viscoelasticity

The structures responsible for the viscoelastic behaviour of the hair suspension are the following (figure 3; Humphrey & Barth 2008).

- (i) The membrane, which connects the hair shaft and the exoskeleton, is suggested to represent the main spring element consisting of a highly elastic

material. Its increase in stiffness may result from viscoelastic effects, such as already shown for a soft cuticular pad of *Cupiennius*, which functions as a high-pass filter in the spider substrate vibration receptor (McConney *et al.* 2007). It seems likely that the hair suspension membrane contains resilin, which is known to elastically store energy with high efficiency in the joints of insects. According to dynamic mechanical testing between 10 and 200 Hz, the elastic modulus of resilin increases with increasing frequency as does the torque T resisting the hair deflection in the present study (Gosline *et al.* 2002).

- (ii) Regarding the dashpot element, we suggest two possible sources for the damping properties of the hair suspension. (a) The lever arm of the hair shaft below the suspension membrane, and the structure coupling the outer dendritic segments of the sensory cells to it, are surrounded by receptor lymph (Anton 1991; Barth 2002). The displacement of receptor lymph in such a confined space can be expected to be highly viscous, and the associated energy dissipation will work to dampen the hair deflection. (b) The region of the coupling structure contacting the dendrites may add to this initial low-velocity damping, but no experimental data are available yet.

4.4. Biological relevance

The velocities of background flows during the activity period of the spider in its natural habitat are typically smaller than 0.1 m s^{-1} , whereas the flow velocities generated by a buzzing fly can reach values of up to 1 m s^{-1} (Barth *et al.* 1995). The even more important difference between flow signals generated by prey insects or predators and the background wind is the flow velocity time history. The signals generated by prey or predators are of a fluctuating nature, characterized by relatively large ranges in the spatial and temporal scales of motion. By contrast, the background wind, in particular, during the night time activity of *Cupiennius*, is characterized by a much more steady flow (Barth *et al.* 1995; Klopsch *et al.* 2007). Angular deflection velocities of trichobothria caused by natural stimuli, such as the background wind or the highly turbulent wake of a fly, span a broad range of values with peak velocities of up to 150 rad s^{-1} (figure 12*a*). Interestingly, only 1.7 per cent of the angular velocity values are less than 0.05 rad s^{-1} (figure 12*b*), falling in the range of the deviation from the Kelvin solid-like behaviour of the suspension material.

At high angular velocities, the viscous dashpot element characterized by R_{3p} in the three-parameter model resists deformation, and as a consequence, the two spring elements S_{3p} and S'_{3p} dictate hair motion (figure 4*b*). This results in torque being directly proportional to the hair's angular deflection. By contrast, at low angular velocities the dashpot element can deform, thus relaxing the material and resulting in a lower torque to attain the same angular deflection. This viscoelastic material behaviour at low angular

velocities facilitates the start of hair motion from rest, thereby contributing to the highly phasic properties of the nervous response of the trichobothria (Barth & Höller 1999; Barth 2002). Note that under biologically relevant stimulus conditions, a trichobothrium generally moves at high angular velocities for which the spring elements dominate hair motion. Highly fluctuating signals such as those produced by potential prey animals result in frequent and sudden changes of the hair's angular velocity. Indeed, directly at the start of a motion with large constant velocity the action potential discharge rate of the hair sensory cells is larger than during ongoing deflection (Barth & Höller 1999). The mechanical properties of the hair suspension seem to specifically support the oscillating nature of the deflections of a trichobothrium caused by biologically relevant stimulus patterns.

In addition to the hair suspension structures, the viscoelastic properties of the dendrites themselves may help to explain the phasic response pattern of the sensory cells of the trichobothria, which readily respond to movement, but not to static deflection (Barth & Höller 1999). It is quite possible that only during movement of the coupling structure, not however during static deflection, the strain exerted on the sensory cell membrane is large enough to open a suprathreshold number of ion channels leading to the generation of the nervous response.

The authors would like to thank Melbourne C. LeMieux, Srikanth Singamaneni, Maryna Ornatska and Christian Klopsch for their valuable discussions. Funding was provided by the DARPA BioSense Program grant no. FA9550-05-1-0459 to F.G.B., J.A.C.H. and V.V.T. J.A.C.H. gratefully acknowledges a Guest Professorship in the Department of Neurobiology and Cognition Research at the University of Vienna during the work on this study. He also thanks T. Baber at UVA for the helpful discussions on viscoelastic materials.

APPENDIX A

For purposes of the estimates provided in this appendix, we model the hair suspension as a two-parameter Kelvin solid model. (For convenience, we drop the 2p subscript notation on the torsional restoring constant S and the damping constant R .) For these conditions, the equation governing the angular momentum of a hair being driven by a mechanical probe is

$$I\ddot{\theta} + R\dot{\theta} + S\theta = T, \quad (\text{A } 1)$$

where, assuming the hair is a straight cylinder, the moment of inertia I is given by

$$I = \frac{\pi\rho_{\text{h}}d^2}{48} \left(4L^3 + \frac{3}{4}d^2L \right), \quad (\text{A } 2)$$

and d , L and ρ_{h} are the hair diameter, length and density, respectively. In equation (A 1), T is the total torque acting on the hair: that is, it is the sum of the imposed mechanical probe torque T_{SFS} and the torque $T_{\text{hair}}^{\text{air}}$ resisting hair motion owing to the interaction of the hair with the air ($T = T_{\text{SFS}} - T_{\text{hair}}^{\text{air}}$).

In the experiment, the hair is displaced by the mechanical probe according to a triangular waveform pattern consisting of a constant displacement velocity during the downward and upward strokes, respectively. Because the hairs are displaced at constant angular velocity, the term $I\ddot{\theta}$ in equation (A 1) is negligible and this equation simplifies to

$$R\dot{\theta} + S\theta = T. \quad (\text{A } 3)$$

We now show for the case of a sinusoidally oscillating system that the torque terms $T_{\text{hair}}^{\text{air}}$ contributing to T are small relative to the mechanical probe torque T_{SFS} imposed in the experiments. For sinusoidal hair oscillations (Humphrey & Barth 2008)

$$T_{\text{hair}}^{\text{air}} = \int_0^L F_{\text{hair}}^{\text{air}} y \, dy, \quad (\text{A } 4)$$

where the total force F per unit hair length is

$$F_{\text{hair}}^{\text{air}} = F(\mu, V_{\text{r}}) + F(\mu, \dot{V}_{\text{r}}) + F(\rho, \dot{V}_{\text{r}}), \quad (\text{A } 5)$$

and the following definitions apply

$$F(\mu, V_{\text{r}}) = 4\pi\mu G V_{\text{r}}, \quad (\text{A } 6a)$$

$$F(\mu, \dot{V}_{\text{r}}) = -\frac{\pi\mu G \dot{V}_{\text{r}}}{2gf}, \quad (\text{A } 6b)$$

and

$$F(\rho, \dot{V}_{\text{r}}) = \pi\rho(d/2)^2 \dot{V}_{\text{r}}. \quad (\text{A } 6c)$$

In equations (A 6a–c), μ and ρ are the dynamic viscosity and density of air; V_{r} and \dot{V}_{r} are the relative velocity and acceleration of the air relative to the hair (see below); and the quantity G is given by

$$G = -\frac{g}{(g^2 + \pi^2/16)}, \quad (\text{A } 7)$$

where

$$g = 0.577 + \ln(s), \quad (\text{A } 8)$$

and

$$s = \left(\frac{d}{4} \right) \left(\frac{2\pi f}{\nu} \right)^{1/2} \ll 1. \quad (\text{A } 9)$$

(with $\nu = \mu/\rho$), which is a necessary condition readily satisfied in our experiments.

For the order of magnitude analysis of interest here, we can assume that the relative velocity and acceleration of the air with respect to the hair are given by (Humphrey & Barth 2008)

$$V_{\text{r}} = U_{\text{o}} \sin(2\pi ft), \quad (\text{A } 10)$$

and

$$\dot{V}_{\text{r}} = (2\pi f) U_{\text{o}} \cos(2\pi ft), \quad (\text{A } 11)$$

with U_{o} given by

$$U_{\text{o}} \approx df, \quad (\text{A } 12)$$

where U_{o} and f are the amplitude and frequency of the oscillating air flow.

Taking $L=1000\ \mu\text{m}$, $d=4\ \mu\text{m}$ and $f=20.8\ \text{Hz}$ yields

$$F(\mu, V_r) \approx 1.5 \times 10^{-9}\ \text{N m}^{-1}, \quad (\text{A } 13a)$$

$$F(\mu, \dot{V}_r) \approx 2 \times 10^{-10}\ \text{N m}^{-1}, \quad (\text{A } 13b)$$

and

$$F(\rho, \dot{V}_r) \approx 6 \times 10^{-14}\ \text{N m}^{-1}. \quad (\text{A } 13c)$$

When substituted into equation (A 4) and integrated over the truncated lengths L_F of the hairs examined, equations (A 13a–c) yield torques of the order of 10^{-17} , 1.4×10^{-18} and 4.32×10^{-22} Nm, respectively. By contrast, from figure 8, we estimate that an upper limit on T_{SFS} is given by

$$\begin{aligned} T_{\text{SFS}} &= F \times L_F = 1.5 \times 10^{-9} \times 114.5 \times 10^{-6} \\ &= 1.718 \times 10^{-13}\ \text{Nm}. \end{aligned}$$

The conclusion is that the air-induced torques opposing hair displacement are small relative to T_{SFS} and the final equation of motion for the hair is

$$R\dot{\theta} + S\theta = T_{\text{SFS}}. \quad (\text{A } 14)$$

REFERENCES

- Anton, S. 1991 Zentrale Projektionen von Mechano- und Chemorezeptoren bei der Jagdspinne *Cupiennius salei* Keys. Dissertation, Universität Wien.
- Barth, F. G. 1969 Die Feinstruktur des Spinnenintguments I. Die Cuticula des Laufbeins adulter häutungsferner Tiere (*Cupiennius salei* Keys). *Z. Zellforsch.* **97**, 137–159. (doi:10.1007/BF00331877)
- Barth, F. G. 2000 How to catch the wind: spider hairs specialized for sensing the movement of air. *Naturwissenschaften* **87**, 51–58. (doi:10.1007/s001140050010)
- Barth, F. G. 2002 *A spider's world: senses and behavior*. Berlin, Heidelberg, Germany; New York, NY: Springer.
- Barth, F. G. & Höller, A. 1999 Dynamics of arthropod filiform hairs V. The response of spider trichobothria to natural stimuli. *Phil. Trans. R. Soc. B* **354**, 183–192. (doi:10.1098/rstb.1999.0370)
- Barth, F. G., Wastl, U., Humphrey, J. A. C. & Devarakonda, R. 1993 Dynamics of arthropod filiform hairs. II. Mechanical properties of spider trichobothria (*Cupiennius salei* Keys.). *Phil. Trans. R. Soc. B* **340**, 445–461. (doi:10.1098/rstb.1993.0084)
- Barth, F. G., Humphrey, J. A. C., Wastl, U., Halbritter, J. & Brittinger, W. 1995 Dynamics of arthropod filiform hairs III. Flow patterns related to air movement detection in a spider (*Cupiennius salei* Keys.). *Phil. Trans. R. Soc. B* **347**, 397–412. (doi:10.1098/rstb.1995.0032)
- Bathellier, B., Barth, F. G., Albert, J. T. & Humphrey, J. A. C. 2005 Viscosity-mediated motion coupling between pairs of trichobothria on the leg of the spider *Cupiennius salei*. *J. Comp. Physiol. A* **191**, 733–746. (doi:10.1007/s00359-005-0629-5)
- Blickhan, R. & Barth, F. G. 1985 Strains in the exoskeleton of spiders. *J. Comp. Physiol. A* **157**, 115–147. (doi:10.1007/BF00611101)
- Cappella, B. & Dietler, G. 1999 Force–distance curves by atomic force microscopy. *Surf. Sci. Rep.* **34**, 1–104. (doi:10.1016/S0167-5729(99)00003-5)
- Casas, J., Steinmann, T. & Dangles, O. 2008 The aerodynamic signature of running spiders. *PLoS ONE* **3**, e2116. (doi:10.1371/journal.pone.0002116)
- Devarakonda, R., Barth, F. G. & Humphrey, J. A. C. 1996 Dynamics of arthropod filiform hairs. IV. Hair motion in air and water. *Phil. Trans. R. Soc. B* **351**, 933–946. (doi:10.1098/rstb.1996.0086)
- Findley, W. N., Lai, J. S. & Onaran, K. 1976 *Creep and relaxation of non-linear viscoelastic materials*. New York, NY: Dover Publications.
- Flügge, W. 1967 *Viscoelasticity*. Waltham, MA: Blaisdell Publishing Company.
- Fuchigami, N., Hazel, J., Gorbunov, V. V., Stone, M., Grace, M. S. & Tsukruk, V. V. 2001 Biological thermal detection. I: ultra-microstructure of pit organs in infra-red imaging snakes. *Biomacromolecules* **2**, 757–764. (doi:10.1021/bm015537z)
- Fung, Y. C. 1993 *Biomechanics*, 2nd edn. New York, NY: Springer.
- Gibson, C. T., Watson, G. S. & Myhra, S. 1996 Determination of the spring constants of probes for force microscopy/spectroscopy. *Nanotechnology* **7**, 259–262. (doi:10.1088/0957-4484/7/3/014)
- Gorbunov, V., Fuchigami, N., Stone, M., Grace, M. & Tsukruk, V. V. 2002 Biological thermal detection: micromechanical and microthermal properties of biological infrared receptors. *Biomacromolecules* **3**, 106–115. (doi:10.1021/bm015591f)
- Gosline, J., Lillie, M., Carrington, E., Guerette, P., Ortlepp, C. & Savage, K. 2002 Elastic proteins: biological roles and mechanical properties. *Phil. Trans. R. Soc. B* **357**, 121–132. (doi:10.1098/rstb.2001.1022)
- Hazel, J. L. & Tsukruk, V. V. 1998 Friction force microscopy measurements: normal and torsional spring constants for V-shaped cantilevers. *J. Tribol.* **120**, 814–819. (doi:10.1115/1.2833784)
- Hazel, J. L. & Tsukruk, V. V. 1999 Spring constants of composite ceramic/gold cantilevers for scanning probe microscopy. *Thin Solid Films* **339**, 249–258. (doi:10.1016/S0040-6090(98)00961-4)
- Humphrey, J. A. C. & Barth, F. G. 2008 Medium flow-sensing hairs: biomechanics and models. In *Insect mechanics and control* (eds J. Casas & S. J. Simpson) *Advances in insect physiology*, vol. 34, pp. 1–80. Amsterdam, The Netherlands: Elsevier.
- Humphrey, J. A. C., Devarakonda, R., Iglesias, I. & Barth, F. G. 1993 Dynamics of arthropod filiform hairs I. Mathematical modelling of the hair and air motions. *Phil. Trans. R. Soc. B* **340**, 423–444. (doi:10.1098/rstb.1993.0083)
- Humphrey, J. A. C., Devarakonda, R., Iglesias, I. & Barth, F. G. 1998 Errata re. Humphrey et al. 1993. *Phil. Trans. R. Soc. B* **352**, 1995.
- Humphrey, J. A. C., Barth, F. G. & Voss, K. 2001 The motion-sensing hairs of arthropods: using physics to understand sensory ecology and adaptive evolution. In *The ecology of sensing* (eds F. G. Barth & A. Schmid), pp. 105–125. Berlin, Heidelberg, Germany; New York, NY: Springer.
- Humphrey, J. A. C., Barth, F. G., Reed, M. & Spak, A. 2003 The physics of arthropod medium-flow sensitive hairs: biological models for artificial sensors. In *Sensors and sensing in biology and engineering* (eds F. G. Barth, J. A. C. Humphrey & T. W. Secomb), pp. 129–144. Wien, Austria; New York, NY: Springer.
- Hutter, J. L. & Bechhoefer, J. 1993a Calibration of atomic-force microscope tips. *Rev. Sci. Instrum.* **64**, 1868–1873. (doi:10.1063/1.1143970)

- Hutter, J. L. & Bechhoefer, J. 1993*b* Erratum re. Hutter & Bechhoefer 1993*a*. *Rev. Sci. Instrum.* **64**, 3342. (doi:10.1063/1.1144449)
- Klopsch, C., Barth, F. G. & Humphrey, J. A. C. 2007 The air flow generated by a flying prey insect around a wandering spider and its motion-sensing hair sensilla. In *Fifth Int. Symp. on turbulence and shear flow phenomena* (eds R. Friedrich, N. A. Adams, J. K. Eaton, J. A. C. Humphrey, N. Kasagi & M. A. Leschziner), pp. 1023–1028. Garching, Germany: TU München.
- Kovalev, A., Shulha, H., LeMieux, M., Myshkin, N. & Tsukruk, V. V. 2004 Nanomechanical probing of layered nanoscale polymer films with atomic force microscopy. *J. Mater. Res.* **19**, 716–728. (doi:10.1557/jmr.2004.0092)
- LeMieux, M., Usov, D., Minko, S., Stamm, M., Shulha, H. & Tsukruk, V. V. 2003 Reorganization of binary polymer brushes: switching surface microstructures and nanomechanical properties. *Macromolecules* **36**, 7244–7255. (doi:10.1021/ma034634c)
- McConney, M. E., Schaber, C. F., Julian, M. D., Barth, F. G. & Tsukruk, V. V. 2007 Viscoelastic nanoscale properties of cuticle contribute to the high-pass properties of spider vibration receptor (*Cupiennius salei* Keys). *J. R. Soc. Interface* **4**, 1135–1143. (doi:10.1098/rsif.2007.1000)
- Peleshanko, S. *et al.* 2007 Hydrogel-encapsulated microfabricated haircell mimicking fish cupula neuromast. *Adv. Mater.* **19**, 2903–2909. (doi:10.1002/adma.200701141)
- Shimozawa, T. & Kanou, M. 1984*a* The aerodynamics and sensory physiology of range fractionation in the cercal filiform sensilla of the cricket *Gryllus bimaculatus*. *J. Comp. Physiol. A* **155**, 495–505. (doi:10.1007/BF00611914)
- Shimozawa, T. & Kanou, M. 1984*b* Varieties of filiform hairs: range fractionation by sensory afferents and cercal interneurons of a cricket. *J. Comp. Physiol. A* **155**, 485–493. (doi:10.1007/BF00611913)
- Shimozawa, T., Kumagai, T. & Baba, Y. 1998 Structural scaling and functional design of the cercal wind-receptor hairs of cricket. *J. Comp. Physiol. A* **183**, 171–186. (doi:10.1007/s003590050245)
- Shimozawa, T., Murakami, J. & Kumagai, T. 2003 Cricket wind receptors: thermal noise for the highest sensitivity known. In *Sensors and sensing in biology and engineering* (eds F. G. Barth, J. A. C. Humphrey & T. W. Secomb), pp. 145–157. Wien, Austria; New York, NY: Springer.
- Sperling, L. H. 2006 *Introduction to physical polymer science*, 4th edn. Hoboken, NJ: Wiley.
- Tsukruk, V. V., Huang, Z., Chizhik, S. A. & Gorbunov, V. V. 1998 Probing of micromechanical properties of compliant polymeric materials. *J. Mater. Sci.* **33**, 4905–4909. (doi:10.1023/A:1004457532183)
- Tsukruk, V. V., Gorbunov, V. V., Huang, Z. & Chizhik, S. A. 2000 Dynamic microprobing of viscoelastic polymer properties. *Polym. Int.* **49**, 441–444. (doi:10.1002/(SICI)1097-0126(200005)49:5<441::AID-PI240>3.0.CO;2-U)
- Wineman, A. & Shaw, J. 2006 Influence of thermally induced chemorheological changes on the torsion of elastomeric circular cylinders. *Continuum Mech. Thermodyn.* **17**, 477–492. (doi:10.1007/s00161-006-0009-6)

Addendum:

Co-authored full papers

Addendum:
Höbl et al. (2009) J Comp Physiol A 195:881–894

Finite element modeling of arachnid slit sensilla: II. Actual lyriform organs and the face deformations of the individual slits

Bernhard Höbl^{1,2}, Helmut J. Böhm¹, Clemens F. Schaber²,
Franz G. Rammerstorfer¹, Friedrich G. Barth^{2,*}

¹ Institute of Lightweight Design and Structural Biomechanics, Vienna University of Technology,
Gubhausstraße 27-29/317, 1040 Vienna, Austria

² Department of Neurobiology and Cognition Research, Faculty of Life Sciences, University of Vienna,
Althanstraße 14, 1090 Wien, Austria

*Author for correspondence (Friedrich.g.barth@univie.ac.at)

Author contributions

BH, HJB and FGB designed, calculated and analyzed the simulations, CFS and FGB designed the biological experiments, CFS performed and analyzed the biological experiments and provided data for the simulations, and BH, HJB, CFS, FGR and FGB wrote the paper.

The following pages contain the final version published online August 14, 2009 and in print in September 2009.

Citation:

Journal of Comparative Physiology A 195:881–894

doi: 10.1007/s00359-009-0467-y

Finite element modeling of arachnid slit sensilla: II. Actual lyriform organs and the face deformations of the individual slits

Bernhard Höbl · Helmut J. Böhm ·
Clemens F. Schaber · Franz G. Rammerstorfer ·
Friedrich G. Barth

Received: 26 March 2009 / Revised: 21 July 2009 / Accepted: 23 July 2009 / Published online: 14 August 2009
© Springer-Verlag 2009

Abstract Arachnid slit sensilla respond to minute strains in the exoskeleton. After having applied Finite Element (FE) analysis to simplified arrays of five straight slits (Höbl et al. J Comp Physiol A 193:445–459, 2007) we now present a computational study of the effects of more subtle natural variations in geometry, number and arrangement of slits on the slit face deformations. Our simulations show that even minor variations in these parameters can substantially influence a slit's directional response. Using white-light interferometric measurements of the surface deformations of a lyriform organ, it is shown that planar FE models are capable of predicting the principal characteristics of the mechanical responses. The magnitudes of the measured and calculated slit face deformations are in good agreement. At threshold, they measure between 1.7 and 43 nm. In a lyriform organ and a closely positioned loose group of slits, the detectable range of loads increases to approximately 3.5 times the range of the lyriform organ alone. Stress concentration factors (up to ca. 29) found in the vicinity of the slits were evaluated from the models. They are mitigated due to local thickening of the exocuticle and the arrangement of the chitinous microfibrils that prevents the formation of cracks under physiological loading conditions.

Keywords Spiders · Strain detection · Slit sensilla · Modeling · Mechanoreception

Abbreviations

| | |
|---------------------|--|
| b | Width of slit |
| D | Slit face displacement |
| D_d | Slit face displacement at the dendrite's position |
| D_{sc} | Slit face displacement at mid-length of a single isolated slit |
| l | Length of the slit |
| l_0 | Length of the largest slit in the array |
| l/b | Aspect ratio (length/width) of the slit |
| S | Lateral spacing between neighboring slits |
| Δl | Difference in the length of neighboring slits |
| ε_a | Applied far-field strain |
| $\varepsilon_{a,r}$ | Reference applied far-field strain |
| Φ | In-plane angle of unidirectional load |
| λ | Longitudinal shift between slits |
| σ_a | Applied far-field stress |
| $\sigma_{a,r}$ | Reference applied far-field stress |

Introduction

Embedded in the exoskeleton of arachnids (Barth and Libera 1970; Barth and Wadepuhl 1975; Barth and Stagl 1976) are slit-shaped sensory organs, which by way of their compression monitor the cuticular strains resulting from muscle activity, hemolymph pressure and substrate vibrations. In spiders, the slits are up to 200 μm long with parallel faces and rounded ends. They have aspect ratios, i.e., ratios of length/width (l/b , see Fig. 1a), of up to 100 (Barth 1971, 1981), which is much higher than in insect campaniform sensilla ($l/b \approx 1$ to 3) (Barth 1981). However, in both types of these cuticular strain detectors, isolated single sensilla as

B. Höbl · H. J. Böhm · F. G. Rammerstorfer
Institute of Lightweight Design and Structural Biomechanics,
Vienna University of Technology, Gußhausstraße 27-29/317,
1040 Vienna, Austria

B. Höbl · C. F. Schaber · F. G. Barth (✉)
Department for Neurobiology and Cognition Research,
Faculty of Life Sciences, University of Vienna,
Althanstraße 14, 1090 Vienna, Austria
e-mail: Friedrich.g.barth@univie.ac.at

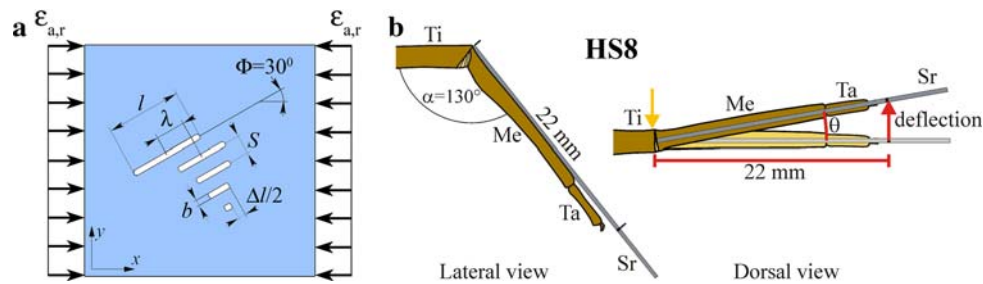


Fig. 1 **a** Geometrical parameters of the slit arrangements tested. $\epsilon_{a,r}$ far-field strain; l slit length; b slit width; S lateral shift; Δl gradation in slit length; λ longitudinal shift; Φ orientation of slits relative to uni-axial compressive loads. **b** Arrangement of the leg for white-light interferometric examination of the deformation of lyriform organ HS8 and

simultaneous force measurements. The angle α between tibia (Ti) and metatarsus (Me) is kept at 130° in the dorsoventral plane. A steel rod, Sr , waxed to the metatarsus deflects it laterally against the fixed tibia. Yellow arrow, location of lyriform organ HS8 on the posterior aspect of the tibia; Ta tarsus

well as groups of sensory units are found. Lyriform organs of arachnids are compounds of up to 30 closely spaced (lateral spacings $S/l \leq 0.04$; for the definition of S see Fig. 1a) elongated slits (see review in Barth 2002). The individual slits fully penetrate the cuticle within a few microns of their tips (Müllan 2005) and therefore can be modeled as capped rectangular openings cut into disks or shells.

Organ HS8 on the tibia of the spider *Cupiennius salei* is a particularly well-studied lyriform slit arrangement. Its mechanical and physiological properties were previously examined (Barth and Bohnenberger 1978; Bohnenberger 1981), and the face deformations of a slit pattern inspired by HS8 and cut into planar polymer discs were analyzed under load using photoelasticity techniques (Barth and Pickelmann 1975). The first (in vivo) measurements of the strains in the exoskeleton at the location of some lyriform organs including HS8 were reported by Blickhan and Barth (1985). They used micro strain gauges glued to spider walking legs to identify the strains at the location of real lyriform organs under biologically relevant loads, such as those occurring during walking.

Later, these studies were extended to include jumping, starting and stopping, and other mechanically more demanding situations in *C. salei* (Brüssel 1987; Barth 2002). Although the influence of the stiffness of the strain gauges on the stiffness of the cuticle could be accounted for, the differences in the face deformations of the individual slits could not be resolved by this method. The present study was supported by optical measurements of the slit face deformations of individual slits of real lyriform organs in intact spiders, done by white-light interferometry, which does not affect the mechanical properties of the integument. By a comparison with the results of the previous strain-gauge measurements and those of interferometric analyses, the accuracy of our present planar FE model of HS8 could be assessed and confirmed. Thus, planar FE models can be used to predict the slit face displacements of actual lyriform organs not accessible to measurement, provided these

organs are located in sufficiently planar regions of the exoskeleton.

In a previous study, we used an analytical fracture mechanical approach (Kachanov's method) as a first step toward quantitative mathematical models of the face deformations of the slits in spider lyriform organs (Höbl et al. 2005, 2006). As this method turned out to be limited to slits more widely spaced than those in lyriform organs, we then focused on the Finite Element (FE) method, which does not have this limitation (Höbl et al. 2007). Planar FE models allow studying arbitrarily positioned openings of any desired number, shape, and spacing. In addition, they can be extended to the third dimension by using shell models taking into account the actual shape of the integument close to many of the organs.

Our first FE study (Höbl 2007) concentrated on simplified planar models of different arrays of five slits (Barth et al. 1984), while Vincent et al. (2007) studied a simplified arrangement of elliptical holes inspired by campaniform sensilla.

In the present work, we approach the natural conditions more closely to see the mechanical effect of variations in the number of slits, their lateral and longitudinal shift, their curvature, and the angles between them. Three-dimensional (3D) FE models based on the morphological details of actual organs and of the exoskeletal parts carrying them are the subject of a manuscript in preparation.

Being part of an effort to computationally model slit sensilla, this study extends the quantitative basis for designing biomimetic micro strain sensors for technical applications, e.g., in robotics or in medical applications such as prostheses.

Materials and methods

Details of slit sensilla

In the legs of the spider *Cupiennius salei*, the exocuticle that dominates the cuticle's stiffness, is about $10 \mu\text{m}$ thick

(Barth 1969). From the engineering point of view, the exocuticle shows a helicoidal variation of the fiber orientations over its thickness and forms a laminate consisting of many sublaminates, which are referred to as lamellae. Thus, according to the lamination theory (Agarwal and Broutman 1990), the cuticle can be treated as isotropic for in-plane loads (Barth 1973). The effective in-plane Young's modulus of the cuticle of the tibia of *C. salei* was reported to be 18 GPa (Blickhan and Barth 1985) and the in-plane Poisson's ratio as 0.3 (in agreement with the estimates of Vincent 1982; Flannigan 1998; Cocatre-Zilgen and Delcomyn 1999; Skordos et al. 2002).

Slit sensilla are covered on the outside by an isotropic, inward-bulged, trough-shaped membrane, which holds a structure known as the coupling cylinder. Inside the coupling cylinder, the dendritic ending of a sensory cell is attached. The Young's modulus of the outer membrane, which is assumed to be resilin-like, can be estimated to be in the range of 1–2 MPa (values reported for materials mainly consisting of resilin by Jensen and Weis-Fogh 1962 and Vincent 2002). Aside from the ionic composition (Rick et al. 1976; French et al. 2002), little is known of the receptor lymph inside the slits with respect to material properties and its possible flow out of the slits toward the extracellular spaces in the hypodermis and across the fibrous inner membrane.

It should be mentioned here that there is the dendrite of a second sensory cell. It ends at the inner, instead of the outer membrane of the slit without being obviously coupled to it (Barth 1971). The mechanical consequences of this difference between the two dendrites still are not fully understood (French et al. 2002; Molina et al. 2009).

Finite Element models

It is assumed that no external surface loads are acting, so that at positions close to the surface of the cuticular exoskeleton a plane stress state prevails, regardless of the shape of the surface. Because the majority of the lyriform organs are found laterally on the leg in areas with little curvature, the effects of the curvature of the cuticle were neglected. The slit geometries of actual lyriform organs were projected to a plane (2D) and their real shapes known from scanning electron micrographs (Müllan 2005) were approximated by elongated openings of constant width with smoothed faces and rounded ends. Unless stated otherwise, the slit face deformations D_d were evaluated at the positions corresponding to those of the dendritic endings in the covering membrane of the slit. The length of the longest slit in a given arrangement was denoted as l_0 . Square discs of size $400 l_0 \times 400 l_0$, at the centers of which the slits were located, were used. This large size of the disks compared to the slit lengths was chosen to avoid boundary effects on the slit face displacements. The Finite Element program

ABAQUS/Standard (Simulia, Providence, RI) was used and all models were meshed with six-noded triangular plane stress elements. Convergence studies were performed and as a result the meshes were strongly refined in the vicinity of the slits.

As discussed before, the cuticle was modeled as a linear elastic in-plane isotropic material. It was assumed that both the fluid inside the slits and the membranes, which are several orders of magnitude softer than the exocuticle, have negligible influence on the slit face displacement under static loading. The present study deals with static loading only. We expect that the fluid inside the slits plays a role in the tuning of actual lyriform organs to dynamic load stimuli (which are not the subject of the present investigation) in a certain frequency range.

The maximum local physical strains in our models were small and similar to those occurring in the cuticle of arachnids under natural loads (Blickhan and Barth 1985; Brüssel 1987), -1.2×10^{-4} ($=-120 \mu\epsilon$), so that all analyses were carried out under the assumption of linear structural behavior.

The models were loaded by prescribed compressive reference far-field strains of $\epsilon_{a,r} = 2.5 \times 10^{-5}$ ($=25 \mu\epsilon$) acting in x -direction along the vertical edges (Fig. 1a). Since linear analysis was used, biaxial load cases can generally be derived from the solutions for these uniaxial load cases by proper superposition. The boundary conditions were completed by allowing the horizontal edges to deform freely. This compressive strain is in the low range of physiologically meaningful values (Blickhan and Barth 1985; Brüssel 1987) and corresponds to an overall uni-axial compressive stress of $\sigma_{a,r} = 4.5 \times 10^5$ Pa. For an easy adaptation to any configuration, we normalized the results to a reference slit face displacement $D_{sc} = 5.034 \times 10^{-5} l_0$, which pertains to the mid-length of a single isolated slit of length l_0 and an aspect ratio $l_0/b = 100$, subjected to a strain $\epsilon_{a,r}$. Series of analyses were carried out in which the slit arrays were rotated within the disk to simulate their behavior under uni-axial stresses acting in different directions. For an example on how to scale the results to a configuration with given l_0 , far-field strain ϵ_a or far-field stress σ_a , see Höbl et al. (2007).

Due to loading by the far-field strain $\epsilon_{a,r}$, the slits are deformed. In each slit, two points occupying opposite positions in the undeformed state predominantly move perpendicularly to the slit faces, leading to a reduction of the slit's width (slit compression) from b in the undeformed configuration to b' in the deformed configuration. Here and in the following, the reduction of the slit's width is referred to as the "slit face deformation" $D = b - b'$. The slit face deformation at the position of the dendrite is called D_d . For details see Höbl et al. (2007).

Note that the load angle Φ is measured relative to the longitudinal axis of slit 1 in each arrangement. In the

combination of the organs HS8 and HS9 (Fig. 6a), the reference slit is slit 1 of lyriform organ HS8.

White-light interferometry

To compare the calculated slit face deformations with those of real lyriform organs, organ HS8 on the tibia of *Cupienius salei* (Barth and Libera 1970) was monitored using white-light interferometry together with the controlled application of known forces. In white-light interferometry, light from the microscope is divided within the microscope objective. Part of the light is directed to the test surface, another part to a reference test surface inside the apparatus. Then, the light paths are directed onto a camera, which captures the interference fringes resulting from the two wavefronts, indicating the surface structure of the examined specimen. In the scanning white-light interferometer used (zygo NewView 5010), the objective of the microscope is moved vertically with a piezoelectric transducer. The continuous recording of the interference patterns results in a series of interferograms, from which the three-dimensional surface structure of the tested specimen is evaluated with the device's software (MetroPro).

Intact adult females of *C. salei* were restrained to a metal plate with adhesive tape with their ventral side up. The tibia of the second right walking leg was embedded in a mixture of colophony and beeswax up to 3 mm from the joint with the metatarsus, its posterior aspect with the lyriform organ HS8 facing up. Cuticular hairs were removed by smoothly wiping with a pad of cotton. The metal plate with the spider was then fixed to the stage of the scanning white-light interferometer. The metatarsus was coupled to a force transducer (FORT 10, World Precision Instruments) with an insect pin waxed to its dorsal side. A motorized micromanipulator (DC3001 R, WPI; control unit MS314, MW) coupled to the force transducer was used to flex the metatarsus so as to subtend an angle of $\alpha = 130^\circ$ with the tibia (Fig. 1b). This arrangement had also been used in previous electrophysiological studies of the same organ (Barth and Bohnenberger 1978; Bohnenberger 1981). The deflections of the metatarsus in the posterior direction were applied to the insect pin in steps of 100 μm at a distance of 22 mm from the pivot point of the joint, resulting in an increase in the angle θ by 0.26° per step (Fig. 1b). Force measurements were recorded continuously and stored on the hard disk of a computer using an analog/digital converter (Biopac MP100, Software ACQ 3.7, sampling rate 500 Hz). The slit's morphology was viewed with the scanning white-light interferometer only 1 min after each force increase to reach constant force and imaging conditions. The blurring of the interference image and the concurrent quick decrease of the recorded forces after an initial peak can be attributed to the hysteresis of the joint material shown by Blickhan (1986).

Force values were measured from the start of the interference scan (1 min after load application) as the mean value for the following 10 s (standard deviations smaller than 1%). The in-plane image resolution was 0.11 μm per pixel and that in the out-of-plane direction 0.1 nm. Therefore, the initial width of a slit of about 2 μm in the unloaded organ was sufficiently well resolved by about 20 pixels. Slit face deformation was analyzed at the positions of the dendrites as relative and absolute change in slit width b in the direction normal to the slit long axis by using image metrology software (SPIP 4.1.1).

Results

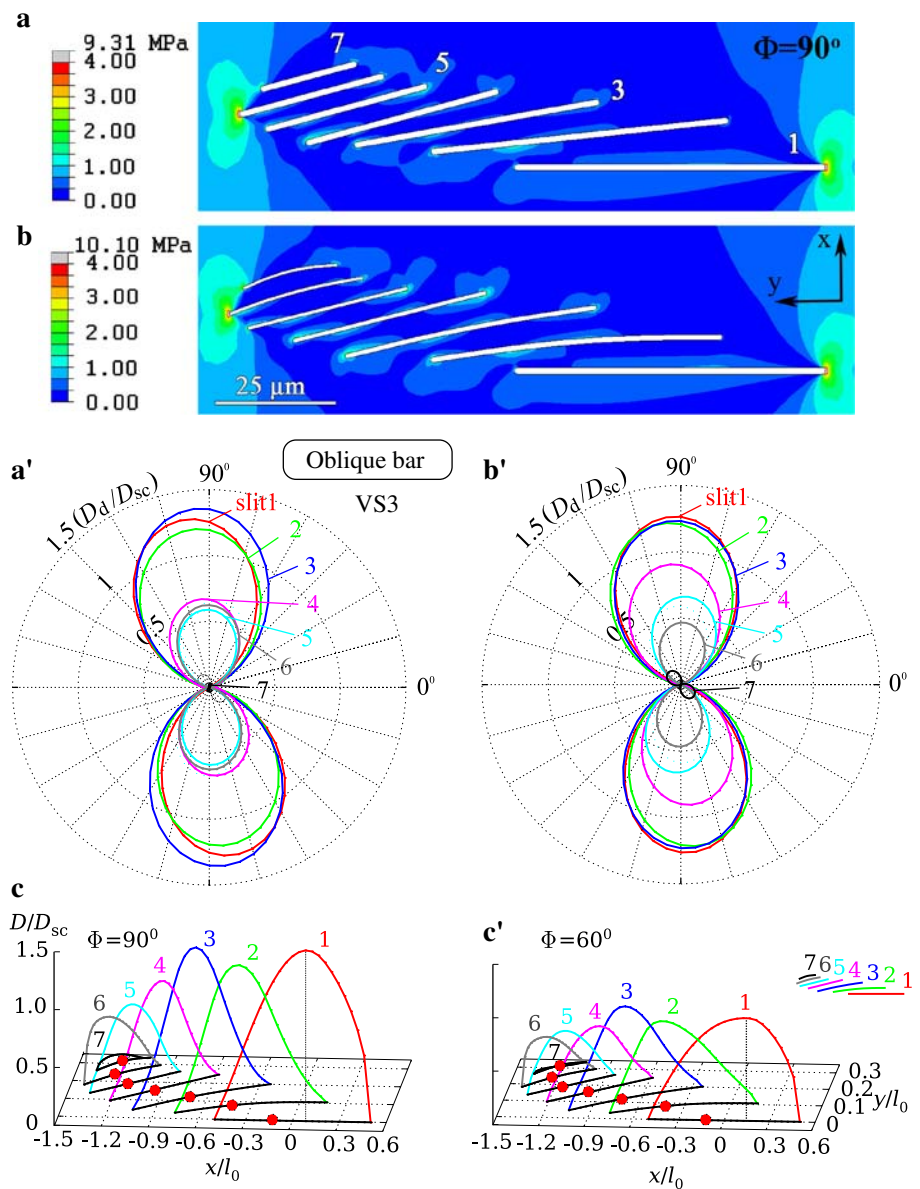
Directional dependence of the face deformations of natural slit patterns

The mechanical responses of some basic simplified slit formations, e.g., oblique bar, triangular, and fan-like arrangements, have been presented earlier (Höbl et al. 2007). We now investigated models of lyriform organs with the same basic arrangements of slits, but also showing the morphological details of the natural cases. For the geometrical parameters describing the tested slit arrays, see Fig. 1a.

Oblique bar formations

In oblique bar formations, the face deformations of the individual slits are very similar, provided the slits are of equal length (Barth et al. 1984). A slightly simplified natural arrangement and a more realistic planar geometry based on the organ VS3 are shown in Fig. 2a and b, respectively. The organ was modeled with straight slits of equal width at longitudinal shifts of $\lambda/l_0 = 0, -0.29, -0.62, -0.86, -1.04, -1.15$ and -1.16 (Fig. 2a), and with slightly curved slits of varying widths at $\lambda/l_0 = 0, -0.3, -0.64, -0.9, -1.1, -1.2$ and -1.22 (Fig. 2b) corresponding to SEM images of VS3. Figure 2a' and b' compare the responses of these arrangements and indicate that minor variations in the curvatures of the slits can considerably influence their face deformations. An obvious effect is the more even distribution of mechanical sensitivity among the shorter slits 4–7. In contrast to the findings of Höbl et al. (2007), where all five parallel slits of equal length respond to similar ranges of loads, in Fig. 2a' slits 1–3 and slits 4–6 form two groups covering two different ranges of compressive loads. When the morphology of the organ is modeled in even more detail, i.e., by using C-shaped slits of varying width (Fig. 2b), slits 4–6 are no longer adjusted to similar load levels, but their mechanical response is more evenly distributed in the range of the

Fig. 2 Results of FE simulation of the directional sensitivities of the seven neighboring slits in lyriform organ VS3, whose arrangement represents the “oblique bar” type. Von Mises equivalent stresses (MPa) in simple (a) and detailed models (b) representing organ VS3 under loads acting normally to the longitudinal direction of slit 1 ($\Phi = 90^\circ$). a' and b' Directional mechanical sensitivity to uni-axial compressive far-field loads of the simple and detailed models. Mechanical sensitivity is given as the ratio between slit face displacement at the dendrite's position (D_d) and the slit face displacement at mid-length of a single isolated slit (D_{sc}). c and c' Slit face deformation $D(x)$ relative to D_{sc} along the seven slits of the organ. Note positions of the dendrites (red filled circles)



magnitudes of the face deformations of the entire organ (Fig. 2b'). The similarities in the directional response emerge clearly when the von Mises equivalent stress (which is a scalar measure of the stress tensor) in the models is compared (Fig. 2a, b). Small differences are mostly seen in the maximum von Mises stresses close to the tips of the slits. In both arrays, slit 7 shows only small face deformations, implying that in real organs it sends signals to the central nervous system under very high loads only. This was expected because slit 7 is arranged almost symmetrically ($\lambda = 0.01$) relative to its much larger neighbor, slit 6, and is therefore heavily shielded from one side (compare Fig. 2a, b) similarly to the smallest slit in a symmetric triangular arrangement of five parallel slits (Höbl 2007). In addition, slit 7 is also much shorter than slit 6, which also decreases its sensitivity.

Dendrite position

To relate the positions of the dendrites to the positions of the maximum slit face displacements, the deformations of the slit faces $D(x)/D_{sc}$ were plotted along the slits (Fig. 2c, c') for the slit arrangement shown in Fig. 2b. In Fig. 2c, the load direction is normal ($\Phi = 90^\circ$) to the longest slit (slit 1), similar to the load direction a single isolated slit is most sensitive to. In Fig. 2c', the results for $\Phi = 60^\circ$ show the dependence of the face deformations along the slits on the load direction. The magnitudes of $D(x)/D_{sc}$ change in a similar way in all slits. However, the positions of the maximum slit face deformations are shifted. For example, in slit 2 of the model based on VS3, the distance between the center of the slit and the location of the maximum slit face displacement changes from $-0.11 l_0$ to $-0.19 l_0$ (=8% of l_0) when the load direction

changes from $\Phi = 90^\circ$ to 60° (Fig. 2c, c'). However, whereas a change in loading direction affects the values of the slit face displacements, the total directional range of loads detected by the organ remains the same (Fig. 2a', b').

Triangular slit arrangements

In triangular slit arrangements, a longitudinal shift λ/l_0 (see Fig. 1a) is required to move the shorter slits out of the shielding zone of the longer slit. In real slit formations, the slits indeed show a conspicuous tendency to be slightly shifted longitudinally as exemplified by the triangular arrangement VS4 (Fig. 3a). Here, the length of slit 1 is l_0 and that of slit 2 is $0.84 l_0$, which in combination with a longitudinal shift of $\lambda/l_0 = 0.14$ moves the left tip of slit 2 out of the shadow of slit 1 by a distance of $0.06 l_0$ (Fig. 3a). Close to $\Phi = 90^\circ$, the ranges of magnitude of the face deformations of the individual slits are more or less evenly distributed over the entire range of the mechanical sensitivity of the organ (Fig. 3b).

The slits are most sensitive to uni-axial loads acting in directions between $\Phi = 60^\circ$ and 105° . In contrast to the model based on organ VS3, in the model of organ VS4 the amount of change in the slit face deformations along the slits is different in each slit when Φ is altered. Thus,

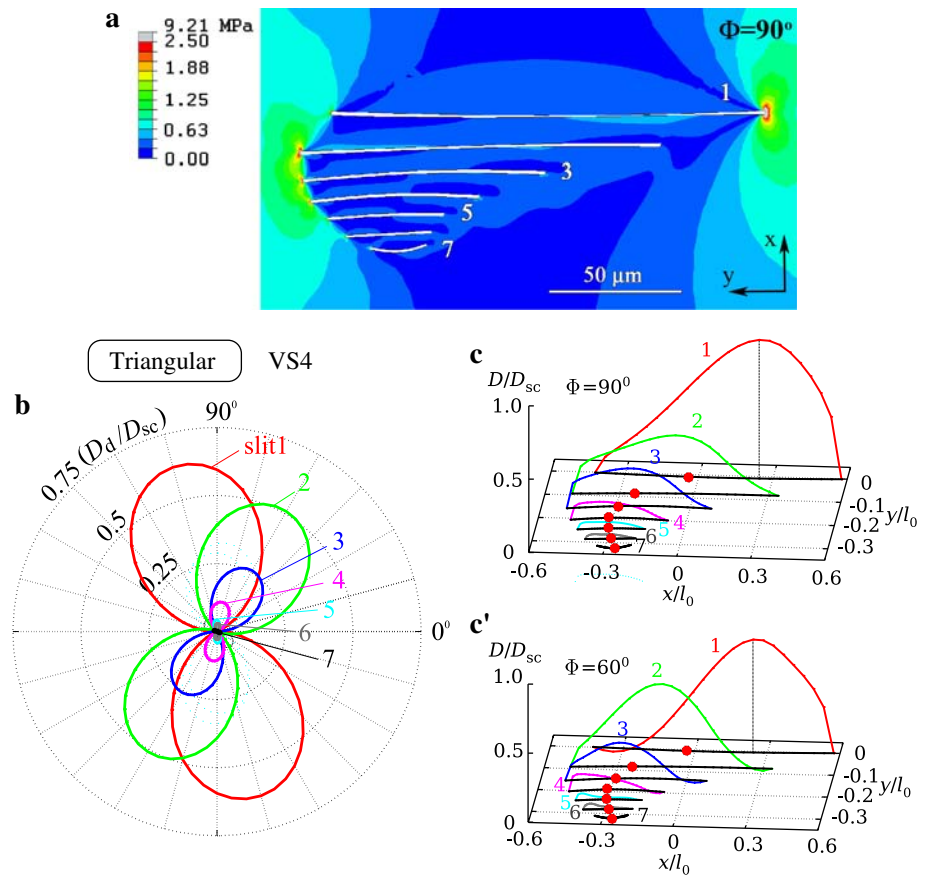
$D(x)/D_{sc}$ strongly increases in slit 2 and decreases in slit 1 when the load direction changes from $\Phi = 90^\circ$ to 60° . The change in positions of the maximum displacements along the slits between the load directions of $\Phi = 90^\circ$ and 60° is less than approximately 2% (Fig. 3c, c'), which is smaller than in VS3. In arrangement VS4, even a small change in the direction of a far-field uni-axial stress influences the face deformations of the slits.

In a model representing organ VS5 of *C. salei* (Fig. 4a) loaded at an angle of $\Phi = 90^\circ$, the slit face deformation at the dendrite of the longer slit is roughly three times the value of that of the shorter slit (Fig. 4a'). In the bird spider *Aphonopelma* sp., this organ has a similar orientation and is located at the same position on the tibia. However, in contrast to that of *C. salei*, it consists of eight slits that are arranged in a triangular pattern (Fig. 4b). According to their face deformations at $\Phi = 90^\circ$, the slits form two groups (slits 1, 2 and 3 vs. slits 4, 6 and 7), which show a ratio of slit face deformations of $1/3$ ($D_d/D_{sc} \approx 0.39$ and ≈ 0.13 , respectively, Fig. 4b').

Fan-like slit patterns

Amplification and shielding effects determine the slit face deformations and the directional response in the model of a

Fig. 3 **a** Von Mises equivalent stresses (MPa) at slits arranged as in lyriform organ VS4 of *C. salei* and loaded at $\Phi = 90^\circ$ (perpendicularly to the slit). **b** Directional mechanical sensitivity of slits under uni-axial compressive far-field loads. **c** and **c'** Slit face deformation along slits for $\Phi = 90^\circ$ and 60°



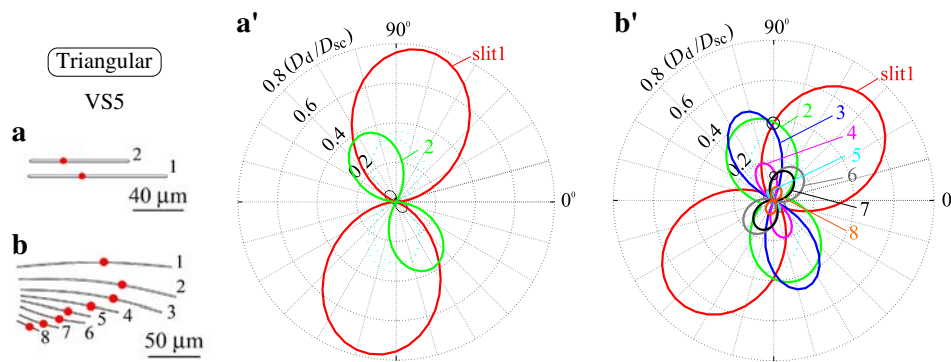


Fig. 4 Comparison of models based on organs VS5 of **a** *C. salei* and **b** the bird spider *Aphonopelma*. **a'** Face deformation of the smaller slit is 1/3 the value of the longer slit at $\Phi = 90^\circ$. **b'** Slits 1, 2 and 3 and slits

4, 6 and 7 form groups of mechanical sensitivity measuring similar load levels each at $\Phi = 90^\circ$ (black circles). Slit face deformation evaluated at the locations of the dendrites (see red filled circles in **a** and **b**)

fan-like slit pattern based on a lyriform organ on the chelicera of *C. salei* (Fig. 5a). Accordingly, the D_d/D_{sc} value of the longest slit is 1.2 at a load direction of $\Phi = 90^\circ$ and that of the smaller slits is less than 0.16 for Φ between approximately 80° and 150° (Fig. 5b). Loads acting in directions between $\Phi = 15^\circ$ and 30° are only detected at high magnitudes ($D_d/D_{sc} \approx 0.035$). This illustrates the very directional mechanical sensitivity of this slit pattern for low to moderate loads ($D_d/D_{sc} = 1.2$), and the more omni-directional response at high loads ($D_d/D_{sc} \leq 0.08$), which is in contrast to the idealized fan-like slit arrangements presented in Höbl et al. (2007). The reason for this difference in behavior may be found in the graded slit lengths in the lyriform organ on the chelicera.

The measured and simulated slit face deformations of organ HS8

Interaction with HS9

Lyriform organs may be positioned in close neighborhood so that interaction effects between the organs may be encountered (Barth and Libera 1970). On the posterior face of the tibia of *C. salei*, two triangular lyriform organs, HS8 and HS9, are found in close proximity (Fig. 6a). The orientations of the two organs differ by approximately 26° and their distance from each other is approximately the size of the longest slit in the arrangements. Therefore, in agreement with Höbl et al. (2006), interaction effects are to be expected between the organs. Two different models were built, one containing both lyriform organs, HS8 and HS9, and the other only HS8. The comparison of the predictions of the two models shows obvious interaction effects, which pertain to the magnitudes of D_d/D_{sc} of the slits 1–3 only (Fig. 6c, d). According to these simulations using planar FE models of HS8 (Fig. 2d) and of HS8 interacting with HS9 (Fig. 6b, c), the slits are most sensitive to uni-directional

loads at angles between approximately $\Phi = 60^\circ$ and 135° . The ranges of stress magnitude to which HS8 and HS9 respond overlap and cannot clearly be separated.

Comparison with the original organ

Because organ HS8 is easily accessible to measurements in live spiders and its mechanical stimulation can be well controlled, the results of interferometric measurements can meaningfully be compared with FE predictions. Figure 7a shows how slit width changes with the deflection angle of the metatarsus for the seven slits composing organ HS8, as evaluated from white-light interferometric images (Fig. 7b, b'). Measured values of the slit face deformations and of the applied force (symbols) as well as quadratic regression curves (lines) are given as functions of the angle θ . At a lateral force of 4 mN, which corresponds to a deflection of the metatarsus by $\theta = 3.8^\circ$, the longest slit (slit 1) is compressed by approximately 860 nm ($\approx 39\%$). When the load is further increased to 10 mN, which corresponds to a deflection angle $\theta = 9.3^\circ$, even the shortest slit (slit 7) in the arrangement is deformed by approximately 80 nm. Since the average strain of the organ is dominated by the deformations of the slits, it can be approximated by the sum of the measured slit face deformations divided by the width of the organ, which for HS8 is approximately 100 μm. For a deflection angle of the metatarsus of $\theta = 0.75^\circ$ (which falls within the detail in Fig. 7), where the regression curves for the face deformations are practically linear, the sum of the slit face deformations evaluated at the location of the dendrites is approximately 555 nm (Fig. 7a), which gives an average strain at the location of the organ of -5.55×10^{-3} ($= -5,550 \mu\epsilon$).

The model of the organ predicts the most uniformly spaced sequence of activation of individual slits for a loading angle of $\Phi \approx 110^\circ$ (Fig. 6c), which is taken to be the direction of maximum sensitivity to uniaxial far-field loads

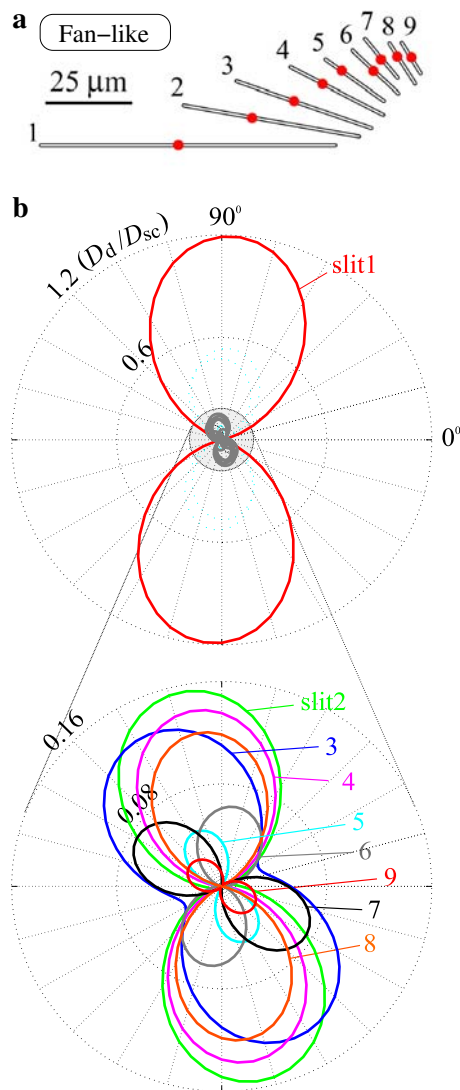


Fig. 5 **a** Hybrid fan-like triangular slit pattern based on cheliceral lyriform organ of *C. salei*. **b** Directional mechanical sensitivity to uni-axial compressive far-field loads

and is used in the following comparisons. When the planar FE model of HS8 is loaded by a far-field strain of $\varepsilon_{a,r} = -2.5 \times 10^{-5}$ acting at $\Phi = 110^\circ$, an average strain at the position of the organ of approximately -4.49×10^{-5} ($= -44.9 \mu\varepsilon$) is predicted. Accordingly, for the model, the far-field strain required for obtaining the above average strain at the position of the organ, -5.55×10^{-3} , is evaluated as $\varepsilon_{a,r} = -3.09 \times 10^{-3}$ ($= -3,090 \mu\varepsilon$). Using this applied strain, the face deformation of slit 1 is predicted to be approximately 206 nm (Fig. 8a), which is close to the value of 218 nm (difference 5%) obtained by quadratic regression from the measurements on the actual organ (Fig. 8b). In addition, in the measurements and in the simulations, the sequence of the slits in terms of magnitude of

the face deformations corresponds closely to the sequence of slit lengths (Fig. 8a, b). This indicates that the models used for FE analysis are well suited to estimating the slit face deformations of real lyriform organs.

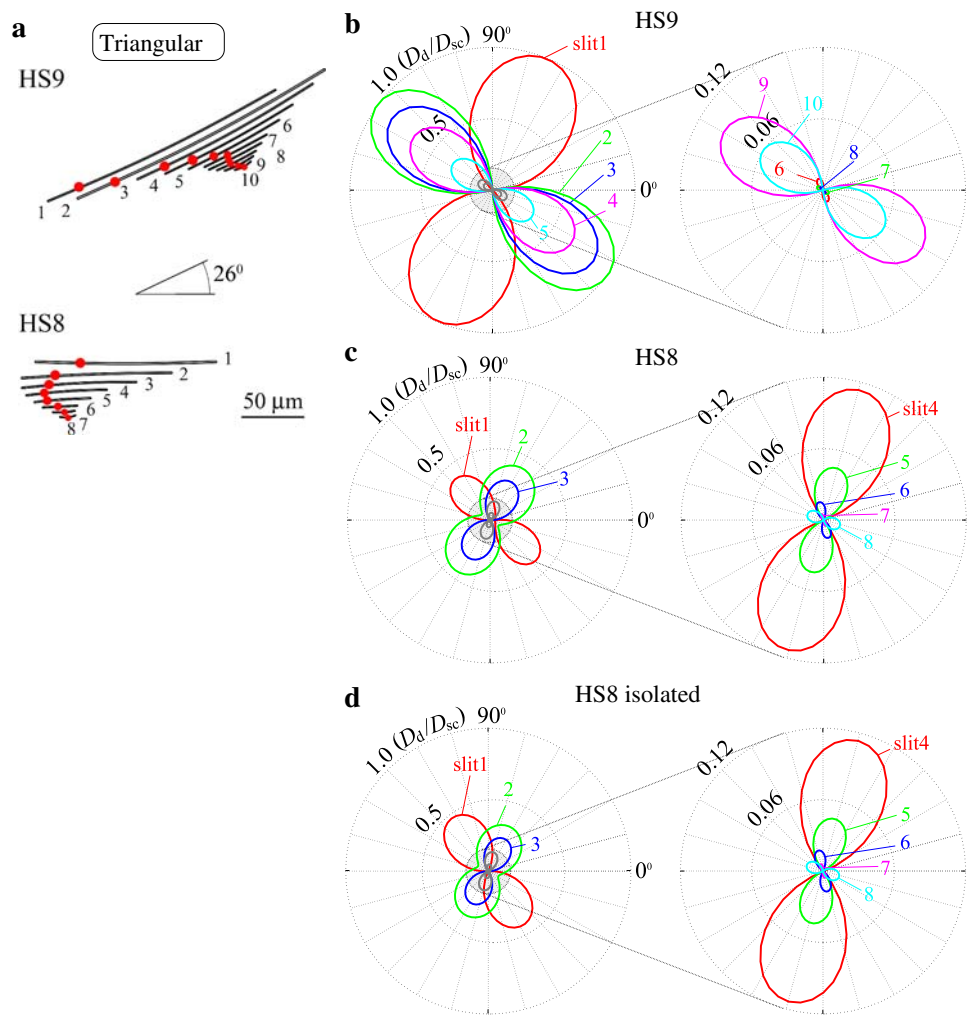
In Fig. 7a, the regression curve for the force closely approaches a linear dependence on the deflection angle of the metatarsus with F [mN] = 1.06θ [°]. The threshold deflection angles of the metatarsus, which elicit nervous impulses of the sensory cells, as previously measured electrophysiologically (Barth and Bohnenberger 1978), were all below 1° . The slit face displacements corresponding to these threshold angles and derived from our interferometric data are ≈ 1.7 nm for slit 2, ≈ 14 nm for slit 3, ≈ 37 nm for slit 4, ≈ 43 nm for slit 5, and ≈ 10 nm for slit 6 (see filled black circles in detail of Fig. 7a).

Interactions between a lyriform organ and a closely positioned loose group of slits

After having investigated the mechanical interaction of two neighboring lyriform organs (HS8 and HS9), we now ask for the interaction effects between a lyriform organ and a nearby loose group of slits. The example chosen is the triangular lyriform organ HS3. Here, the closest longitudinal distance between the organ HS3 and the slits of the loose group is $0.3 l_0$, and the closest lateral distance is $0.6 l_0$ (Fig. 9a). The interaction effects are clearly seen when comparing the response of HS3 (slits 1–11) in the presence (Fig. 9a, a'') and absence (Fig. 9b, b') of the nearby loose group (slits 12–27). The magnitudes of D_d/D_{sc} , the directions of maximum sensitivity, and also the order of the slits in terms of maximum mechanical sensitivity in the slit pattern change for the lyriform organ in the presence of the nearby loose group. Remarkably, slit 1 has a more omnidirectional response when the organ HS3 is isolated due to the absence of shielding by the slits of the loose group.

The combination of HS3 with the loose group of slits increases the working range and the directional sensitivity of the ensemble. The maximum slit face deformation in the loose group, in slit 13, is approximately 3.5 times larger than that of the longest slit, slit 1, of the lyriform organ. Accordingly, as load levels increase for $\Phi \approx 90^\circ$, first the slits of the loose group respond (Fig. 9a'), followed by the slits of the lyriform organ (Fig. 9a''). The highest sensitivities of the slits of the loose group are found at load directions close to $\Phi = 90^\circ$, whereas at larger loads a fine resolution of load direction between $\Phi = 0^\circ$ and 120° can be obtained by organ HS3. At $\Phi = 90^\circ$, slit 1 is shielded by the other slits in the arrangement (compare Fig. 9a, b). Slit 1 in HS3, in contrast to the remaining slits of the organ, is most sensitive at $\Phi \approx 10^\circ$ with and without the presence of the loose group of slits.

Fig. 6 Results of FE simulations on the directional sensitivities of neighboring lyriform organs, HS8 and HS9, on the tibia of *C. salei*. **a** Models of the organs, orientation, distance and locations of the dendrites (red filled circles) taken from SEM images. Distance between HS8 and HS9 is to scale. **b** Directional responses of the slits 1–10 of organ HS9 interacting with organ HS8. **c** Directional responses of the slits of organ HS8 interacting with organ HS9. **d** Response of the organ HS8 in isolation. The inner parts of the polar diagrams are shown in detail on the right



Discussion

Threshold stimulus amplitudes

Organ HS8 is unique among the lyriform organs with regard to the diversity of studies done on it. Apart from the present FE simulations and interferometric analyses, these include earlier electrophysiological studies (Barth and Bohnenberger 1978; Bohnenberger 1981). The results of all these studies agree in important aspects: (1) the amount of maximum slit face deformation found in the longest slit in the simulations is in good agreement with the interferometrically measured value (only 5% difference); (2) the order of the slits in terms of threshold stimulus amplitudes eliciting action potentials corresponds to the order of the magnitudes of slit face displacements found with both interferometry and FE modeling (Fig. 8). In the following, some quantitative details are given.

The threshold stimulus amplitudes reported in Barth and Bohnenberger (1978) correspond to slit face displacements of ≈ 43 nm (slit 4) or less. For slit 2, which is the most

sensitive slit analyzed electrophysiologically in HS8, the physiologically effective threshold stimulus amplitude corresponds to a slit compression of 1.7 nm only (Bohnenberger 1981). This is close to the value of 3 nm as estimated for slit 1 by Blickhan (1983) when exposed to natural strains (-1.4×10^{-5} or $-14 \mu\epsilon$) measured with micro strain gauges in live spiders during slow locomotion. Our FE simulations show a slit face deformation of 1.7 nm of slit 2 ($D_{sc} = 8.6$ nm) at $\Phi \approx 110^\circ$ for an applied uni-axial far-field strain of -1.8×10^{-5} ($-18 \mu\epsilon$), which again is well within the range measured by Blickhan and Barth (1985). The deformation values now found for the slit sensilla can be compared to those obtained from recent micro-mechanical studies (Schaber and Barth, in preparation) on spider airflow sensors (trichobothria). The deflection of the hair shaft of these sensors at the site of stimulus transduction is about 6 nm/ $^\circ$ and only 0.06 nm at the lowest physiologically effective hair deflection of 0.01 $^\circ$ (Barth and Höller 1999), a displacement value similar to those known for insects (Gnatzy and Tautz 1980; Thurm 1982). Larger values are found for the compression of slit sensilla. However,

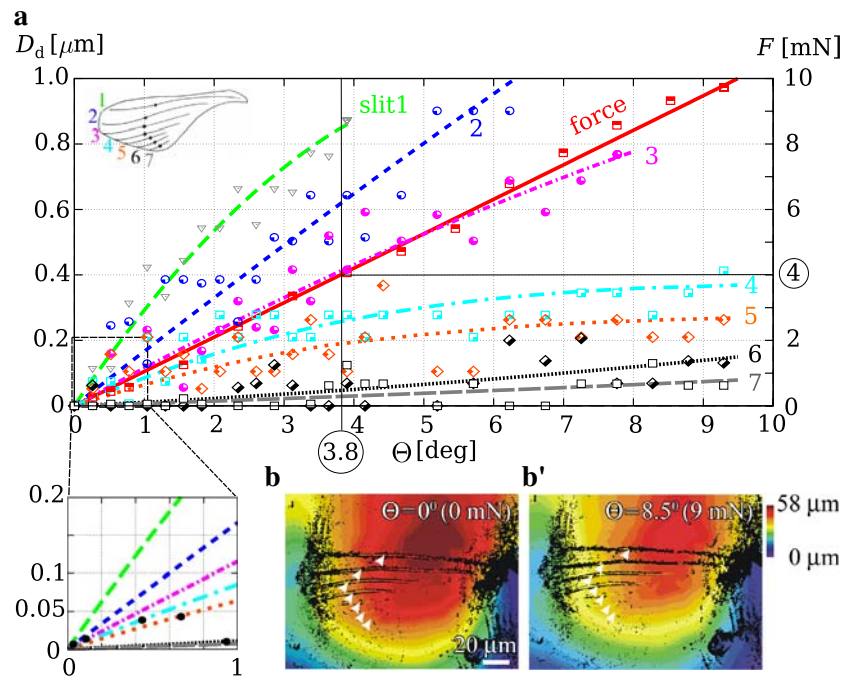


Fig. 7 **a** Slit face deformations D_d in lyriform organ HS8 of *C. salex* measured using white-light interferometry. Note linear increase of force (scale on right side of the diagram) required to deflect the metatarsus by angle Θ (solid red line). Experimental results are given as symbols, and the lines are quadratic regression curves. Black dots in enlarged detail indicate deflection angles Θ for the electrophysiologi-

cally measured threshold stimulus amplitudes of slits 2–6 (Barth and Bohnenberger 1978). **b** White-light interferometric images of lyriform organ HS8 in undeformed and **b'** deformed condition ($\Theta = 8.5^\circ$). Color code represents distance in out-of-plane direction; arrowheads point to the attachment sites of the dendrites where the widths of the slits were measured

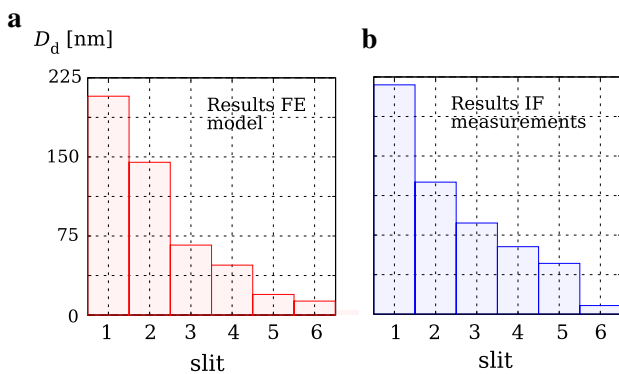


Fig. 8 Face deformations of the slits of organ HS8 at a deflection angle of the metatarsus of $\Theta = 0.75^\circ$ according to **a** FE analysis at $\Phi = 110^\circ$, scaled to a far-field strain of $\epsilon_{a,r} = -3.09 \times 10^{-3}$ (compare Fig. 2c) and **b** interferometric (IF) measurements

these displacements are scaled down on their way to the dendrite proper (Barth 2002).

Blickhan (1986) reported a nonlinear and hysteretic relationship between the force applied at the tip of the metatarsus and its deflection (maximum ca. 20°), different from the linear response shown in Fig. 7. This discrepancy is probably due to the visco-elastic material behavior of the cuticle and the fact that Blickhan (1986) used cyclic loads, whereas our measurements were quasistatic.

From simple generalized to more realistic slit patterns

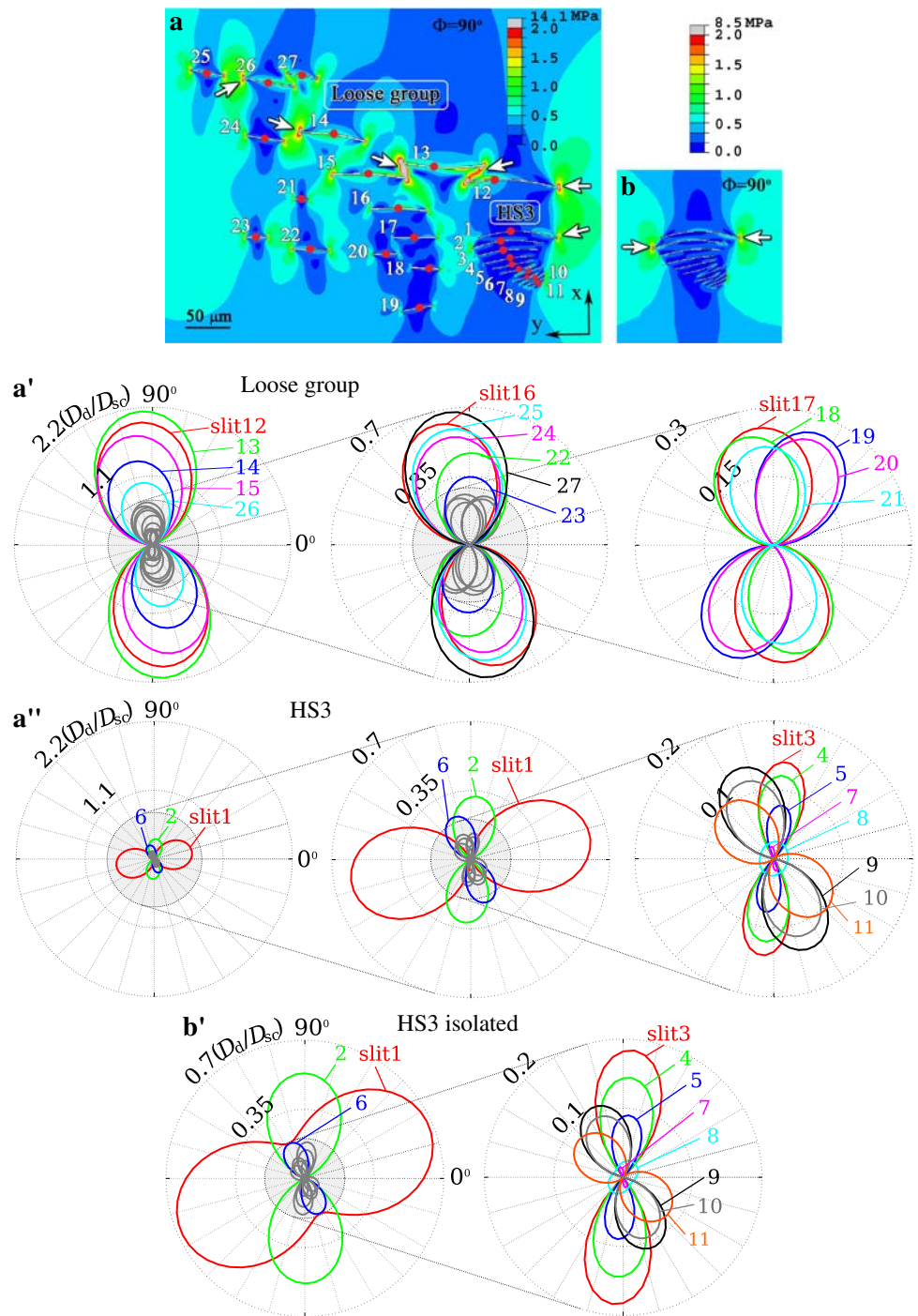
Generalized patterns

The generalized patterns of lyriform slit sense organs previously examined (Barth et al. 1984) are: (1) oblique bar formation (slits of equal length, but laterally shifted and all of them sensitive to same load magnitude and direction; potential increase of the signal to noise ratio by central convergence of nervous signals); (2) triangular patterns (slits of graded length; considerable increase of working range for load magnitude as compared to a single slit); (3) heart shaped or fan-like arrangements (with the potential of sensing load direction based on the patterns of active slits).

Broken symmetry

For slits spaced as closely as in actual lyriform organs ($S/l_0 = 0.04$), symmetric triangular arrangements cannot be used for range fractionation, that is, for measuring different neighboring response ranges for load magnitudes, because all shorter slits are too strongly shielded by the longest slit (Höbl et al. 2007). However, even a slight longitudinal shift between the largest slit and its neighbor, which is a prominent feature of most arachnid lyriform organs

Fig. 9 Von Mises stresses (MPa) at organ HS3 on the coxa of *C. salei* loaded at $\Phi = 90^\circ$ and interacting with a loose group of slits. **a** HS3 near loose group of slits, **b** isolated lyriform organ HS3. Regions of high stresses are shown in red and regions of low stresses in blue; white arrows point to regions of highest stresses. **a'** and **a''** Directional mechanical sensitivity of the organ HS3 interacting with the slits of the loose group. **b'** Directional response of slits of HS3 in absence of the loose group. Red dots indicate dendrite positions



(see e.g., organ VS4, Fig. 3a), effectively reduces this effect. Remarkably, the slits of an asymmetric triangular arrangement can also be used to measure similar load magnitude ranges, employing slits of different length (see e.g., organ VS5 of the bird spider *Aphonopelma*, Fig. 4b, b'). This characteristic was so far thought to be typical only for oblique bar formations (Barth et al. 1984; Höbl et al. 2007).

Lyriform organs and nearby groups of slits

Mechanical interactions between loose groups and lyriform organs and between neighboring lyriform organs must be expected if the minimum distance between them is less than approximately three times the length of the longest slit in the arrangement (Höbl et al. 2006). There are several examples found on the walking legs of *C. salei* where this is the

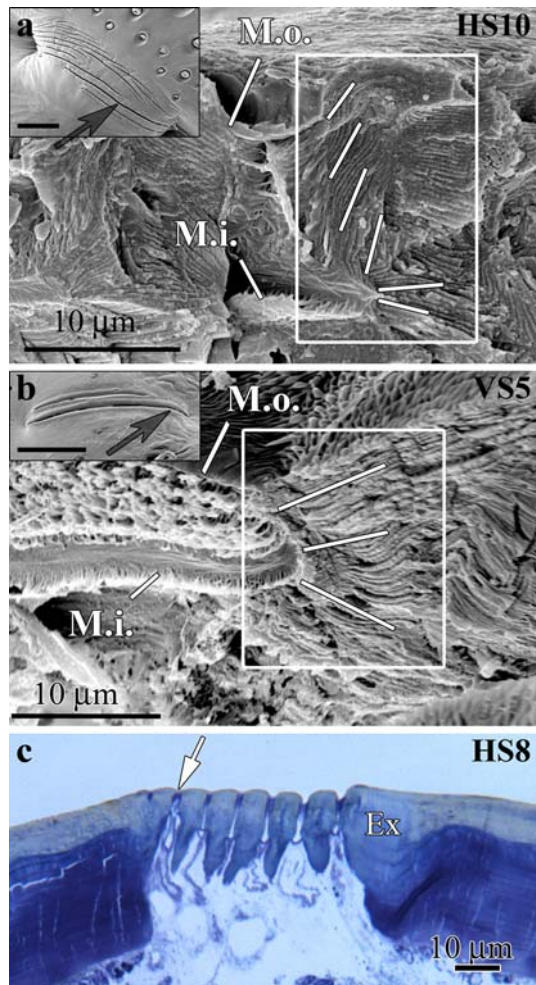


Fig. 10 Structural details of tibial lyriform organs VS5 and HS8 and of the metatarsal organ HS10 of *C. salei*. **a** SEM surface image of organ HS10 (inset) and of fracture perpendicular to its slits. **b** SEM surface image of organ VS5 (inset) and of the fracture along the long axis of the longer slit. **c** Semi-thin section normal to the longitudinal axes of HS8 slits close to the location of dendrite of the smallest slit (see *arrow*) in the arrangement (Müllan 2005). *Black arrows* in the insets of (a) and (b) point to the location of the fracture. *White lines* in (a) and (b) indicate the orientations of cuticular lamellae. *Ex* exocuticle, *M.o.* outer membrane, *M.i.* inner membrane. The length of the *scale bars* in the insets corresponds to 50 μm

case (Barth and Libera 1970). In most of these cases, triangular formations of lyriform organs are involved. The principle behind the close neighborhood between lyriform organs or between lyriform organs and loose groups appears to be an increase of the working range regarding load levels in a particular region of the exoskeleton (Figs. 6, 9). Interacting lyriform organs are found in stiffening rings (e.g., organs HS8 and HS9, Fig. 6), whereas interacting arrangements of a lyriform organ and a loose group are found in flat regions of the exoskeleton (e.g., organ HS3, Fig. 9).

Because the closest distance between neighboring slits in loose groups is typically ≥ 0.25 times the length of the

longest slit in the group, interaction effects are much less pronounced than in lyriform organs. Therefore, although extending over a larger area, a loose group has the advantage of the slit face displacements being less sensitive to changes of the geometrical arrangement of the slits with respect to each other, i.e., position, orientation and length of the slit. This implies a high diversity in the number, position, and size of the slits within such arrangements, which indeed can be found when the loose group investigated here is compared to those presented in Barth and Libera (1970).

Dendrite positions

In models imitating lyriform organs, the maxima of the slit face displacements typically are not found at the mid-length of the slits due to the broken symmetry of the slit patterns and the gradations in the length of the slit (Figs. 2c, c'; 3c, c'). In general, when the direction of a uni-directional load is altered, the positions of the maxima of the face deformations along the slits change as they do in generic slit arrangements (Höbl et al. 2007). For instance, in slit 1 of organ VS3, the difference between dendrite position and maximum face displacement is approximately $0.18 l_0$ for $\Phi = 90^\circ$ and $0.22 l_0$ for $\Phi = 60^\circ$. This is less than the value of $0.29 l_0$ estimated earlier (Höbl et al. 2007) on the basis of a generic oblique bar formation consisting of five perfectly parallel slits of equal length. Even larger differences between the actual positions of the dendrites and the maximum face displacements predicted by the models were found for the triangular formation of VS4. For $\Phi = 90^\circ$ and 60° , the shift of the dendrite from the position of maximum face displacement in slit 1 is approximately $0.37 l_0$. Therefore, in agreement with Barth et al. (1984) and Höbl et al. (2007), even in the more refined models based on the projected geometries of real lyriform organs, the positions of the maximum slit face displacements, which depend on the loading direction, do not always correspond exactly to the positions of the dendrite attachment sites in real organs. This may indicate that they are designed for maximum sensitivity to loads from a certain range of directions. Vice versa, the dendrite positions in the individual slits may indicate the main load direction to be expected under natural conditions.

Stress concentration factors

Because slits represent openings in the cuticle, these give rise to local stress concentrations at their ends, which can be described by stress concentration factors ($\text{SCF} = \text{local maximum equivalent stress/far-field stress}$) (Peterson 1974). Obviously, the slit sensilla of spiders keep the SCF at safe levels that do not give rise to failure of the cuticular material. Dangerous stress concentrations in the exocuticle are

Table 1 Predicted stress concentration factors (SCF) at the tips of the slits cut into homogeneous plates of constant thickness

| Slit formation | Load direction Φ (deg) | SCF |
|--|-----------------------------|------|
| Single isolated slit (aspect ratio = 100) | 90 | 21.9 |
| Single isolated slit (aspect ratio = 2.5) | 90 | 4.2 |
| Single isolated ellipse (aspect ratio = 2.5) | 90 | 5.96 |
| VS3 (straight slits) | 95 | 20.7 |
| VS3 (detailed model) | 95 | 23 |
| VS4 | 100 | 19.5 |
| VS5 (<i>C. salei</i>) | 80 | 15.9 |
| VS5 (<i>Aphonopelma</i> sp.) | 45 | 15.6 |
| HS3 (isolated) | 10 | 17.3 |
| HS3 (neighboring loose group) | 10 | 19.5 |
| Loose group neighboring HS3 | 90 | 29.3 |
| HS8/HS9 | 145 | 25.9 |

Data pertains to single slits or ellipses and for slit arrangements studied within the present work. For the definition of the angle Φ see Fig. 1

probably avoided by the particular alignment of the lamellae (Barth 1972, 1973) and the chitinous microfibrils (Müllan 2005) close to the slits, which can be visualized by fracturing the cuticle along and transversely to the slits (Müllan 2005) as shown for organs HS10 (Fig. 10a) and VS5 (Fig. 10b). Typically, the lamellae are not parallel to the surface of the cuticle close to the slits. In addition, the exocuticle is thickened in regions where stress concentrations may be expected, as shown by semi-thin sections (Fig. 10c).

Fringe plots can be used to visualize the stress concentrations within arrangements of slits obtained with our models, which do not fully describe the complex morphology of lyriform organs, but rather homogeneous, in-plane isotropic plates of constant thickness. Under these conditions, the SCF depend on the radii of the rounded ends of the slits, on the slit aspect ratio, on the interaction between individual slits and on the loading direction. The SCF at the ends of a single isolated capped rectangular slit with an aspect ratio of $l/b = 100$ is about 22. When the aspect ratio is reduced to $l/b = 2.5$, the SCF decreases to 4.2, which is close to that of a circular opening (SCF = 3). For ellipses with aspect ratios of 2.5, as found in insect campaniform sensilla, an SCF of approximately 6 is found.

The results found in homogeneous plates of constant thickness indicate a correlation between the mechanical sensitivity of the slit sensilla (in terms of slit face deformation) and the SCF. High stress concentration factors are found when amplification effects between the slits determine the slit face displacements of slit sensilla. In the model of the loose group of slits closely neighboring organ HS3, the SCF is approximately 29 (max. $D_d/D_{sc} \approx 2.2$),

which is the highest value found in the present study (see Table 1). Note that there is a nonlinear relation between the D_d/D_{sc} and the SCF as seen from a comparison between HS3 and a single isolated slit (SCF ≈ 22 ; $D_d/D_{sc} = 1$).

Acknowledgments This study was supported by grant P16348 of the Austrian Science Foundation (FWF) to FGB and FGR. We thank Prof. S. Gorb and Prof. E. Arzt of the Max Planck Institute for Metals Research in Stuttgart, Germany, for providing the interferometry facilities and for their kind hospitality to CFS.

References

Agarwal BD, Broutman LJ (1990) Analysis and performance for fiber composites. Wiley, New York

Barth FG (1969) Die Feinstruktur des Spinneninteguments. I. Die Cuticula des Laufbeins adulter häutungsferner Tiere (*Cupiennius salei* Keys.). Z Zellforsch 97:137–159

Barth FG (1971) Der sensorische Apparat der Spaltsinnesorgane (*Cupiennius salei* Keys. Araneae). Z Zellforsch 112:212–246

Barth FG (1972) Die Physiologie der Spaltsinnesorgane. I. Modellversuche zur Rolle des cuticularen Spaltes beim Reiztransport. J Comp Physiol 78:315–336

Barth FG (1973) Microfiber reinforcement of an arthropod cuticle; laminated composite material in biology. Z Zellforsch 144:409–433

Barth FG (1981) Strain detection in the arthropod exoskeleton. In: Laverack MS, Cosens DJ (eds) Sense organs. Blackie, Glasgow, pp 112–141

Barth FG (2002) A spider’s world: senses and behavior. Springer, Berlin, Heidelberg

Barth FG, Bohnenberger J (1978) Lyriform slit sense organ: thresholds and stimulus amplitude ranges in a multi-unit mechanoreceptor. J Comp Physiol A 125:37–43

Barth FG, Höller A (1999) Dynamics of arthropod filiform hairs. V. The response of spider trichobothria to natural stimuli. Philos Trans R Soc Lond B 354:183–192

Barth FG, Libera W (1970) Ein Atlas der Spaltsinnesorgane von *Cupiennius salei* Keys Chelicerata (Araneae). Z Morphol Tiere 68:343–369

Barth FG, Pickelmann P (1975) Lyriform slit sense organ: modelling an arthropod mechanoreceptor. J Comp Physiol 103:39–54

Barth FG, Stagl J (1976) The slit sense organs of arachnids: a comparative study of their topography on the walking legs (Chelicerata, Arachnida). Zoomorphology 86:1–23

Barth FG, Wadeuhl M (1975) Slit sense organs on the scorpion leg (*Androctonus australis* L., Buthidae). J Morph 145(2):209–228

Barth FG, Ficker E, Federle HU (1984) Model studies on the mechanical significance of grouping in spider slit sensilla (Chelicerata, Araneida). Zoomorphology 104:204–215

Blickhan R (1983) Dehnungen im Außenskelett von Spinnen. PhD thesis, University of Frankfurt, Frankfurt am Main

Blickhan R (1986) Stiffness of an arthropod leg joint. J Biomech 19:375–384

Blickhan R, Barth FG (1985) Strains in the exoskeleton of spiders. J Comp Physiol A 157:115–147

Bohnenberger J (1981) Matched transfer characteristics of single units in a compound slit sense organ. J Comp Physiol A 142:391–401

Brüssel A (1987) Belastungen und Dehnungen im Spinnenskelett unter natürlichen Verhaltensbedingungen. PhD thesis, University of Frankfurt, Frankfurt am Main

Cocatre-Zilgen JH, Delcomyn F (1999) Modeling stress and strain in an insect leg for simulation of campaniform sensilla responses to external forces. Biol Cybern 81:149–160

- Flannigan WC (1998) Finite element modeling of arthropod exoskeleton. Master's thesis, Case Western Reserve University
- French AS, Torkkeli PH, Seyfarth E-A (2002) From stress and strain to spikes: mechanotransduction in spider slit sensilla. *J Comp Physiol A* 188:739–752
- Gnatzy W, Tautz J (1980) Ultrastructure and mechanical properties of an insect mechanoreceptor: stimulus-transmitting structures and sensory apparatus of the cercal filiform hairs of *Gryllus*. *Cell Tissue Res* 213:441–463
- Höbl B (2007) Mechanical simulation of slit sensors of arachnids. Doctoral Thesis, Vienna University of Technology
- Höbl B, Böhm HJ, Rammerstorfer FG, Barth FG (2005) Mechanoreception in the exoskeleton of arachnids: engineering meets biology. In: Proceedings of the 3rd IASTED Conference Biomech, Benidorm, 44–48
- Höbl B, Böhm HJ, Rammerstorfer FG, Müllan R, Barth FG (2006) Studying the deformation of arachnid slit sensilla by a fracture mechanical approach. *J Biomech* 39:1761–1768
- Höbl B, Böhm HJ, Rammerstorfer FG, Barth FG (2007) Finite element modeling of arachnid slit sensilla—I. The mechanical significance of different slit arrays. *J Comp Physiol A* 193:445–459
- Jensen M, Weis-Fogh T (1962) Biology and physics of locust flight - V. Strength and elasticity of locust cuticle. *Philos Trans R Soc Lond B* 245:137–169
- Molina J, Schaber CF, Barth FG (2009) In search of differences between the two types of sensory cells innervating spider slit sensilla (*Cupiennius salei* Keys.) *J Comp Physiol A* (in review)
- Müllan R (2005) Feinbau und Rekonstruktion der Cuticulastrukturen lyraförmiger Sinnesorgane der Spinne *Cupiennius salei*. Diploma thesis, University of Vienna
- Peterson RE (1974) Stress concentration factors. Wiley, New York
- Rick R, Barth FG, Pawel A (1976) X-ray microanalysis of receptor lymph in a cuticular arthropod sensillum. *J Comp Physiol* 110:89–95
- Skordos A, Chan C, Jeronimidis G, Vincent JFV (2002) A novel strain sensor based on the campaniform sensillum of insects. *Philos Trans R Soc Lond A* 360:239–254
- Thurm U (1982) Grundzüge der Transduktionsmechanismen in Sinneszellen. Mechano-elektrische Transduktion. In: Hoppe W, Lohmann W, Markl H, Ziegler H (eds) *Biophysik*. Springer, Berlin, pp 681–696
- Vincent JFV (1982) Structural biomaterials. The MacMillan Press Ltd., London
- Vincent JFV (2002) Arthropod cuticle: a natural composite shell system. *Composites Part A* 33:1311–1315
- Vincent JFV, Clift SE, Menon C (2007) Biomimetics of campaniform sensilla: measuring strains from the deformation of holes. *J Bionic Eng* 4:63–76

Addendum:
Molina et al. (2009) J Comp Physiol A 195:1031–1041

**In search of differences between the two types of sensory cells
innervating spider slit sensilla (*Cupiennius salei* Keys.)**

Jorge Molina^{1,2,*}, Clemens F. Schaber², Friedrich G. Barth²

¹ Departamento de Ciencias Biológicas, Universidad de Los Andes, Apartado Aereo 4976, Bogotá,
Colombia

² Department of Neurobiology and Behavioral Sciences, Life Sciences, University of Vienna,
Althanstraße 14, 1090 Wien, Austria

*Author for correspondence (jmolina@uniandes.edu.co)

Author contributions

JM and CFS designed the experiments, JM performed and analyzed the electrophysiological experiments, CFS provided the natural stimulus patterns, and JM, FGB, and CFS wrote the paper.

The following pages contain the final version published online September 17, 2009 and in print in November, 2009.

Citation:

Journal of Comparative Physiology A 195:1031–1041
doi: 10.1007/s00359-009-0477-9

In search of differences between the two types of sensory cells innervating spider slit sensilla (*Cupiennius salei* Keys.)

Jorge Molina · Clemens F. Schaber · Friedrich G. Barth

Received: 11 May 2009 / Revised: 19 July 2009 / Accepted: 31 August 2009 / Published online: 17 September 2009
© Springer-Verlag 2009

Abstract The metatarsal lyriform organ of the spider *Cupiennius salei* is a vibration detector consisting of 21 cuticular slits supplied by two sensory cells each, one ending in the outer and the other at the inner slit membrane. In search of functional differences between the two cell types due to differences in stimulus transmission, we analyzed (1) the adaptation of responses to electrical stimulation, (2) the thresholds for mechanical stimulation and (3) the representation of male courtship vibrations using intracellular recording and staining techniques. Single- and multi-spiking receptor neurons were found among both cell types, which showed high-pass filter characteristics. Below 100-Hz threshold, tarsal deflections were between 1° and 10°. At higher frequencies, they decreased down to values as small as 0.05°, corresponding to 4.5-nm tarsal deflection in the most sensitive cases. Different slits in the organ and receptor cells with slow or fast adaptation did not differ in this regard. When stimulated with male courtship vibrations, both types of receptor cells again did not differ significantly regarding number of action potentials, latency and synchronization coefficients. Surprisingly, the differences in dendrite coupling were not reflected by the physiological responses of the two cell types innervating the slits.

Keywords *Cupiennius salei* · Compound slit sense organ · Vibration receptor · Current clamp recording · Courtship vibrations

Introduction

For the vast majority of spiders, vibratory information is of overwhelming behavioral significance. A case intensively studied in this regard is *Cupiennius salei*, a wandering spider that is active in the night (Barth 1997).

As in other spiders, the metatarsal organ in *C. salei* (a compound or ‘lyriform’ slit sense organ) is the main vibration detector (Barth and Geethabali 1982; Speck and Barth 1982; Speck-Hergenröder and Barth 1988). This organ is well suited for the reception of substrate vibrations due to its dorsal position on the metatarsus (asterisk in Fig. 1a), the orientation of its slits perpendicular to the long axis of the leg and the presence of a stimulus-transmitting cuticular pad (bold arrow in Fig. 1a), which exhibits pronounced high-pass properties due to its viscoelasticity and therefore is important in shaping the threshold response curve (see below) (Barth 2002 and McConney et al. 2007). In *C. salei*, the metatarsal organ (HS10, nomenclature of Barth and Libera 1970) comprises 21 slits (Fig. 2a), which are between ca. 20 and 120- μ m long (Barth 1971). Each slit is innervated by two bipolar receptor cells: one of them ends at the inner cuticular membrane of the slit without obvious morphological specialization and the other one terminates in an elaborate coupling cylinder in the outer membrane covering the slit (Fig. 2d; Barth 1971).

Cupiennius salei lives on bromeliads, banana plants and agaves in the tropical forests of Central America (Barth and Seyfarth 1979). Like many other spiders, *C. salei* uses vibrations to detect prey and predators. During its elaborate

J. Molina (✉)
Departamento de Ciencias Biológicas,
Universidad de Los Andes, Apartado Aereo 4976,
Bogotá, Colombia
e-mail: jmolina@uniandes.edu.co

J. Molina · C. F. Schaber · F. G. Barth
Life Sciences, Department for Neurobiology
and Behavioral Sciences, University of Vienna,
Althanstrasse 14, 1090 Vienna, Austria

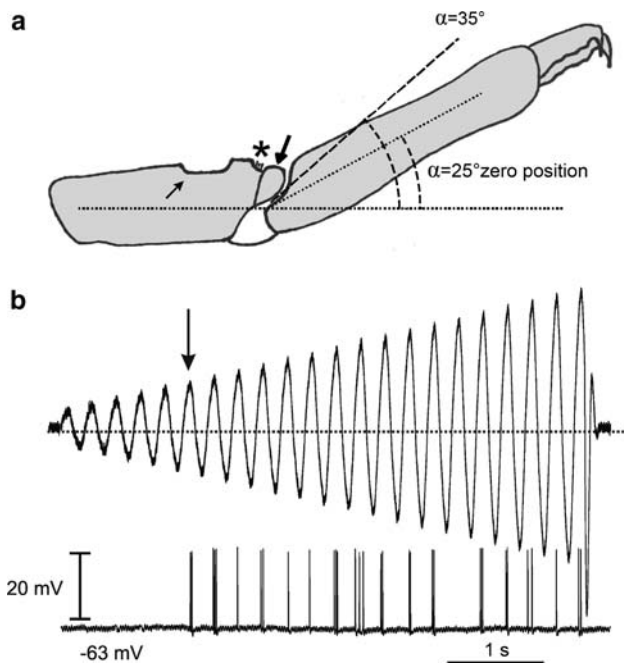


Fig. 1 Mechanical stimulation of HS10. **a** Asterisk indicates position of HS10, *short arrow* that of the window cut into the cuticle for recording, and *bold arrow* indicates position of the cuticular pad. **b** Sample trace with threshold response of a sensory cell in HS10 mechanically stimulated at 5 Hz and ranging from 0 to 72 μm in displacement amplitude. *Arrow* shows deflection amplitude of tarsus at threshold

courtship, species-specific patterns of vibratory signals (Schüch and Barth 1990) ensure reproductive isolation (Rovner and Barth 1981; Barth and Schmitt 1991; Barth 1997). According to behavioral experiments, the females are tuned to both temporal and spectral characteristics of the male opisthosomal signals (Schüch and Barth 1990).

Extracellular recordings from female vibration receptors (Baurecht and Barth 1992, 1993) showed the particular importance of individual signal parameters during courtship and provided evidence for parallel processing of the opisthosomal and pedipalpal signals by different slits. While the responses recorded in these studies are believed to have come exclusively or at least largely from the sensory neurons ending in the outer membrane of the slits, the particular role of the receptor cells ending at the inner membrane of the slits remains unknown.

Thus, a most puzzling question still remains: how do the response characteristics of the receptor cells ending in the outer and at the inner membrane of a slit differ? Considering the obvious differences in their mechanical coupling to the slit, a difference seems indeed likely.

The objective of the present work was to determine possible functional differences between the two receptor cell types, due to their different coupling to the slit, by studying their threshold curves and their responses to male vibratory courtship signals. The application of intracellular recording

techniques (Gingl et al. 2006) and the subsequent dye injection were fundamental prerequisites for being able to safely identify the cells and distinguish between the two types.

Our results extend previous work done with another lyriform organ, VS3, on the patella of the spider leg (Höger and Seyfarth 2001) and several studies summarized by French et al. (2002). Contrary to these studies on VS3, however, which concentrated on an analysis of processes of stimulus transduction and on membrane physiology, the present study focused on the potential effect of differences in stimulus transmission on the physiological response of the two cells innervating a slit. Consequently, in the present study, the processes of stimulus transmission had to be left intact and the organ was not isolated. Also, different from the studies on VS3, mechanical stimulation of the vibration sensor HS10 occurred in a natural way instead of by the localized pressure onto the organ generated by the small tip (diameter ca. 50 μm) of a stylus, which was displaced as much as 4 μm and oriented perpendicular to the exoskeleton's surface (Höger et al. 1997; Höger and Seyfarth 2001).

Materials and methods

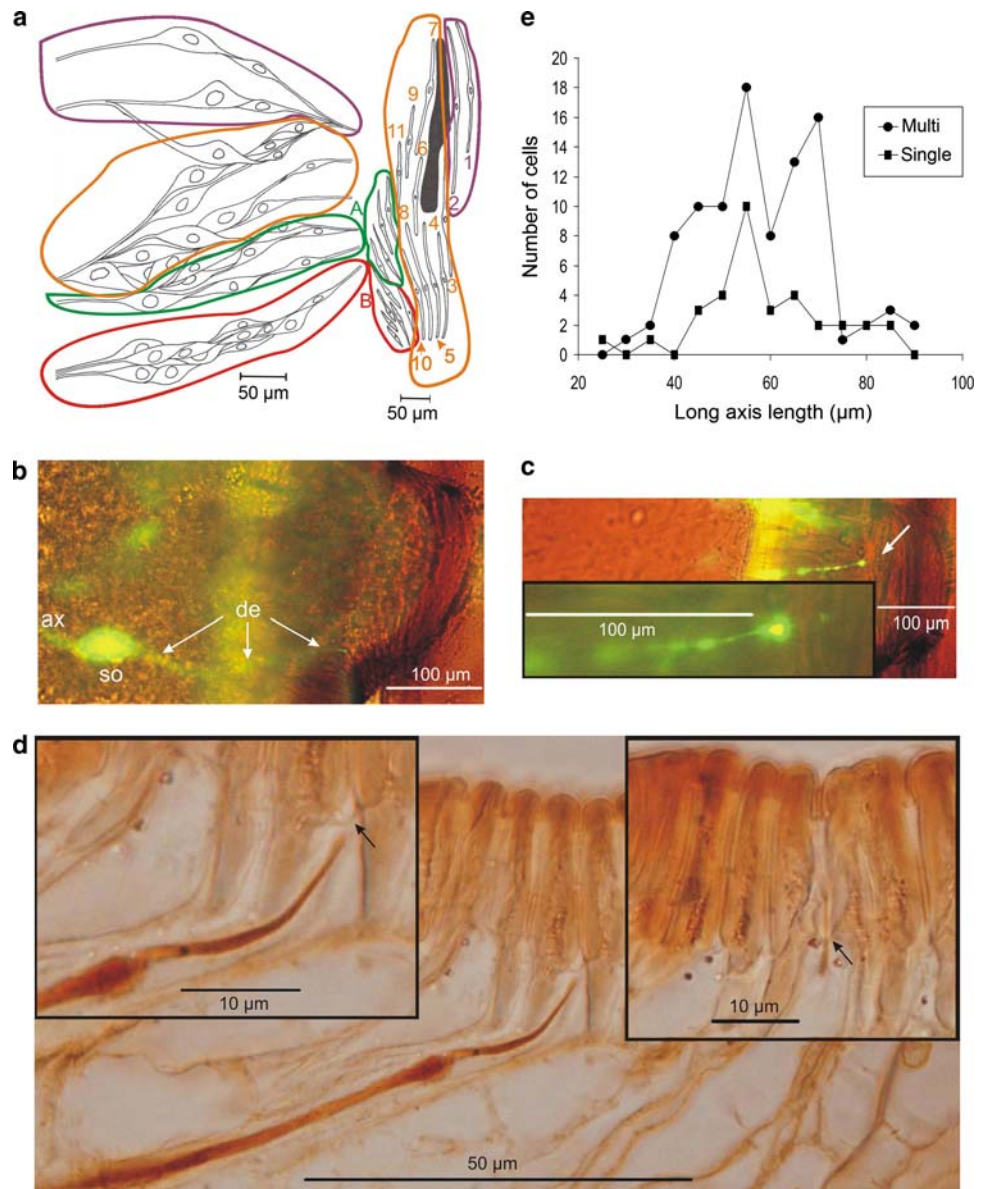
Animals

Adult females of the Central American hunting spider *C. salei* Keys. (Barth 2002) from our laboratory stock were used for the experiments. Isolated legs were obtained by mechanically inducing autotomy between coxa and trochanter. The preparation, dissection (cuticular window close to HS10) and fixation of the legs onto a Plexiglas® holder followed Gingl et al. (2006).

Distribution of the sensory cells of HS10

To allow proper intracellular recording and morphological identification (assignment to a particular slit and soma size group), the number, size and distribution of the receptor cells were studied in detail in the metatarsal organ (HS10). Whole mounts of the metatarsus–tarsus joint with a cuticular window close to HS10 were stained with 4% methylene blue dissolved in AAF (AAF = 1 ml 37% formaldehyde, 0.5 ml glacial acetic acid and 8.5 ml absolute ethanol). When the area of interest appeared in light blue, staining was stopped by washing briefly with distilled water and fixing overnight at room temperature in 12% ammonium heptamolybdate-tetrahydrate dissolved in distilled water. The entire group of receptor neurons was removed from the fixed whole mount and photographed with a CCD camera (Sony, DXC-950P) attached to a light microscope (Leitz, Laborlux D).

Fig. 2 Metatarsal vibration-sensitive organ HS10 in *Cupiennius salei*. **a** Distribution and size of the receptor cells in a preparation with 38 identifiable somata. The somata and slits are not to scale (somata are 1.5 times magnified in comparison to HS10 size). **b** Receptor cell labeled with *Oregon Green-Avidin* and showing axon (*ax*), a large soma (*so*) and dendrite (*de*) innervating a slit of group A (preparation observed from inside the leg). **c** Dendrite of another receptor cell developed with *Oregon Green-Avidin*; note mitochondrion-rich swelling and dendrite connection. *Inset*, the same dendrite magnified. **d** Transversal view of a histological slice showing a dendrite labeled with the DAB method. *Left inset*, the same dendrite ending at the inner membrane; *right inset*, another dendrite passing through the inner membrane to the outer membrane. In both insets, the position of the inner membrane is marked by an *arrow*. **e** Number of receptor cells studied electrophysiologically according to soma sizes and type of response to electrical stimulation



Controls for unwanted mechanical effects

For recording from the sensory cells intracellularly, a window was cut into the cuticle of the autotomized leg slightly proximal to the organ (Gingl et al. 2006). The following controls were used to evaluate possible mechanical effects of this procedure on the organ’s mechanical stimulation.

(1) The overall compression of HS10 by vertically displacing the tarsus was the same in intact and autotomized legs as seen with an optical resolution of around 2 µm and using image analysis software (Lucia, Laboratory Imaging Ltd). (2) We also measured the displacement of the distal edge of the cuticular window cut into the skeleton behind HS10 by tarsal upward deflection (Fig. 1a). Even at values of $\alpha = 50^\circ$ (α being the angle between tarsus and metatarsus), we could not measure any displacement of the edge of

the cuticular window indicating the absence of a “weakening” effect relevant at the small forces used to adequately stimulate HS10 by tarsal deflection. Only when $\alpha = 55^\circ$, the forces applied produce an average displacement of the distal edge of the cuticular window of $4.36 \pm 2.13 \mu\text{m}$ ($n = 4$). Importantly, in our experiments, α never exceeded 35° and often was even way below this value, since it takes a value of at most 10° only to elicit threshold responses in sensory cells (Fig. 3a–c).

Recordings of natural courtship signals

A bromeliad (*Aechmea fasciata*) with two accelerometers (Brüel & Kjaer 4374) waxed onto the mid region of different leaves was used to record courtship signals as previously done (Schüch and Barth 1985). The output of the

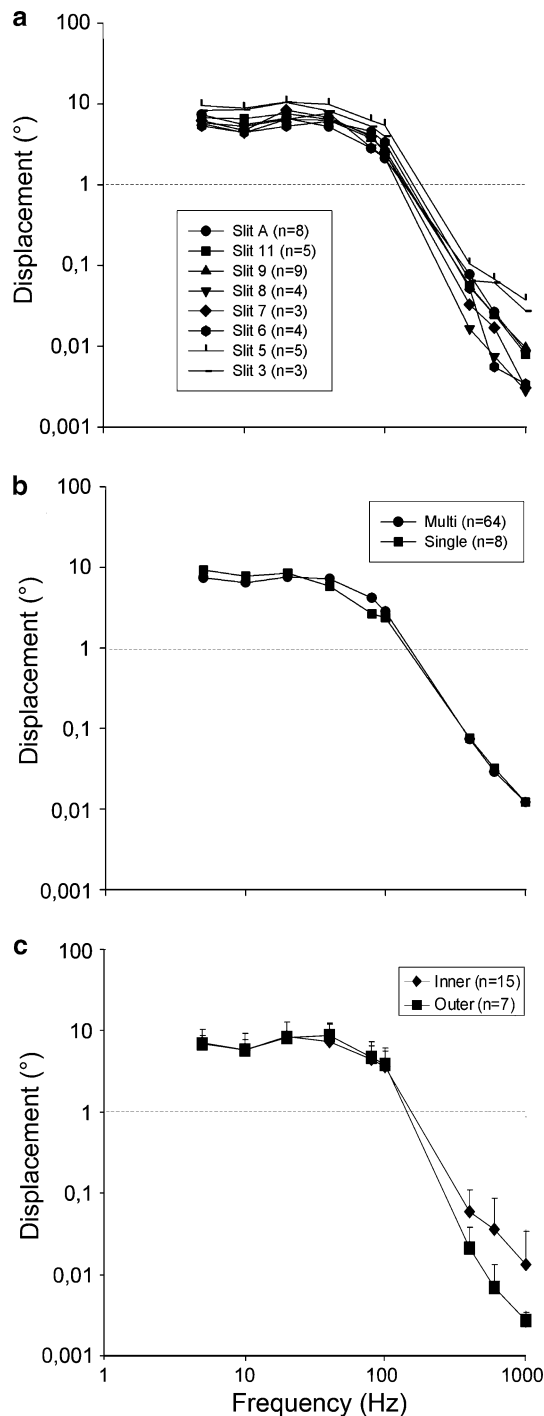


Fig. 3 Threshold responses of HS10 to mechanical sinusoidal stimulation. **a** Average response thresholds of receptor cells innervating different slits. **b** Average response thresholds at vertical tarsus deflection of sensory cells showing multi- or single-spike response properties when stimulated electrically. **c** Average threshold responses with standard deviation of vertical tarsus deflection obtained from receptor cells innervating the outer or inner slit, respectively. The number of trials (electrical or mechanical stimulation) applied to each preparation was normally one. Exceptionally, stable recordings allowed some repetitions

accelerometers was amplified using a charge amplifier with integrator (Brüel & Kjaer 2635). Male and female courtship signals were digitized with an analog-digital converter (CED 1401) and stored on a computer using the software Spike 2 (Cambridge Electronic Design, Spike 2 5.08).

Females of *C. salei* were allowed to move on the bromeliad to ensure the presence of dragline silk with sexual pheromone on the leaves (Tichy et al. 2001). Later, pairs of male and female were put on different leaves of the same plant (average distance between male and female, 50 cm) and pre-copulatory vibratory communication initiated (Barth 1997, 2002). The experiments were performed at room temperature (25–27°C).

Intracellular recordings and stainings

Current clamp recordings from the sensory cell somata were performed technically following Gingl et al. (2006). Quartz-glass electrodes were pulled using a horizontal laser puller (Sutter Instrument, P-2000) and their tips filled with 5% neurobiotin (Vector, SP-1120) in 1 M potassium acetate, while their shank contained 1 M potassium acetate only. Electrode resistances ranged between 30 and 100 MΩ during the experiments.

After having recorded their activity, the receptor cells were stained with neurobiotin applying no less than 0.5 nA positive DC current through the electrode for more than 10 min. After staining, the tracer was allowed to diffuse for at least 1 h. For overnight fixation at 4°C, we applied 4% paraformaldehyde in Millonig's phosphate buffer. The neurobiotin tracer was detected either with the Oregon Green-avidin (Molecular Probes, A-6374) method (Anton et al. 2003) or with the DAB-method (Vector Laboratories, Elite ABC Kit, PK-6100). After incubation, the samples were washed three times for 10 min with Millonig's phosphate buffer, dehydrated by immersion in the alcohol series and observed either with an epifluorescence microscope or a light microscope in methyl salicylate. To reliably identify the connectivity of individual receptor cells with a particular slit, the path of their dendrites was followed from the soma up to the corresponding slit. For this purpose, the metatarsal organ was cut out together with the cuticular window and observed from inside the leg segment with an epifluorescence microscope.

For technical reasons, we did not record from both sensory cells of the same slit. One problem was that the precise location of the cells was not known with the necessary spatial resolution, and another was that tracing the histologically labeled dendrites would have been much more difficult.

Histology

In this study, it was crucial to safely determine whether the sensory cell from which recording was done ended in the outer or at the inner slit membrane. Accordingly, the following procedures were applied to the cells, which had been intracellularly stained with neurobiotin. Samples treated with methyl salicylate were washed three times for 10 min with acetone, followed by 6 h of impregnation with a 1:1 mixture of acetone:epoxy resin (modified after Spurr 1969; 10 g ERL 4206, 6 g DER 736, 26 g NSA, 0.4 g DMAE; Serva). Then the samples were transferred to pure resin for 1 h and finally to fresh resin. Complete polymerization took place at 70°C within 2 days. After cooling, the blocks with the samples were stored at 4°C. Serial slices, 8 µm thick, were cut perpendicular to the long axis of the slits with a microtome (Reichert, 403354) and a tungsten knife (Reichert-Jung, D-profile). Cover glasses were mounted with Fluoromount (Serva, 21648) and photographs of the slices taken with an epifluorescence microscope and a CCD camera (see Fig. 2b–d).

Stimulation and recording

Threshold curves

Electrical stimulation followed Gingl et al. (2006), while mechanical stimuli were generated with a feedback-controlled electrodynamic shaker (Ling Dynamic Systems, V101) mounted separately from the air table with the recording equipment to avoid unwanted vibrations of the setup.

Sinusoidal vibrations between 5 and 1,000 Hz with amplitudes of up to 72-µm peak to peak (pp) at 5–100 Hz, up to 5.8 µm (pp) at 400 Hz, and up to 2.2 µm (pp) at 600 and 1,000 Hz were generated using computer software (Sony, Sound Forge 6.0). Different stimulus frequencies were applied in random order using a hook contacting the most distal part of the tarsus (Gingl et al. 2006). To assure mechanical stimulation, the zero position (which corresponded to an angle α of approximately 25°; see Fig. 1a) was adjusted as a light contact between the proximal part of the tarsus and the distal part of the metatarsus (Barth and Geethabali 1982). Threshold deflection amplitudes were defined as those amplitudes (peak to peak in micrometer) at which one or two action potentials occurred over background activity, of which there was none in many cases, at each frequency tested (Fig. 1b) (Barth and Geethabali 1982).

The deflection amplitudes actually applied to the tarsus with the electrodynamic shaker were measured and calibrated using a laser Doppler vibrometer (Polytec, OFV 2100HR).

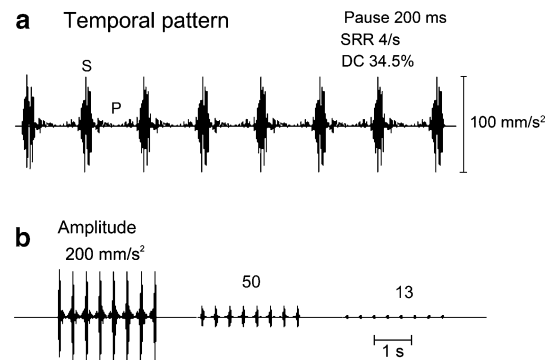


Fig. 4 Male opisthosomal vibrations. **a** Standard series of eight syllables. **b** Series of eight male opisthosomal syllables with different amplitudes. *DC* duty cycle, *P* pause, *S* syllable, *SRR* syllable repetition rate

Natural courtship signals

Natural courtship signals were attenuated to different degrees and fed to the shaker using computer software (Sony, Sound Forge 6.0). Male opisthosomal signals with eight syllables and 200-ms pauses between them were used as a standard opisthosomal signal (Fig. 4a).

Two groups of experiments were performed: (1) to evaluate the effects of syllable amplitude, series with eight syllables of male opisthosomal signals with decreasing amplitude (200, 100, 50, 25 and 13 mm/s²) were tested (Fig. 4b); (2) to evaluate the response of the receptor cells to different duty cycles (DCs) (known to be of particular behavioral relevance; Schüch and Barth 1990), opisthosomal vibrations with different pause durations (PDs) between syllables were tested (50, 200 and 400 ms, implying syllable repetition rates (SRRs) of 8, 4 and 2/s, and DCs of 67.7, 34.5 and 20.8%). Acceleration amplitudes of 100 mm/s², which are well above threshold (Barth and Geethabali 1982; Baurecht and Barth 1992, 1993), were used in these experiments.

The degree of synchronization between action potentials and vibration syllable (copying properties) was expressed by the coefficient of synchronization (Schildberger 1984), which ranges between 1 for perfect copying and 0 for no copying at all.

Data evaluation

Threshold curves, courtship signals and the responses of the receptor cells were stored using recording software (NPI Electronics, Cell Works 5.5), digitized with an analog-digital converter (NPI Electronics, INT-20X) and analyzed using Spike 2 (Cambridge Electronic Design, Spike 2 5.08) and standard software. The significance of differences between the means of the values obtained was

Table 1 Recordings from sensory cells ending at the inner or in the outer membrane of the slits in the lyriform organ HS10: number and response type according to electrical stimulation

| Slit designation | Response to electrical stimulation | | | |
|------------------|------------------------------------|----------------|----------------|----------------|
| | Multi spike | | Single spike | |
| | Inner membrane | Outer membrane | Inner membrane | Outer membrane |
| B | 2 | 0 | 1 | 0 |
| A | 1 | 2 | 0 | 0 |
| 11 | 4 | 1 | 0 | 0 |
| 9 | 4 | 1 | 2 | 0 |
| 8 | 2 | 1 | 0 | 0 |
| 7 | 1 | 0 | 1 | 0 |
| 6 | 4 | 1 | 0 | 1 |
| 5 | 1 | 2 | 1 | 0 |
| 3 | 3 | 1 | 0 | 0 |
| Total | 22 | 9 | 5 | 1 |

tested with the Student's two-tailed *t* test, assuming different variances (Zar 1999). ANOVAs were performed with SigmaStat (Systat Software Inc., SigmaStat) and SPSS 15.0.

Results

Assignment of sensory cells to slits

Although HS10 has been extensively studied in *C. salei*, the size and distribution of the receptor cells in the organ, which are relevant for their identification, have so far not been described. The spindle-shaped cell bodies of the receptor cells form four clusters, which reflect the arrangement of the slits in this lyriform organ (Fig. 2a). According to a total of 152 intracellular stainings, soma sizes fall into four groups as well: (1) a main group ($n = 63$ somata) with long axes measuring ca. 50 μm and wide axes close to 20 μm , (2) a second group ($n = 50$ somata) with soma sizes of around 65 by 20 μm , (3) a small group ($n = 29$ somata) with somata close to 45 by 15 μm and (4) few cells ($n = 10$ somata) with large long and wide axes (80 by 25 μm , respectively). Soma sizes correlate neither with the length of the cuticular slits nor with the four clusters of the receptor cells or those of the arrangement of the slits shown in Fig. 2a. However, the position of each soma does reflect the arrangement of the slits in the organ (Fig. 2a). In no case did a dendrite of a receptor cell cross from one side of the organ to the other (Fig. 2b). Up to 38 cells were found to innervate HS10, and cells with large somata were always located proximally while cells with small somata were frequently found more distally. The positions and sizes of the neurons are similar in each leg and in different animals (data not shown). Dendrite lengths ranged between 60 and 300 μm .

No significant difference between responses of the two sensory cells innervating a slit

Data used for the analysis presented in the following all refer to receptor cells showing adequate resting potentials (see below) and producing action potentials in response to both electrical and mechanical stimulation.

Response to electrical stimulation

Stimulation of the receptor cells in HS10 with rectangular current pulses of 40-ms duration elicited either one or several action potentials, as has been previously shown (Gingl et al. 2006; Table 1). The resting membrane potential of the sensory cells showing multi-spike (69.14 ± 10.51 mV, $n = 94$) and single-spike patterns (66.89 ± 9.82 mV, $n = 34$), respectively, did not differ significantly ($P = 0.26$). We found almost three times as many cells with multi-spike ($n = 94$) than cells with single-spike response properties ($n = 34$). In 73 of these experiments, it was possible to relate the response properties of the cells to the slits they innervate. Several times, both mechanoreceptor cells with short and longer-lasting responses were found to innervate slits B, A, 11, 9, 8, 7, 6, 5 and 3 (Fig. 2a). When the soma size of the receptor cells recorded from was compared to the response properties on electrical stimulation in 128 experiments, the average sizes of the multi-spike neurons (55.83 ± 12.64 μm) were found not to differ ($P = 0.73$) from those of the single-spike receptor cells (56.71 ± 12.72 μm). Figure 2e shows the number of receptor cells recorded from intracellularly and their response types seen with electrical stimulation as a function of their soma sizes.

Response to mechanical stimulation

Threshold curves for 82 receptor cells were obtained from metatarsal organs of the four pairs of legs. The overall

shape of the threshold curves was the same in different slits, from different legs, and in different animals: low sensitivities at low frequencies, steeply rising to higher sensitivities at frequencies above around 40 Hz, and with no marked tuning to limited frequency ranges (Fig. 3). Vertical tarsal displacements (starting from the resting or zero position) of around 35 μm were needed to reach threshold at stimulus frequencies between 5 and 40 Hz, and 13–20 μm for frequencies between 80 and 100 Hz. Displacements between 0.3 and 0.05 μm sufficed for frequencies in the range between 400 and 1,000 Hz. Cases with extreme sensitivity were observed in some receptor cells at 1,000 Hz, the highest frequency tested, with tarsal threshold displacements of 4.5 nm only. Threshold displacement of the tarsus thus covers a range of four orders of magnitude between low and high frequencies. Measured in degrees, the vertical displacements of the tarsus needed to elicit action potentials were between 10° and 1° in the range 5–100 Hz, and less than 1° and down to 0.005° at frequencies higher than 100 Hz (Fig. 3).

In 41 experiments, staining subsequent to intracellular recording allowed us to unambiguously identify the slit innervated by the sensory cell (Fig. 2). Comparisons of the threshold curves obtained from different receptor cells in different slits showed lower sensitivities at higher frequencies for slits 3 and 5 than for slits 6, 7, 8, 9, 11 and A (Fig. 3a). Single- and multi-spike receptor cells did not differ significantly (ANOVA $P = 0.96$) with regard to their average threshold curves (Fig. 3b).

Dendrite connection to slit

The dendrites of 37 receptor cells of HS10 could be unambiguously followed in histological slices up to their termination in the slit (Fig. 2). Multi- and single spiking neurons were found several times to end at either the inner or the outer membrane of the same slits (Table 1). Average threshold curves from receptor cells ending at the inner membranes of the slits showed a lower sensitivity at frequencies higher than 100 Hz than the receptor cells innervating the outer membrane (Fig. 3c). However, the differences between both types of receptor cells were not significant (ANOVA $P = 0.92$).

Effects of signal amplitude on the neuronal response

Not having identified any significant difference in the response pattern of the two sensory cell types innervating a slit, we hypothesized that natural stimulus patterns such as the male courtship signal instead of simple sinusoidal stimuli might reveal the differences we searched for.

As expected, the average frequency of action potentials in response to the eight syllables of a series decreased when

the amplitude of the opisthosomal signals was progressively reduced from 200 to 13 mm/s^2 (ANOVA $P = 0.0019$, Fig. 5a). When the stimulus amplitude was large, the receptor neurons innervating the inner membrane produced a higher frequency of action potentials than those ending in the outer membrane. Similarly, the neurons ending in the outer membrane started to produce more action potentials than the other cell type when the amplitude of the courtship signal decreased. However, these differences were not statistically significant (ANOVA $P = 0.104$; Fig. 5a).

A progressive, but not significant (ANOVA $P = 0.063$), increase in the latency time was observed with a reduction in the amplitude of the signal (Fig. 5b). The response of the neurons ending at the inner membrane had a longer latency in all cases, but not significantly so (ANOVA $P = 0.01$; Fig. 5b).

The averaged synchronization coefficients were very similar (ANOVA $P = 0.342$) with no statistically significant differences between the inner and outer receptor cells (ANOVA $P = 0.84$; Fig. 5c).

Copying the temporal structure of the male courtship signals

A comparison of receptor cells innervating the outer and inner membrane, respectively, showed that the former responded to all syllables in a series of courtship vibrations with more action potentials than the neurons ending at the inner membrane of the slits. However, the differences were not significant (ANOVA $P = 0.01$; Fig. 6a). Likewise, independent of the number of action potentials and the latency of the response, the synchronization coefficient showed no statistically significant differences between the two receptor cell types (ANOVA $P = 0.53$; Fig. 6a') and between the different syllables within a series (ANOVA $P = 0.73$).

The response of a receptor cell of the metatarsal organ to the standardized opisthosomal courtship vibrations was significantly higher (given in hertz per syllable) to the first opisthosomal syllable than to the rest of the syllables in a series (ANOVA $P < 0.0008$; Fig. 6a, b). Not only did the first syllable lead to more action potentials, but also the latency time was significantly shorter (ANOVA $P < 0.001$) than the one obtained for the subsequent syllables (Fig. 6a', b'). The only significant difference found between the two cell types was the latency of the receptor cell response (Fig. 6a', b'). It was shorter in the cells ending in the outer membrane than those ending at the inner membrane (ANOVA $P = 0.007$).

Varying the DC of the opisthosomal signal did change the temporal pattern of the cell response, but did not affect the responses (measured in hertz) of the receptor cells in the neurons ending at the inner and in the outer membrane (Fig. 6a, b). No statistically relevant effects were observed

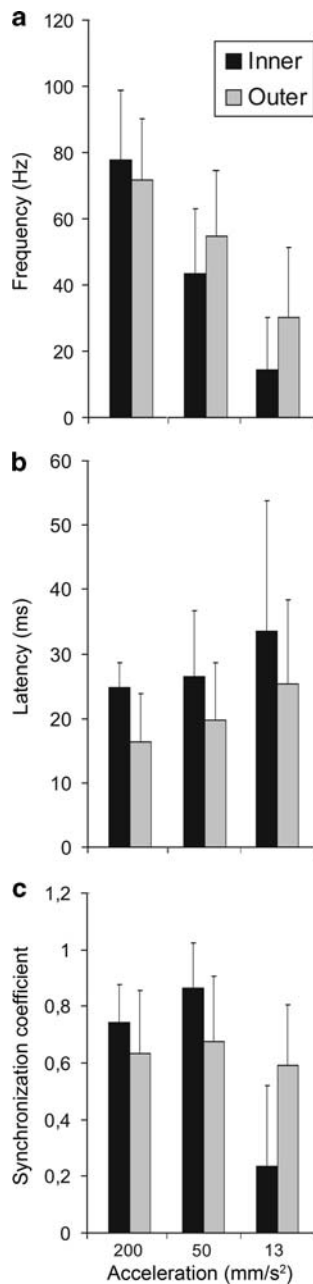


Fig. 5 Effects of the acceleration amplitude of the male courtship vibrations on the response of the receptor cells. **a** Average frequency of action potentials per syllable in a series increases with amplitude ($P = 0.0019$). Differences between the sensory cells with regard to their dendrite coupling were not significant ($P = 0.104$). **b** Average response latency of syllables within a series. Decrease in latency with amplitude ($P = 0.063$) and differences between the two types of receptor cells ($P = 0.01$) were not significant. **c** Average synchronization coefficient of syllables within a series. No significant differences with change in amplitude ($P = 0.342$) or between the two cell types ($P = 0.84$) ($n = 5$ legs each for cells with dendrite ending at the inner or in the outer slit membrane, respectively). Bars indicate standard deviation

on the latencies and synchronization coefficients either, when the receptor cells of HS10 were exposed to series of syllables with different DCs (Fig. 6a'–b"). The receptor

cells innervating the inner and the outer membrane responded in the same way.

Discussion

Controls for unwanted mechanical effects

In spider legs isolated by autotomy and with a window cut into the cuticle above the sensory cells, the overall compression of HS10 was the same as in intact legs. At tarsal deflection angles $\alpha < 50^\circ$, no displacement of the distal edge of the cuticular window could be measured (see Fig. 1a). Using white-light interferometry, Schaber et al. (2005) and C.F. Schaber et al. (in prep.) showed that in intact spiders, all slits of HS10, including the shortest ones, are fully compressed at $\alpha = 40^\circ$ – 45° (that is at tarsal deflection angles of 15° to 20° beyond the resting position; Fig. 1a). These findings suggest that at least in the physiological range tested in our experiments, no changes in the mechanical sensitivity of HS10 due to mechanical manipulations are to be expected. The similarity of the threshold curves found in this study with those gained earlier by extracellular recordings from intact animals (Barth and Geethabali 1982) supports this argument. Finally, it seems fair to assume that tiny mechanical effects of cutting the recording window not detected by us would have influenced the responses of the two sensory cells of a slit in the same way and thus not affected the main conclusions drawn from the experiments of the present study.

Sensory cell distribution and morphology

The distribution pattern of the sensory cells in HS10 is related to the arrangement of the cuticular slits in the organ (Fig. 2a). Such a relation has also been found previously in other lyriform organs of *C. salei* (HS8 and HS9: Seyfarth and Pflüger 1984; VS3: Seyfarth and French 1994; Fabian and Seyfarth 1997). As in VS3 (Seyfarth and French 1994), no differences between the legs or between animals were observed in HS10, suggesting that the sensory cells in general are arranged according to slit position in *Cupiennius*. The largest cell bodies in HS10 (long axes $\sim 80 \mu\text{m}$) are similar in size to the largest ones in organs HS8 and HS9 (Seyfarth and Pflüger 1984) and VS3 (Fabian and Seyfarth 1997). In VS3 and HS8, sensory cells with the largest bodies innervate the slits located in the center of the lyriform array, while some of the smallest cells innervate the shortest slits (Seyfarth and Pflüger 1984; Fabian and Seyfarth 1997). We did not find a similar pattern in HS10. Here, the short slits of group B were innervated by sensory cells as large as those for the longest slits 1 or 2 (see Fig. 2a). In

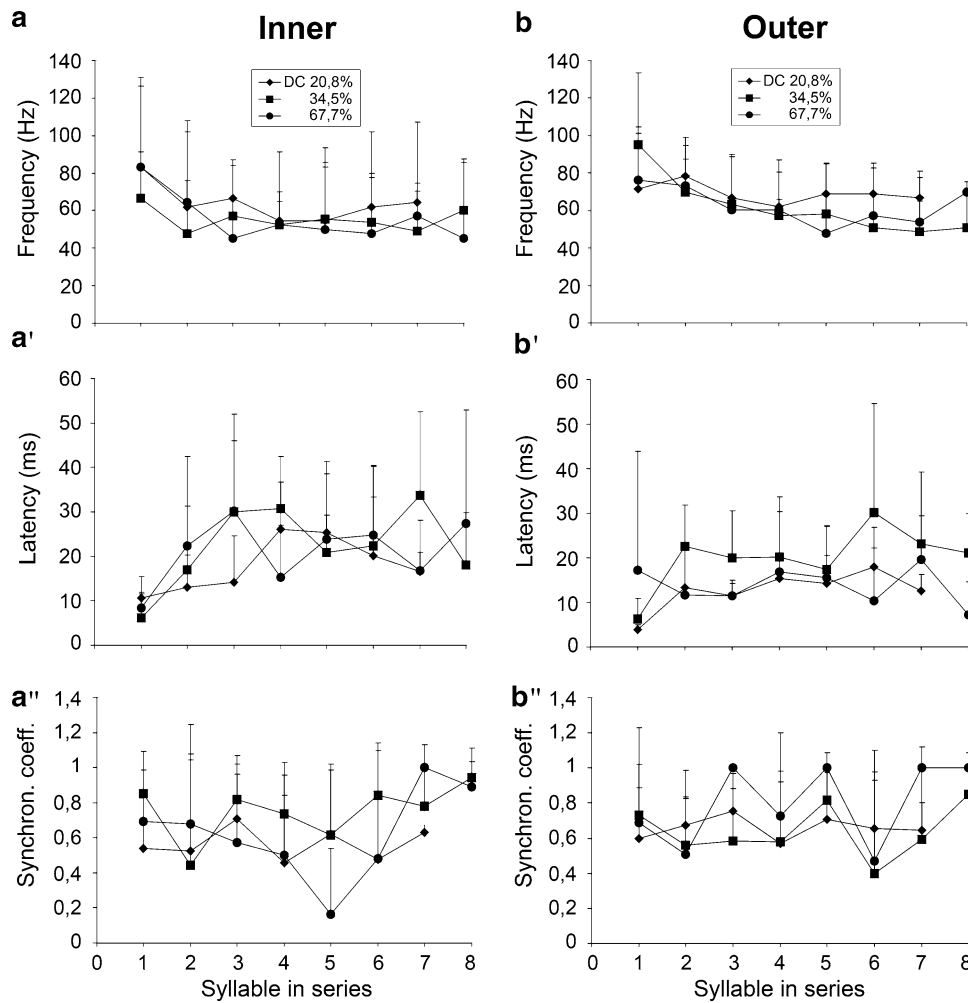


Fig. 6 Effect of pauses between syllables (and therefore DC) of the opisthosomal vibrations on the response of the receptor neurons. Signal amplitude 100 mm/s^2 in all cases. **a** Average frequency of action potentials per syllable of receptor cells innervating the inner membrane in response to vibration patterns differing with respect to their DC. Due to the long pauses of 400 ms, each series consisted of only seven instead of eight syllables in all cases with $\text{DC} = 20.8\%$. **b** Average frequency of action potentials per syllable of receptor cells ending at the outer membrane in response to opisthosomal vibration series with different DCs. Differences between cell types were not significant

($P = 0.01$). Note that there was a stronger response to the first syllable ($P = 0.0008$). **a'**, **b'** Average response latency of receptor cells ending at the inner or in the outer membrane. Latency was shorter for cells attached to the outer slit membrane ($P = 0.007$) and for responses to the first syllable as compared to the following ones ($P < 0.001$). **a''**, **b''** Average synchronization coefficient of response to opisthosomal courtship vibrations with different DCs. Differences between two cell types ($P = 0.53$) or between syllables ($P = 0.73$) were not significant. ($n = 5$ legs each for the two types of sensory cells). Bars indicate standard deviation

HS10, large cell bodies were located further away from the slits than small cell bodies (see Fig. 2a).

Response type independent of cell soma size and slit

Our present results confirm (Gingl et al. 2006) that there are multi-spike and single-spike receptor cell responses in HS10 to rectangular electrical stimuli. Similar responses have been obtained both for HS8 (unpublished data from our group) and VS3 (Seyfarth and French 1994). Gingl et al. (2006) suggested that cells with a longer lasting response are the minority in experiments with HS10, because smaller somata are difficult to penetrate. However,

in our experiments, both response types were represented by a large number of recordings from cells with similar soma sizes (about $55 \mu\text{m}$ in the long axis). Likewise, in VS3, soma size and the response to electrical stimulation did not correlate (Seyfarth and French 1994).

Indeed, in HS10, the response properties of the receptor cells are not related to the soma size, the innervated slit or to the ending of their dendrite at the slit's inner or outer membrane (see Table 1). Moreover, threshold curves of the two types of neurons obtained with mechanical stimulation did not differ significantly (see Fig. 3c).

In all lyriform organs studied so far in *Cupiennius*, the response properties of the receptor cells as seen from

electrical stimulation and intracellular recordings are not correlated with: (1) soma size (Seyfarth and French 1994 for VS3; Fig. 2e for HS10); (2) relative soma position (Höger and Seyfarth 2001 for VS3; Table 1 for HS10); (3) length and position of the slits (Seyfarth and French 1994 for VS3 and Table 1 for HS10); (4) passive neuronal properties (Seyfarth and French 1994 for VS3; Gingl et al. 2006 for HS10) and (5) type of dendrite ending (Höger and Seyfarth 2001 for VS3 and Table 1 for HS10). Unpublished data from our group confirm findings (1) to (5) for the tibial lyriform organ HS8.

Therefore, as suggested by Torkkeli et al. (2001) for VS3, it seems likely that intrinsic differences in the inactivation properties of voltage-activated sodium currents are responsible for the differences in response properties (single- vs. multi-spike) found in all lyriform organs of *C. salei* so far studied, and not, however, for differences in the coupling of the dendrite tips to the slit as amply demonstrated for HS10.

Responses to mechanical stimulation

Results obtained from three types of experiments show differences in mechanical sensitivity for different slits in lyriform organs: (1) deformation and tension optical experiments with models and finite element calculations (Barth and Pickelmann 1975; Barth et al. 1984; Höbl et al. 2007, 2009), (2) extracellular recordings from different slits in HS8 (Barth and Bohnenberger 1978; Bohnenberger 1981) and (3) differences in the degree of compression observed between the longest and the shortest slits in HS10 in interferometric studies of live animals (Schaber et al. 2005). Referring to the present study, we did expect additional differences in threshold sensitivities and potentially also in response type between sensory cells ending in the outer and at the inner membrane of the slits in HS10, respectively. The slight differences in threshold values observed at frequencies higher than 100 Hz (see Fig. 3c) are, however, not statistically significant. As recently shown by McConney et al. (2007), the high-pass properties of the spider vibration receptor HS10 are largely explained by the viscoelastic properties of the cuticular pad lying in front of it (bold arrow in Fig. 1a). This pad seems to have an overriding influence on the shape of the threshold curves of all the slits making up the spider metatarsal vibration sensor.

In view of all the similarities between the two sensory cell types, one has to ask for potential differences seen in response to natural vibratory stimuli, such as courtship vibrations. We manipulated PD, SRR and the DC (see Fig. 4) of the male signal, which are known to be the most influential parameters in behavioral experiments (keeping the main frequency $CF = 94$ Hz, syllable duration $SD = 105$ ms and less influential parameters such as the

acceleration amplitude within the ranges known to elicit maximal behavioral responses) (Schüch and Barth 1990). Neither the frequency of the action potential response, nor its latency or synchronization coefficients differed significantly between both types of neurons (see Figs. 5a–c, 6a–b"), suggesting that they represent the microstructure of the opisthosomal signal in a very similar way.

To summarize, the two morphological types of sensory cells innervating each of the slits in HS10 do not represent the two functional groups showing short and longer lasting responses to electrical stimulation. Also, their sensitivity in response to mechanical stimulation and the fidelity in copying the structure of the opisthosomal courtship signals do not differ. Thus, from a functional point of view, the question why the two sensory cells supplying the slits of spider slit sensilla differ with regard to the coupling of their dendrite tips remains unanswered.

Notwithstanding the remaining gap in our understanding of the mechanical consequences for stimulus transmission of the two modes of dendrite coupling, the physiological differences reported earlier (French et al. 2002), but not related to the type of coupling, have been confirmed by the present study. Knowledge of these physiological differences may eventually have to be complemented by that on differences in the efferent control of the sensory cells (Fabian-Fine et al. 1999, 2000, 2002). Likewise there may be differences in details of the central nervous projection patterns of the primary sensory cells onto interneurons. According to Anton and Barth (1993), the central nervous projections of HS10 and other lyriform organs are organized somatotopically with the afferent fibers of HS10 arborizing in the respective leg ganglion and ending in a sensory longitudinal tract (SLT 3) in the center of the subesophageal nervous mass.

Regarding stimulus transmission, our new data particularly seek a detailed examination of the mechanical processes leading to the stimulation of the cell with its dendrite ending at the inner membrane of the slit. This will not be an easy task. In the end, the mechanical events leading to the stimulation of the two morphological cell types may be much more similar than expected.

Acknowledgments We thank Andreas Szpetkowski for the assistance in electronics and Elisabeth Fritz-Palank, Karina Jorke and Margit Kainerstorfer for their technical assistance. The comments of the two reviewers of this paper are much appreciated. This study was supported by the Austrian Science Fund FWF (grant P16348 to FGB). All experiments were carried out in accordance with the current laws in Austria.

References

- Anton S, Barth FG (1993) Central nervous projection patterns of trichobothria and other cuticular sensilla in the wandering

- spider *Cupiennius salei* (Arachnida, Araneae). Zoomorphology 113:21–32
- Anton S, Loon van JJA, Meijerink J, Smid HM, Takken W, Rospars JP (2003) Central projections of olfactory receptor neurons from single antennal and palpal sensilla in mosquitoes. Arthropod Struct Dev 32:319–327
- Barth FG (1971) Der sensorische Apparat der Spaltsinnesorgane (*Cupiennius salei* Keys. Araneae). Z Zellforsch 112:212–246
- Barth FG (1997) Vibratory communication in spiders: adaptation and compromise at many levels. In: Lehrer M (ed) Orientation and communication in arthropods. Birkhäuser Verlag, Basel, pp 247–272
- Barth FG (2002) A spider's world: senses and behavior. Springer, Heidelberg
- Barth FG, Bohnenberger J (1978) Lyriform slit sense organ: thresholds and stimulus amplitude ranges in a multi-unit mechanoreceptor. J Comp Physiol A 125:37–43
- Barth FG, Geethabali (1982) Spider vibration receptors: threshold curves of individual slits in the metatarsal lyriform organ. J Comp Physiol A 148:175–185
- Barth FG, Libera W (1970) Ein Atlas der Spaltsinnesorgane von *Cupiennius salei* Keys. Chelicerata (Araneae). Z Morphol Tiere 68:343–369
- Barth FG, Pickelmann P (1975) Lyriform slit sense organs. Modelling an arthropod mechanoreceptor. J Comp Physiol 103:39–54
- Barth FG, Schmitt A (1991) Species recognition and species isolation in wandering spiders (*Cupiennius* spp.; Ctenidae). Behav Ecol Sociobiol 29:333–339
- Barth FG, Seyfarth E-A (1979) *Cupiennius salei* Keys. (Araneae) in the highlands of central Guatemala. J Arachnol 7:255–263
- Barth FG, Ficker E, Federle H-U (1984) Model studies on the mechanical significance of grouping in compound spider slit sensilla. Zoomorphology 104:204–215
- Baurecht D, Barth FG (1992) Vibratory communication in spiders. I. Representation of male courtship signals by female vibration receptor. J Comp Physiol A 171:231–243
- Baurecht D, Barth FG (1993) Vibratory communication in spiders. II. Representation of parameters contained in synthetic male courtship signals by female vibration receptor. J Comp Physiol A 173:309–319
- Bohnenberger J (1981) Matched transfer characteristics of single units in a compound slit sense organ. J Comp Physiol A 142:391–401
- Fabian R, Seyfarth E-A (1997) Acetylcholine and histamine are transmitter candidates in identifiable mechanosensitive neurons of the spider *Cupiennius salei*: An immunocytochemical study. Cell Tissue Res 287:413–423
- Fabian-Fine R, Höger U, Seyfarth E-A, Meinertzhagen IA (1999) Peripheral synapses at identified mechanosensory neurons in spiders: three-dimensional reconstruction and GABA immunocytochemistry. J Neurosci 19:298–310
- Fabian-Fine R, Meinertzhagen IA, Seyfarth E-A (2000) Organization of efferent peripheral synapses at mechanosensory neurons in spiders. J Comp Neurol 420:195–210
- Fabian-Fine R, Seyfarth E-A, Meinertzhagen IA (2002) Peripheral synaptic contacts at mechanoreceptors in arachnids and crustaceans: morphological and immunocytochemical characteristics. Microsc Res Tech 58:283–298
- French AS, Torkkeli PH, Seyfarth EA (2002) From stress and strain to spikes: mechanotransduction in spider slit sensilla. J Comp Physiol A 188:739–752
- Gingl E, Burger AM, Barth FG (2006) Intracellular recording from a spider vibration receptor. J Comp Physiol A 192:551–558
- Höger U, Seyfarth E-A (2001) Structural correlates of mechanosensory transduction and adaptation in identified neurons of spider slit sensilla. J Comp Physiol A 187:727–736
- Höger U, Torkkeli PH, Seyfarth EA, French AS (1997) Ionic selectivity of mechanically activated channels in spider mechanoreceptor neurons. J Neurophysiol 78:2079–2085
- Höböl B, Böhm HJ, Rammerstorfer FG, Barth FG (2007) Finite element modeling of arachnid slit sensilla I. The mechanical significance of different slit arrays. J Comp Physiol A 193:445–459
- Höböl B, Böhm HJ, Schaber CF, Rammerstorfer FG, Barth FG (2009) Finite element modeling of arachnid slit sensilla. II. Actual lyriform organs and the face deformations of the individual slits. J Comp Physiol A 195:881–894
- McConney ME, Schaber CF, Julian MD, Barth FG, Tsukruk VV (2007) Viscoelastic nanoscale properties of cuticle contribute to the high-pass properties of spider vibration receptor (*Cupiennius salei* Keys). J R Soc Interface 4:1135–1143
- Rovner JS, Barth FG (1981) Vibratory communication through living plants by a tropical wandering spider. Science 214:464–466
- Schaber CF, Gorb S, Barth FG (2005) Explorations into space: nanomechanics of embedded spider strain detectors. Proceedings of 9th meeting of the Austrian Neuroscience Association, Obergurgl, p 50
- Schildberger K (1984) Temporal selectivity of identified auditory neurons in the cricket brain. J Comp Physiol A 155:171–185
- Schüch W, Barth FG (1985) Temporal patterns in the vibratory courtship signals of the wandering spider *Cupiennius salei* Keys. Behav Ecol Sociobiol 16:263–271
- Schüch W, Barth FG (1990) Vibratory communication in a spider: female responses to synthetic male vibrations. J Comp Physiol A 166:817–826
- Seyfarth E-A, French AS (1994) Intracellular characterization of identified sensory cells in a new spider mechanoreceptor preparation. J Neurophysiol 71:1422–1427
- Seyfarth E-A, Pflüger HJ (1984) Proprioceptor distribution and control of a muscle reflex in the tibia of spider legs. J Neurobiol 15:365–374
- Speck J, Barth FG (1982) Vibration sensitivity of pretarsal slit sensilla in the spider leg. J Comp Physiol A 148:187–194
- Speck-Hergenröder J, Barth FG (1988) Vibration sensitive hairs on the spider leg. Experientia 44:13–14
- Spurr AR (1969) A low viscosity epoxy resin embedding medium for electron microscopy. J Ultrastruct Res 26:31–43
- Tichy H, Gingl E, Ehn R, Papke M, Schulz S (2001) Female sex pheromone of a wandering spider (*Cupiennius salei*). Identification and sensory reception. J Comp Physiol A 187:75–78
- Torkkeli PH, Sekizawa SI, French AS (2001) Inactivation of voltage-activated Na⁺ currents contributes to different adaptation properties of paired mechanosensory neurons. J Neurophysiol 85:1595–1602
- Zar JH (1999) Biostatistical analysis. Prentice Hall, Upper Saddle River

Addendum:

Published Abstracts

Poster presentation

Explorations into space: nanomechanics of embedded spider strain detectors

Clemens F. Schaber ¹, Stanislav N. Gorb ², Friedrich G. Barth ¹

¹ Department of Neurobiology and Behavioral Sciences, Faculty of Life Sciences, University of Vienna,
Althanstraße 14, 1090 Wien, Austria

² Evolutionary Biomaterials Group, Department Arzt, Max Planck Institute for Metals Research,
Heisenbergstraße 3, 70569 Stuttgart, Germany

Slit sense organs of arachnids are strain detectors embedded in the chitinous exoskeleton (review in Barth 2002). In lyriform organs the various patterns of slit arrangement strongly affect their mechanical behavior and consequently their response to various stimulus parameters. Scanning white light interferometry and microforce measurements were applied in order to quantitatively determine the relation between the stimulus force and the deformation of the organ's slits (leading to a neural response) and of the cuticle surrounding it. With the techniques applied it was possible to obtain for the first time spatially highly resolved pictures of three dimensional deformations in vivo and under controlled load conditions.

Two different organs were selected to study the mechanics of stimulation. (i) Lyriform organ HS-10 on the metatarsus is a highly sensitive vibration receptor and adequately stimulated by substrate vibrations which push the tarsus against the metatarsus. Quasinatural stimuli were applied by dorsad deflection of the tarsus. The threshold for organ compression indicated by the compression of the longest slit is reached when the tarsus is deflected by slightly more than 25° (relative to fully stretched position). The load at threshold is about 2 mN and rises with 240 µN/° at higher deflection values. From 40° to 45° onwards all the slits are fully compressed and the force increases more steeply with 3 mN/° to more than 40 mN. (ii) Lyriform organ HS-8 on the tibia is effectively stimulated by lateral deflection of the metatarsus which is linked to the tibia by a dorsally located hinge joint. The stimulation force rises linearly (approximately 1.1 mN/°; N=6, n=18) in the tested range from 0° to 10°. The threshold for compression of the two longest slits is below 0.26° and 300 µN. The dome on which the organ is located slightly flattens under the load, which enhances slit compression (adequate stimulation).

The linearity of the stimulus transformation in HS-8 underlines the organ's proprioceptive function. The curvature of the cuticle at the site of the organ leads to an amplification of strain. The exponential rise of the force with increasing stimulus amplitude makes HS-10 perfectly suited for coding a large range of vibrational amplitudes. The evident differences in the mechanical properties of stimulus transport and stimulus transformation in different lyriform organs point to the value of quantitative mechanical measurements at the micro scale and below.

References

Barth FG (2002) *A Spider's World: Senses and Behavior*. Springer, Berlin Heidelberg New York

Supported by grant P16348 of the Austrian Science Fund FWF to FGB

Poster presentation

Arthropod strain detectors: III. Micromechanics of stimulus transformation by cuticular structures

Clemens F. Schaber¹, Stanislav N. Gorb², Friedrich G. Barth¹

¹ Department of Neurobiology and Behavioral Science, Faculty of Life Sciences, University of Vienna, Vienna, Austria; ² Evolutionary Biomaterials Group, Department Arzt, Max-Planck-Institute for Metals Research, Stuttgart, Germany

Among arthropods spiders have the most elaborate system of strain detectors embedded in their exoskeleton. Their lyriform organs form arrays of up to 30 fine slits closely arranged in parallel in widely differing patterns and locations (Barth and Libera 1970).

The mechanical consequences of the three-dimensional arrangement of the slits on stimulus transformation and thus response properties were studied in a highly sensitive vibration detector on the metatarsus (organ HS10) and a proprioceptive organ (HS8) on the tibia of the spider leg using micro force measurements and white light interferometry.

Our main findings are the following.

- (i) The force needed to adequately stimulate HS10 by tarsal deflections rises exponentially from ca. 240 $\mu\text{N}/^\circ$ at threshold to 3 $\text{mN}/^\circ$ at the natural upper limit. In HS8, however, force applied by lateral shift of the metatarsus rises linearly with 1 to 2 $\text{mN}/^\circ$ ($N=6$) in the range from 0° to 10° .
- (ii) In HS10 the stimulus is transmitted from the tarsus to the slits through a soft and viscoelastic cuticular pad (Young's Modulus about 1 MPa) located distally on the metatarsus and at least partly explaining the high-pass characteristics of the organ. In case of HS8 the stimulus slightly flattens the cuticular dome the organ is located on. Thus slit deformation is enhanced. Compression at the site of the sensory dendrite is in the range of 4.4 to 136 nm/mN in individual slits.

The mechanical adaptation of HS10 to a large range of stimulus amplitudes by an exponential transformation of forces and the linear dependence of HS8 highlight the functional significance of the specific location of a lyriform organ on the leg and of the material involved in stimulus transport.

References

Barth FG, Libera W (1970) Ein Atlas der Spaltsinnesorgane von *Cupiennius salei* Keys. Chelicerata (Araneae). Z Morph Tiere 68:343-369

Supported by the Hochschuljubiläumsstiftung Vienna and project P16348 of the Austrian Science Fund FWF to FGB.

Materials Research Society (MRS) Fall Meeting
Boston, MA, USA; November 2006

Oral presentation by Michael E. McConney

Characterization of Ultra-Sensitive Air Flow Receptors of live Wandering Spiders

Michael E. McConney^{1,2}, Clemens F. Schaber³, Michael D. Julian¹, Friedrich G. Barth³
and Vladimir V. Tsukruk^{1,2}

¹Department of Materials Science and Engineering, Iowa State University, Ames, Iowa

²School of Materials Science and Engineering, Georgia Institute of Technology, Atlanta, Georgia

³Department of Neurobiology and Behavioral Sciences, University of Vienna, Vienna, Vienna, Austria

Wandering spiders (*Cupiennius salei*) have wind-sensing hairs with extremely high sensitivity. We made direct point-load measurements of the nanomechanical properties of these ultra-sensitive wind sensing hairs on the legs of live wandering spiders using force spectroscopy based upon atomic force microscopy. All measurements were done on intact hairs cut to between 10-100 μm . These measurements lead to calculations of the maximum deflection angle, and the spring constant of the hair itself. Preliminary results show that the torsional constant of the hair-membrane structure is between 5×10^{-12} and 3×10^{-11} Nm/rad. An estimation of the hair's overall Young's modulus and the threshold sensing energy is also discussed.

Meeting of the Society for Experimental Biology
Glasgow, UK; April 2007
Comparative Biochemistry and Physiology 146A Supplement: S134, 2007

Lecture by Friedrich G. Barth

Arthropod Mechanoreceptors: from Biology to Engineering

Friedrich G. Barth, University of Vienna, Austria, Bernhard Hössl, Vienna University of Technology, Austria, Clemens F. Schaber, University of Vienna, Austria, Stanislav N. Gorb, Max Planck Institute for Metals Research, Germany, Helmut Böhm, Vienna University of Technology, Austria and Franz G. Rammerstorfer, Vienna University of Technology, Austria

Arachnid slit sensilla monitor minute cuticular strains in the exoskeleton which are due to muscle activity, hemolymph pressure and substrate vibrations. Their highly refined micromechanical properties are modelled to establish a basis for the design of biomimetic force sensors. We report on finite element (FE) and interferometric (IF) analyses and on atomic force microscopy (AFM) of close parallel, lyriform slit arrays.

FE analysis. Even minor morphological variations of slit arrangement affect slit interaction and thus stimulus transformation. The compressive slit face displacement D , which leads to nervous excitation, is mainly influenced by slit length l and load direction F whereas a slit's aspect ratio (20–100) is hardly relevant. At lateral distances between slits typical of lyriform organs ($S = 0.03 l$) their lateral shift considerably influences slit compression.

White light IF, micro force measurements. Forces needed to stimulate the metatarsal lyriform vibration detector by deflecting the tarsus rise *exponentially* from ca. 240 $\mu\text{N}/^\circ$ at threshold to 3 $\text{mN}/^\circ$ at the upper natural limit. The equivalent relation is *linear* (1 to 2 $\text{mN}/^\circ$) for a proprioceptive lyriform organ, stimulated by lateral displacement of the metatarsus. Thus the biologically most relevant difference regarding working range and amplitude resolution has a strong mechanical basis. Similarly, the physiological high pass characteristics of the vibration detector correlates with the visco-elasticity of a cuticular pad in front of the organ which transforms the stimulus on its way to the slits. Slit compression varies between 4.4 and 136 nm/mN depending on the slit within the array.

Oral and poster presentation

Arthropod force detectors: threshold curve of vibration receptor determined by material properties of stimulus transforming cuticle in *Cupiennius salei*

Clemens F. Schaber¹, Michael E. McConney², Michael D. Julian², Elisabeth Vogel¹,
Vladimir V. Tsukruk², Friedrich G. Barth¹

¹ Department of Neurobiology and Cognition Research, Faculty of Life Sciences, University of Vienna,
Vienna, Austria

² School of Materials Science and Engineering, Georgia Institute of Technology, Atlanta, USA

Spiders make use of vibrations for prey detection, communication during courtship and other behaviors. Their most sensitive vibration receptor organ is the metatarsal organ. It is located in between a highly viscoelastic cuticular pad distally and stiff sclerotized cuticle proximally dorsally on the metatarsus at the joint with the tarsus (Barth 2002). The tarsus contacts the pad when the spider is active and effectively filters vibrations of the substrate on their way to the metatarsal organ.

According to atomic force microscopy (AFM) and surface force spectroscopy (SFS) Young's modulus of the pad material is close to 15 MPa at low frequencies of stimulation beyond ca. 30 Hz. It increases rapidly with increasing frequency and reaches ca. 70 MPa at the highest frequency tested (112 Hz). Being soft the pad absorbs more energy at low frequencies and its increasing stiffness at higher frequencies results in less energy absorption and more efficient stimulus transmission to the vibration sensor (McConney et al. 2007). For this reason the pad is responsible for the unusual high-pass characteristics exhibited by the sensory thresholds of the metatarsal organ, with low sensitivity for low frequency vibrations (threshold 10–100 μm at 0.1 to 30 Hz) and steeply increasing sensitivity at higher frequencies (threshold 0.001–0.01 μm at 600 Hz) (Barth and Geethabali 1982). The viscoelastic cuticular pad unburdens the sensory system by filtering out biologically irrelevant low-frequency vibratory noise before it even reaches the sensory cells.

High viscoelasticity is typical for polymeric materials near their glass transition temperature. This is a temperature range, where by a drop of 20–30°C the stiffness of the material increases by a factor of 1000. Electrophysiological experiments support the

applicability of this concept to the cuticular pad. In experiments with spider legs cooled down from 32°C to 14°C the sensitivity rises up to tenfold indicating that the stiffness of the pad increases as predicted for a material near its glass transition temperature.

Supported by grant P16348 of the Austrian Science Foundation FWF to FGB and by the DARPA BioSenSE project grant FA9550-05-1-0459 to FGB and VVT.

References

- Barth FG (2002) A spider's world: senses and behavior. Springer Berlin Heidelberg New York
- Barth FG, Geethabali (1982) Spider vibration receptors: threshold curves of individual slits in the metatarsal lyriform organ. *J Comp Physiol A* 148:175–185
- McConney ME, Schaber CF, Julian MD, Barth FG, Tsukruk VV (2007) Viscoelastic nanoscale properties of cuticle contribute to the high-pass properties of spider vibration receptor (*Cupiennius salei* Keys.). *J R Soc Interface* doi:10.1098/rsif.2007.1000

10th Meeting of the Austrian Neuroscience Society (ANA)
Seggau, Austria; September 2007

Poster presentation

Arthropod medium flow sensors: I. Sensory hair biomechanics of spider trichobothria (*Cupiennius salei*)

Clemens F. Schaber, Friedrich G. Barth

Department of Neurobiology and Cognition Research, Faculty of Life Sciences, University of Vienna,
Vienna, Austria

The spider *Cupiennius* carries about 1000 wind sensitive hairs (trichobothria) on its exoskeleton, each of them capable to sense mechanical energy smaller than that of a photon of green light by the deflection of its hair shaft (Barth 2002). The hair shaft is suspended in the exoskeleton by a highly elastic cuticular membrane. The outer part of the hair shaft is long (up to 1.6 mm) and protrudes into the air, whereas the inner part of the hair shaft below the membrane is short (up to 2 μm) and surrounded by lymph. The dendrites of four sensory cells are coupled to the inner hair shaft, which ends as a cuticular tube (length up to 4 μm).

Forces in the range of 10^{-16} Nm to 10^{-15} Nm suffice to reach the sensory threshold of hair shaft deflections at 0.1–0.01 degrees. Because the hair shaft and the inner cuticular tube are stiff and do not bend during adequate stimulation, deflections of the hair tip are scaled down by a factor of 1/250 on their way to the sensory cells. Correspondingly, the forces deflecting the hair are amplified 250-fold. The displacements of the cuticular tube at the hair shaft's threshold deflection of 0.01° are within 7 to 10 \AA only (N=5). These values are well within the range of the shifts (4–7 \AA) calculated from the lengths of the lever arms (N=5) and likely represent the adequate stimulus opening mechanically sensitive ion channels in the dendritic cell membrane.

The extreme sensitivity and the outstanding mechanical robustness of the spider trichobothria (billions of loading cycles during the lifetime of an adult spider) make them an attractive model for engineers developing and improving artificial hair-like medium-flow sensors.

Supported by the DARPA BioSenSE project grant FA9550-05-1-0459 to FGB.

References

Barth FG (2002) A spider's world: senses and behavior. Springer Berlin Heidelberg New York

Materials Research Society (MRS) Spring Meeting
San Francisco, CA, USA; March 2008

Oral presentation by Michael E. McConney

Wandering spider uses viscoelastic properties of cuticle for mechanical signal filtering

Michael E. McConney^{1,2}, Clemens F. Schaber³, Michael D. Julian⁴, Friedrich G. Barth³,
Vladimir V. Tsukruk^{1,2}

1. School of Materials Science and Engineering, Georgia Institute of Technology, Atlanta, GA, 30332

2. School of Polymer, Textile and Fiber Engineering, Georgia Institute of Technology, Atlanta, GA,
30332

3. Department of Neurobiology and Cognition Research, Faculty of Life Sciences, University of Vienna,
Vienna, Austria

4. Department of Chemistry, University of Arkansas Fort Smith, Fort Smith, AK, 72916

Wandering spiders (*Cupiennius salei*) utilize bio-polymeric materials near glass transition for mechanical signal filtering of vibration sensors. We used the AFM to probe the time dependent mechanical behavior of these materials and measured Young's modulus of a rubber-like pad-shaped material situated in between the stimulus source and the vibration sensors. Previous electrophysiological measurements showed a dramatic rise in the vibration amplitude needed to elicit an electrophysiological response below 10 Hz stimulation frequency. Our AFM elastic modulus measurements showed a similar decrease in stiffness as the frequency dropped to around 10 Hz, due to viscoelastic effects. The pad is acting as a high-pass filter for the vibration sensors.

According to point-load measurements on wind-sensing hair receptors of spiders the torsional stiffness of the hair suspension dropped off as the probing frequency was below 20 Hz. Like in the pad system previous electrophysiological measurements showed very low sensitivity to low stimulus frequencies, which may be partly due to the viscoelastic properties of the biopolymer.

Oral and poster presentation

Micromechanics of spider mechanoreceptors

Clemens F. Schaber, Friedrich G. Barth

University of Vienna, Faculty of Life Sciences, Department of Neurobiology and Cognition Research,
Althanstr. 14, A-1090 Vienna, Austria; clemens.schaber@univie.ac.at

Spiders are equipped with exquisite mechanoreceptors like vibration and air-flow detectors, which enable them to orient towards prey and mates. We report on micromechanical processes underlying stimulus transformation in these two types of sensors.

(i) The main *vibration receptors* of spiders are the metatarsal organs. In *Cupiennius salei* they consist of 21 innervated slits each about 2 μm wide and up to 150 μm long (1). The organ is stimulated by compression when the most distal leg segment (tarsus) pushes against the metatarsus due to its deflection by substrate vibrations. The force to deflect the tarsus above threshold amounts to 240 $\mu\text{N}/\text{deg}$. According to white light interferometric studies slit compression amounts to 20 to 100 nm/deg , strongly depending on the location of the slit within the array. At the behaviorally relevant threshold deflection of the tarsus by 0.05 deg at 400 Hz, slit compressions by 0.5 nm and forces of 12 μN generate a nervous response.

(ii) Spider *air-flow sensors* are hair-like sensilla (trichobothria) on the legs and pedipalps. Due to their minute mass and low stiffness of their suspension (about 10^{-12} Nm/rad), (2) trichobothria are deflected by the slightest air movements. A trichobothrium forms a lever with an outer hair shaft (up to 1.6 mm long) protruding into the air and an inner hair shaft (0.5-1.8 μm) below the center of rotation to which four sensory cells attach. The length ratio of the two lever arms is about 900:1. Forces deflecting the hair tip are amplified 900-fold on their way to the sensory cells, whereas the deflection is scaled down by the same amount. Hair deflection by 0.01 deg (physiological threshold; (3)) displaces the sensory dendrites by 0.4 to 1 nm.

The displacements at the sensory cells are in the same range in both mechanoreceptor types, and close to the values estimated for cricket filiform hairs (0.1 nm; (4)), *Drosophila* bristles (2 nm; (5)), fish neuromasts (2.5 nm; (6)), and vertebrate hair cells

(< 1 nm; (7)). In all cases they are thought to increase the conductivity of mechanosensitive ion channels and to thereby elicit a nervous response.

Frequency tuning is achieved in different ways. Whereas in the vibration sensor the viscoelastic properties of specialized cuticle substantially contribute to its high-pass characteristics (8), it is the boundary layer thickness (low frequency end) and the hair's inertia (high frequency end), which largely determine the mechanical band-pass properties of a trichobothrium.

- 1 Barth FG (2002) A spider's world: senses and behavior. Springer.
- 2 Humphrey JAC, Barth FG (2008) In: Casas J, Simpson SJ (eds) Advances in Insect Physiology. Insect Mechanics and Control, Vol.34, Elsevier:1–80
- 3 Barth FG, Höller A (1999) Phil Trans R Soc Lond B 354:183–192
- 4 Thurm U (1982) In: Hoppe W, Lohmann W, Markl H, Ziegler H (eds) Biophysik, 2nd ed., Springer:691–696
- 5 Walker RG, Willingham AT, Zuker CS (2000) Science 287:2229–2234
- 6 Van Netten SM (2006) Biol Cybern 94:67–85
- 7 Vollrath MA, Kwan KY, Corey DP (2007) Annu Rev Neurosci 30:339–365
- 8 McConney ME, Schaber CF, Julian MD, Barth FG, Tsukruk VV (2007) J R Soc Interface 4:1135–1143

Meeting of The American Physical Society
Pittsburg, PA, USA; March 2009

Oral presentation by Michael E. McConney

Mechanical Signal Filtering by Viscoelastic Properties of Cuticle in a Wandering Spider

MICHAEL E. MCCONNEY, Georgia Institute of Technology, CLEMENS F. SCHABER, University of Vienna, MICHAEL D. JULIAN, California State University Stanislaus, JOSEPH A. C. HUMPHREY, University of Virginia, FRIEDRICH G. BARTH, University of Vienna, VLADIMIR V. TSUKRUK, Georgia Institute of Technology; mccconney@gatech.edu

As recently found, in mechano-sensors of wandering spiders (*Cupiennius salei*) viscoelastic materials are important in signal filtering. We used atomic force microscopy to probe the time dependent mechanical behavior of these materials in live animals. We measured Young's modulus of a rubbery material located between a vibration receptor and the stimulus source. Earlier electrophysiological studies had demonstrated that the strain needed to elicit a sensory response (action potential) increased drastically as stimulus frequencies went below 10 Hz. Our surface force spectroscopy data similarly indicated a significant decrease in stiffness of the cuticular material and therefore less efficient energy transmission due to viscoelastic effects, as the frequency dropped to around 10 Hz. The stimulus transmitting cuticular material is acting as a high-pass filter for the mechanical stimulus on its way to the strain receptors. Again our results indicate that viscoelastic mechanical signal filtering is an important tool for arthropods to specifically respond to biologically relevant stimulus patterns.

Australasian Society for the Study of Animal Behaviour Annual Conference
Auckland, New Zealand; April 2009

Oral presentation by Anne E. Wignall

Vibrations in 3-dimensional spider webs: what characterises prey?

Anne E. Wignall¹, Clemens F. Schaber² & Phillip W. Taylor¹

¹Department of Brain, Behaviour and Evolution, Macquarie University, Sydney NSW 2109

²Department of Neurobiology, University of Vienna, Vienna, Austria

Corresponding author email: anne@galliform.bhs.mq.edu.au

Web-building spiders rely on vibrations generated in their webs as a source of vital information. Prey, predators and conspecifics can be characterised by the vibrations they generate in the web. As a result, how a vibration propagates through a spider's web has important implications for how a spider will interpret and respond to the vibration source. While vibration propagation has been characterised in the 2-dimensional orb-webs of several spider species, the 3-dimensional webs of other spiders remain poorly understood. Here, we present the findings of a preliminary study examining propagation of vibrations through the tangle web of *Achaearanea tepidariorum*. Higher frequencies are attenuated more than lower frequencies, with resonance in the web affecting frequencies above 100 Hz. These results will be important for defining the characteristics used by spiders to classify sources of vibration, particularly the characteristics of vibrations generated by prey.

Oral presentation

Arachnid mechanoreception: I. Micromechanics of spider air flow sensors

Clemens F. Schaber, Friedrich G. Barth

Department of Neurobiology and Cognition Research, Center for Organismal Systems Biology,
University of Vienna; clemens.schaber@univie.ac.at

Apart from using their substrate vibration sense, spiders orient towards prey and avoid predators by detecting air flows with extreme sensitivity. Torques of 10^{-15} Nm suffice to deflect their hair-like air flow sensors above firing threshold (0.1° – 0.01° (1)).

The outstanding sensitivity of the trichobothria is to a considerable degree based on their mechanical properties: tiny mass, elaborate lever system (scaling up stimulus force by a factor of 245 ± 36 (N=5)), mechanical tuning related to boundary layer thickness, and a delicate suspension of the sensory hair.

To examine the dynamics of their suspension trichobothria were deflected at angular velocities from 0.0004 to 0.26 rad s⁻¹ using the cantilever in an atomic force microscope. Surprisingly, the torque needed to deflect the hair shaft dropped significantly at deflection velocities below 0.05 rad s⁻¹ indicating a strong viscoelasticity of the hair suspension. A three-parameter viscoelastic standard solid model derived from the experimental data yielded two spring parameters $S_1=2.9 \times 10^{-11}$ Nm rad⁻¹ and $S_2=2.8 \times 10^{-11}$ Nm rad⁻¹, and a damping parameter $R=1.5 \times 10^{-12}$ Nm s rad⁻¹ (2).

The viscoelasticity of the trichobothrium's suspension facilitates the start of hair motion and therefore the detection of the rapid changes characteristic of biologically relevant air flow signals. It thus works to promote the electrophysiologically measured highly phasic response character of the sensory cells.

Supported by the program BioSenSE of DARPA to FGB.

¹ Barth FG, Höller A (1999) Dynamics of arthropod filiform hairs V. The response of spider trichobothria to natural stimuli. *Phil Trans R Soc B* 354:183–192

² McConney ME, Schaber CF, Julian MD, Eberhardt WC, Humphrey JAC, Barth FG, Tsukruk VV (2009) Surface force spectroscopic point load measurements and viscoelastic modelling of the micromechanical properties of air flow sensitive hairs of a spider (*Cupiennius salei*). *J R Soc Interface* doi:10.1098/rsif.2008.0463 (in print)

Oral presentation

Micromechanics of spider mechanoreceptors: viscoelastic properties of cuticle for the tuning of vibration and air flow sensors

Clemens F. Schaber¹, Elisabeth Vogel^{1,2}, Friedrich G. Barth¹

¹Universität Wien, Neurobiology and Cognition Research, Centre for Organismal Systems Biology, Wien

²Medical University of Vienna, Biochemistry and Molecular Biology, Center for Brain Research, Wien

Spiders use vibrations and air flows to court, localize prey, and to avoid predators. The vibration sensitive metatarsal lyriform organ and the air flow sensitive hair-like trichobothria show outstanding sensibility. The physiological threshold of single slits of the metatarsal organ has a pronounced high-pass characteristic with low sensitivity up to about 30 Hz and rapidly decreasing thresholds down to 4.5 nm tarsal deflection at 1 kHz (1). Torques of 10^{-15} Nm suffice to deflect trichobothria by threshold angles between 0.1-0.01° (2).

To characterize the effect of material properties of cuticular structures on stimulus transmission to the sensory cells and the cells' dynamic behavior atomic force microscopy (AFM) and surface force spectroscopy were applied. A soft cuticular pad located on the way of the vibrations from the substrate to the metatarsal vibration sensor was analyzed with probing frequencies between 0.1 and 112 Hz (3). The mechanical properties of the suspension of trichobothria were examined by deflecting the hair shaft using the AFM cantilever at angular velocities from 0.0004-0.26 rad s⁻¹ (4).

Whereas the Young's modulus of the pad material is close to 15 MPa at frequencies below 30 Hz, it increases rapidly with increasing frequencies reaching 70 MPa at 112 Hz. The pad's viscoelasticity nicely explains the high-pass characteristics measured earlier electrophysiologically. Further electrophysiological experiments performed on the organ at different temperatures show a tenfold increase of sensitivity by cooling it

down from 32° C to 14° C, which supports the earlier assumption that the material's rubber-glass transition temperature is close to 25° C (3).

The torque needed to deflect the trichobothrium drops significantly at deflection velocities smaller than 0.05 rad s⁻¹. The measured data can be fitted with a three-parameter viscoelastic standard solid model yielding two spring parameters $S_1=2.9 \times 10^{-11}$ Nm rad⁻¹, $S_2=2.8 \times 10^{-11}$ Nm rad⁻¹ and a damping parameter of $R=1.5 \times 10^{-12}$ Nm s rad⁻¹ for the hair suspension (4).

The mechanical high-pass filtering by the pad unburdens the spider from processing information about biologically irrelevant low-frequency noise (typically below 30 Hz). Similarly, the viscoelastic properties of the trichobothrium's suspension facilitate the start of hair motion and therefore the detection of rapid changes in air flows characteristic of biologically relevant air flow signals.

Supported by the program BioSenSE of DARPA to FGB.

¹ Molina J, Schaber CF, Barth FG (2009) J Comp Physiol A (in print)

² Barth FG, Höller A (1999) Phil Trans R Soc Lond B 354:183-192

³ McConney ME, Schaber CF, Julian MD, Barth FG, Tsukruk VV (2007) J R Soc Interface 4:1135-1143

⁴ McConney ME, Schaber CF, Julian MD, Eberhardt WC, Humphrey JAC, Barth FG, Tsukruk VV (2009) J R Soc Interface (in print)

Proceedings of the COST Strategic Workshop:
Principles and Development of Bio-Inspired Materials
Vienna, Austria; April 2010

Lecture by Friedrich G. Barth

Biologically applied physics in sensory organs: spider mechanoreceptors

Friedrich G. Barth, Elisabeth Vogel, Clemens F. Schaber

Department of Neurobiology, Center for Organismal Systems Biology, University of Vienna, Althanstr.
14, 1090 Vienna, Austria; friedrich.g.barth@univie.ac.at

The importance of sensory information for the guidance of animal behavior is reflected by a fascinating wealth of sensory organs. These exhibit an enormous variety which is a consequence of the different evolutionary potentials and needs of individual species. All these sensory organs and their corresponding neuronal pathways have to be tuned to the reception and perception of the biologically relevant spatio-temporal stimulus patterns as they occur in the respective habitat of a species. It is the invertebrate animals in particular, where one finds the most exotic sense organs and outstanding sensory capacities. Quite a few of these capacities are alien to us humans.

The variation among sense organs serving the detection and analysis of stimuli belonging to the same modality (form of stimulus energy) is not much due to differences at the level of the sensory cells themselves, but to differences in the morphology and functional properties of the non-nervous structures responsible for the uptake of the stimulus and its transformation on its way to the sensory cell. Here we have a most impressive evolutionary playground and inventiveness for biologically applied physics.

The purpose of the lecture is to illustrate this aspect using two examples taken from our own research on spider mechanoreceptors [1] [2]. Both examples will make it clear that none of the sense organs can be adequately understood unless we are aware of its biological significance that is the role it plays in normal behavior under biologically relevant conditions.

(i) The first example will address the Bauplan of **mechanosensory hairs**, the most common of all biological sensors. It will contrast a *tactile hair* [3] and an *airflow sensor* [4] [5], showing how one can be converted into the other by attending to a few physical parameters only. Obviously, the properties of the materials involved and their adjustment to the particular measurement task are of prime importance. Whereas in case of the tactile hair a most relevant “design question” is how to combine sufficient mechanical sensitivity with the necessary mechanical robustness, it is the outstandingly high mechanical sensitivity in case of the flow sensors which attracts attention.

(ii) The second example refers to **slit sensilla**, a type of sensor which in a way is the opposite of a hair [1]. Whereas the mechanosensitive hair sensillum can be classified as a movement detector (responding to the deflection of the hair shaft), slit sensilla are *strain detectors* embedded in the cuticular exoskeleton and responding to the slightest deformation due to loads caused by muscular activity, gravity, substrate vibrations, etc.. Among the several thousand slit sensilla monitoring strain in a spider exoskeleton the vibration detector located distally on the walking legs will receive particular attention. Again, material properties are highly relevant in determining functional properties. Recently, a small cuticular pad in front of the organ, a special stimulus transforming structure, has turned out to be the main cause of the organ’s high pass characteristics. Due to the pad’s viscoelastic properties energy loss of stimulus transmission is much reduced at high frequencies as compared to low frequency stimulation. The result is a biologically highly relevant selectivity of the organ for frequencies higher than about 10 Hz [2] [6].

It is the area of stimulus transformation in particular where engineers can hope for bio-inspiration and for cleverly simple and unconventional solutions of technically demanding problems.

References

- [1] F.G. Barth, *A Spider’s World. Senses and Behavior*. Springer Verlag, Berlin Heidelberg New York, 394p, (2002)
- [2] P. Fratzl, F.G. Barth, *Biomaterial systems for mechanosensing and actuation*. Nature, 462, 442-448, (2009)
- [3] H.-E. Dechant, F.G. Rammerstorfer, F.G. Barth, *Arthropod touch reception: stimulus transformation and finite element model of spider tactile hairs*. J Comp Physiol A, 187, 313-323 (see also Erratum p. 851), (2001)
- [4] J.A.C. Humphrey, F.G. Barth, *Medium flow-sensing hairs: biomechanics and models*. In: J. Casas, S.J. Simpson (eds.) *Advances in Insect Physiology. Insect Mechanics and Control*, 34, 1-80, Elsevier Ltd., (2008)
- [5] M.E. McConney, C.F. Schaber, M.D. Julian, W.C. Eberhardt, J.A.C. Humphrey, F.G. Barth, V.V. Tsukruk, *Surface force spectroscopic point load measurements and viscoelastic modelling of the*

micromechanical properties of air flow sensitive hairs of a spider (Cupiennius salei). J R Soc Interface, 6, 681-694, (2009)

[6] M.E. McConney, C.F. Schaber, M.D. Julian, F.G. Barth, V.V. Tsukruk, *Viscoelastic nanoscale properties of cuticle contribute to the high-pass properties of spider vibration receptor (Cupiennius salei Keys.)*, J R Soc Interface, 4, 1135-1143, (2007)

Original research supported by grants of the Austrian Science Fund (FWF) and DARPA project BioSenSE to FGB.

Research Activities Clemens F. Schaber

I. Full papers

- McConney ME*, Schaber CF*, Julian MD, Barth FG, Tsukruk VV (2007) Viscoelastic nanoscale properties of cuticle contribute to the high-pass properties of spider vibration receptor (*Cupiennius salei* Keys). *J R Soc Interface* 4:1135–1143 (doi:10.1098/rsif.2007.1000)
- McConney ME*, Schaber CF*, Julian MD, Humphrey JAC, Barth FG, Tsukruk VV (2009) Surface force spectroscopic point load measurements and viscoelastic modelling of the micromechanical properties of air flow sensitive hairs of a spider (*Cupiennius salei*). *J R Soc Interface* 4:681–694 (doi:10.1098/rsif.2008.0463)
- Höbl B, Böhm HJ, Schaber CF, Rammerstorfer FG, Barth FG (2009) Finite element modelling of arachnid slit sensilla II. Actual lyriform organs and the deformation of the individual slits. *J Comp Physiol A* 195:881–894 (doi:10.1007/s00359-009-0467-y)
- Molina J, Schaber CF, Barth FG (2009) In search of differences between the two types of sensory cells innervating spider slit sensilla (*Cupiennius salei* Keys.) *J Comp Physiol A* 195:1031–1041 (doi:10.1007/s00359-009-0477-9)
- Schaber CF, Vogel E, Barth FG (2009) Micromechanics of spider mechanoreceptors: viscoelastic properties of cuticle for the tuning of vibration and air flow sensors. In: *Proceedings of the 1st International Conference on Natural and Biomimetic Mechanosensing*. Schriften des Forschungszentrums Jülich Reihe Allgemeines / General 5:14
- Schaber CF, Barth FG (2011) Spider joint hair sensilla: micromechanics and adaptation to proprioceptive stimulation. (in preparation)
- Schaber CF, Barth FG (2011) Force transformation in spider strain sensors: white light interferometry. (in preparation)
- Schaber CF, Barth FG (2011) Micromechanics of arthropod air flow sensors: functional morphology of the hair suspension in spider, scorpion, cricket, and cockroach. (in preparation)

* Equally contributing authors.

II. Abstracts

- Schaber CF, Gorb S, Barth FG (2005) Explorations into space: nanomechanics of embedded spider strain receptors. 9th Meeting of the Austrian Neuroscience Association (ANA), Obergurgl, Austria. (Poster)

- Schaber CF, Gorb SN, Barth FG (2006) Arthropod strain detectors: III. Micromechanics of stimulus transformation by cuticular structures. FENS Abstr 3: A039.13. 5th Forum of European Neuroscience Societies (FENS), Wien, Austria. (Poster)
- McConney ME, Schaber CF, Julian MD, Barth FG, Tsukruk VV (2006) Characterization of ultra-sensitive air flow receptors of live wandering spiders. Materials Research Society (MRS) 2006 Fall Meeting, Symposium DD7.6, Boston, MA, USA. (Oral presentation by ME McConney)
- Barth F, Schaber C, Hössl B, Böhm H, Rammerstorfer F, Gorb S (2007) Arthropod mechanoreceptors: from biology to engineering. Comp Biochem Physiol 146A Suppl: S134. Meeting of the Society for Experimental Biology (SEB), Glasgow, UK. (Lecture by FG Barth)
- Schaber CF, McConney ME, Julian MD, Vogel E, Tsukruk VV, Barth FG (2007) Arthropod force detectors: threshold curve of vibration receptor determined by material properties of stimulus transforming cuticle in *Cupiennius salei*. 10th Meeting of the Austrian Neuroscience Association (ANA), Seggau, Austria. (Oral presentation and poster)
- Schaber CF, Barth FG (2007) Arthropod medium flow sensors I. Sensory hair biomechanics of spider trichobothria (*Cupiennius salei*). 10th Meeting of the Austrian Neuroscience Association (ANA), Seggau, Austria. (Poster)
- McConney ME, Schaber CF, Julian M, Barth FG, Tsukruk VV (2008) Wandering spiders use viscoelastic properties of cuticle for mechanical signal filtering. Materials Research Society (MRS) 2008 Spring Meeting, Symposium GG7.6, San Francisco, CA, USA. (Oral presentation by ME McConney)
- Schaber CF, Barth FG (2008) Micromechanics of spider mechanoreceptors. Sensors and Sensing in Biology and Engineering, Cetraro, Italy. (Oral presentation and poster)
- McConney ME, Schaber CF, Julian M, Humphrey JAC, Barth FG, Tsukruk VV (2009) Mechanical signal filtering by viscoelastic properties of cuticle in a wandering spider. American Physical Society (APS) Meeting March 2009, Pittsburg, PA, USA. (Oral presentation by ME McConney)
- Wignall A, Schaber CF, Taylor P (2009) Vibrations in 3-dimensional spider webs: what characterises prey? Australasian Society for the Study of Animal Behaviour Annual Conference, Auckland, New Zealand. (Oral presentation Anne Wignall and abstract handout)
- Schaber CF, Barth FG (2009) Arachnid mechanoreception: I. Micromechanics of spider air flow sensors. 11th Meeting of the Austrian Neuroscience Association (ANA), Salzburg, Austria. (Oral presentation)
- Schaber CF, Vogel E, Barth FG (2009) Micromechanics of spider mechanoreceptors: viscoelastic properties of cuticle for the tuning of vibration and air flow sensors. 1st

International Conference on Natural and Biomimetic Mechanosensing, Dresden, Germany. (Oral presentation)

Barth FG, Vogel E, Schaber CF (2010) Biologically applied physics in sensory organs: spider mechanoreceptors. Proc COST Strategic Workshop “Principles and Development of Bio-Inspired Materials”, April 2010, Vienna, Austria. (Lecture by FG Barth)

III. Presentations without abstract

Schaber CF (2008) Sensor-Bionik. BIONIK AUSTRIA NETZWERK Meeting, Austrian Federal Economic Chamber Tirol, Innsbruck, July 2008

IV. Grants

- Grant for short term scientific work abroad of the University of Vienna, 3 months research in Stuttgart, Germany, March 2005 (1.500.- €)
- Travel grant of the Austrian Neuroscience Association to attend the 9th Meeting of the Austrian Neuroscience Association in Obergurgl, Austria, June 2005 (150.- €)
- Travel grant of the Österreichische Forschungsgemeinschaft to attend the conference “Sensors and Sensing in Biology and Engineering” in Cetraro, Italy, October 2008 (400.- €)
- Grant of the organizing committee of the conference “Sensors and Sensing in Biology and Engineering” to attend the conference in Cetraro, Italy, October 2008 (1.000.- USD)
- Travel grant of the Austrian Neuroscience Association to attend the 11th Meeting of the Austrian Neuroscience Association in Salzburg, Austria, September 2009 (150.- €)
- Travel grant of the Österreichische Forschungsgemeinschaft to attend the conference “1st International Conference on Natural and Biomimetic Mechanosensors” in Dresden, Germany, October 2009 (400.- €)

V. Projects

- Collaboration with the project “Arthropod Touch Reception” of the Austrian Science Foundation (FWF), principal investigator Friedrich G. Barth
- Collaboration with the project “Arthropod Force Detectors” of the Austrian Science Foundation (FWF), principal investigator Friedrich G. Barth
- Investigator in the project “Biosensorik: Mikromechnik von Mechanosensoren“ of the Hochschuljubiläumsstiftung der Stadt Wien, together with Friedrich G. Barth
- Investigator in the project and research network “Bio-Sensory Structure Emulation (BioSenSE)“ of DARPA, principal investigator Chang Liu (Northwestern University, Evanston, IL, USA), Vienna group leader Friedrich G. Barth

VI. Visiting scientist

- July – September 2004, March/April 2005, September/October 2005, Max Planck Institute for Metals Research, Stuttgart, Germany (total 6 months) for micro force testing, white light interferometry, and atomic force microscopy with Prof. Dr. Stanislav N. Gorb
- February/March 2006, Iowa State University, Ames, USA (2 weeks) for atomic force microscopy and surface force spectroscopy with Prof. Dr. Vladimir V. Tsukruk
- November 2007, Universität Konstanz, Germany (1 week) to learn and perfect calcium imaging with Prof. Dr. C. Giovanni Galizia

VII. Teaching

- Summer term 2002 tutor at the Institute of Zoology of the University of Vienna
- since summer term 2005 tutor und assistant lecturer at the Department of Neurobiology, Faculty of Life Sciences, University of Vienna (winter term: Project course neurobiology, summer term: Animal physiology course)
- since 2009 coaching of unattended refugee minors in biology, chemistry, physics, German, English, and mathematics (complimentary)

VIII. Membership

- since 2005 member of the Austrian Neuroscience Association

IX. Language skills

- German (mother tongue)
- English (excellent)
- Italian (basic skills)
- Spanish (basic skills)

X. Methodological skills

- Light microscopy (conventional, fluorescence, confocal)
- Calcium imaging
- Electrophysiology (extracellularly (perfect), intracellularly (basic skills))
- Electron microscopy (SEM, Cryo-SEM; TEM (basic skills))
- White light interferometry
- Mechanical testing (micro force testing, AFM)
- Atomic force microscopy
- Surface force spectroscopy
- Particle image velocimetry

XI. Varia

- Cover image of the Journal of the Royal Society Interface, volume 4, number 17, December 22nd, 2007 (photographer Friedrich G. Barth)
- Cover image of the Journal of the Royal Society Interface, volume 6, number 37, August 6th, 2009 (photographer Clemens F. Schaber)

Lebenslauf

Name: Clemens Florian Schaber

Geburtsdatum: 14. Juli 1976

Geburtsort: Innsbruck, Österreich

Staatbürgerschaft: österreichisch

Schulbildung:

- Beginn 1982
- 4 Jahre Volksschule Mühlau, Innsbruck, Österreich
- 4 Jahre Akademisches Gymnasium Innsbruck, Österreich
- 4 Jahre Akademisches Gymnasium Salzburg, Österreich
- Reifeprüfung am 22. Juni 1994.

Universitätsstudien:

- 1994 – 2004 Diplomstudium der Biologie/Zoologie an der Universität Wien
- 1999 – 2000 Wahlfach Chemie im Rahmen des Zoologiestudiums
- 2000 – 2001 Hilfsfach Biomathematik im Rahmen des Zoologiestudiums
- 1996 – 2000 Erweiterungsstudium in Publizistik und Kommunikationswissenschaften
- seit 2004 Doktoratsstudium der Naturwissenschaften, Fachgebiet Zoologie/Neurobiologie

Akademische Abschlüsse:

- 22. März 2004 Magister der Naturwissenschaften (Mag. rer. nat.) mit der Diplomarbeit „Propriorezeptive Haarsensillen am Tibia-Metatarsus-Gelenk von *Cupiennius salei*“ an der Universität Wien
- seit 2004 Dissertation „Mikromechanik von Mechanorezeptoren bei Arthropoden“ an der Universität Wien

Bisherige Tätigkeiten:

- 2005 – 2010 Lehrbeauftragter und Tutor am Department für Neurobiologie, Universität Wien (Wintersemester „Projektpraktikum Neurobiologie“, Sommersemester „Tierphysiologische Übungen“)

- 2005 – 2008 Wissenschaftlicher Mitarbeiter am Department für Neurobiologie, Universität Wien
- 2002 Tutor für Zoologie, Universität Wien (Sommersemester „Biologische Einführungsübungen“)
- 1994 – 2002 Projekt- und Organisationsmitarbeiter bei „Finance Trainer International G.m.b.H“ in Wien
- 1992 – 2000 Laborassistent im „Paracelsus Forschungsinstitut“ in Salzburg (Aufarbeitung von Gewässerproben)

Präsenzdienst:

- befreit

Privatadresse:

Mag. Clemens Schaber
Sonnenfelsgasse 7/10
1010 Wien
Österreich
Europa

Telefon +43 (0)1 512 6934

e-mail: clemens.schaber@gmail.com

